Tingyue Gu

Mathematical Modeling and Scale-Up of Liquid Chromatography

With Application Examples

Second Edition

Springer

Mathematical Modeling and Scale-Up of Liquid Chromatography

Tingyue Gu

Mathematical Modeling and Scale-Up of Liquid Chromatography

With Application Examples

Second Edition

Springer

Tingyue Gu
Department of Chemical & Biomolecular Engineering
Ohio University
Athens
Ohio
USA

ISBN 978-3-319-16144-0 ISBN 978-3-319-16145-7 (eBook)
DOI 10.1007/978-3-319-16145-7

Library of Congress Control Number: 2015936154

Springer Cham Heidelberg New York Dordrecht London
© Springer International Publishing Switzerland 1995, 2015
This work is subject to copyright. All rights are reserved by the Publisher, whether the whole or part of the material is concerned, specifically the rights of translation, reprinting, reuse of illustrations, recitation, broadcasting, reproduction on microfilms or in any other physical way, and transmission or information storage and retrieval, electronic adaptation, computer software, or by similar or dissimilar methodology now known or hereafter developed.
The use of general descriptive names, registered names, trademarks, service marks, etc. in this publication does not imply, even in the absence of a specific statement, that such names are exempt from the relevant protective laws and regulations and therefore free for general use.
The publisher, the authors and the editors are safe to assume that the advice and information in this book are believed to be true and accurate at the date of publication. Neither the publisher nor the authors or the editors give a warranty, express or implied, with respect to the material contained herein or for any errors or omissions that may have been made.

Printed on acid-free paper

Springer International Publishing AG Switzerland is part of Springer Science+Business Media (www.springer.com)

Preface

Liquid chromatography is no longer limited to chemical analysis. It has become an indispensable tool for the preparative- and large-scale purification of proteins and other fine chemicals including those from biorefineries. So far, the scale-up of liquid chromatography relies mostly on trial and error and a few scaling rules that are not precise enough.

This book provides numerical solutions to a series of general multicomponent rate models for liquid chromatography. The models consider dispersion in the main flow direction, interfacial film mass transfer between the bulk-fluid phase and the particle phase, intraparticle diffusion, and nonlinear multicomponent isotherms or the second-order kinetics. The models can be used to simulate various chromatographic operations such as breakthrough, elution (including gradient elution), and displacement. Various forms of liquid chromatography are covered, including adsorption, size-exclusion, reversed phase, hydrophobic interaction, ion-exchange, and affinity chromatography. The models provide more realistic descriptions of preparative- and large-scale liquid chromatography than the equilibrium theory and plate models because various mass transfer mechanisms are included.

The first edition of this book was published in the spring of 1995 when personal computers were not powerful enough to run stiff cases quickly. With the advances in computer hardware and software, the chromatography simulation software known as Chromulator described in this book can be easily run on today's personal computers. The software with graphic user interface provides near-real-time displays of simulated chromatograms. Comparisons using different input parameters are made effortlessly. In the past two decades, researchers have developed systematic methods to estimate the various parameters in the rate models, making the models much more useful in applications. A small chromatography column can be used in a lab setting to obtain parameters related to the packing structure and binding characteristics experimentally, while mass transfer parameters can be estimated using existing correlations without any experiments. Assuming that a large column has the same packing structure as in the small column, a priori chromatogram predictions can be made through computer simulation before the large column is built or purchased.

Some academic instructors have adopted the simulation software in this work for teaching, while others have used it for research and product development. Most readers do not need to be concerned with the complicated model equations and numerical methods when the primary purpose is to use the chromatography simulator to study chromatographic behaviors or for prediction and scale-up. It is only essential to understand the binding characteristics (e.g., isotherms) and three basic mass transfer mechanisms such that parameter estimation work can be carried out. The application examples provided in this second edition contain sufficient details for the estimation of parameters needed to run the simulators. Two Microsoft Excel spreadsheet programs are provided for parameter estimation calculations. Sufficient details are given for almost all simulated chromatograms so users can reproduce using the Chromulator software.

Some parts of this book are based on the author's Ph.D. dissertation work at Purdue University, West Lafayette, Indiana, USA. The author is deeply indebted to his dissertation advisor Prof. George T. Tsao for his guidance and encouragement. The author would like to thank Drs. Xueliang Fang and Zhiguo Su of Institute for Processing Engineering, Chinese Academy of Sciences, for coding the C++ graphical user interface. The newly added chapters and sections in this second edition dealing with the expansion of the rate models and application examples of the various models are mostly from research work conducted by the author, his graduate students, and external collaborators. The author would especially like to thank Millipore researchers who collaborated with the author in the modeling of cored beads.

Athens, OH Tingyue Gu
Fall 2014

Contents

List of Symbols

Symbol Description

A	Cross-sectional area of an LC column
A_1	Area above a breakthrough curve
A_2	Area under a breakthrough curve
a_i	Constant in Langmuir isotherm for component i, b_iC
b_i	Adsorption equilibrium constant for component i, k_{ai}/k_{di}
Bi_i	Biot number of mass transfer for component i, $k_iR_\mathrm{p}/(\varepsilon_\mathrm{p}D_{\mathrm{p}i})$ or $k_iR_\mathrm{p}/(\varepsilon_\mathrm{p}^\mathrm{a}D_{\mathrm{p}i})$
C_{0i}	Concentration used for nondimensionalization for component i, max $\{C_{fi}(t)\}$
$c_{\mathrm{b}i}$	$=C_{\mathrm{b}i}/C_{0i}$
$C_{\mathrm{b}i}$	Bulk-fluid phase concentration of component i
$C_{\mathrm{f}i}$	Feed concentration profile of component i, a time-dependent variable
c_i^∞	$= C_i^\infty/C_{0i}$
C_i^∞	Adsorption saturation capacity for component i (based on unit volume of particle skeleton)
C_m	Modulator concentration or volume fraction in gradient elution
$C_{\mathrm{m}0}$	Initial C_m value used to presaturate a column
C_p^c	Critical concentration for concentration crossover in a binary isotherm
$c_{\mathrm{p}i}$	$=C_{\mathrm{p}i}/C_{0i}$
$C_{\mathrm{p}i}$	Concentration of component i in the stagnant fluid phase inside particle macropores
$c_{\mathrm{p}i}^*$	$= C_{\mathrm{p}i}^*/C_{0i}$
$C_{\mathrm{p}i}^*$	Concentration of component i in the solid phase of particle (based on unit volume of particle skeleton)
CA_i	Dimensionless column holdup capacity area for component i
Da_i^a	Damköhler number for adsorption reaction for component i, $L(k_{ai}C_{0i})/v$
Da_i^d	Damköhler number for desorption reaction for component i, Lk_{di}/v
$D_{\mathrm{b}i}$	Axial or radial dispersion coefficient of component i

d_c	Inner diameter of a column
d_m	Diameter of a molecule
D_{mi}	Molecular diffusivity for component i
d_p	Average particle macropore diameter for the stationary phase particles
D_{pi}	Effective diffusivity of component i, porosity not included
F_i^{ex}	Size-exclusion factor for component i ($F^{ex} = 0$ means complete exclusion), $\varepsilon_{pi}{}^a/\varepsilon_p$
h	RFC column height
k'	Retention factor (capacity factor) for component i
k_{ai}	Adsorption reaction rate constant for component i in second-order kinetics
k_{di}	Desorption reaction rate constant for component i in second-order kinetics
k_i	Film mass transfer coefficient of component i
k_{ij}	Rate constant in ion-exchange reaction
K_{ij}	Equilibrium constant in ion exchange reaction
L	Column length
m_0	Moles of a solute mixed with W grams of an adsorbent in batch adsorption test
MW	Molecular weight
N	Number of interior collocation points
N_e	Number of quadratic elements in the finite element method
N_s	Number of components
Pe_L	Peclet number of axial dispersion for component i, vL/D_{bi}
$\overline{Q}_1$	The concentration of salt ion sorbed on the stationary phase available for ion exchange after steric hindrance
Q	Mobile phase volumetric flow rate
q_i	$=Q_i/C_{0i}$
Q_i	Sorbed concentration of component i on the ion-exchange resin
r	$=R/R_p$
R	Radial coordinate for particle
R_{core}	Radius of impenetrable inert core of a cored bead
Re	Reynolds number, $v\rho_f(2R_p)/\mu$
R_p	Particle radius
Sc	Schmidt number, $\mu/(\rho_f D_m)$
Sh	Sherwood number, $k(2R_p)/D_m$
t	Dimensional time ($t = 0$ is the moment a sample enters the column inlet)
T	Temperature in Kelvin
t_0	Dead volume time of unretained small molecules, such as salts and solvents
t_d	Dead volume time of unretained large molecules, such as blue dextran
t_{delay}	Delay time due to tubing, etc.
t_G	Gradient time
t_R	Dimensional retention time
v	Interstitial velocity, $4Q/(\pi d_c^2 \varepsilon_b)$
V	Dimensionless volumetric coordinate for RFC

V_0 Ratio of RFC hollow center cylinder volume to RFC bed volume, $X_0^2/\left(X_1^2 - X_0^2\right)$
V_b Bed volume of a chromatography column
V_{delay} Delay volume due to tubing, etc.
V_{e0} Elution volume corresponding to t_0
V_{ed} Elution volume corresponding to t_d
V_{loop} Volume of a sample loop
V_m Atomic volume
V_{sm} Total volume of the solution mixed with the adsorbent in batch adsorption test
W Weight of adsorbent
w_s Saturation capacity for the entire column
w_x Amount of eluite in the large sample for testing adsorption saturation capacity
X Radial coordinate for RFC column
X_0 Inner radius of RFC column
X_1 Outer radius of RFC column
z Dimensionless axial coordinate, Z/L
Z Axial coordinate

Greek Letters

α $= 2(V + V_0)^{1/2}\left[(1 + V_0)^{1/2} - V_0^{1/2}\right]$ for RFC column
$\alpha_i, \beta_i, \gamma_i$ Parameters for the eluite-modulator correlation
β Core radius fraction for cored beads, R_{core}/R_p
γ Dimensionless radial coordinate for cored beads, $(r - \beta)/(1 - \beta)$
ε_b Bed void volume fraction
ε_p Particle porosity
ε_p^a Accessible particle porosity in size exclusion chromatography
η_i Dimensionless constant for component i, $\varepsilon_p D_{pi} L/(R_p v)$ or $\varepsilon_{pi}^a D_{pi} L/(R_p v)$
θ_{ij} Discount factors for extended multicomponent Langmuir isotherm
Λ Ion-exchange capacity
λ $= d_m/d_p$
μ Mobile phase viscosity
ν_i Stoichiometric coefficient for component i in ion exchange (drop negative sign)
ξ_i Dimensionless constant for component i, $3\mathrm{Bi}_i\eta_i(1 - \varepsilon_b)/\varepsilon_b$
ρ, ρ_f Mobile phase density
ρ_p Post-swelling particle density, based on unit volume of particle skeleton
σ Steric factor in steric mass action isotherm for ion exchange
τ Dimensionless time, $t(v/L)$
τ_{delay} $= t_{delay}(v/L)$
τ_e A τ value at which the breakthrough curve has already leveled off

τ_{imp}	Dimensionless time duration for a rectangular pulse in elution
τ_R	Dimensionless retention time
τ_{shift}	Dimensionless shift time for mobile phase change
τ_{tor}	Tortuosity of porous particles
φ	Phase ratio (stationary phase to mobile phase), $(1-\varepsilon_b)(1-\varepsilon_p)/[\varepsilon_b+(1-\varepsilon_b)\varepsilon_p]$
ϕ	Basis function in the finite element method

Subscripts

a	Adsorption reaction
b	Bulk-fluid phase
d	Desorption reaction
i	ith component
j	jth component
imp	Sample impulse for injection
L	Column axial direction
p	Particle phase

Superscripts

a	Adsorption
c	Isotherm crossover concentration point
d	Desorption
*	Particle phase concentration
∞	Saturation capacity

List of Abbreviations

AFC	Axial flow chromatography
atol	Absolute tolerance in DVODE ODE solver
BC	Boundary condition
CPU	Central processing unit
DOS	Disk operating system
DVODE	Double (precision) VODE
FE	Finite element
GUI	Graphical user interface
HPLC	High performance liquid chromatography
IAST	Ideal adsorbed solution theory
IC	Initial condition
IEC	Ion-exchange chromatography
LC	Liquid chromatography
NBC	Natural boundary condition
OC	Orthogonal collocation
ODE	Ordinary differential equation
PC	Personal computer
PDE	Partial differential equation
RFC	Radial flow chromatography
RP-HPLC	Reverse phase high-performance liquid chromatography
RP-LC	Reverse phase liquid chromatography
SEC	Size-exclusion chromatography
SMA	Steric mass action
UV	Ultraviolet
VODE	Variable (coefficient) ODE (solver)

Chapter 1
Introduction

High-Performance Liquid Chromatography (HPLC) is undoubtedly one of the most important tools in chemical analysis [1]. It has become increasingly popular at preparative- and large scales, especially in purifying proteins and other high-value products [2]. At these scales, larger particles are often used to pack the columns in order to facilitate column packing and to reduce column pressure. Unlike small-scale analytical HPLC columns that can provide near plug-flow performances, large LC columns suffer from deteriorated performances due to dispersion and other effects.

At smaller scales, the scale-up of LC columns can usually be carried out by trial and error. To a large extent, the success depends on the experience of the researcher. A failure is often not costly. The situation changes when large-scale columns are concerned. Such columns may easily cost many thousands of US dollars. There is much more at stake in scale-up. A wrong estimation will render a custom-made column unsuitable for a particular application because of either insufficient resolution or a low feed capacity. When a mathematical model is applied appropriately, it can be very helpful in supplementing the researcher's experience during scale-up.

There are several kinds of mathematical models for LC with different complexities. A review of the models is given in Chap. 2. The equilibrium theory and plate models generally are not adequate for the realistic modeling and scale-up of multicomponent LC, because of their inability to depict mass transfer mechanisms involved in preparative- and large-scale LC separations.

The comprehensive mathematical models for LC are often called the general multicomponent rate models, since they consider axial dispersion, interfacial mass transfer between the mobile and the stationary phases, intraparticle diffusion, and multicomponent isotherms. They are more attractive than the equilibrium theory and plate models for the modeling and scale-up of multicomponent chromatography. Due to rapid advances in computer hardware, the rate models can now be solved numerically in usually a fraction of a second instead of minutes in the early 1990s. Because a general rate model considers different mass transfer mechanisms

© Springer International Publishing Switzerland 2015

T. Gu, *Mathematical Modeling and Scale-Up of Liquid Chromatography*,
DOI 10.1007/978-3-319-16145-7_1

in a column, it is suitable for the realistic modeling of preparative- and large-scale LC. Computer simulation using the model also provides an excellent tool for studying many chromatographic phenomena without doing actual lab experiments. Parameters that are not easily adjusted in experiments can be effortlessly changed in computer simulation to investigate various LC behaviors.

In Chap. 3 of this book, a robust and efficient numerical procedure is presented to solve a general nonlinear multicomponent rate model for adsorption that considers axial dispersion, external film mass transfer, intraparticle diffusion, and multicomponent Langmuir isotherms. It uses quadratic finite elements (FEs) for the discretization of the bulk-fluid phase partial differential equation (PDE) and the orthogonal collocation (OC) methods for the particle phase PDE in the model. The resulting ordinary differential equation (ODE) system can be solved using the Gear's stiff method [3] or the variable coefficient method [4]. An alternative boundary condition at the column exit to the Danckwerts boundary condition is also analyzed. Computer simulation suggests that it is unnecessary or even harmful to mass transfer if one of the Danckwerts boundary conditions is modified to make it physically more meaningful.

Chapter 4 describes parameter estimation methods for LC models in this work. System void volume due to tubing volume, etc., as well as bed voidage and particle porosity can be obtained using a few simple LC runs on a small bench-scale column. The three key dimensionless mass transfer parameters Pe_L, η, and Biot numbers can be evaluated using existing mass transfer correlations without any experimental work. A Microsoft Excel spreadsheet program can be obtained by contacting the author to estimate the three key parameters. Methods for obtaining isotherm parameters are also discussed.

The theoretical study of mass transfer in LC in Chap. 5 points out the effects of mass transfer on multicomponent chromatographic separations. The influences of the three key dimensionless mass transfer parameters are presented using computer simulation. Concentration profiles tend to be sharper when any of these three mass transfer parameters is increased. However, all of them become insensitive when their values are sufficiently large. In Chap. 6, a unified approach to a better understanding of multicomponent interference effects under mass transfer conditions is proposed. It has been shown that a displacement effect can be used to explain the dominating interference effects arising from the competition for binding sites among different components in multicomponent LC. It has been concluded that the concentration profile of a component usually becomes sharper due to the displacement effect from the next component in the elution order, while the concentration front of the displacer is often diffused as a consequence. Five factors stemming from equilibrium isotherms, which tend to escalate the displacement effect in multicomponent elutions, have been investigated. They have important implications for interference effects in multicomponent elutions under column-overload conditions.

In multicomponent elutions, a competing modifier is sometimes added to the mobile phase to compete with sample solutes for binding sites in order to reduce the retention times of strongly retained eluites [5]. Peaks in a chromatogram

corresponding to a modifier are called system peaks [6]. Studies of system peaks may provide useful information on the effect of modifiers on the eluites and interpretation of some unknown peaks in chromatograms. In Chap. 7, system peaks are studied systematically using the general multicomponent rate model. Systems peak patterns have been summarized for binary elutions with one competing modifier in the mobile phase involving samples that are either prepared in the mobile phase or in an inert solution. Binary elutions with two competing modifiers have also been investigated briefly.

Size-exclusion chromatography (SEC) is ubiquitous in downstream purification processes in modern biotechnology. Its separation is entirely based on mass transfer of molecules with different sizes and shapes with no specific binding. Chapter 8 presents a rate model for SEC that considers axial dispersion, interfacial film mass transfer, and intraparticle diffusion. Size exclusion is quantified by the accessible particle porosity concept. A size-exclusion factor defined as the ratio of the accessible particle porosity to particle porosity is found to have the same value as the distribution coefficient in SEC obtained from elution volumes. A case study is used to demonstrate how computer simulation can be used to scale up SEC together with details for parameter estimation.

In recent years, LC beads with impenetrable cores (e.g., stainless steel cores) have gained attention for their advantages in improved mass transfer due to a shortened radial distance for mass transfer [7]. Their rigid core also provides better hydrodynamic properties resulting in column pressures that are several times lower. This increases the room for scale-up in the axial direction. Chapter 9 presents a rate model for adsorption LC and for a model for SEC with cored beads. Using a radial-axis mathematical transformation for the particle phase mass transfer governing equation, the models allow the adjustment of core size at will by the simulation software user. Computer simulation confirms published experimental results pointing to superior adsorption LC separation performances for columns packed with cored beads over columns packed with conventional fully porous beads by optimizing the core radius fraction. Although cored beads have not been used in practice for SEC yet, computer simulation in this book suggests much improved SEC separation of two proteins based on the physical properties of commercially available fully porous Bio-Rad P60 gel by assuming that a core is inserted. This ahead-of-its-time finding will encourage the introduction of cored beads for SEC applications in the marketplace.

In Chap. 10, slow binding and dissociation reactions are described using the second-order kinetics. This has been used to replace the Langmuir isotherm in the basic rate model for adsorption LC to create the kinetic model simulator. The effects of slow kinetics and slow mass transfer on LC effluent concentration profiles are simulated. Affinity LC is prone to slow kinetics. The kinetic model has been modified to account for a reaction in the fluid phase between macromolecules (e.g., large proteins) and soluble ligands for the study of affinity chromatography. The adsorption, wash and elution stages in affinity chromatography have been simulated and analyzed. A scale-up example is given in this chapter based on experimental affinity LC separation of lysozyme and bovine serum albumin on Affi-Gel Cibacron

Blue F-3GA affinity gel using Cibacron Blue as a soluble ligand for the elution stage. It shows that a priori chromatogram prediction of a larger column can be obtained using parameters systematically estimated from a small column and existing mass transfer correlations in the literature.

A methodology is presented in Chap. 11 for the development of kinetic and isotherm models for multicomponent adsorption systems with uneven saturation capacities for different components, which are due to steric hindrance or due to chiral discrimination of binding sites among various possible reasons. An extended multicomponent Langmuir isotherm derived with this methodology, which is thermodynamically consistent while having different molar adsorption saturation capacities, has been used to explain isotherm crossovers and to demonstrate the peak reversal phenomenon under column-overload conditions.

Chapter 12 presents a general rate model for multicomponent gradient elution. The semi-empirical relationship between the modulator concentration and eluite affinity with the stationary phase developed by Melander et al. [8] is used in the model. Examples of multicomponent elution with linear and nonlinear gradients are demonstrated using computer simulation. A scale-up example is given for protein separation on C4 reverse-phase columns. Details on parameter estimation are presented. In Chap. 13, a general rate model for ion-exchange chromatography with gradient elution is presented. The model uses the mass action and steric mass action isotherms for stoichiometric ion exchange. Simulation examples are used to explain how to use the simulator. The experimental phenomenon of pH spikes and dips due to a step change in the NaCl concentration in the mobile phase has been successfully reproduced using computer simulation.

Radial flow chromatography (RFC) entered the bioseparations market not too long ago as an alternative to the conventional axial flow chromatography (AFC). A general multicomponent rate model for RFC has been solved in Chap. 14 using the same numerical approach as that for AFC. The radial dispersion and external film mass transfer coefficients are treated as variables in the model for RFC. The RFC model can be used by researchers to company RFC and AFC, or to improve the design and performance of an RFC column. The extension of the general multicomponent rate model for RFC to include second-order kinetics, the size exclusion effect, and liquid phase reaction for the study of affinity RFC is also briefly mentioned.

Various simulation software modules for Microsoft Windows in the Chromulator software except the simulators for cored beads and ion exchange are available free of charge for academic research and teaching. The software is a useful tool to study the various LC behaviors and phenomena without performing difficult and costly lab experiments. Educators and researchers from over 34 countries have used Chromulator for teaching and research. The software has also been used by several commercial companies for separation medium design and chromatography column scale-up.

References

1. Snyder LR, Kirkland JJ, Dolan JW (2011) Introduction to modern liquid chromatography. Wiley, New York
2. Ladisch MR (2001) Bioseparations engineering: principles, practice, and economics. Wiley, New York
3. Gear CW (1971) Numerical initial value problems in ordinary differential equations. Prentice-Hall, Englewood Cliffs, NJ
4. Brown PN, Byrne GD, Hindmarsh AC (1989) VODE: a variable-coefficient ODE solver. SIAM J Sci Stat Comput 10:1038–1051. doi:10.1137/0910062
5. Snyder LR, Kirkland JJ, Glajch JL (2012) Practical HPLC method development. Wiley, New York
6. Levin S, Grushka E (1986) System peaks in liquid chromatography: their origin, formation, and importance. Anal Chem 58:1602–1607
7. Wang C, Soice NP, Ramaswamy S, Gagnon BA, Umana J, Cotoni KA, Bian N, Cheng K-SC (2007) Cored anion-exchange chromatography media for antibody flow-through purification. J Chromatogr A 1155:74–84. doi:10.1016/j.chroma.2007.04.030
8. Melander WR, El Rassi Z, Horváth C (1989) Interplay of hydrophobic and electrostatic interactions in biopolymer chromatography: effect of salts on the retention of proteins. J Chromatogr A 469:3–27

Chapter 2
Literature Review

2.1 Theories for Nonlinear Multicomponent Liquid Chromatography

Many researchers have contributed to LC modeling. There exist a dozen or more theories with different complexities. A comprehensive review on the dynamics and mathematical modeling of isothermal adsorption and chromatography was given by Ruthven [1] who classified models into three general categories: equilibrium theory, plate models, and rate models.

2.1.1 Equilibrium Theory

According to Ruthven, the equilibrium theory of multicomponent isothermal adsorption was first developed by Glueckauf [2]. The interference theory by Helfferich and Klein [3] that is mainly aimed at stoichiometric ion-exchange systems with constant separation factors and the mathematically parallel treatise for systems with multicomponent Langmuir isotherms by Rhee and coworkers [4,5] are both extensions of the equilibrium theory.

Equilibrium theory assumes a direct local equilibrium between the mobile phase and the stationary phase, neglecting axial dispersion and mass transfer resistances. It effectively predicts experimental retention times for chromatographic columns with fast mass transfer rates (e.g., high resolution columns). It provides general locations, or retention times of elution peaks, but it fails to describe peak shapes accurately if mass transfer effects are significant. Equilibrium theory has been used for the study of multicomponent interference effects [3] and the ideal displacement development in LC [5]. Many practical applications have been reported [3,6–10].

© Springer International Publishing Switzerland 2015

T. Gu, *Mathematical Modeling and Scale-Up of Liquid Chromatography*,
DOI 10.1007/978-3-319-16145-7_2

2.1.2 Plate Models

Generally speaking, there are two kinds of plate models. One is directly analogous to the tanks in series model for nonideal flow systems [1]. In such a model, the column is divided into a series of small artificial cells, each with complete mixing. This gives a set of first-order ordinary differential equations (ODEs) that describes the adsorption and interfacial mass transfer between the bulk fluid phase and the particle phase. Many researchers have contributed to this kind of plate model [1,11–13]. However, plate models of this kind generally are not suitable for multicomponent LC since the equilibrium stages may not be assumed equal for different components. Thus, plate models are limited to single-component LC modeling.

The other kind of plate model is formulated based on distribution factors that determine the equilibrium of each component in each artificial stage. The model solution involves recursive iterations, rather than solving ODE systems. The most popular ones are the Craig distribution models. By considering the so-called blockage effect, the Craig models are applicable to multicomponent systems. Descriptions of Craig models were given by Eble et al. [14], Seshadri and Deming [15], and Solms et al. [16]. The Craig models have been used for the study of column-overload problems [14,17]. Velayudhan and Ladisch [18] used a Craig model with a corrected plate count to simulate elution and frontal adsorption.

2.1.3 Rate Models

Rate models refer to models containing a rate expression, or rate equation, which describes the interfacial mass transfer between the mobile phase and the stationary phase. A rate model usually consists of two sets of differential mass balance equations, one for the bulk-fluid phase and the other for the particle phase. Different rate models have varying complexities [1].

2.1.3.1 Rate Expressions

The solid film resistance hypothesis was first proposed by Glueckauf and Coates [19]. It assumes a linear driving force between the equilibrium concentrations in the stationary phase (determined from the isotherm) and the average fictitious concentrations in the stationary phase. This simple rate expression has been used by many researchers [1,20–22] because of its simplicity, but this model cannot describe mass transfer details in the particle phase, which are important for larger particles used in preparative- and large-scale LC.

The fluid film mass transfer mechanism with a linear driving force is also widely used [1]. The driving force is the concentration difference of a component between

that on the surface of a particle and that in the surrounding bulk fluid. It is assumed that there is a stagnant fluid film between the particle surface and the bulk fluid. The fluid film exerts a mass transfer resistance between the bulk fluid phase and the particle phase, often called the external mass transfer resistance. If the concentration gradient inside the particle phase is ignored, the LC model then becomes a lumped particle model, which has been used by some researchers [23–25]. If the mass transfer Biot number, which reflects the ratio of the characteristic rate of film mass transfer to that of intraparticle diffusion, is much greater than unity, the external film mass transfer resistance can be neglected with respect to intraparticle diffusion. This is usually the case in LC operations using porous beads.

In some cases, both external mass transfer and intraparticle diffusion must be considered. A local equilibrium is often assumed between the concentration in the stagnant fluid phase inside macropores and the solid phase of the particle. Such a rate mechanism is adequate to describe the adsorption and mass transfer between the bulk-fluid and particle phases, and inside the particle phase in most chromatographic processes. The local equilibrium assumption here is different from that made for the equilibrium theory. The equilibrium theory assumes a direct equilibrium of concentrations in the solid and the liquid phases without any mass transfer resistance.

If the adsorption and desorption rates are not sufficiently high, the local equilibrium assumption is no longer valid. A kinetic model must be used. Some kinetic models were reviewed by Ruthven [1] and Lee [26]. Second-order kinetics has been widely used in kinetic models for affinity chromatography because affinity binding and dissociation reactions often suffer from slow kinetics. Thus, the reactions may not be assumed to be at equilibrium for accurate modeling [27–34].

2.1.3.2 Governing Equation for the Bulk-Fluid Phase

The governing partial differential equation (PDE) for the bulk-fluid phase can be easily obtained from a differential mass balance of the bulk-fluid phase for each component. Axial dispersion, convection, transient, and the interfacial flux terms are usually included. Such equations themselves are generally linear if physical parameters are not concentration dependent. They become nonlinear when coupled with a rate expression involving nonlinear isotherms or second-order kinetics.

For some rate models, such as models for isothermal, single-component systems with linear isotherms, analytical solutions may be obtained using the Laplace transform [1]. For more complex systems, especially those involving nonlinear isotherms, analytical solutions cannot be derived. Numerical methods must be used to obtain solutions to complex rate models that consider various forms of mass transfer mechanisms with nonlinear isotherms. Detailed rate models are becoming increasingly popular, especially in the study of preparative- and large-scale LC. With today's fast personal computers, there is no need to simplify a model to make it solvable. Simplified models often have mass transfer parameters that are nonstandard, which means they lack existing correlations for their estimation.

In this book, all the numerical solved LC models are full-blown mass transfer models as discussed below. This makes their mass transfer parameters fully compatible with classical transport phenomena theories for mass transfer in the chemical engineering literature.

2.1.3.3 General Multicomponent Rate Models

A rate model that considers axial dispersion, external mass transfer, intraparticle diffusion, and nonlinear isotherms is called a general multicomponent rate model. Such a model is adequate in most cases to describe the adsorption and mass transfer processes in multicomponent chromatography. In some cases, surface adsorption, size exclusion, and adsorption kinetics may have to be included to give an adequate description of a particular system. Although particle sizes and shapes used in an LC column are usually not uniform, except in some rare cases with uniform spherical silica beads, an average particle diameter can be used for modeling. Some researchers have used models with a particle size distribution term [35], but this treatment makes parameter estimation for mass transfer coefficients overly complicated since mass transfer correlations usually use a single particle diameter value. In the particle phase, pore diffusion and surface diffusion mechanisms can both be modeled. However, surface diffusion coefficient is usually not available [36]. An "effective" diffusivity is more conveniently used to cover both mechanisms without involving the specifics, although such diffusivity may be concentration dependent [36]. Parameter sensitivity analysis can always be carried out through computer simulation. It is possible that changes in some mass transfer parameters do not cause significant deviations in simulated effluent profiles because other parameters such as isotherm parameters, bed voidage, and particle porosity are far more sensitive, or the mass transfer parameters are already in the insensitive region to start with.

2.1.3.4 Numerical Solutions

A general multicomponent rate model consists of a coupled PDE system with two sets of mass balance equations, one for the bulk-fluid phase and one for the particle phase for each component. Several groups of researchers have used different numerical procedures to solve various general multicomponent rate models [37–40]. The finite difference method is a simple numerical procedure that can be directly applied to the discretization of the bulk-fluid phase PDE and the particle phase PDE [39,41]. To achieve a stable solution with a good accuracy, a huge number of discretization points are needed for a relatively stiff case. This is computational demanding. Its efficiency and accuracy are not competitive compared with other more advanced numerical methods, such as orthogonal collocation (OC), finite element (FE), or orthogonal collocation on finite element (OCFE) methods. To write an LC simulator for a specific project, simplicity may be a

major concern. Computation time is less important. However, if one wants to create LC software for broad applications with repeated simulation runs that may cover very stiff systems, an efficient numerical method is critical. This is why commercial software such as those for computational fluid dynamics use finite element and finite difference is never an option.

For the particle phase-governing equation, the OC method is the obvious choice. It is a very accurate, efficient, and relatively simple method for the discretization of a particle. It has been widely used with success for many particle problems [42,43]. The formulation of the OC method for particles is readily available in Finlayson's book [43].

Unfortunately, concentration gradients in the bulk-fluid phase can be very stiff; thus the OC method is no longer a desirable choice since global splines using high-order polynomials are computationally very expensive [43] and sometimes not stable. The method of OCFE uses linear finite elements for global splines and collocation points inside each element. No numerical integration for element matrices is needed because of the use of linear elements. This discretization method can be used for systems with stiff gradients [43].

The FE method with higher order of interpolation functions (typically quadratic or occasionally cubic) is a very powerful method for stiff systems. Its highly streamlined structure provides unsurpassed convenience and versatility. This method is especially useful for systems with variable physical parameters, as in radial flow chromatography and nonisothermal adsorption with or without chemical reactions. Chromatography of some biopolymers also involves a variable axial dispersion coefficient [44]. The FE method is used throughout this book for the discretization of the bulk-fluid phase PDE.

2.1.3.5 Solution to the ODE System

If the FE method is used for the discretization of the bulk-fluid phase PDE and the OC method for the particle phase equations, an ODE system is produced from the LC model equations. The ODE system with initial values can be readily solved using an ODE solver such as subroutine "IVPAG" of the commercial IMSL software package [45], which uses the Gear's stiff method [40]. Another choice is the public domain Variable coefficient ODE (VODE) solver [46] freely available for download from http://computation.llnl.gov/casc/software.php. Because the ODE system is solved as an initial value problem, there is no need to treat the isotherm equations as algebraic equations with unknowns that have to be coupled with the ODEs to create an equation system coupling both ODEs and algebraic equations. That approach would require an ODE-algebraic equation solver that is less efficient than the more commonplace ODE solvers. The author initially used IVPAG, but later successfully switched to VODE to avoid the use of a commercial software package.

2.2 Scale-Up in Liquid Chromatography

Currently, LC scale-up is carried out largely based on trial-and-error and experience, with the help of some general scale-up rules that are not necessarily accurate [47]. Some of these rules were discussed by Snyder and Kirkland [48], Ladisch [47], and others [1,45,49]. They are mostly empirical or semiempirical relationships about particle size, flow rate, column length, and resolution. The correlations are more of a "rule of thumb" nature when they are used for scale-up. Knox and Pyper [50] did an extensive study on column overload. Some of their results on concentration and volume overload are also helpful in the scale-up of LC. There are many papers in this area.

Instead of following these scale-up rules, a rate model can be used to simulate chromatograms of a larger column a priori, i.e., before it is built or purchased. The model uses only few experimental data from a small column with the same packing as a large column. This step is necessary unless packaging structure data such as bed voidage and particles porosity, as well as isotherm parameters, are already available. Although rate models hold great potentials in more accurate scale-up of liquid chromatography, most papers in the literature have been on the investigation of LC behaviors and simulation of smaller columns to match experimental chromatograms. This book attempts to describe parameter estimation methods and modeling steps that lead to a priori predictions of the performances of larger LC columns based on some experimental work [51–53]. It is hoped that more and more chromatographers will come to realize that it is actually not that difficult to use the software for various LC models in this work for scale-up of LC after digesting the examples in this book. There is no need for them to get involved in the details of the numerical methods since the models have already been solved. However, an understanding of the effects of isotherm parameters and mass transfer-related parameters is essential.

References

1. Ruthven DM (1984) Principles of adsorption and adsorption processes. Wiley, New York
2. Glueckauf E (1949) Theory of chromatography. Part VII. The general theory of two solutes following non-linear isotherms. Discuss Faraday Soc 7:12–25
3. Helfferich FG, Klein G (1970) Multicomponent chromatography: theory of interference. Dekker, New York
4. Rhee H-K, Aris R, Amundson NR (1970) On the theory of multicomponent chromatography. Philos Trans R Soc Lond A Math Phys Sci 267:419–455
5. Rhee H-K, Amundson NR (1982) Analysis of multicomponent separation by displacement development. AIChE J 28:423–433
6. Glueckauf E (1947) Theory of chromatography. Part II. Chromatograms of a single solute. J Chem Soc 1302–1308 (Resumed)
7. Helfferich F, James DB (1970) An equilibrium theory for rare-earth separation by displacement development. J Chromatogr A 46:1–28

8. Bailly M, Tondeur D (1981) Two-way chromatography: flow reversal in non-linear preparative liquid chromatography. Chem Eng Sci 36:455–469
9. Frenz J, Horvath CG (1985) High performance displacement chromatography: calculation and experimental verification of zone development. AIChE J 31:400–409
10. Frenz J, Horvath C (1988) High performance liquid chromatography. In: Horvath C (ed) Advances and perspectives, vol 5. Academic, San Diego, CA, pp 211–314
11. Martin AJP, Synge RM (1941) A new form of chromatogram employing two liquid phases: a theory of chromatography. 2. Application to the micro-determination of the higher monoamino-acids in proteins. Biochem J 35:1358
12. Yang CM (1980) Affinity chromatography and plate model for nonlinear packed-column processes. Purdue University, West Lafayette, IN
13. Villermaux J (1981) Theory of linear chromatography. In: Rodrigues AE, Tondeur D (eds) Percolation processes: theory and applications. Sijthoff and Noordhoff, Rockville, MA, pp 83–140
14. Eble JE, Grob RL, Antle PE, Snyder LR (1987) Simplified description of high-performance liquid chromatographic separation under overload conditions, based on the Craig distribution model. III. Computer simulations for two co-eluting bands assuming a Langmuir isotherm. J Chromatogr A 405:1–29
15. Seshadri S, Deming SN (1984) Simulation of component interactions in high-performance liquid chromatography. Anal Chem 56:1567–1572
16. Solms DJ, Smuts TW, Pretorius V (1971) Displacement peaks in liquid elution chromatography. J Chromatogr Sci 9:600–603
17. Ernst P (1987) Radial flow chromatography. Aust J Biotechnol 1:22–24
18. Velayudhan A, Ladisch MR (1993) Plate models in chromatography: analysis and implications for scale-up. In: Tsao GT (ed) Chromatography. Springer, Berlin, pp 123–145
19. Glueckauf E, Coates JI (1947) Theory of chromatography. Part IV. The influence of incomplete equilibrium on the front boundary of chromatograms and on the effectiveness of separation. J Chem Soc 1315–1321 (Resumed)
20. Rhee H, Amundson NR (1974) Shock layer in two solute chromatography: effect of axial dispersion and mass transfer. Chem Eng Sci 29:2049–2060
21. Bradley WG, Sweed NH (1975) Rate controlled constant pattern fixed-bed sorption with axial dispersion and non-linear multicomponent equilibria. AIChE Symp Ser 71:59
22. Farooq S, Ruthven DM (1990) A comparison of linear driving force and pore diffusion models for a pressure swing adsorption bulk separation process. Chem Eng Sci 45:107–115
23. Lin B, Golshan-Shirazi S, Ma Z, Guiochon G (1988) Shock effects in nonlinear chromatography. Anal Chem 60:2647–2653
24. Santacesaria E, Morbidelli M, Servida A, Storti G, Carra S (1982) Separation of xylenes on Y zeolites. 2. Breakthrough curves and their interpretation. Ind Eng Chem Process Des Dev 21:446–451
25. Carra S, Santacesaria E, Morbidelli M, Storti G, Gelosa D (1982) Separation of xylenes on Y zeolites. 3. Pulse curves and their interpretation. Ind Eng Chem Process Des Dev 21:451–457
26. Lee W-C, Huang SH, Tsao GT (1988) A unified approach for moments in chromatography. AIChE J 34:2083–2087. doi:10.1002/aic.690341221
27. Chase HA (1984) Affinity separations utilising immobilised monoclonal antibodies—a new tool for the biochemical engineer. Chem Eng Sci 39:1099–1125. doi:10.1016/0009-2509(84)85074-5
28. Chase HA (1984) Prediction of the performance of preparative affinity chromatography. J Chromatogr A 297:179–202. doi:10.1016/S0021-9673(01)89041-5
29. Arnold FH, Blanch HW, Wilke CR (1985) Analysis of affinity separations II: The characterization of affinity columns by pulse techniques. Chem Eng J 30:B25–B36. doi:10.1016/0300-9467(85)80017-4

30. Arnold FH, Blanch HW, Wilke CR (1985) Analysis of affinity separations. I: Predicting the performance of affinity adsorbers. Chem Eng J 30:B9–B23. doi:10.1016/0300-9467(85)80016-2
31. Arnold FH, Schofield SA, Blanch HW (1986) Analytical affinity chromatography: I. Local equilibrium theory and the measurement of association and inhibition constants. J Chromatogr A 355:1–12. doi:10.1016/S0021-9673(01)97299-1
32. Arnold FH, Blanch HW (1986) Analytical affinity chromatography: II. Rate theory and the measurement of biological binding kinetics. J Chromatogr A 355:13–27. doi:10.1016/S0021-9673(01)97300-5
33. Arve BH, Liapis AI (1987) Modeling and analysis of biospecific adsorption in a finite bath. AIChE J 33:179–193. doi:10.1002/aic.690330203
34. Arve BH, Liapis AI (1988) Modeling and analysis of elution stage of biospecific adsorption in finite bath. Biotechnol Bioeng 31:240–249. doi:10.1002/bit.260310310
35. Carta G, Bauer JS (1990) Analytic solution for chromatography with nonuniform sorbent particles. AIChE J 36:147–150
36. Ma Z, Whitley RD, Wang N-H (1996) Pore and surface diffusion in multicomponent adsorption and liquid chromatography systems. AIChE J 42:1244–1262
37. Gu T, Tsai G-J, Tsao GT (1990) New approach to a general nonlinear multicomponent chromatography model. AIChE J 36:784–788. doi:10.1002/aic.690360517
38. Liapis AI, Rippin DWT (1978) The simulation of binary adsorption in activated carbon columns using estimates of diffusional resistance within the carbon particles derived from batc. Chem Eng Sci 33:593–600. doi:10.1016/0009-2509(78)80021-9
39. Mansour AR (1989) The simulation of multicomponent sorption processes with axial diffusion. Sep Sci Technol 24:1047–1058
40. Yu Q, Wang NHL (1989) Computer simulations of the dynamics of multicomponent ion exchange and adsorption in fixed beds—gradient-directed moving finite element method. Comput Chem Eng 13:915–926
41. Mansour A, Von Rosenberg DU, Sylvester ND (1982) Numerical solution of liquid-phase multicomponent adsorption in fixed beds. AIChE J 28:765–772. doi:10.1002/aic.690280510
42. Villadsen J, Michelsen ML (1978) Solutions of differential equation models by polynomial approximation. Prentice Hall, Englewood Cliff, NJ
43. Finlayson BA (2003) Nonlinear analysis in chemical engineering. Ravenna Park Publishing, Seattle
44. Antia FD, Horváth C (1989) Operational modes of chromatographic separation processes. Ber Bunsenges Phys Chem 93:961–968. doi:10.1002/bbpc.19890930907
45. Rathore A, Velayudhan A (2002) Scale-up and optimization in preparative chromatography: principles and biopharmaceutical applications. CRC, Boca Raton, FL
46. Brown PN, Byrne GD, Hindmarsh AC (1989) VODE: a variable-coefficient ODE solver. SIAM J Sci Stat Comput 10:1038–1051. doi:10.1137/0910062
47. Ladisch MR (2001) Bioseparations engineering: principles, practice, and economics. Wiley, New York
48. Snyder LR, Kirkland JJ, Glajch JL (2012) Practical HPLC method development. Wiley, New York
49. Guiochon G, Felinger A, Shirazi DGG (2006) Fundamentals of preparative and nonlinear chromatography. Academic, Waltham, MA
50. Knox JH, Pyper HM (1986) Framework for maximizing throughput in preparative liquid chromatography. J Chromatogr A 363:1–30. doi:10.1016/S0021-9673(00)88988-8
51. Li Z, Gu Y, Gu T (1998) Mathematical modeling and scale-up of size-exclusion chromatography. Biochem Eng J 2:145–155. doi:10.1016/S1369-703X(98)00027-8
52. Gu T, Zheng Y (1999) A study of the scale-up of reversed-phase liquid chromatography. Sep Purif Technol 15:41–58. doi:10.1016/S1383-5866(98)00083-5
53. Gu T, Hsu KH, Syu MJ (2003) Scale-up of affinity chromatography for purification of enzymes and other proteins. Enzym Microb Technol 33:430–437

Chapter 3
General Multicomponent Rate Model for Column Liquid Chromatography

3.1 Model Assumptions

For the modeling of multicomponent LC, the column is divided into the bulk-fluid phase and the particle phase. The anatomy of a fixed-bed axial flow chromatography column is given in Fig. 3.1. To formulate a general rate model, the following basic assumptions are made:

1. The chromatographic process is isothermal
2. The porous particles in the column are spherical and uniform in diameter
3. The concentration gradients in the column's radial direction are negligible
4. The fluid inside particle macropores is stagnant, i.e., there is no convective flow inside the macropores
5. An instantaneous local equilibrium exists between the macropore surfaces and the stagnant fluid inside the macropores of the particles and
6. The diffusional and mass transfer parameters are constant and independent of the mixing effects of the components involved.

If the process is not isothermal, physical properties and isotherm parameters would be time-dependent or zone-dependent. The model would be more complicated. Specific cases like these should be modeled separately to avoid complicating the basic isothermal system that is true for the overwhelming majority of adsorption LC applications. Column stationary phases are usually not spherical beads with a uniform diameter. However, for nonuniform beads or nonspherical beads, an average or "effective" particle diameter may be used. The fluid film mass transfer mechanism with a linear driving force is used to describe mass transfer between the bulk-fluid phase and the particle phase.

© Springer International Publishing Switzerland 2015

T. Gu, *Mathematical Modeling and Scale-Up of Liquid Chromatography*,
DOI 10.1007/978-3-319-16145-7_3

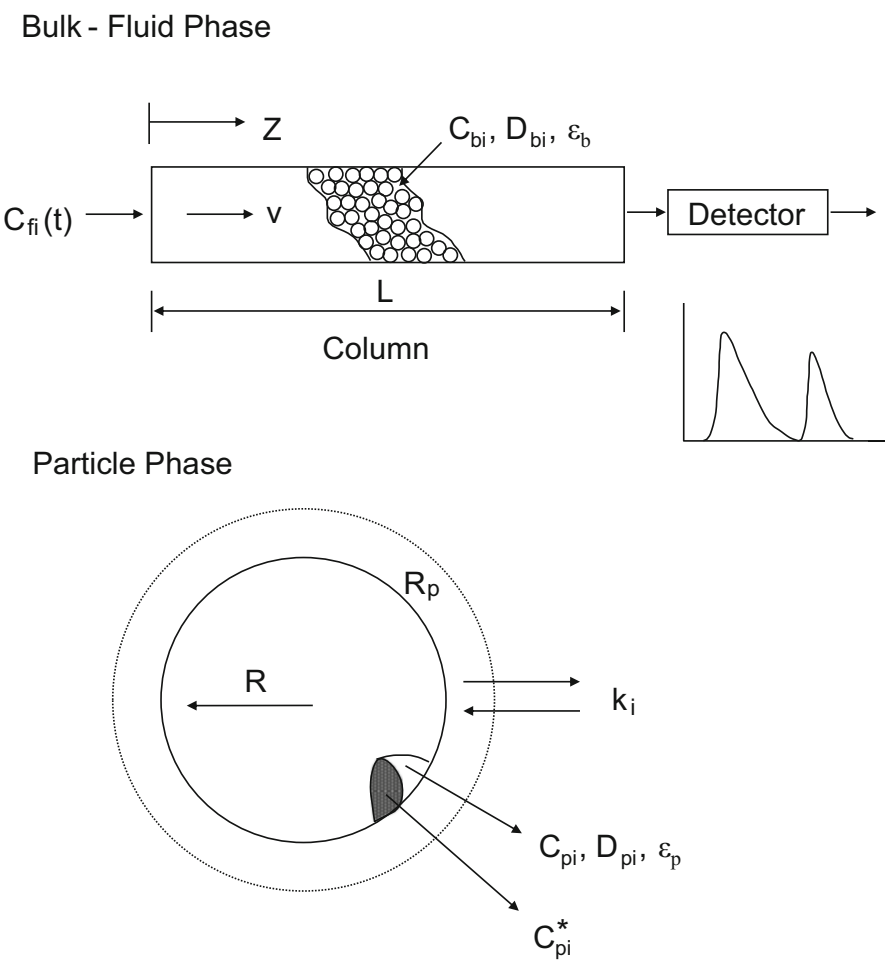

Fig. 3.1 Schematic of bulk-fluid phase and particle phase of an LC column for modeling

3.2 Model Formulation

Based on the assumptions above, the governing equations can be obtained from differential mass balances of the bulk-fluid phase and the particle phase for component i. The following equations can also be derived from equations of continuity in the classical transport phenomena textbook by Bird et al. [1]

$$-D_{bi}\frac{\partial^2 C_{bi}}{\partial Z^2}+v\frac{\partial C_{bi}}{\partial Z}+\frac{\partial C_{bi}}{\partial t}+\frac{3k_i(1-\varepsilon_b)}{\varepsilon_b R_p}\left(C_{bi}-C_{pi,R=R_p}\right)=0 \qquad (3.1)$$

$$\left(1-\varepsilon_{\mathrm{p}}\right)\frac{\partial C_{\mathrm{p}i}^{*}}{\partial t}+\varepsilon_{\mathrm{p}}\frac{\partial C_{\mathrm{p}i}}{\partial t}-\varepsilon_{\mathrm{p}}D_{\mathrm{p}i}\left[\frac{1}{R^{2}}\frac{\partial}{\partial R}\left(R^{2}\frac{\partial C_{\mathrm{p}i}}{\partial R}\right)\right]=0 \tag{3.2}$$

The fourth term in Eq. (3.1) is a source term in the bulk-fluid phase mass balance, in which $3(1-\varepsilon_{\mathrm{b}})/(\varepsilon_{\mathrm{b}}R_{\mathrm{p}})$ is the ratio of total particle shell surface area inside the column to total fluid volume inside a column ($\varepsilon_{\mathrm{b}}V_{\mathrm{b}}$), not counting the fluid inside the particle macropores. The particle shell surface area to particle volume (including particle pore volume) ratio is $3/R_{\mathrm{p}}$. When it is multiplied by the total particle volume (including particle pore volume) of $(1-\varepsilon_{\mathrm{b}})V_{\mathrm{b}}$ in the column, one obtains $3(1-\varepsilon_{\mathrm{b}})V_{\mathrm{b}}/R_{\mathrm{p}}$ for the total particle shell surface area inside the column. $D_{\mathrm{p}i}$ in Eq. (3.2) is the effective diffusivity of species i in the particle macropores. Any surface diffusion effect will be lumped into this parameter as discussed in Chap. 2. It should be noted that some researchers use a diffusivity that considers the particle porosity already. In that case, its value should be divided by ε_{p} before it is used in the models throughout this book. The PDEs above come with the initial conditions (ICs) and boundary conditions (BCs) below,

ICs:. $t=0$

$$C_{\mathrm{b}i}=C_{\mathrm{b}i}(0,Z) \tag{3.3}$$

$$C_{\mathrm{p}i}=C_{\mathrm{p}i}(0,R,Z) \tag{3.4}$$

BCs:.

$$Z=0,\quad \frac{\partial C_{\mathrm{b}i}}{\partial Z}=\frac{v}{D_{\mathrm{b}i}}\left(C_{\mathrm{b}i}-C_{\mathrm{fi}}(t)\right) \tag{3.5}$$

$$Z=L,\quad \frac{\partial C_{\mathrm{b}i}}{\partial Z}=0 \tag{3.6}$$

BCs:.

$$R=0,\quad \frac{\partial C_{\mathrm{p}i}}{\partial R}=0 \tag{3.7}$$

$$R=R_{\mathrm{p}},\quad \frac{\partial C_{\mathrm{p}i}}{\partial R}=\frac{k_{i}}{\varepsilon_{\mathrm{p}}D_{\mathrm{p}i}}\left(C_{\mathrm{b}i}-C_{\mathrm{p}i,R=R_{\mathrm{p}}}\right) \tag{3.8}$$

Time zero is defined as the moment when a sample starts to enter the column inlet. In reality, a chromatogram's time zero is typically set at the time when a sample starts to exit the sample loop. It may take a few seconds for the sample to reach the column inlet. It may also take some time for the effluent to travel from the column exit to the detector. Thus, an adjustment of the simulated chromatogram's timescale is needed when modeling a practical case to account for the time delays.

The complicated LC model system above contains numerous physical parameters. A typical modeling approach by chemical engineers would call for nondimensionalization to reduce the number of parameters by introducing dimensionless parameters. This would greatly simplify the parametric discussions of the

model system and some commonly used dimensionless parameters may surface. Defining the following dimensionless constants:

$$c_{\mathrm{b}i} = C_{\mathrm{b}i}/C_{0i},\ \ c_{\mathrm{p}i} = C_{\mathrm{p}i}/C_{0i},\ \ c_i = C_i/C_{0i},\ \ \tau = vt/L,\ \ r = R/R_{\mathrm{p}},\ \ z = Z/L$$
$$\mathrm{Pe}_{\mathrm{L}i} = vL/D_{\mathrm{b}i},\ \ \mathrm{Bi}_i = k_i R_{\mathrm{p}}/\left(\varepsilon_{\mathrm{p}} D_{\mathrm{p}i}\right),\ \ \eta_i = \varepsilon_{\mathrm{p}} D_{\mathrm{p}i} L/\left(R_{\mathrm{p}}^2 v\right),\ \ \xi_i = 3\mathrm{Bi}_i \eta_i (1-\varepsilon_{\mathrm{b}})/\varepsilon_{\mathrm{b}}$$

the model equations above can be transformed into the following dimensionless equations:

$$-\frac{1}{\mathrm{Pe}_{\mathrm{L}i}}\frac{\partial^2 c_{\mathrm{b}i}}{\partial z^2} + \frac{\partial c_{\mathrm{b}i}}{\partial z} + \frac{\partial c_{\mathrm{b}i}}{\partial \tau} + \xi_i\left(c_{\mathrm{b}i} - c_{\mathrm{p}i,r=1}\right) = 0 \tag{3.9}$$

$$\frac{\partial}{\partial \tau}\left[\left(1 - \varepsilon_{\mathrm{p}}\right)c_{\mathrm{p}i}^{*} + \varepsilon_{\mathrm{p}} c_{\mathrm{p}i}\right] - \eta_i\left[\frac{1}{r^2}\frac{\partial}{\partial r}\left(r^2\frac{\partial c_{\mathrm{p}i}}{\partial r}\right)\right] = 0 \tag{3.10}$$

with ICs: $\tau = 0$

$$c_{\mathrm{b}i} = c_{\mathrm{b}i}(0, z) \tag{3.11}$$
$$c_{\mathrm{p}i} = c_{\mathrm{p}i}(0, r, z) \tag{3.12}$$

and BCs:

$$\text{at } z = 0, \quad \partial c_{\mathrm{b}i}/\partial z = \mathrm{Pe}_{\mathrm{L}i}\left[c_{\mathrm{b}i} - C_{\mathrm{fi}}(\tau)/C_{0i}\right] \tag{3.13}$$
$$\text{at } z = 1, \quad \partial c_{\mathrm{b}i}/\partial z = 0 \tag{3.14}$$
$$\text{at } r = 0, \quad \partial c_{\mathrm{p}i}/\partial r = 0 \tag{3.15}$$
$$\text{at } r = 1, \quad \partial c_{\mathrm{p}i}/\partial r = \mathrm{Bi}_i\left(c_{\mathrm{b}i} - c_{\mathrm{p}i,r=1}\right) \tag{3.16}$$

The BCs at $z = 0$ and $z = 1$ above are known as the Danckwerts boundary conditions. C_{0i} is the concentration used to nondimensionalize other concentrations for component i (e.g., its concentration in the particle pores). It is typically the highest concentration of component i encountered by the column, i.e., $C_{0i} = \max\{C_{\mathrm{f}i}(t)\}$ with $-\infty < t < +\infty$. Three dimensionless mass transfer parameters are introduced above. They are the well-known Peclet number for axial dispersion (Pe_{L}), Biot number for mass transfer (Bi), and the specially introduced η number for LC. Dimensionless parameter ξ can be calculated from Bi and η. The effects of Pe_{L}, Bi, and η on chromatographic concentration profiles are discussed in Chap. 4.

The feed profile $C_{\mathrm{f}i}(\tau)/C_{0i}$ at $z = 0$ in Eq. (3.13) determines the mode of the LC operations. For frontal adsorption (i.e., breakthrough analysis), $C_{\mathrm{f}i}(\tau)/C_{0i} \equiv 1$. For elution

$$C_{fi}(\tau)/C_{0i} = \begin{cases} 1 & 0 \le \tau \le \tau_{\text{imp}} \\ 0 & \text{else} \end{cases} \tag{3.17}$$

in which τ_{imp} is the dimensionless time duration for a rectangular pulse injection. It corresponds to dimensional impulse time duration of t_{imp} with the following conversion relationship:

$$\tau_{\text{imp}} = t_{\text{imp}}(v/L) = \left(V_{\text{samp}}/Q\right)(v/L) \tag{3.18}$$

where V_{samp} is the dimensional sample volume in ml, etc. In the equation above, the interstitial velocity v ("real velocity" passing the particle surface rather than the imagined "empty tower velocity") is defined by the following relationship:

$$v = Q/(\varepsilon_{\text{b}}A) = 4Q/\left(\pi d^2 \varepsilon_{\text{b}}\right) \tag{3.19}$$

in which A is the cross-sectional area of the column. If ε_{b} is dropped from Eq. (3.19), the velocity will be the empty tower velocity, which is smaller than the interstitial velocity. A combination of Eqs. (3.18) and (3.19) leads to a relationship that can be used to convert dimensional sample volume to dimensionless impulse time,

$$\tau_{\text{imp}} = 4V_{\text{samp}}/\left(\pi d^2 L \varepsilon_{\text{b}}\right) \tag{3.20}$$

After the sample introduction (in the form of rectangular pulse), if component i is displaced, $C_{\text{fi}}(\tau)/C_{0i} = 0$. If component i is a displacer, $C_{fi}(\tau)/C_{0i} = 1$.

The definitions of all the dimensionless variables and parameters are listed in the List of Symbols. In Eq. (3.10), $c^*_{\text{p}i}$ is the dimensionless concentration of component i in the solid phase of the particles. It is directly linked to an isotherm such as the following commonly used multicomponent Langmuir isotherm in adsorption LC:

$$C^*_{\text{p}i} = \frac{a_i C_{\text{p}i}}{1 + \sum_{j=1}^{N_{\text{s}}} b_j C_{\text{p}j}} \quad \text{(dimensionless)} \tag{3.21a}$$

or

$$c^*_{\text{p}i} = \frac{a_i c_{\text{p}i}}{1 + \sum_{j=1}^{N_{\text{s}}} \left(b_j C_{0j}\right) c_{\text{p}j}} \quad \text{(dimensionless)} \tag{3.21b}$$

In the Langmuir isotherm, $a_i/b_i = C_i^{\infty}$ (adsorption saturation capacity for component i). The molar-based C_i^{∞} values must be the same for all the binding

components to satisfy the thermodynamic consistency for the Langmuir isotherm [2]. In LC modeling, C_{p}^{*} and C^{∞} should be based on the unit volume of particle skeleton. For a column with bed voidage of ε_{b} and particle porosity ε_{p}, its total particle volume (including particle macropores) and particle skeleton volume are $(1-\varepsilon_{\mathrm{b}})V_{\mathrm{b}}$ and $(1-\varepsilon_{\mathrm{b}})(1-\varepsilon_{\mathrm{p}})V_{\mathrm{b}}$, respectively. Some researchers tend to use the particle volume instead of particle skeleton volume for C_{p}^{*} during isotherm measurements. If so, their a and C^{∞} values must be converted by dividing them with $(1-\varepsilon_{\mathrm{p}})$ to make them larger before they can be used for the rate models throughout this book. For a single-component system, gram may be used instead of mole for convenience. For multicomponent systems, moles are used so the Langmuir isotherm's thermodynamic consistency can be checked by comparing the C_{i}^{∞} values.

If the general rate model is solved, it provides the effluent history (chromatogram), i.e., $c_{\mathrm{b}i}|_{z=1}$ vs. τ. In the solution process, the model has to calculate the transient concentration profiles anywhere inside the column, in the bulk fluid [$c_{\mathrm{b}i}(r, z)$], in the stagnant fluid inside particle macropores [$c_{\mathrm{p}i}(\tau,r,z)$], and in the solid skeleton of the particles [$c_{\mathrm{p}i}^{*}(\tau,r,z)$]. Usually, only the effluent history is used to study chromatographic phenomena because in practice it is extremely inconvenient to measure the concentration profiles inside a column in a lab setting. However, the transient concentration profiles in the bulk-fluid phase inside the column can be used to understand peak migration patterns inside the column. It may be useful in some theoretical studies. Figure 3.2 shows the simulated dimensionless concentration profiles of two peaks migrating inside a column.

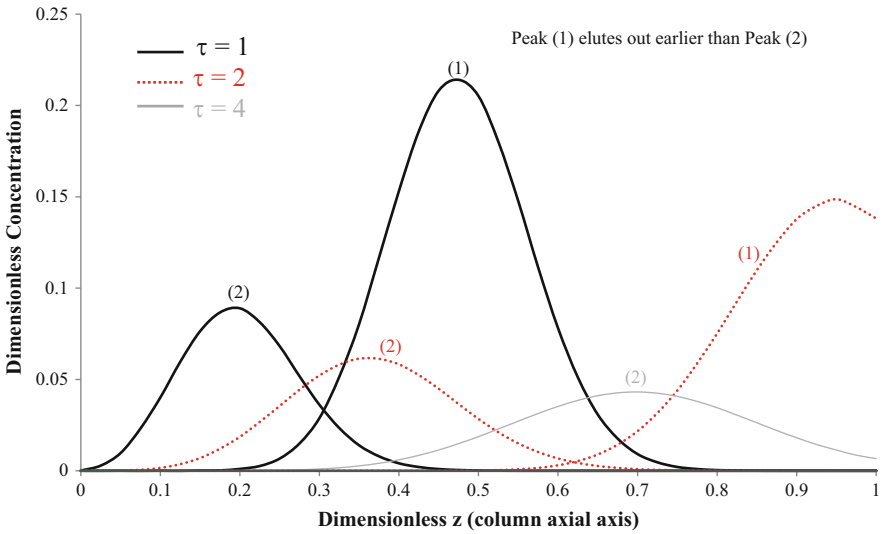

Fig. 3.2 Simulated dimensionless concentration profiles inside a column

The model PDEs are not necessarily nonlinear, but the model system becomes nonlinear whenever a nonlinear isotherm, such as the Langmuir isotherm, or its precursor, the second-order kinetics, is used. A true multicomponent case is almost always nonlinear, since no linear isotherms are suitable to describe true multicomponent adsorptions that involve interactions among different components. For such a nonlinear multicomponent model, there is no analytical solution. The model equations must be solved numerically. Figure 3.3 shows the strategy of the numerical method used to solve the PDE system in the model. The bulk-fluid phase and the particle phase equations are first discretized using the FE and the OC methods, respectively. The resulting ODE system is solved using the VODE ODE solver.

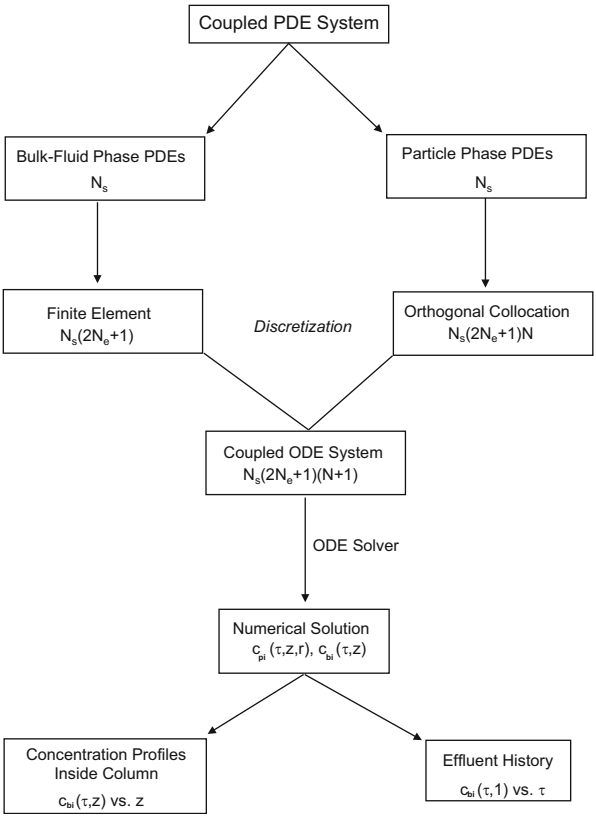

Fig. 3.3 Numerical solution strategy

3.3 Finite Element Formulation for the Bulk-Fluid Phase Governing Equation

Applying the Galerkin weighted residual method [3] to Eq. (3.9), one obtains

$$\int_{z_A}^{z_B} \phi_m \left[-\frac{1}{\mathrm{Pe}_{\mathrm{L}i}} \frac{\partial^2 c_{\mathrm{b}i}}{\partial z^2} + \frac{\partial c_{\mathrm{b}i}}{\partial z} + \frac{\partial c_{\mathrm{b}i}}{\partial \tau} + \xi_i \left(c_{\mathrm{b}i} - c_{\mathrm{p}i,r=1} \right) \right] \mathrm{d}z = 0 \tag{3.22}$$

where the integration limits z_A and z_B are the two boundary points of a typical finite element. The ϕ function is the so-called basis function. Rearrangement using integration by parts on the second-order partial derivative term in Eq. (3.22) gives

$$\begin{aligned} &\int_{z_A}^{z_B} \frac{1}{\mathrm{Pe}_{\mathrm{L}i}} \frac{\partial c_{\mathrm{b}i}}{\partial z} \frac{\partial \phi_m}{\partial z} \mathrm{d}z + \left(-\frac{1}{\mathrm{Pe}_{\mathrm{L}i}} \right) \phi_m \frac{\partial c_{\mathrm{b}i}}{\partial z} \Big|_{z_A}^{z_B} + \int_{z_A}^{z_B} \phi_m \frac{\partial c_{\mathrm{b}i}}{\partial \tau} \mathrm{d}z \\ &+ \int_{z_A}^{z_B} \left(\phi_m \frac{\partial c_{\mathrm{b}i}}{\partial z} + \xi_i \phi_m c_{\mathrm{b}i} \right) \mathrm{d}z - \int_{z_A}^{z_B} \xi_i \phi_m c_{\mathrm{p}i,\mathrm{r}=1} \mathrm{d}z = 0. \end{aligned} \tag{3.23}$$

Inserting the interpolation form for quadratic elements $c_{\mathrm{b}i} = \sum_{n=1}^{3} \phi_n c_{\mathrm{b}i,n}$ into Eq. (3.23) yields

$$\begin{aligned} &\sum_{n=1}^{3} c_{\mathrm{b}i,n} \int_{z_A}^{z_B} \frac{1}{\mathrm{Pe}_{\mathrm{L}i}} \frac{\partial \phi_m}{\partial z} \frac{\partial \phi_n}{\partial z} \mathrm{d}z + \sum_{n=1}^{3} c_{\mathrm{b}i,n} \int_{z_A}^{z_B} \left(\phi_m \frac{\partial \phi_n}{\partial z} + \xi_i \phi_m \phi_n \right) \mathrm{d}z + \sum_{n=1}^{3} c'_{\mathrm{b}i,n} \int_{z_A}^{Z_B} \phi_m \phi_n \mathrm{d}z \\ &= (\mathrm{PB}_i)_m + \int_{z_A}^{z_B} \xi_i \phi_m c_{\mathrm{p}i,r=1} \mathrm{d}z \end{aligned} \tag{3.24}$$

where $(\mathrm{PB}_i)_m = -\frac{1}{\mathrm{Pe}_{\mathrm{L}i}} \phi_m \frac{\partial c_{\mathrm{b}i}}{\partial z} \Big|_{z_A}^{z_B}$.

Equation (3.24) can be expressed as an ODE in the matrix form as follows:

$$[\mathbf{DB}_i] \left[\mathbf{cb}_i' \right] + [\mathbf{AKB}_i][\mathbf{cb}_i] = [\mathbf{PB}_i] + [\mathbf{AFB}_i] \tag{3.25}$$

where the bold face indicates a matrix or a vector for each quadratic element, and

$$(\mathrm{DB}_\mathrm{i})_{m,n} = \int_{z_A}^{z_B} \phi_m \phi_n \mathrm{d}z \tag{3.26}$$

$$(\mathrm{AKB}_i)_{m,n} = \int_{z_\mathrm{A}}^{z_\mathrm{B}} \left(\frac{1}{\mathrm{Pe}_{\mathrm{L}i}} \frac{\partial \phi_m}{\partial z} \frac{\partial \phi_n}{\partial z} + \phi_m \frac{\partial \phi_n}{\partial z} + \xi_i \phi_m \phi_n \right) \mathrm{d}z \tag{3.27}$$

$$(\mathrm{AFB}_i)_m = \int_{z_\mathrm{A}}^{z_\mathrm{B}} \xi_i \phi_m c_{\mathrm{p}i,r=1} \mathrm{d}z \tag{3.28}$$

in which $m, n \in \{1, 2, 3\}$. The FE matrices and vectors are evaluated over each individual element before a global assembly. After the global assembly, the natural boundary condition $(\mathbf{PB}_i)|_{z=0} = -c_{\mathrm{b}i} + C_{\mathrm{fi}}(\tau)/C_{0i}$ will be applied to $[\mathbf{AKB}_i]$ and $[\mathbf{AFB}_i]$ at $z = 0$. $(\mathbf{PB}_i) = 0$ is held anywhere else.

3.4 Orthogonal Collocation Formulation of the Particle Phase Governing Equation

Using the same symmetric polynomials as defined by Finlayson [4], Eq. (3.10) is transformed into the following equation by the OC method for the interior collocation point position indexed by the letter l:

$$\left(\sum_{j=1}^{N_\mathrm{s}} \frac{\partial g_i}{\partial c_{\mathrm{p}j}} \frac{\mathrm{d}c_{\mathrm{p}j}}{\mathrm{d}\tau} \right)_\mathrm{l} = \eta_i \sum_{k=1}^{N+1} \mathrm{B}_{\mathrm{l},k} \left(c_{\mathrm{p}i}\right)_k, \quad \mathrm{l} = 1, 2, \ldots, N \tag{3.29}$$

in which $g_i = \left(1 - \varepsilon_\mathrm{p}\right) c^*_{\mathrm{p}i} + \varepsilon_\mathrm{p} c_{\mathrm{p}i}$. Equation (3.29) is needed for N interior collocation points. Note that for component i, $c^*_{\mathrm{p}i}$ is related to $c_{\mathrm{p}j}$ values for all the components involved via multicomponent isotherms, such as Eq. (3.21). The value of $(c_{\mathrm{p}i})_{N+1}$, i.e, $c_{\mathrm{p}i,r=1}$ is needed in Eq. (3.29). It can be obtained from the boundary condition at $r = 1$, which gives,

$$\sum_{j=1}^{N+1} A_{N+1,\,j} \left(c_{\mathrm{p}i}\right)_j = \mathrm{Bi}_i \left(c_{\mathrm{b}i} - c_{\mathrm{p}i,r=1}\right) \tag{3.30}$$

$$\left(c_{\mathrm{p}i}\right)_{N+1} = c_{\mathrm{p}i,r=1} = \frac{\mathrm{Bi}_i c_{\mathrm{b}i} - \sum_{j=1}^{N} A_{N+1,\,j} \left(c_{\mathrm{p}i}\right)_j}{A_{N+1,N+1} + \mathrm{Bi}_i} \tag{3.31}$$

In Eqs. (3.29)–(3.31), the matrices **A** and **B** are the same as defined by Finlayson [4] on p. 94 of his book for spherical geometry. The interior collocation point at $r = 0$ is not included in index l in Eq. (3.29) either. Due to symmetry, $\partial c_{\mathrm{p}i}/\partial r = 0$ at $r = 0$ and "that condition is already built into the trial function" in the OC method for particles as commented by Finlayson [4].

3.5 Solution to the ODE System

If N_e quadratic elements [i.e. $(2N_e + 1)$ nodes] are used for the z-axis in the bulk-fluid phase PDE and N interior OC points are used for the r-axis in the particle phase equation, the discretization procedure above gives a total of $N_s(2N_e + 1)(N + 1)$ ODEs that are then solvable simultaneously using the public domain ODE solver VODE [5]. Its double-precision version DVODE is used throughout this book. A function subroutine must be supplied to the ODE solver to evaluate concentration derivatives at each element node and interior OC point with given trial concentration values supplied by the ODE solver. The concentration derivatives at each element node $[c_{bi}^{'}]$ are determined from Eq. (3.25). The concentration derivatives at each OC point $[c_{pj}^{'}]$ are coupled because of the complexity of the isotherms that are related to g_i via c_{pi}^{*} in multicomponent cases. At each interior OC point, Eq. (3.29) can be rewritten in the matrix below,

$$[\mathbf{GP}]\left[\mathbf{c}_{\mathbf{p}}^{'}\right] = [\mathbf{RH}] \tag{3.32}$$

where $GP_{ij} = \partial g_i / \partial c_{pj}$, $c_{pj}^{'} = dc_{pj}/d\tau$, and $[\mathbf{RH}]$ = right-hand side of Eq. (3.29). Since the matrix $[\mathbf{GP}]$ and the vector $[\mathbf{RH}]$ are known with given trial concentration values at each interior OC point in the function subroutine of the Fortran 77 code implementation, the derivative vector $[\mathbf{c}_{\mathbf{p}}^{'}]$ can be readily calculated from Eq. (3.32).

3.6 Fortran 77 Code for the General Multicomponent Rate Model

A Fortran 77 code has been written for the numerical solution to the general multicomponent rate model above for adsorption LC with the multicomponent Langmuir isotherm. The code is named "RATE.FOR" which uses the public domain ODE solver VODE. It can be compiled using Microsoft Visual Fortran 6.6.a to produce RATE.EXE as a stand-alone console application. This is part of the LC simulator software package known as Chromulator Version 1 that is available for free to academic researchers. Double precision is used in the Fortran 77 code. Concentration values of c_{bi} and c_{pi} are stored in the vector named "u." The vector "u" is divided first according to the sequence of components. It is then subdivided into c_{bi} values and c_{pi} values for all element nodes on the z-axis. The c_{pi} values are subdivided according to the sequence of interior collocation points for particles. The exterior collocation point $(N + 1)$ is not stored in "u." Normally, only c_{bi} values at the column exit at different dimensionless time τ are needed in the output. These values can be used directly to plot a simulated effluent history (chromatogram).

The core of the Fortran 77 code is subroutine "fcn." It supplies concentration derivatives to the ODE solver. The error tolerance for DVODE is set to tol $= 10^{-6}$ throughout this book unless otherwise indicated. The main program of the LC simulation Fortran 77 code does the preparation of calling DVODE, and input and output operations. The FE notations used in the code generally follow those used in the textbook by Reddy [3]. A separate data (text) file named "data" containing simulation parameter values must be supplied in the same file director as the compiled Fortran 77 code for simulation. When the simulator is executed, it reads the file "data" automatically for input data.

Each LC operation (or mode) is assigned an "index" value that is included in the file "data" that can be edited using Microsoft Windows Notepad software. The following is a list of operations allowed in the code:

index = 1 breakthrough curve.
index = 2 isocratic elution with an inert mobile phase (containing no modifier).
index = 3 step-change displacement. The last component is displacer.
index = 4 breakthrough switched to displacement at t = tshift.
index = 5 same as index = 4, but the flow direction is reversed for displacement.
index = 6 isocratic elution with a modifier in the mobile phase (component N_s).
The sample contains the same modifier concentration as in the mobile phase.
index = 7 same as index = 6, but sample is in an inert solution.

If the user desires other forms of operation, the user may change the initial conditions in the MAIN program, and the natural boundary condition (NBC) in the subroutine "fcn" in the Fortran 77 source code accordingly. The NBC is linked to the column feed profiles of all components. Such changes are quite easy to make.

The input data file for the Fortran code contains the number of components, elements and interior collocation points, process index, time control data, dimensionless mass transfer parameters, and isotherm parameters. Note that the code is based on the dimensionless PDE system, and C_{0i} can be combined with b_i to form a dimensionless group, b_iC_{0i}. This does not necessarily mean that increasing the C_{0i} value has the same effect as increasing the b_i value, since the latter also increases the a_i value proportionally.

Below is the input file "data" used to obtain Fig. 3.4 that shows a binary elution with an inert mobile phase. The numbers in file "data" can be separated by a space (or spaces), or a comma, or a new line.

```
2  7  2  2  0.1 0.03 10 0.4 0.5
 300  4  20  0.1  1.2  1.5
 300  4  20  0.1  8.0  10.0
```

There is no designated output file for the simulator. The user may use a DOS batch file with the command "Rate.exe > results.txt" to save the output into a file named "results.txt." The file "results.txt" for Fig. 3.4 has the following heading:

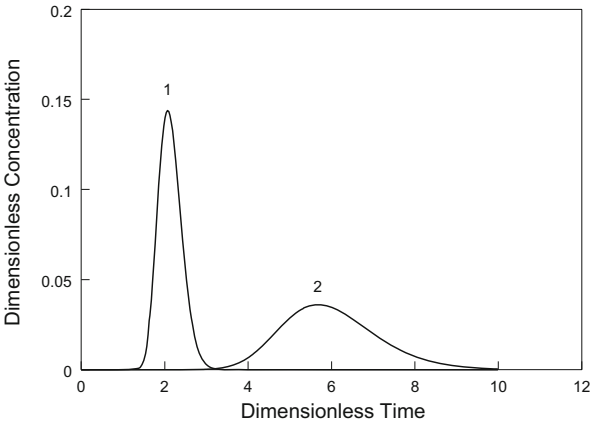

Fig. 3.4 Simulation of a binary elution using the rate model

```
Multicomponent Chromatography Simulator by Tingyue Gu (Ohio U.)
=======================================================
nsp nelemb nc index timp  tint tmax epsip epsib
 2  7   2  2  0.100 0.030 10.0 0.400 0.500
-------------------------------------------------------------
  PeL    eta    Bi   C0    consta  constb
 300.00  4.000  20.000 0.10000  1.200  1.500
 300.00  4.000  20.000 0.10000  8.000  10.000
=======================================================
End of data file
Total ODE = 90  data pts = 333
-------------------------------------------------------------
index =1 Breakthru; =2, Elution with inert MP
index =3 Step-change disp. Last comp. is displacer
index =4 BT, switch to displacement at t = tshift
index =5 Same as index=4, but reverse flow
index =6 Elution, the last component is modifier
index =7 Same as =6, but sample is in inert...
index =10+ use separation factors
-------------------------------------------------------------
 Results (t, c1, c2, ...) follow.  Please wait...
   0.0300  0.00000  0.00000
   (...more data points)
```

The numerical numbers in the heading before the phrase "End of data file" are the data read from the input file "data" by the computer code upon its execution. They are the number of components (nsp), the number of elements (nelemb), the number of interior collocation points (nc), the operation index, τ_{imp} (timp), the dimensionless time interval in the output data (tint), the maximum τ for calculation (tmax), ε_{p} (epsip) ε_{b} (epsib), $\text{Pe}_{\text{L}i}$ (PeL), η_i (eta), Bi_i (Bi), the maximum

concentration C_{0i} (C_0) for each component, a_i (consta), and b_i (constb). Note that a_i/b_i (moles per unit volume of particle skeleton) value for all the components must be in the same in order to have the same adsorption saturation capacity (C^{∞}) for all the components. This is required by the thermodynamic consistency for the Langmuir isotherm [2]. There are cases that cause the saturation capacity to differ for different components such as size-exclusion blocking access to binding sites in small macropores and macromolecules blocking access to binding sites underneath them as discussed in Chap. 11.

If a τ_{imp} value is not needed for a chromatographic operation, such as breakthrough operation, an arbitrary value, say 1.0, is still assigned to it in the file "data" to maintain the data input structure. The code will read this value, but it is not used in calculation. If index = 4 or 5, an additional dimensionless shift time must be provided at the end of file "data." This time value indicates when the column's feed is switched to the displacer after the rest of the components have been going through a frontal adsorption stage. The displacer is listed as the last component in file "data." A "tmax" value is required to tell the code to stop calculation after τ reaches this value. A "tint" value is needed to control the data points in the output file by specifying a time interval. This and "tmax" together determine how many data points are there in the output file. Simulated chromatograms are plotted by linearly linking data points generated by the LC simulator, which usually has 200–500 points.

Figure 3.2 simulation uses the same physical parameters as Fig. 3.4, but with numerical parameter nelemb = 20 instead of 7 to show smoother profiles inside the column. For Fig. 3.2, special case index = 202 is used. By adding 200 to index = 2 for elution, it signals RATE simulator in Chromulator V.1 to output concentration profiles inside the column for plotting in a spreadsheet program. The column exit ($z = 1$) concentrations in Fig. 3.2 match those in Fig. 3.4 for their respective dimensionless times. It should be noted that the peak sequence and skewness in the two figures are reversed in the two figures.

If the user wants to use a different isotherm other than the multicomponent Langmuir isotherm, the subroutine named "getdgdc" in RATE.FOR has to be rewritten to provide $(\partial g_i/\partial c_{\text{p}j})$ values. $g_i = \left(1-\varepsilon_{\text{p}}\right)c^{*}_{\text{p}i} + \varepsilon_{\text{p}}c_{\text{p}i}$, in which $c^{*}_{\text{p}i}$ is related to the isotherm. Of course, the input of the Fortran 77 code also needs to be modified to receive the new isotherm parameters. All the modifications should be rather straightforward to an experienced person.

The so-called "equilibrium-dispersive model" used by Lin et al. [6] is a subcase of the general rate model. The former is actually a lumped particle model with the Langmuir isotherm. The "equilibrium-dispersive model" is accommodated by the RATE simulator. The user only has to set the particle porosity very close to zero in the input data file. Note that the "equilibrium-dispersive model" lumps the intraparticle diffusion into the axial dispersion and film mass transfer resistance; thus the pseudo-axial dispersion and pseudo-film mass transfer coefficients cannot be readily evaluated using the existing mass transfer correlations in the literature during parameter estimation. This is a major drawback of such simplified models.

In view of this, the general rate model, although more complicated, offers a huge advantage. The major impetus for using a simplified model is to avoid the numerical solution difficulties encountered in solving the general rate model. This, however, has evaporated in this modern era due to advances in numerical methods and computer hardware. It is much easier to estimate the mass transfer parameters in the general rate model because they are frequently used in mass transfer studies in chemical engineering literature.

The Fortran 77-based LC simulator has been interfaced with a graphical user interface (GUI) written in the C++ computer language (in the Microsoft Visual Studio 6.0 environment) coded by Drs. Xueliang Fan and Zhiguo Li of the Institute of Process Engineering at the Chinese Academy of Sciences in Beijing in collaboration with the author. The LC simulation package with GUI is known as Chromulator Version 2, which is available free of charge for academic research and teaching. It is compatible with all Windows operating systems to date including Windows XP/Vista/7/8. Figure 3.5 is a reproduction of Fig. 3.4 using Chromulator 2.2. There are nine icons on the tool bar. The fourth icon is the printer. The fifth is an icon that copies the simulated numerical results in the columns left of the simulated chromatogram in Fig. 3.5 to the clipboard for pasting into a spreadsheet program such as Microsoft Excel. The sixth icon is used to copy the simulated

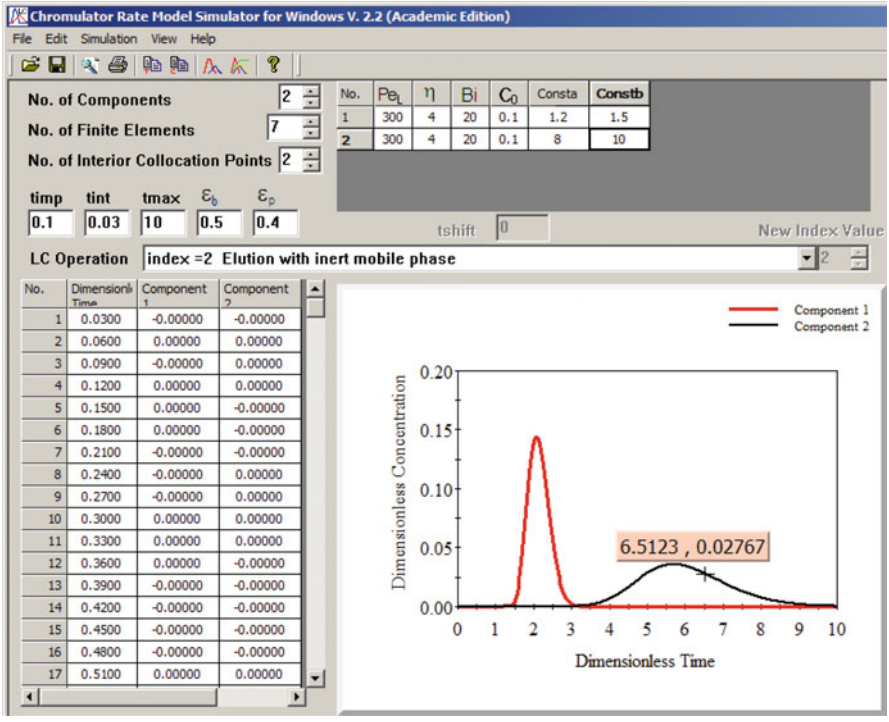

Fig. 3.5 Chromulator V. 2.2 reproduction of Fig. 3.4

chromatogram (chart) to the clipboard for pasting elsewhere. The seventh icon (with two peaks) is used to "run and plot" the simulation after the parameters are in place. The eighth icon (left of the question mark) is the "run and plot over previous results" button. This icon allows the user to plot two sets of chromatograms calculated from two sets of parameters for comparison. The first set is shown in solid lines and the second in dashed lines. It offers a convenient way to investigate the effects of parameters on chromatograms by superimposing two sets of chromatograms. The top File/Save Text Result menu allows the user to save the output as a text file that is generated by the Fortran 77 engine (a .dll file compiled using a modified RATE.FOR file by the Compaq Visual Fortran 6.6.a compiler), which is the same output generated by Chromulator V.1. Chart axis scales can be readjusted using the Edit/Adjust Chart menu. Another useful feature is that by placing the mouse cursor anywhere in the chromatogram, x-axis and y-axis values are displayed on the computer screen instantly. This allows accurate reading of peak positions and heights. For this Windows GUI, the user must hit the Enter key on the keyboard or click a different parameter entry field after a parameter value is entered. Otherwise, the new value may not take effect, because the new value has not yet been "read" by the software.

3.7 CPU Time for Computer Simulation

Effluent concentration profiles can be obtained from the numerical solution to the model. The model also provides the effluent history and the moving concentration profiles inside the column for each component. The concentration profile of each component inside the stagnant fluid phase and the solid phase of the particle can also be obtained through custom modification of the software, but they are rarely used for discussions. Only effluent history (chromatogram) is used as an output in standard Chromulator software packages.

The central processing unit (CPU) time required for the simulation of a chromatogram depends largely on how many ODEs need to be solved and how stiff they are. The total number of ODEs is equal to $N_s(2N_e+1)(N+1)$. Systems with more components (large N_s) and stiffer concentration profiles (requiring large N_e) require more ODEs to be solved. Usually, two interior collocation points ($N=2$) are needed, especially when D_{pi} values are small, which in turn give large Bi and small η values. Sometimes, one interior collocation point ($N=1$) is sufficient. The value of N does not affect the stability of the numerical solution. For theoretical studies involving nonstiff cases, using $N=1$ saves simulation time while achieving the same qualitative results. This practice usually is not needed nowadays due to fast PCs. Insufficient N tends to give diffused concentration profiles as shown in Figs. 3.6, 3.7 and 3.8. Using $N=1$ instead of $N=2$ in Figs. 3.6, 3.7 and 3.8 saves about 60 % CPU time on a personal computer (PC). In most cases, time saving is not meaningful because today's fast computers often give results in a fraction of a second or seconds instead of minutes in the 1990s. For the so-called "big beads"

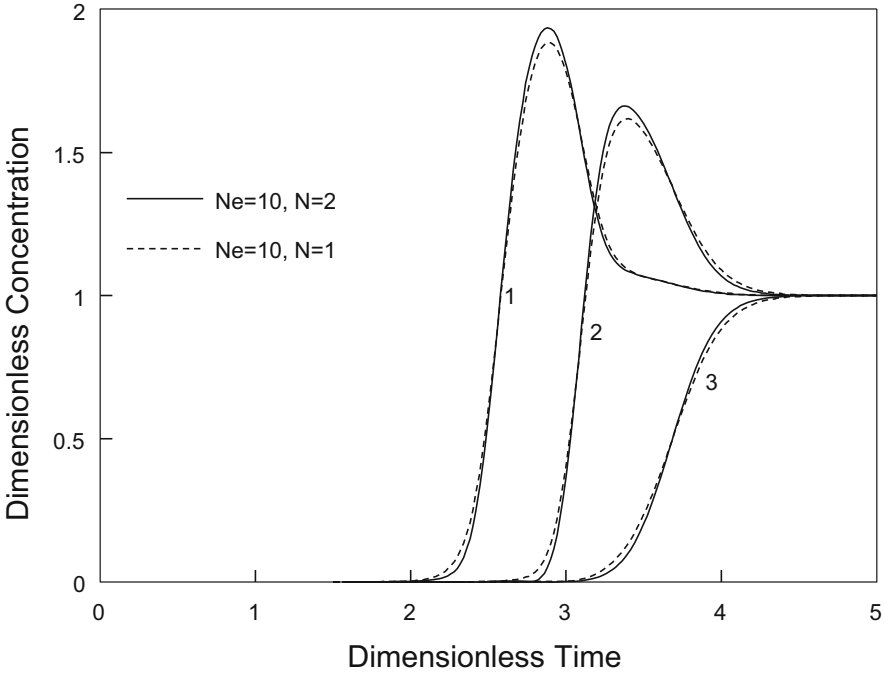

Fig. 3.6 Effect of the number of interior OC points (N) in the simulation of frontal adsorption

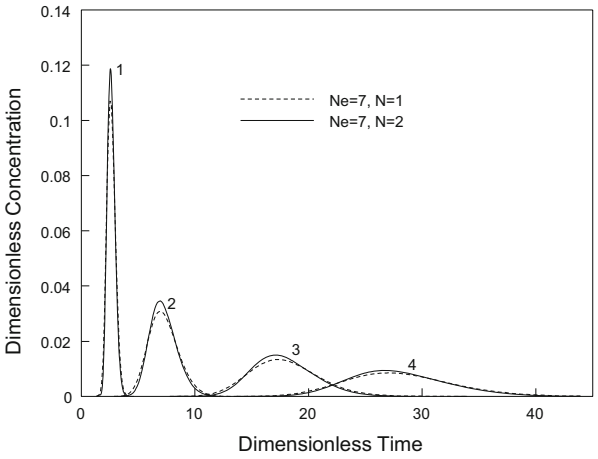

Fig. 3.7 Effect of the number of interior OC points (N) in the simulation of elution

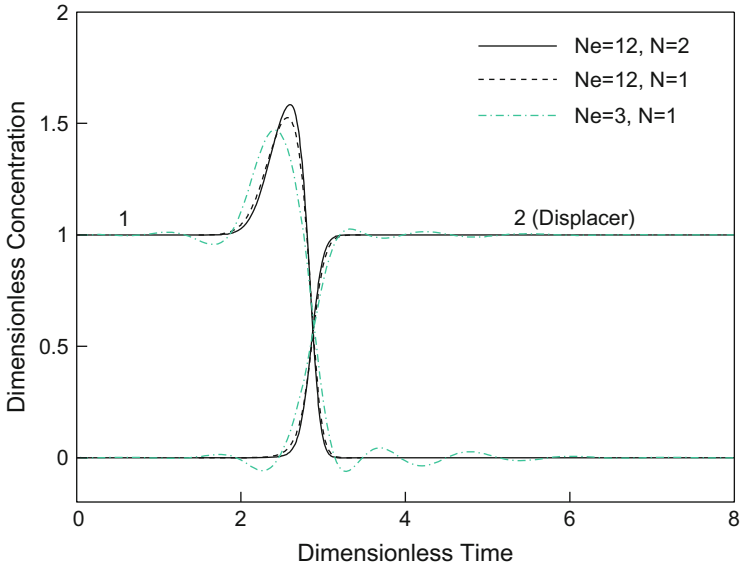

Fig. 3.8 Convergence of the concentration profiles in step-change displacement operation to elute out species 1 that presaturated the column

that have diameters reaching 100 μm or even higher, the concentration profiles inside particles are more complicated. This requires a much higher N for more accurate simulation. Gu et al. [7] showed a case using $N = 6$. The roots of polynomials for spherical geometry are listed in Table 4.5 in Finlayson's book [4] for $N = 1$–6. The roots for $N = 7$ and $N = 8$ are shown below from literature elsewhere [8],

$N = 7$	$N = 8$
0.2011940939974345223 0	0.17848418149584785585
0.3941513470775633698 9	0.35123176345387631529
0.5709721726085388475 3	0.51269053708647696788
0.7244177313601700474 1	0.65767115921669076585
0.8482065834104272162 0	0.78151400389680140692
0.9372733924007059043 0	0.88023915372698590212
0.9879925180204854284 8	0.95067552176876776122
	0.99057547531441733567

Using the roots above, an unreleased version of RATE simulator increased the maximum allowed N from 6 to 8 in case the particle diameter is particularly large. In most cases, a large N above 4 or 6 is not warranted. The drawback for using an excessively large N is that the stability problem of the orthogonal collocation method may surface. For example, a simulated breakthrough curve may appear slightly "wavy," like someone's drawing with a shaky hand.

The selection of the number of elements, N_e, is quite important. There is no exact criterion to dictate an N_e value, though the general rule of thumb is that the more stiff the concentration profiles the higher the N_e value. An insufficient N_e value will result in a numerical solution that has oscillation. $N_e = 5–10$ is usually sufficient for systems with nonstiff or slightly stiff concentration profiles. For stiff cases, $N_e = 20–30$ is often enough. A small N_e value can be tried out first. If the solution shows oscillation, a rerun can be carried out with an increased N_e value. In Fig. 3.8, the converged concentration profiles (solid line) take a fraction of a second on a 2013 era PC with a quad core i5-4570 3.20 GHz CPU, while it would take several minutes on a 1994 PC with single core Pentium 100 MHz CPU.

In Chap. 4, it will be shown that large Pe_L, Bi, and η values contribute to stiff concentration profiles. Isotherm parameters can also have major effects. For example, if the sample concentration falls into the nonlinear range of the Langmuir isotherm during elution, the self-sharpening effect causes very stiff front-flank of the peak. In theoretical studies, it is not necessary to run very stiff cases unless needed to demonstrate the effect under investigation. Most arguments can be made based on simulations of less stiff concentration profiles without excessive CPU times. Excessive CPU times are typically the results of stiffness caused by a very large Peclet number that is in the thousands. Such a large Pe value may be common in analytical columns, but it is not likely in preparative- and large-scale columns. One may use a lower value than parameter estimation yields to avoid the often unnecessary stiffness.

3.8 Extensions of the General Multicomponent Rate Model

Various extensions of the general multicomponent rate model are discussed in this book in separate chapters. They include the inclusion of second-order kinetics in order to describe a system with slow binding and dissociation reactions that may occur in cases like affinity chromatography, size-exclusion effect for SEC, and cored beads. Gradient elution can be modeled by adjusting the column feed profile. Ion-exchange chromatography (IEC) can be tackled using the mass action ion-exchange isotherm.

3.9 The Question of Choosing Column Boundary Conditions

In this book, the Danckwerts boundary conditions [9] shown as Eqs. (3.5) and (3.6) are used for the two column ends ($Z = 0$ and L). The validity of the Danckwerts boundary conditions in transient axial dispersion models has been argued for decades by some researchers. A review was given by Parulekar and Ramkrishna

[10]. For axial dispersions in some linear systems, they provided some seemingly physically more reasonable alternatives to the Danckwerts boundary conditions for transient systems based on analytical analyses. Unfortunately, for nonlinear systems, their analytical approach is not possible. Lee and coworkers [11] discussed the use of alternative boundary conditions for both column inlet and exit in some rate models.

In nonlinear chromatography, the Danckwerts boundary conditions are generally accepted. However, for the column exit some researchers [12, 13] implied that it is better to use finite values for the concentration flux instead of zero as in the Danckwerts boundary conditions. This is equivalent to assuming that the column is semi-infinitely long, and the effluent history is detected at $z = 1$. This alternative boundary condition at the column exit while leaving the boundary condition at the column inlet unchanged is hardly appropriate, since it tends to destroy the mass balance of the model system as shown below.

In the effluent history of a frontal analysis, each breakthrough curve can be integrated to see whether it matches the dimensionless column holdup capacity for the corresponding component, which is expressed by the following expression assuming that there is no size-exclusion effect:

$$\mathrm{CA}_i = \left[(1-\varepsilon_\mathrm{b})\left(1-\varepsilon_\mathrm{p}\right) \frac{b_i C^\infty}{1+\sum_{j=1}^{N_\mathrm{s}} b_j C_{0j}} + (1+\varepsilon_\mathrm{b})\varepsilon_\mathrm{p} + \varepsilon_\mathrm{b} \right] \Big/ \varepsilon_\mathrm{b} \tag{3.33}$$

In the equation above, CA_i consists of three parts, the amount of component i adsorbed onto the solid part of the particles, that in the stagnant fluid inside particles, and that in the bulk fluid. This equation is actually equal to the first moment of a breakthrough curve. It is equivalent to the expression of the first moment in a single-component system with the Danckwerts boundary conditions and Langmuir isotherm derived by Lee et al. [14] from differential mass balance equations. The holdup capacity should also be equal to the area integrated from the equation below,

$$\mathrm{CA}_i = \tau_\mathrm{e} - \int_0^{\tau_\mathrm{e}} c_{\mathrm{b}i}\big|_{z=1} \mathrm{d}\tau \tag{3.34}$$

where τ_e is a time value at which the breakthrough curve has already leveled off. Since the holdup capacity reflects the steady state of the column, mass transfer and dispersion effects do not affect its value. The two equations above are very helpful in checking the mass balance of an effluent history in frontal analysis and step-change displacement. A free small utility software program (called PEAKAREA) for Windows has been created by the author for the calculation of the area above a

concentration curve and below the dimensionless concentration of unity line, and the area under a concentration peak. Upon launching the software, it asks for the name of a user's concentration profile data file that contains time and concentration data points in pairs for a single component. This code can also be used to calculate peak areas in elution chromatography. For multicomponent data, one may use Microsoft Excel spreadsheet to sort the data to get single-component data pairs.

The use of the Danckwerts boundary condition at the column exit needs no additional effort in the FE formulation, since in the FE method, the zero flux as an NBC is a default boundary condition. The implementation of the alternative boundary condition at the column exit can also be easily accommodated in the existing code that uses the Danckwerts boundary conditions. In the function subroutine of the code that evaluates concentration derivatives, the trial concentration values are given; thus $(\partial c_{\mathrm{b}i}/\partial z)|_{z=1}$ can be obtained by using the concentration values at the three element nodes for derivative calculations. In the actual code, adding a few lines and a simple extra subroutine for the derivative calculations will suffice for the modifications needed. Note that the natural boundary condition at $z = 1$ is,

$$(\mathrm{PB}_i)\big|_{z=1} = \frac{1}{\mathrm{Pe}_{\mathrm{L}i}} \frac{\partial c_{\mathrm{b}i}}{\partial z}\Big|_{z=1} \tag{3.35}$$

and it should be added to $[\mathbf{AFB}_{\mathrm{i}}]$ at $z = 1$. Figure 3.9 shows single-component breakthrough curves with the Danckwerts boundary condition and the alternative boundary condition at the column exit, respectively. Parameter values used for simulation are listed in Table 3.1. It is obvious that the use of the alternative boundary condition results in a later breakthrough, and thus a larger capacity area that is not equal to the correct theoretical value, unlike in the case with the Danckwerts boundary condition. This violation of a basic mass balance is clearly undesirable. In fact, any attempt to change the Danckwerts boundary condition at one column end while leaving the other end intact may lead to such a violation because the complete Danckwerts boundary conditions are mass balanced.

Figure 3.10 shows the concentration profiles inside the column at different times, corresponding to the breakthrough curve in Fig. 3.9. It shows that when the Danckwerts boundary condition is used at $z = 1$, the concentration curves bend upward trying to approximate the zero flux requirement. Note that this boundary condition may not be completely satisfied with an insufficient number of FE nodes, but the $c_{\mathrm{b}i}$ values at $z = 1$ easily converge. Figure 3.10 also shows that the concentration profiles are quite smooth at the column exit when the alternative boundary condition is used. This is because the alternative boundary condition assumes that the column has no discontinuity at the column exit. Unrelated to the boundary condition choices, in Fig. 3.10, when τ is not very small (say $\tau \geq 1$), the concentration profiles are very similar in shape for different τ. This is the so-called "constant pattern" phenomenon [2].

The mass balance violation may not be noticeable in elution, as is shown in Fig. 3.11, in which the areas for each component for the Danckwerts boundary

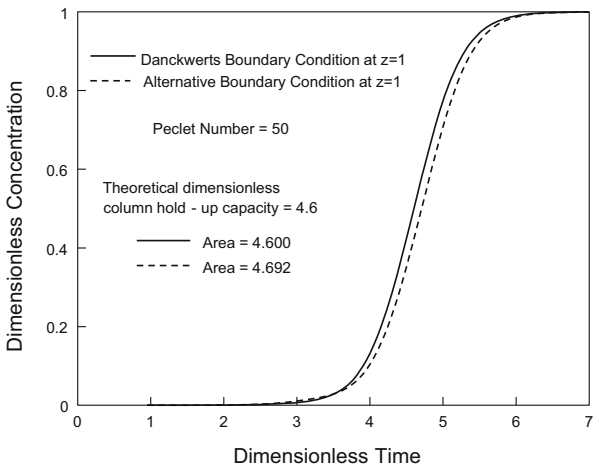

Fig. 3.9 Single-component breakthrough curves (Peclet number = 50)

Table 3.1 Parameter values used for simulation in this chapter[a]

		Physical parameters					Numerical parameters	
Figure	Species	Pe_{Li}	η_i	Bi_i	a_i	$b_i \times C_{0i}$	N_e	N
3.6	1	400	6	10	2	4×0.1	10	2
	2	400	6	10	7	12×0.1		
	3	400	6	10	15	30×0.1		
3.7	1	300	4	20	1.2	1.5×0.1		
	2	320	4.2	17	8	10×0.1	7	2
	3	400	5.5	16	24	30×0.1		
	4	500	7	15	38.4	48×0.1		
3.8	1	600	6	5	3	6×0.1	12	2
	2	600	3	6	12	24×0.3		
3.9	1	50	2	10	8	7×0.2	4	2
3.10	1	50	2	10	8	7×0.2	20	2
3.11	1	50	10	4	4	3.5×0.2	8	2
	2	50	10	4	8	7×0.2		
3.12	1	200	2	10	8	7×0.2	5	2

[a]For Figs. 3.6, 3.7, 3.8, 3.9, 3.10, 3.11, and 3.12, $\varepsilon_b = \varepsilon_p = 0.4$. Sample pulse size for Fig. 3.7 is $\tau_{imp} = 0.1$; for Fig. 3.11 $\tau_{imp} = 0.2$

condition and the alternative boundary conditions at $z = 1$ are both 0.2000, matching the value of sample size τ_{imp}.

It is shown in Eq. (3.35) that the $(\mathbf{PB}_i)|_{z=1}$ value can be set to zero if the Pe_{Li} values are large. Figure 3.12 has the same conditions as Fig. 3.9, except that the Peclet number in Fig. 3.12 is 300, which is much larger than that in Fig. 3.9. Figure 3.12 shows that the differences are quite small using the Danckwerts boundary condition vs. using the alternative boundary condition at the column exit when the Peclet number is not very small. This is in agreement with the results

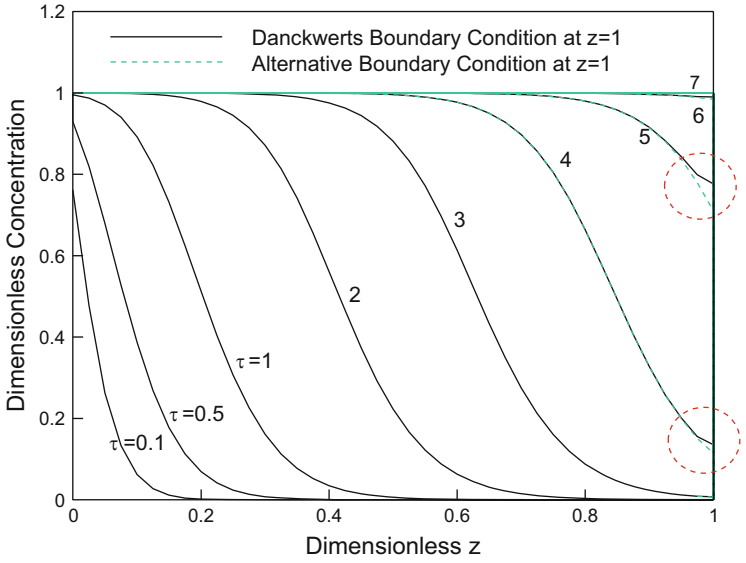

Fig. 3.10 Breakthrough concentration profiles inside the column

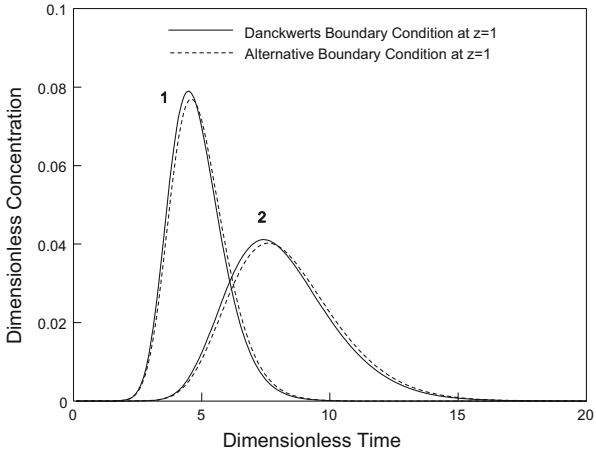

Fig. 3.11 Binary elution with different boundary conditions at the column exit

obtained by Brian et al. [12]. In fact, in common axial flow chromatography, the Peclet number for axial dispersion is often in the upper hundreds or 1,000 or higher. Thus, the differences resulting from using different boundary conditions at the column exit are negligible. Thus, seeking an alternative boundary condition to replace the Danckwerts boundary condition for the column exit seems practically meaningless and even counterproductive in view of a possible mass balance violation.

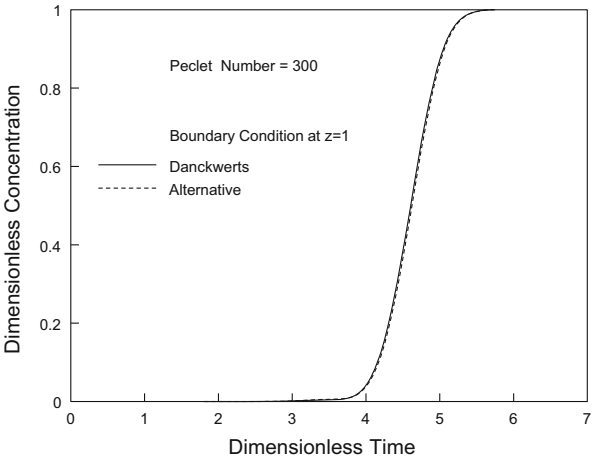

Fig. 3.12 Single-component breakthrough curves (Peclet number = 300)

References

1. Bird RB, Stewart WE, Lightfoot EN (2007) Transport phenomena. Wiley, New York
2. Ruthven DM (1984) Principles of adsorption and adsorption processes. Wiley, New York
3. Reddy JN (1984) An introduction to the finite element method. McGraw-Hill, New York
4. Finlayson BA (2003) Nonlinear analysis in chemical engineering. Ravenna Park, Seattle, WA
5. Brown PN, Byrne GD, Hindmarsh AC (1989) VODE: a variable-coefficient ODE solver. SIAM J Sci Stat Comp 10:1038–1051. doi:10.1137/0910062
6. Lin B, Golshan-Shirazi S, Ma Z, Guiochon G (1988) Shock effects in nonlinear chromatography. Anal Chem 60:2647–2653
7. Gu T, Iyer G, Cheng K-SC (2013) Parameter estimation and rate model simulation of partial breakthrough of bovine serum albumin on a column packed with large Q Sepharose anion-exchange particles. Sep Purif Technol 116:319–326
8. Stroud AH, Secrest D (1966) Gaussian quadrature formulas. Prentice-Hall, London
9. Danckwerts PV (1953) Continuous flow systems: distribution of residence times. Chem Eng Sci 2:1–13. doi:10.1016/0009-2509(53)80001-1
10. Parulekar SJ, Ramkrishna D (1984) Analysis of axially dispersed systems with general boundary conditions-I-, II, III. Chem Eng Sci 39:1571–1611. doi:10.1016/0009-2509(84)80085-8
11. Lee WC, Huang SH, Tsao GT (1988) A unified approach for moments in chromatography. AIChE J 34:2083–2087
12. Brian BF, Zwiebel I, Artigue RS (1987) Numerical simulation of fixed bed adsorption dynamics by the method of lines. AIChE Symp Ser 83:80–86
13. Lin B, Ma Z, Guiochon G (1989) Study of the influence of axial dispersion on the band profile in nonlinear chromatography using the Lax-Wendroff method. Sep Sci Technol 24:809–829. doi:10.1080/01496398908049877
14. Lee W-C, Tsai G-J, Tsao GT (1990) Radial-flow affinity chromatography for trypsin purification. ACS Symp Ser 427:104–117

Chapter 4
Parameter Estimation

One of the critical factors for a successful scale-up of LC using the rate models is accurate parameter estimation. Three types of parameters are needed to carry out model calculations using the rate models. Isotherm parameters, the particle porosity, and the bed void volume fraction are most important to the accuracy of model calculations. Physical dimensions of the column are also important, but they can be specified or precisely measured. Less important parameters are the mass transfer parameters that usually do not affect the general location of an elution peak. They affect the sharpness of a peak or breakthrough curve. However, such an influence is not extremely sensitive to the minor fluctuations of the mass transfer parameters. Thus, the estimation of these parameters does not have to be very stringent. As always, parameter sensitivity analysis can be carried out using computer simulation by varying a parameter (say 10 %, 20 %, or more) to see the impact on the chromatogram.

4.1 Bed Voidage and Particle Porosity

Bed voidage (ε_b) and particle porosity (ε_p) are two key parameters in accurate LC modeling. They influence the mass balances in breakthrough curves and retention times of eluted peaks considerably. In LC, porosity refers to the particle macropore porosity. The so-called particle micropores are relevant only in gas chromatography with small molecules [1]. Particle porosity is determined by the particle internal pore structure, while bed voidage depends on the particle size, shape, and how they are packed. For soft gel beds, bed voidage can change due to column pressure change. It is also possible that an excessive pressure may alter the particle porosity

Electronic supplementary material The online version of this chapter (doi:10.1007/978-3-319-16145-7_4) contains supplementary material, which is available to authorized users.

© Springer International Publishing Switzerland 2015

T. Gu, *Mathematical Modeling and Scale-Up of Liquid Chromatography*,
DOI 10.1007/978-3-319-16145-7_4

of a soft gel. In this book, bed voidage and particle porosity are considered constant in all discussions. The effect of pressure on physical parameters is not dealt with for the sake of simplicity.

Bed voidage and particle porosity are usually not provided by separation media vendors and must be determined experimentally if they are not available from the literature. If a column does not retain any solute, for example, a column with a zero column volume (i.e., no LC separation media inside), the breakthrough curve is a vertical line at time zero, assuming that tubing volume delay is neglected. For any other columns packed with particles, the breakthrough curve takes off at a later time. The delay is due to (1) solute retained in the bed void space between particles, (2) solute in the fluid trapped in particle macropores, and (3) solute adsorbed by the particles. Assuming that time zero is the moment when the solute first enters the column in a breakthrough analysis, the following mass balance equation [2] can be established for the single-component breakthrough curve in Fig. 4.1 with a level-off cutoff time of t_e to account for all the three delay factors.

$$\begin{aligned} A_1 Q &= C_0 t_e Q - A_2 Q \\ &= V_b \varepsilon_b C_0 + V_b (1-\varepsilon_b)\varepsilon_p C_0 + V_b (1-\varepsilon_b)\left(1-\varepsilon_p\right)\frac{a}{1+bC_0} \end{aligned} \tag{4.1}$$

In Eq. (4.1), it is assumed that the solute-stationary phase binding follows the Langmuir isotherm. Blue dextran is a large polysaccharide molecule that does not penetrate particle macropores. If it is nonbinding as well, Eq. (4.1) loses the corresponding second and third terms on the right-hand side to become

$$A_1 Q = V_b \varepsilon_b C_0 \tag{4.2}$$

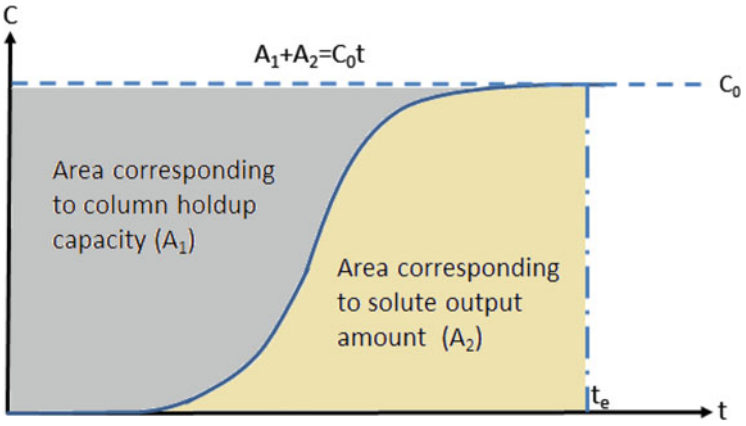

Fig. 4.1 Dimensionless column holdup capacity area for a breakthrough curve

in which A_1 is the dimensional column holdup capacity area for a breakthrough curve (Fig. 4.1). Equation (4.2) leads to the following equation for the estimation of bed voidage using a blue dextran breakthrough curve:

$$\varepsilon_b = QA_1/(V_bC_0) \tag{4.3}$$

Blue dextran will bind with some ion-exchange resins; thus it is not a good choice for them. For some ion-exchange resins, ions that are completely excluded by the resins as in ion exclusion chromatography may be used to replace blue dextran.

To obtain particle porosity ε_p, a breakthrough curve using a nonbinding small solute (e.g., acetone or sodium chloride) at a concentration of C_0 in the mobile phase that penetrates the particle macropores is needed by adding the second term on the right-hand side of Eqs. (4.1)–(4.2), which yields the following equation:

$$A_1Q = V_b\varepsilon_bC_0 + V_b(1-\varepsilon_b)\varepsilon_pC_0 \tag{4.4}$$

The equation below is an expression for mobile phase flow rate based on interstitial mobile phase velocity, column length, column packing volume, and bed voidage,

$$Q = 0.25\pi {d_c}^2(v\varepsilon_b) = (V_b/L)v\varepsilon_b \tag{4.5}$$

Combining Eqs. (4.4) and (4.5) produces the following equation:

$$[A_1v/(LC_0)]\varepsilon_b = \varepsilon_b + (1-\varepsilon_b)\varepsilon_p \tag{4.6}$$

A_1 can be nondimensionalized using C_0 for the y-axis and L/v for the x-axis in Fig. 4.1 to give a dimensionless column holdup capacity area,

$$\mathrm{CA} = \frac{A_1}{C_0(L/v)} \tag{4.7}$$

Thus, Eq. (4.6) becomes,

$$\mathrm{CA}\cdot\varepsilon_b = \varepsilon_b + (1-\varepsilon_b)\varepsilon_p \tag{4.8}$$

This yields an equation that can be used to calculate particle porosity,

$$\varepsilon_p = \frac{\mathrm{CA}\cdot\varepsilon_b - \varepsilon_b}{1-\varepsilon_b} \tag{4.9}$$

Pulse elution analysis can be used instead of frontal analysis above to obtain ε_b and ε_p. With the experimental dead volume time of unretained large molecules (such as blue dextran) in a pulse analysis with a small sample volume, a symmetric peak is obtained. Its retention time t_d is equal to the average breakthrough time of the corresponding breakthrough curve (or $A_1 = C_0t_d$ in Fig. 4.1). Thus, Eq. (4.2) leads to the following relationship readily:

$$t_d = V_b \varepsilon_b / Q = \pi {d_c}^2 L \varepsilon_b / (4Q) \tag{4.10}$$

Based on the definition of interstitial velocity,

$$v = \frac{Q}{\frac{\pi}{4} d_c^2 \varepsilon_b} \tag{4.11}$$

Equation (4.10) gives

$$t_d = L/v \tag{4.12}$$

which corresponds to $\tau_d = 1$ because $\tau = t/(L/v)$ by definition. The mass balance equation using t_0, the dead volume time in pulse analysis of unretained small molecules, such as salt and solvent molecules that penetrate the particle macropores, can be obtained by inserting $A_1 = C_0 t_0$ into Eq. (4.4) to yield

$$(t_0 Q) C_0 = (V_b \varepsilon_b) C_0 + \left[V_b (1 - \varepsilon_b) \varepsilon_p \right] C_0 \tag{4.13}$$

which leads to

$$t_0 = V_b \left[\varepsilon_b + (1 - \varepsilon_b) \varepsilon_p \right] / Q \tag{4.14}$$

In the equation above, $\varepsilon_b + (1 - \varepsilon_b)\varepsilon_p$ is the total void volume fraction consisting of bed voidage and particle macropores [3]. If ε_b is already known, Eq. (4.14) can be directly used to yield ε_p. It gives [3]

$$\varepsilon_p = \frac{Q t_0 - \varepsilon_b V_b}{(1 - \varepsilon_b) V_b} \tag{4.15}$$

Dividing Eq. (4.10) by Eq. (4.14) gives the following relationship:

$$\frac{t_0}{t_d} = 1 + \frac{(1 - \varepsilon_b)\varepsilon_p}{\varepsilon_b} \tag{4.16}$$

This dimensionless equation can also be used to calculate ε_p using the ratio of the two retention times and ε_b. This equation easily leads to the following relationship because t is proportional to τ and $\tau_d = 1$:

$$\tau_0 = 1 + \frac{(1 - \varepsilon_b)\varepsilon_p}{\varepsilon_b} \tag{4.17}$$

In LC, t_0 is referred to as "solvent time" in elution by chromatographers. There is usually a blip early in an elution chromatogram caused by the factor that the injected sample often has a different chemical background than the mobile phase. For example, the mobile has a solvent or salt in it, while the sample may be a

protein in water without solvent or salt. The solvent time t_0 is larger than t_d as shown in Eq. (4.16), since small molecules penetrate the macropores. In fact, t_d and t_0 in pulse elution analysis have the same values as the average breakthrough times in single-component frontal analysis for a large unretained solute (e.g., blue dextran) and a small unretained solute, respectively. The breakthrough curve area integration method is more accurate because it is insensitive to mobile phase flow pattern maldistribution inside a column. With the t_0 read from the solvent time in a chromatogram and τ_0 calculated from ε_b and ε_p, the ratio t_0/τ_0 can be conveniently used to convert τ to t instead of using $t = \tau(L/v)$ for time conversion. Caution must be exercised to avoid treating an impurity peak as the solvent peak especially when the y-axis range is large, which can make a tiny solvent peak disappear from an experimental chromatogram. Thus, it is always safer to use $t = \tau(L/v)$ or to use it for double-checking.

4.2 Isotherms

Adsorption isotherms, especially multicomponent isotherms, are generally not available for a particular system from existing publications in the literature. They may have to be measured experimentally. Isotherm data points are first measured experimentally and then fitted or correlated with an isotherm model, such as the most commonly used Langmuir isotherm model. For a single-component system, the isotherm data can always be correlated using a polynomial equation with reasonable accuracy if there are no other better isotherm models to use. Unfortunately, the simple polynomial model is not a substitute for a multicomponent isotherm model. There are generally two experimental methods to obtain isotherm data.

4.2.1 Column Method

The frontal adsorption (also known as breakthrough analysis) method [4] can be used to obtain isotherms. Jacobson et al. [5] provided a detailed experimental procedure and equations for the evaluation of isotherm data.

The Langmuir isotherm in Eqs. (3.21a) and (3.21b) is most commonly used in LC. The measurement of a single-component Langmuir isotherm can be done by performing frontal adsorption on a mini column. If the Langmuir isotherm binding term in Eq. (4.1) is not dropped, Eq. (4.8) should be modified as shown below with an extra term as shown below:

$$\mathrm{CA} \cdot \varepsilon_b = \varepsilon_b + (1 - \varepsilon_b)\varepsilon_p + (1 - \varepsilon_b)\left(1 - \varepsilon_p\right)\frac{a}{1 + bC_0} \tag{4.18}$$

For a multicomponent system, the equation above can be re-written as

$$\mathrm{CA}\cdot\varepsilon_\mathrm{b}=\varepsilon_\mathrm{b}+(1-\varepsilon_\mathrm{b})\varepsilon_\mathrm{p}+(1-\varepsilon_\mathrm{b})\left(1-\varepsilon_\mathrm{p}\right)\frac{b_iC^{\infty}}{1+\sum_{j=1}^{N_\mathrm{s}}b_jC_{0j}} \tag{4.19}$$

When ε_b and ε_p are known, performing two frontal (breakthrough) analyses with two different solute concentrations in the mobile phase gives two CA values. Equation (4.18) can then be used to obtain Langmuir isotherm parameters a and b for a single-component system. If more than two C_0 values are available, Eq. (4.18) can be readily linearized for linear regression of a and b values using a double reciprocal linear plot [2]. This kind of breakthrough analysis for isotherm parameters may require a large amount of solute if the column is not very small. One way to save solute is to use step-changes of the solute concentration in the mobile phase.

Another method to obtain parameter a in the Langmuir isotherm with minimized use of a solute is to perform an isocratic elution with a dilute sample on the column. It gives the retention factor k' (also known as the capacity factor, which is defined as the ratio of the total moles of solute in the stationary phase to that in the mobile phase at equilibrium) based on the following relationship by Snyder et al. [6] for linear LC:

$$k^{'}=(t_\mathrm{R}-t_0)/t_0 \tag{4.20}$$

where t_R is the retention time of the solute. Based on the definition of the capacity factor, it is easy to show that for an isocratic elution with a dilute sample that observes the linear range of the Langmuir isotherm,

$$k^{'}=\varphi C^{\infty}b=\varphi a \tag{4.21}$$

where φ is the phase ratio (the stationary phase particle skeleton volume to mobile phase volume including that in the particle macropores). φ can be determined from the following equation based on its definition:

$$\varphi=(1-\varepsilon_\mathrm{b})\left(1-\varepsilon_\mathrm{p}\right)/\left[\varepsilon_\mathrm{b}+(1-\varepsilon_\mathrm{b})\varepsilon_\mathrm{p}\right] \tag{4.22}$$

When a is known, b can be calculated using Eq. (4.18) with only one frontal analysis. Parameter b can also be obtained with frontal analysis using a method by Snyder et al. [4]. The method measures the column saturation capacity based on the slightly different retention times of two gradient elution runs: one using a small sample size and the other using a large overload sample size. They provided a semiempirical equation for the calculation of the column saturation capacity, which can be converted to get C^{∞}. Parameter b is subsequently calculated from $b=a/C^{\infty}$. A procedure for this method is described by Gu and Zheng [3] and Chap. 12.

In his book, *Principles of Adsorption and Adsorption Processes*, Ruthven [1] devoted a chapter to the discussion of many different kinds of multicomponent isotherm models apart from the Langmuir isotherm model, such as the Langmuir–Freundlich Equations, the General Statistical Model, the Dubini–Polanyi Theory, the Ideal Adsorbed Solution Theory (IAST), and the Vacancy Solution Theory. These models were first used in gas–solid absorption or adsorption of liquid hydrocarbons on solid adsorbents such as zeolites. Some of the models, such as the IAST, have been used in protein adsorptions on chromatographic media with certain degrees of success. Artificial neural network has also been used to correlate multicomponent isotherms [7]. This method is attractive for multicomponent systems that do not follow the multicomponent Langmuir isotherm and other existing isotherm models.

In some practical multicomponent systems, the interference effect may be negligible. For example, in a binary elution system, if the two components quickly separate from each other inside the column, the duration of the interference effect will be short; thus the system may be treated as two separate single-component systems. This may happen if the sample size is small or the affinity (b value) difference of the two components is large. Discussions provided in Chap. 6 should be helpful in making such a judgment. In some cases, several components with similar retention times may be lumped together and be treated as a pseudo-component to simplify a large system.

4.2.2 Batch Adsorption Equilibrium Method

This is a straightforward method. A solution with a fixed concentration of solute is mixed with a certain amount of adsorbent in a test tube. The content is then stirred or shaken well for a sufficient amount of time until adsorption equilibrium is established. The supernatant is then analyzed for the liquid phase concentration. Centrifugation is preferred over membrane filtration to remove fines of the adsorbent from the supernatant before analysis because some membranes will bind with solutes such as proteins. Suppose a solution with m_0 moles of a solute is mixed with W grams of an adsorbent that has a post-swelling density of ρ_p (grams of particle per unit volume of adsorbent particle skeleton). The equilibrium concentration in the stationary phase can be obtained using the following relationship:

$$C_p^* = \left[m_0 - C_p\left(V_{sm} - W/\rho_p\right)\right] / \left(W/\rho_p\right) \tag{4.23}$$

where C_p is the equilibrium concentration of the solute in the supernatant and V_{sm} is the total volume of the solution mixed with the adsorbent. With a set of experimental data points of C_p^* vs. C_p, an analytical expression of a single-component isotherm can be obtained by correlating these data points using an isotherm model, such as the Langmuir isotherm. Linear regression can be carried out using a double reciprocal plot for the Langmuir isotherm. If ρ_p is based on the particle volume

including the macropores, Eq. (4.23) requires the total macropore volume to be negligible compared with the total fluid volume. The C_p^* value obtained this way must be converted to a value based on particle skeleton volume by dividing it by $(1 - \varepsilon_p)$ before the value can be used in the LC models throughout this book. Some people may overlook this and encounter gross mass balance problems in the process of matching experimental chromatograms with simulated ones.

4.3 Mass Transfer Parameters

In this book, it is assumed that mass transfer parameters of different components in a multicomponent system are the same as those in a single-component system, i.e., there are no mixing effects. The effect of concentration on mass transfer parameters is also ignored. Mass transfer parameters such as k_i, D_{bi}, and D_{pi} often are not available from literature or not easily measured through experiments. However, they can be estimated from existing correlations in the literature without doing new experiments. Fortunately, rate models are not very sensitive to mass transfer parameters. Errors to a certain degree do not affect the outcome by a great deal. On the contrary, bed voidage, particle porosity, and isotherm parameters impact the simulation outcome strongly, and thus their accuracies, rather than the accuracies for mass transfer parameters, are of concern. Keep in mind that one may always use computer simulation to check the effects of parameter variations on simulated chromatograms.

It should be pointed out that using a general rate model for parameter estimation is not a good practice. Chapter 5 shows that changes in different mass transfer parameters may offset or compensate each other. One must use limiting cases for parameter estimation by using a degenerated rate model, i.e., minimizing other effects before measuring one mass transfer effect. Otherwise, unpredictable large errors may occur.

4.3.1 Peclet Number

Peclet number is calculated from its definition which requires the value of the axial dispersion coefficient D_b:

$$\mathrm{Pe}_L = vL/D_b \tag{4.24}$$

Axial dispersion in a fixed-bed LC column is caused by molecular diffusion and turbulent mixing around the particles due to splitting and merging of flow streams [1]. Ligny [8] provided the following semiempirical correlation for D_b in fixed beds packed with spherical particles to account for both contributions to axial dispersion:

$$D_b = 0.7D_m + \frac{5.0R_p v}{1 + 4.4D_m/(R_p v)} \tag{4.25}$$

In this correlation, the molecular diffusion term ($0.7D_m$) comes from Langer et al. [9] and the turbulent mixing term (second term on the right-hand side) from Giddings' random-walk analysis [10]. The molecular diffusivity (D_m) can be calculated using the following correlation from Polson [11] for molecules with a molecular weight (MW) above 1,000:

$$D_m\left(m^2/s\right) = \frac{9.40 \times 10^{-15} T}{\mu (MW)^{1/3}} \tag{4.26}$$

in which temperature T is in Kelvin and viscosity is in Pa s. This leads to the following simpler semiempirical correlation using MW only:

$$D_m(m^2/s) = 2.74 \times 10^{-9} (MW)^{-1/3} \quad (MW > 1,000) \tag{4.27}$$

For molecules with MW less than about 1,000, the Stokes–Einstein equation below may be used [12] for better accuracy,

$$D_m\left(m^2/s\right) = \frac{9.96 \times 10^{-16} T}{\mu V_m^{1/3}} \tag{4.28}$$

where V_m is the atomic volume in m^3/kg mol. Its evaluation was discussed by Geankoplis [12]. In practice, the use of a more complicated equation for D_m often does not bring any noticeable differences in simulated chromatograms because its impact on η and Biot numbers is not big enough. For example, using Eq. (4.28) may yield a D_m value for a small molecule that is 10 % higher than that from Eq. (4.26). This impacts the η and Biot numbers. However, this kind of difference usually does not bring any noticeable changes in the simulated chromatograms. Thus, it is safe to use the simple relationship in Eq. (4.27) even for small molecules. A parameter sensitivity analysis using computer simulation can be easily performed to verify.

Chung and Wen [13] suggested that D_b is usually one or two orders of magnitude higher than D_m. When molecular diffusion is ignored (e.g., when the solute has a very large MW leading to very small D_m), Eq. (4.25) simplifies to

$$D_b \approx 5.0R_p v \tag{4.29}$$

A more accurate correlation is the Chung and Wen empirical correlation [13] that considers bed voidage:

$$D_b = \frac{2R_p v\varepsilon_b}{0.2 + 0.011Re^{0.48}} \quad \left(10^{-3} < Re < 10^3\right) \tag{4.30}$$

The Reynolds number is defined as $Re = v\rho_f(2R_p)/\mu$ in LC. It is typically much smaller than 1. Thus, the Chung and Wen correlation simplifies to

$$D_b \approx 10R_p v\varepsilon_b \quad \left(10^{-3} < Re < 1\right) \tag{4.31}$$

This leads to

$$\mathrm{Pe_L} \approx \frac{L}{10R_p\varepsilon_b} \quad \left(10^{-3} < Re < 1\right) \tag{4.32}$$

It should be noted that in mass transfer correlations in the literature, the superficial velocity (i.e., "empty-tower" velocity or $v\varepsilon_b$) is often used instead of the interstitial velocity v (i.e., actual fluid velocity). Thus, conversion may be needed when adopting some correlations.

For turbulent mixing, the Chung and Wen correlation is more accurate, because it was based on a large amount of experimental data for fixed beds while the Ligny correlation relied on a much smaller dataset and it does not consider bed voidage. One disadvantage for the Chung and Wen correlation is that it ignores the molecular diffusion term that can be more pronounced for small solutes with small MW. Gu et al. [2] proposed the following correlation by introducing the bed voidage into the Ligny correlation:

$$D_b = 0.7D_m + \frac{10R_p v\varepsilon_b}{1 + 2.2D_m/\left(R_p v\varepsilon_b\right)} \quad (Re < 1) \tag{4.33}$$

Equation (4.33) reduces to Eq. (4.25) if $\varepsilon_b = 0.5$. This new D_b correlation agrees well with Eq. (4.30), for almost any reasonable ε_b values. Because it accounts for molecular diffusion in addition to turbulent mixing, it is particularly useful for fixed beds including LC columns with small particles, slow fluid velocity, and small solutes.

4.3.2 η *Number Estimation*

η is calculated using the following definition:

$$\eta = \frac{\varepsilon_p D_p L}{R_p^2 v} \tag{4.34}$$

in which the effective intraparticle diffusivity (D_p) can be evaluated from the following experimental correlation [14]:

$$D_p = D_m\left[1 - 2.104\left(d_m/d_p\right) + 2.09\left(d_m/d_p\right)^3 - 0.95\left(d_m/d_p\right)^5\right]/\tau_{tor} \qquad (4.35)$$

The molecular diameter of a solute to the average particle macropore diameter ratio d_m/d_p is sometimes denoted as parameter λ_m. The tortuosity τ_{tor} (also known as the labyrinth factor) value is not easy to measure experimentally and it is not supplied by vendors of the LC stationary phase. Although its range is 1.5 to over 10, it is said that the reasonable value for many commercial porous particles is around 2–6 [15, 16]. An increase in τ_{tor} will decrease the D_p value proportionally as seen in Eq. (4.35). This leads to a proportionally smaller η value and proportionally larger Biot number. Li et al. showed that a larger τ_{tor} makes a peak less sharp in SEC [17]. A smaller η value will make the peak less sharp, while a larger Biot number will make the peak sharper. However, Biot number is usually already large and insensitive. Thus, the decrease in η usually has a more profound impact on the peak sharp, resulting in a net effect of a more diffused peak. Figure 4.2 shows that doubling of tortuosity makes the elution peak less sharp in adsorption LC. This can be explained by the slowed mass transfer due to the extra time needed for molecules to travel inside the particles' pores when the travel path becomes more complicated. A median τ_{tor} value of 4 may be used for LC simulation. Another way to treat is to use it as an adjustable parameter for chromatogram fitting.

In Eq. (4.35), particle macropore diameter d_p is often supplied by vendors to allow users to judge whether the pore size is sufficiently large for a protein molecule to be separated. For example, some RP-HPLC media have 300-Å pore size according to vendors. The molecular diameter d_m in the equation can be calculated from the solute's MW using the semiempirical correlation below derived for hydrated proteins in water [3]:

$$d_m(\text{Å}) = 1.44(\text{MW})^{1/3} \qquad (4.36)$$

4.3.3 Biot Number Estimation

The Biot number for mass transfer (Bi) is defined as

$$\text{Bi} = \frac{kR_p}{\varepsilon_p D_p} \qquad (4.37)$$

which requires the film mass transfer coefficient (k). Two experimental correlations in the literature are suitable for the estimation of k in LC operations that typically have a very small Re number. One is the Wilson and Geankoplis empirical correlation [18],

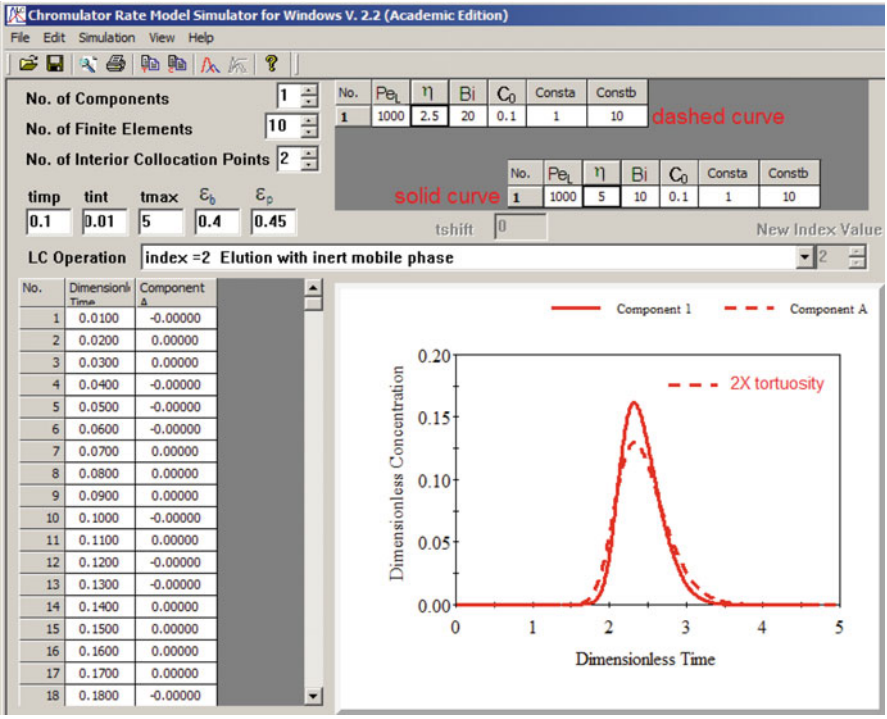

Fig. 4.2 Effect of particle tortuosity doubling (equivalent to doubling Bi while halving η values) on elution peak band spreading in adsorption LC

$$k = 0.687v^{1/3}\left(\varepsilon_b R_p/D_m\right)^{-2/3} \quad (0.0016 \le Re \le 55) \tag{4.38}$$

in which 0.687 is a dimensionless coefficient. Another one is the Kataoka et al. correlation [19] with a dimensionless coefficient of 1.165,

$$k = 1.165v^{1/3}\left(R_p/D_m\right)^{-2/3}[(1-\varepsilon_b)/\varepsilon_b]^{1/3} \quad Re/(1-\varepsilon_b) < 100 \tag{4.39}$$

Gu and Zheng demonstrated that these two k correlations deviate by only 6 % or less from each other for $0.25 < \varepsilon_b < 0.75$. Both correlations are based on experimental data with the latter one using additional datasets. There are additional correlations in the literature. One of them is the Carberry correlation [20], but it deviates significantly from experimental data when $Re/(1-\varepsilon_b)$ is smaller than 10 [19]. Thus, it is not suitable for LC operations. The Pfeffer correlation [21] yields a slightly larger k value compared with the Kataoka et al. correlation [19], but it is difficult to use.

Table 4.1 Microsoft excel formulas and calculation results for mass transfer parameters

A	*B*	*C*	*D*	
Raw data		Eq.	Results	1
MW	10,000			2
Q (ml/min)	1			3
L (cm)	10			4
Column diameter, d_c (cm)	1			5
Particle radius, R_p (cm)	0.01125			6
ε_b (bed voidage)	0.4			7
Particle tortuosity, τ_{tor}	4			8
Pore diameter, d_p (Å)	300			9
ε_p (particle porosity)	0.5			10
				11
Calculated				12
Bed volume, V_b (ml)	=(1/4) * PI() * B5 * B5 * B4		7.85398	13
v (cm/s) (interstitial)	=B3/60 * B4/(B13 * B7)	(4.11)	0.05305	14
Mol. diameter, d_m (Å)	=1.44 * B2^(1/3)	(4.36)	31.0239	15
λ (d_m/d_p)	=B15/B9		0.10341	16
D_m (cm^2/s)	=0.0000274 * B2^(–1/3)	(4.27)	0.000001272	17
D_p (cm^2/s)	=B17 * (1 – 2.104 * B16 + 2.09*B16^3 – 0.95 * B16^5)/B8	(4.35)	2.495006E–07	18
k (cm/s)	=0.687 * (B14^(1/3)) * ((B17/(B7 * B6))^(2/3))	(4.38)	0.0011116	19
Pe	=0.1 * B4/(B6 * B7)	(4.32)	222.22	20
η	=B10 * B18 * B4/(B6 * B6 * B14)	(4.34)	0.1858	21
Biot	=B19 * B6/(B10 * B18)	(4.37)	100.24	22
				23
τ to t conversion factor				24
L/v (min)	=B4/B14/60			25

In LC modeling, smaller variations in k may not produce any significant change in simulated chromatograms especially when Bi number is already much larger than 2, i.e., intraparticle diffusion control of the mass transfer process. The user can always perform a parameter sensitivity analysis to see whether a few percentages of variation in k will exhibit noticeable changes in simulated chromatograms. In this book, the Wilson and Geankoplis correlation is used for k. A spreadsheet program can easily be written to use the mass transfer correlations above to yield Peclet, η,

and Biot numbers for the LC models in this work. Readers may request a Microsoft Excel sheet from the author by e-mail. Table 4.1 is an example showing Excel formulas and a sample of calculated results. The third column shows the equations needed for the calculations. For verification, calculation results are listed in the fourth column. The online version of this chapter contains a supplement for the Microsoft Excel file.

4.4 Pre- and Postcolumn System Delay Volumes/Times

To simplify model formulation, LC models in this book assume that time zero is the moment a sample starts to enter the column inlet and the effluent is detected by a detector for its concentration determination the moment it exits the column. This means both pre- and postcolumn system delay times are assumed zero in modeling. This assumption is acceptable when the column volume is large or a solute has a large retention time due to strong binding because the system delay times will be relatively small. However, this is not true if the column volume is small such as in a case when a small column is used for parameter estimation [2]. If so, when a model-simulated chromatogram is used to match an experimental chromatogram after the dimensionless time has been converted to real time or elution volume, a peak in the simulated chromatogram will have a significantly shorter retention time because the experimental chromatogram records system delay times. Gu et al. showed how to measure the total system delay volume that is the sum of precolumn system delay volume and postcolumn system delay volume [2]. The total system delay volume is converted to the total system delay time using the flow rate. They used a column that had a zero column volume (i.e., the two plungers in their glass column touched each other). They integrated an acetone breakthrough curve for the estimation of the total system delay volume. The rational is that acetone breakthrough peak should take off vertically at time zero if there were no system delay because the column volume is zero. By calculating the area corresponding to the breakthrough takeoff delay (A_1 in Fig. 4.1), the total system volume and time can be calculated. These values can then be used to adjust the x-axis of a simulated chromatogram. They showed a case in which the total system delay was 1.10 ml, which was very significant compared with 2.39 ml that was the volume of the small column used in their parameter estimation.

References

1. Ruthven DM (1984) Principles of adsorption and adsorption processes. Wiley, New York
2. Gu T, Iyer G, Cheng K-SC (2013) Parameter estimation and rate model simulation of partial breakthrough of bovine serum albumin on a column packed with large Q Sepharose anion-exchange particles. Sep Purif Technol 116:319–326

3. Gu T, Zheng Y (1999) A study of the scale-up of reversed-phase liquid chromatography. Sep Purif Technol 15:41–58. doi:10.1016/S1383-5866(98)00083-5
4. Snyder LR, Cox GB, Antle PE (1988) Preparative separation of peptide and protein samples by high-performance liquid chromatography with gradient elution: I. The Craig model as a basis for computer simulations. J Chromatogr A 444:303–324. doi:10.1016/S0021-9673(01)94033-6
5. Jacobson J, Frenz J, Horváth C (1984) Measurement of adsorption isotherms by liquid chromatography. J Chromatogr A 316:53–68. doi:10.1016/S0021-9673(00)96140-5
6. Snyder LR, Kirkland JJ, Glajch JL (2012) Practical HPLC method development. Wiley, New York
7. Syu M-J, Tsai G-J, Tsao G (1993) Artificial neural network modeling of adsorptive separation. In: Tsao GT (ed) Chromatography. Springer, Berlin, pp 97–122
8. De Ligny CL (1970) Coupling between diffusion and convection in radial dispersion of matter by fluid flow through packed beds. Chem Eng Sci 25:1177–1181. doi:10.1016/0009-2509(70)85007-2
9. Langer G, Roethe A, Roethe KP, Gelbin D (1978) Heat and mass transfer in packed beds—III. Axial mass dispersion. Int J Heat Mass Transf 21:751–759
10. Giddings JC (1959) "Eddy" diffusion in chromatography. Nature 184:357–358
11. Polson A (1950) Some aspects of diffusion in solution and a definition of a colloidal particle. J Phys Chem 54:649–652
12. Geankoplis CJ (1993) Transport processes and unit operations. Prentice-Hall, Englewood Cliffs
13. Chung SF, Wen CY (1968) Longitudinal dispersion of liquid flowing through fixed and fluidized beds. AIChE J 14:857–866
14. Striegel A, Yau WW, Kirkland JJ, Bly DD (2009) Modern size-exclusion liquid chromatography: practice of gel permeation and gel filtration chromatography. Wiley, New York, p 84
15. Geankoplis CJ (1993) Drying of process materials. Transport processes and unit operations. Prentice-Hall, Englewood Cliffs, pp 520–583
16. Satterfield CN (1970) Mass transfer in heterogeneous catalysis. MIT Press, Cambridge, MA
17. Li Z, Gu Y, Gu T (1998) Mathematical modeling and scale-up of size-exclusion chromatography. Biochem Eng J 2:145–155. doi:10.1016/S1369-703X(98)00027-8
18. Wilson EJ, Geankoplis CJ (1966) Liquid mass transfer at very low Reynolds numbers in packed beds. Ind Eng Chem Fundam 5:9–14. doi:10.1021/i160017a002
19. Kataoka T, Yoshida H, Ueyama K (1972) Mass transfer in laminar region between liquid and packing material surface in the packed bed. J Chem Eng Jpn 5:132–136
20. Carberry JJ (1960) A boundary-layer model of fluid-particle mass transfer in fixed beds. AIChE J 6:460–463. doi:10.1002/aic.690060323
21. Pfeffer R (1964) Heat and mass transport in multiparticle systems. Ind Eng Chem Fundam 3:380–383. doi:10.1021/i160012a018

Chapter 5
Mass Transfer Effects in Liquid Chromatography Simulation

For analytical and some small preparative columns in LC, mass transfer resistance is usually negligible and the equilibrium theory suffices [1]. However, for preparative columns with smaller plate numbers and large-scale columns, mass transfer effects are often significant and usually cannot be neglected. The study of mass transfer effects for single-component systems has been carried out by many researchers [2]. For example, Lee et al. [3] studied the mass transfer effects in nonlinear multicomponent elution ion-exchange chromatography. They discussed the differences between a general rate model and the equilibrium theory under various mass transfer conditions.

5.1 Effects of Parameters Pe_L, Bi, and η

The Peclet number for axial dispersion (Pe_L) reflects the ratio of the convection rate to the dispersion rate, while the Biot number (Bi) reflects the ratio of the external film mass transfer rate to the intraparticle diffusion rate. Figures 5.1, 5.2, and 5.3 show that the increase of Pe_L values (while fixing other parameters) sharpens the concentration profiles in the effluent history in cases of frontal adsorption, elution, and step-change displacement. This well-known effect has been reported by numerous researchers and summarized by Ruthven [2]. Parameter values used for simulation in this chapter are listed in Table 5.1.

Figures 5.4, 5.5, and 5.6 show that increasing η or Bi also gives sharper concentration profiles. Increasing k will proportionally increase Bi according to Eq. (4.37), while Pe_L and η are not affected. Increasing D_p will proportionally increase η while proportionally decreasing Bi without affecting Pe_L. The net effect of increased η and decreased Bi results in a sharper elution peak as discussed in Fig. 4.2 previously. Clearly, mass transfer effects tend to diffuse concentration profiles when any of the three dimensionless mass transfer parameters decreases alone. It is well known that when Pe_L is large (e.g., 1,000 and above), further

© Springer International Publishing Switzerland 2015

T. Gu, *Mathematical Modeling and Scale-Up of Liquid Chromatography*,
DOI 10.1007/978-3-319-16145-7_5

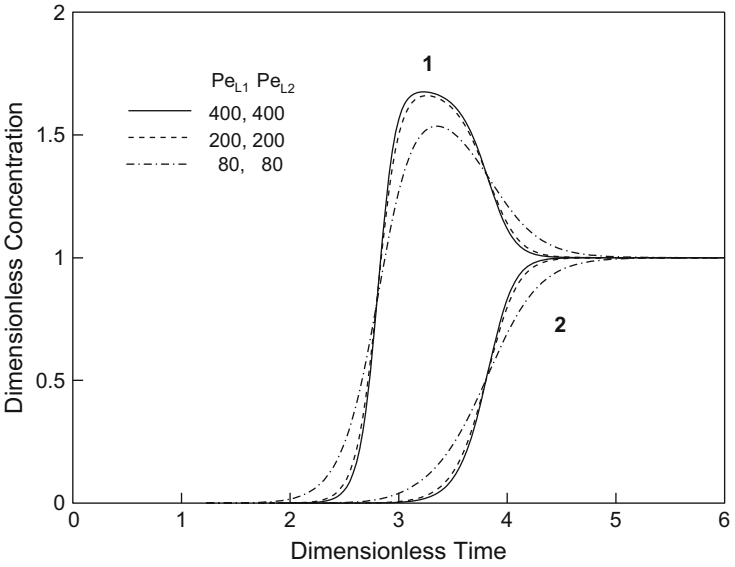

Fig. 5.1 Effect of Peclet numbers on two-component frontal adsorption

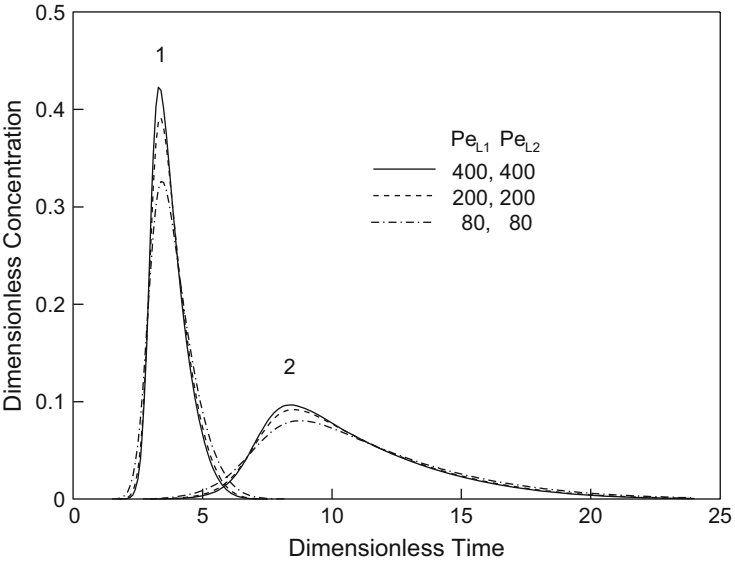

Fig. 5.2 Effect of Peclet numbers on two-component elution

increasing it will slow down the peak-sharpening effect, indicating a "saturation" behavior. This can be easily demonstrated using Chromulator 2.2. The other two parameters (Bi and η) also exhibit a similar "saturation" behavior when their numbers reach two digits.

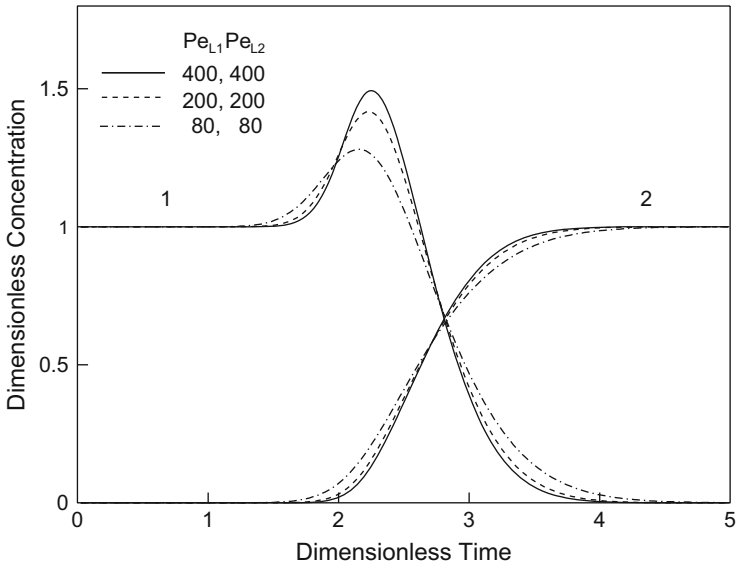

Fig. 5.3 Effect of Peclet numbers on two-component step-change displacement

Table 5.1 Parameter values used for simulation in this chapter[a]

Figure(s)	Species	Physical parameters					Numerical parameters	
		Pe_{Li}	η_i	Bi_i	a_i	$b_i \times C_{0i}$	N_e	N
5.1–5.3	1	400	5	4	5	5×0.2	15	2
	2	400	5	4	20	20×0.2		
5.4, 5.5	1	400			5	5×0.2	15	2
	2	400			20	20×0.2		
5.6	1	400			5	5×0.2	15	2
	2	400			5	5×0.4		
5.7	1	400			5	5×0.2	15	2
	2	400			20	20×0.2		
5.9	1	300	5	10		$\times 0.8$	10	2

[a]In all cases, $\varepsilon_b = \varepsilon_p = 0.45$. For elution cases the dimensionless sample sizes are $\tau_{imp} = 0.6$

5.2 Effect of Flow Rate

The volumetric mobile phase flow rate Q in an axial flow chromatography column is directly proportional to the interstitial velocity v as shown in Eq. (4.11). This velocity affects axial dispersion coefficient D_b and film mass transfer coefficient k values. Meanwhile, the intraparticle diffusivities D_p can be regarded as independent of v [4]. If molecular diffusivity contribution to axial dispersion is negligible, which is often true, Eq. (4.25) shows $D_b \propto v$. This relationship has been acknowledged by some researchers [5, 6]. Thus, Pe_L is independent of v based on Pe_L definition in Eq. (4.24). This is reflected by Eq. (4.32) as well.

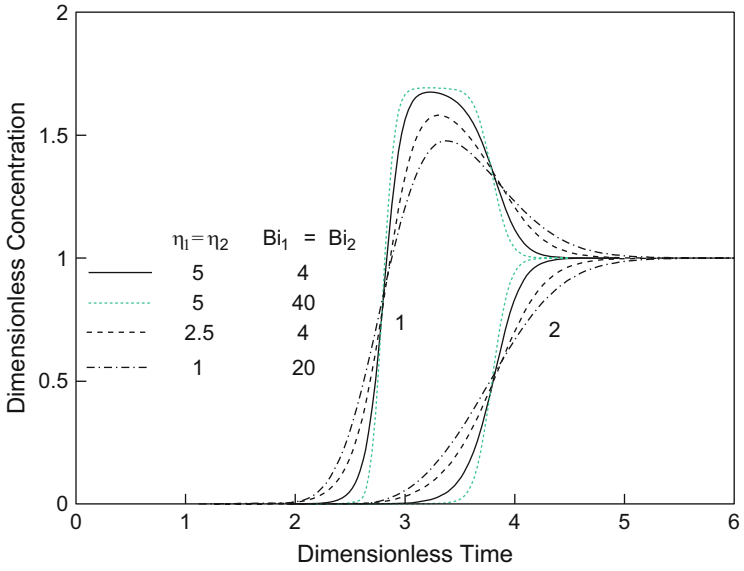

Fig. 5.4 Effect of η and Bi on binary frontal adsorption

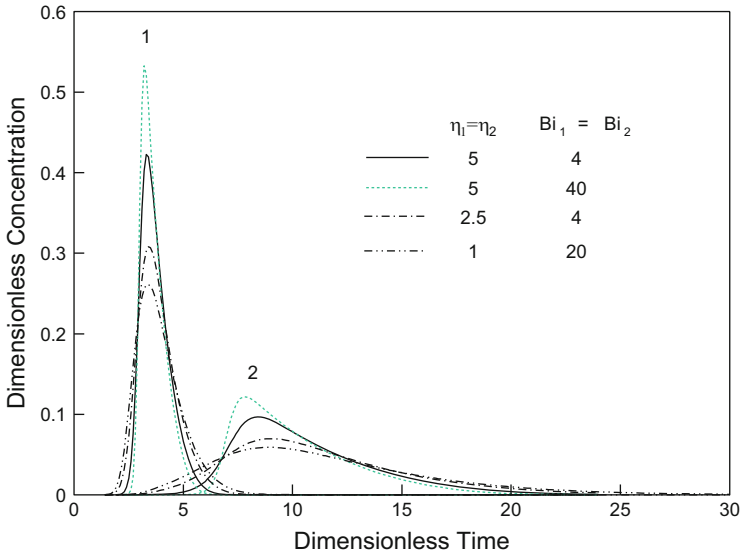

Fig. 5.5 Effect of η and Bi on binary elution

The relationship between k and v can be simply expressed as $k \propto v^{1/3}$ as shown in Eq. (4.38). It is in agreement with different experimental correlations reported by Pfeffer and Happel [7], Wilson and Geankoplis [8], and Ruthven [2] for liquid systems at low Reynolds numbers ($Re = 2R_p v\rho/\mu$) that cover the range for liquid

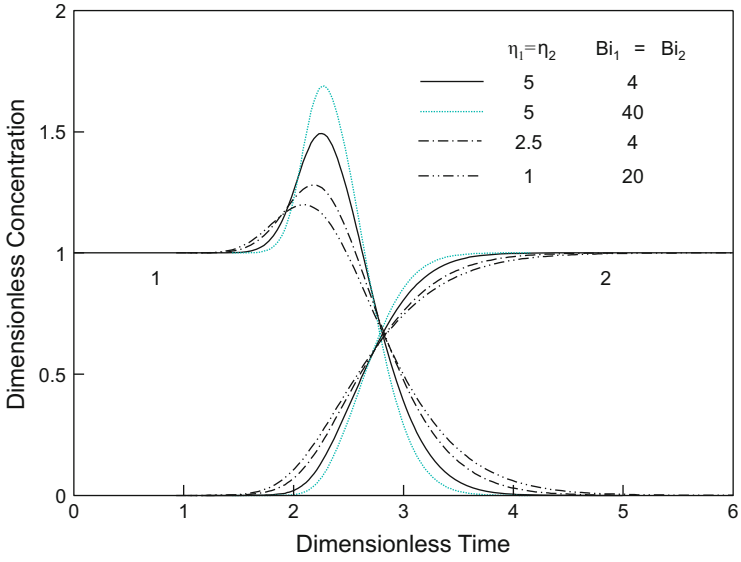

Fig. 5.6 Effect of η and Bi on binary step-change displacement

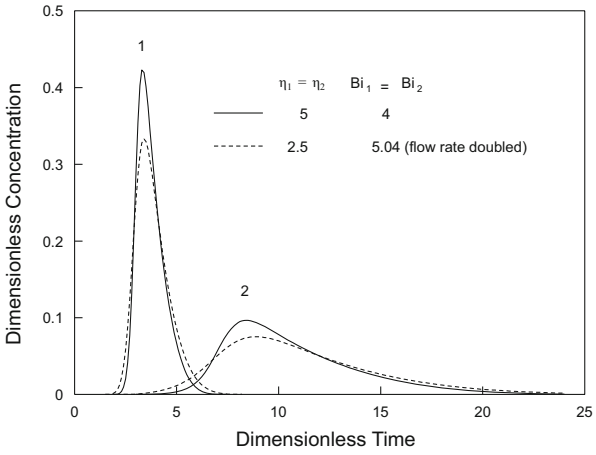

Fig. 5.7 Effect of interstitial velocity on binary elution

chromatography [9, 10]. The relationship $k \propto v^{1/3}$ further leads to $\text{Bi} \propto k \propto v^{1/3}$. It is easy to observe the changes in Pe_L, η, and Bi values following the change of flow rate or a different parameter by using the Microsoft Excel spreadsheet in Table 4.1.

Figure 5.7 clearly shows a case in which the sharpness and resolution of the elution peaks decrease when v is doubled (dashed lines). The values of η and Bi for both cases are listed in the legend of the figure. Due to doubling of v, η is halved, while Bi is increased by $2^{1/3}$. Note that the comparisons are based on the dimensionless time rather than dimensional time. The effect of increasing v is somewhat similar to that of decreasing D_{pi}, since both result in the increase of Bi_i and the

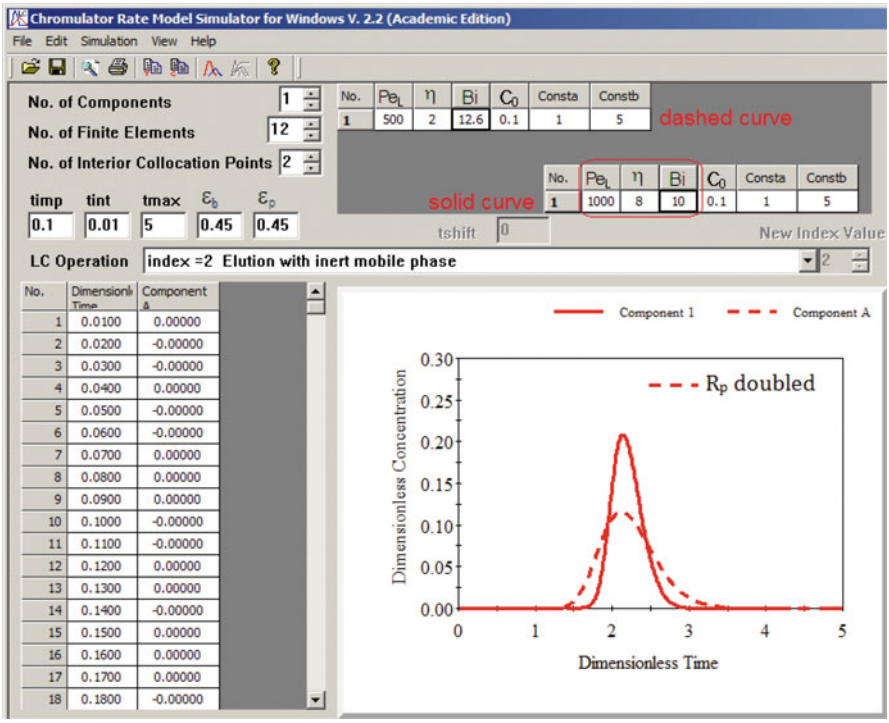

Fig. 5.8 Effect of doubling particle radius on elution

decrease of η_i. But the increase of v value reduces the sharpness and resolution of the peaks more severely because the increase of Bi_i values is smaller than that in the case of decreasing D_{pi} when v is doubled. Note that in Fig. 5.7, the dimensionless retention times are not affected by the changes in v. In the simulation of Fig. 5.7, τ_{imp} is kept the same. This means the t_{imp} is cut by half when v is doubled to keep the sample volume constant.

Bed voidage impacts Pe_L and v, while η is impacted by v. Bi is also impacted by v because v affects k. ε_b may be affected by particle size R_p. The relationship between ε_b and R_p is complicated when the particles are nonuniform, nonspherical, or deformed (e.g., for soft gel beads). In LC, due to the very small R_p to column diameter ratio, rigid particles with uniform R_p theoretically yield the same ε_b. Thus, for simplicity, in the parametric study for R_p, it is assumed that ε_b will not change significantly when R_p changes. It is also assumed that R_p will not impact D_p, which means the particle's inner structures such as porosity and tortuosity remain unchanged. Figure 5.8 shows that doubling the particle radius R_p makes a peak more diffused. Its definition suggests that

$$\eta \propto 1/R_p^2 \tag{5.1}$$

Equation (4.32) leads to

$$\mathrm{Pe_L} \propto 1/R_\mathrm{p} \tag{5.2}$$

The effect of R_p on Bi is more complicated because according to Eq. (4.38),

$$k \propto R_\mathrm{p}^{-2/3} \tag{5.3}$$

Plugging this relationship into the Bi definition in Eq. (4.37), one obtains

$$\mathrm{Bi} \propto R_\mathrm{p}^{1/3} \tag{5.4}$$

Thus, doubling R_p will reduce $\mathrm{Pe_L}$ by twofold while reducing η by fourfold. Doubling R_p will also increase Bi by a factor of $2^{1/3}$. With considerably decreased $\mathrm{Pe_L}$ and η and a slightly increased Bi, the net effect is a considerably more diffused peak with a longer tail when particle radius is doubled. This is a reason why smaller particles are used in analytical HPLC to improve mass transfer and to avoid maldistribution of flow at an increased cost and bed pressure. It should be stressed that in the simulation of Fig. 5.8, the effect of R_p on ε_b is ignored. If the particles are uniform and spherical, an increase in R_p will not change ε_b significantly when R_p is much smaller than the column diameter.

5.3 Effect of Mass Transfer in a Case with Unfavorable Isotherm

In elution chromatography, a peak's front is usually sharper than its rear boundary if the isotherm is in the nonlinear range and the isotherm is of favorable type, i.e., concave downward or $\partial^2 C_\mathrm{p}^*/\partial C_\mathrm{p}^2 < 0$, of which the Langmuir isotherm is a typical example. This is due to the well-known peak self-sharpening effect caused by favorable isotherms [11, 12].

Some adsorption systems, namely cooperative adsorption systems, have unfavorable isotherms. It was found that in elution, when the isotherm is of unfavorable type, a peak's front tends to get diffused and its rear boundary sharpened [11, 12]. Such a phenomenon has also been observed in experiments and is known in nonlinear chromatography. This is generally true for systems with fast mass transfer rates. For systems with slow mass transfer rates this may not be the case. Figure 5.9 shows that a single-component elution with an inert mobile phase gives a peak of anti-Langmuirian asymmetry. When k or D_p is decreased to some extent, the peak symmetry is reversed to that of Langmuir type. In Fig. 5.9, a parabolically shaped unfavorable isotherm is used for the simulation. This phenomenon of peak shape reversal due to mass transfer effects may be attributed to fact that the peak tail in the chromatogram stays inside the column longer and suffers from more diffusion than the peak front. In this case, it overcomes the effect of the unfavorable isotherm. An experimental proof should be helpful.

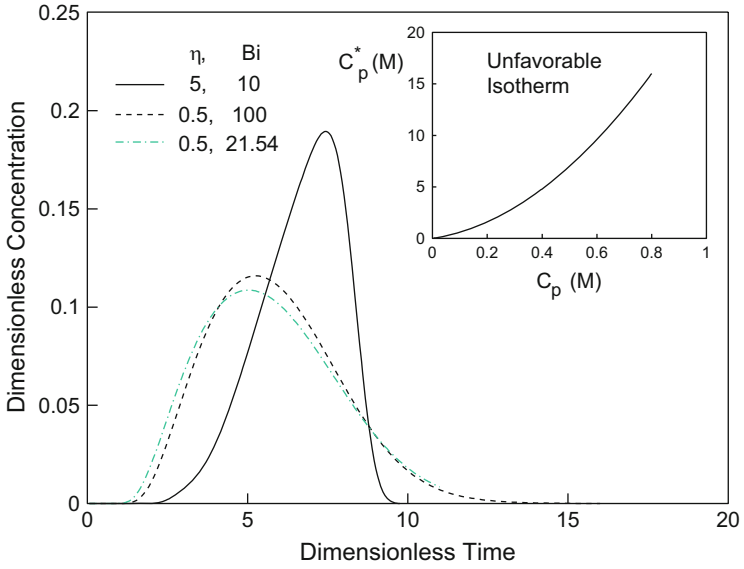

Fig. 5.9 Effect of mass transfer on an elution system with an unfavorable isotherm

References

1. Helfferich FG, Klein G (1970) Multicomponent chromatography: theory of interference. Marcel Dekker, New York
2. Ruthven DM (1984) Principles of adsorption and adsorption processes. Wiley, New York
3. Lee CK, Yu Q, Kim SU, Wang N-HL (1989) Mass transfer effects in isocratic non-linear elution chromatography. J Chromatogr A 484:29–59. doi:10.1016/S0021-9673(01)88961-5
4. Gu T, Tsai G-J, Tsao GT (1991) A theoretical study of multicomponent radial flow chromatography. Chem Eng Sci 46:1279–1288
5. Lee W-C (1989) PhD thesis. Purdue University, West Lafayette, IN
6. Weber SG, Carr PW (1989) The theory of the dynamics of liquid chromatography. In: Brown PR, Hartwick RA (eds) High performance liquid chromatography. Wiley, New York
7. Pfeffer R, Happel J (1964) An analytical study of heat and mass transfer in multiparticle systems at low Reynolds numbers. AIChE J 10:605–611. doi:10.1002/aic.690100507
8. Wilson EJ, Geankoplis CJ (1966) Liquid mass transfer at very low Reynolds numbers in packed beds. Ind Eng Chem Fund 5:9–14. doi:10.1021/i160017a002
9. Kaizuma H, Myers MN, Giddings JC (1970) Evaluation of coupling and turbulence by the dynamical comparison of gas and liquid chromatography. J Chromatogr Sci 8:630–634. doi:10.1093/chromsci/8.11.630
10. Horvath C, Lin H-J (1976) Movement and band spreading of unsorbed solutes in liquid chromatography. J Chromatogr A 126:401–420. doi:10.1016/S0021-9673(01)84088-7
11. Antia FD, Horváth C (1989) Operational modes of chromatographic separation processes. Berichte der Bunsengesellschaft für physikalische Chemie 93:961–968. doi:10.1002/bbpc.19890930907
12. Giddings JC (1965) Dynamics of chromatography. Part 1, Principles and theory. Marcel Dekker, New York

Chapter 6
Interference Effects in Multicomponent Chromatography

6.1 Introduction

For an isotherm such as the Langmuir isotherm, it becomes linear if the concentration range is sufficiently low. Each component's isotherm will be independent of the other components. There will be no competition among the components for binding sites. Analytical LC usually involves small or dilute samples. Components in the sample are quickly diluted and/or separated away from each other during migration inside a column. Thus, interference effects among different sample components are often negligible. With the rapid growth of biotechnology, preparative- and large-scale LC operations become more and more important. High-feed concentrations and large sample volumes are often used to increase productivity. In such cases, interference effects may no longer be ignored.

Systematic studies of the interference effects in the literature are based mostly on the equilibrium theory [1–4]. They assume a direct local equilibrium between the liquid phase and the stationary phase, and mass transfer effects are ignored. In this chapter, the general multicomponent rate model described in Chap. 3 is used to study the multicomponent interference effects. The model is able to describe some important phenomena such as roll-up in all the three major modes of chromatography (i.e., frontal, displacement, and elution) under mass transfer conditions. The use of the rate model that considers various mass transfer mechanisms gives a more accurate account and thus helps the visualization of the dynamics of the preparative- and large-scale chromatographic processes.

Tiselius [5] was the first to use the phrase "displacement effect" to describe the competition for binding sites in multicomponent elution. It will be shown in this chapter that the displacement effect is, in fact, the dominating effect in multicomponent interactions that are directly attributed to the competition for binding sites among different components, and this effect exists in all the three major LC operational modes with binding and dissociation. Many observed multicomponent interactions due to competitive adsorption can be satisfactorily

© Springer International Publishing Switzerland 2015

T. Gu, *Mathematical Modeling and Scale-Up of Liquid Chromatography*,
DOI 10.1007/978-3-319-16145-7_6

explained using this simple concept. Although a few systems exist with synergistic (cooperative) isotherms [1] where the presence of other solutes enhances adsorption, the competitive isotherms are the most common type in practical LC operations [6].

6.2 Computer Simulation and Discussion

The general rate model presented in Chap. 3 with the multicomponent Langmuir isotherm for adsorption LC is used to study the interference effects here. The conclusions in most cases can be readily extended to multicomponent systems with other types of competitive isotherms. For comparison and simplicity, the component mixing effect on physical properties, such as diffusion and mass transfer coefficients, is ignored. All computer simulations have been carried out using the RATE model simulator's "index 6" and "index 7" operations. Parameter values used for simulations are listed in Table 6.1, or mentioned during discussions.

6.2.1 Displacement Mode

The displacement effect is most noticeable in displacement chromatography. Figure 6.1 (solid lines) shows a simulated chromatogram (effluent history) of a step-change displacement process in which component 2 (displacer) is introduced via a step change at $\tau = 0$ to a column presaturated with component 1. A roll-up peak appears in the concentration profile of component 1, which is a clear indication of the displacement effect. This phenomenon is corroborated by the experimental chromatogram for L-phenylalanine adsorption and displacement by ethanol on a β-cyclodextrin column in Fig. 6.2 (replotted with data from [7]). In Fig. 6.1, The concentration profile of component 1 is sharpened compared with the dashed line that represents the corresponding desorption operation when only an inert mobile phase is used to "wash out" component 1 from the column. In other words, the use of a displacer reduces tailing and thus concentrates component 1. This is also evident in Fig. 6.3 that shows a simulated chromatogram of a binary displacement system, in which components 1 and 2 are introduced to the column via a frontal adsorption lasting $\tau_{\text{imp}} = 4.0$ before component 3 (displacer) is pumped into the column. In this volume overload case, component 2 has two peaks, between which the roll-up peak is due to the displacement effect from the displacer (component 3). Such a concentrating effect has been proven by experiments carried out by Helfferich [8]. In Fig. 6.3, there is also a roll-up peak for component 1 as a result of the displacement effect from component 2. The first smaller component 2 peak should not be mistaken as a displacement band of a separate component.

Competition can be viewed as a mutual interaction. The displaced component, while being displaced, in return also exerts some influence on the displacer.

Table 6.1 Parameter values used for simulation in this chapter[a]

Figure(s)	Species	Physical parameters					Numerical parameters	
		Pe_{Li}	η_i	Bi_i	a_i	$b_i \times C_{0i}$	N_e	N
6.1	1	300	10	6	3	6×0.1	16	2
	2	300	15	8	2	4×0.4		
6.3	1	200	10	10	2	2×0.2	25	1
	2	200	10	10	30	30×0.2		
	3	200	10	10	80	80×0.24		
6.4, 6.5	1	300	1	20	1	2×0.1		
	2	300	1	20	10	20×0.1	8	2
	3	300	1	20	20	40×0.1		
6.6	1	300	1	20	1	20×0.1	8	2
	2	300	1	20	10	200×0.1		
6.7	1	300	30	8	1	10×1	18	1
	2	400	40	7	4	40×0		
	3	500	90	6	9	90×0.1		
6.8	1	300	40	10	0.4	0.8×0.1	12	1
	2	350	50	9	4	8×0.1		
6.9	1	300	40	10	2	4×0.1	11	1
	2	350	50	9	4	8×0.1		
6.10	1	300	30	8	4	10×0.1	20	1
	2	400	40	7	16	40×0.1		
	3	500	90	6	36	90×0.1		
6.12	1	300	40	10	0.4	0.8×0.1	14	1
	2	350	50	9	4	8×0.1		
	3	350	50	9	10	20×0.1		

[a]In all cases, $\varepsilon_b = 0.4$ and $\varepsilon_p = 0.5$. For elution cases, $\tau_{imp} = 0.1$, or mentioned otherwise

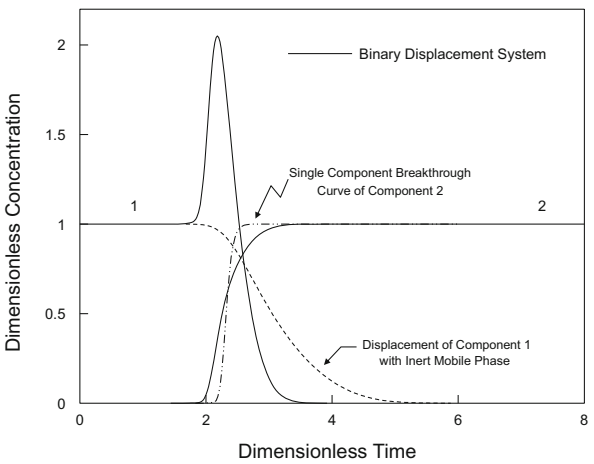

Fig. 6.1 Two-component step-change displacement process

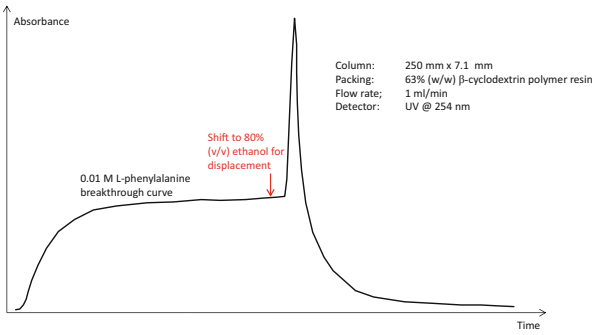

Fig. 6.2 Breakthrough and displacement curves for L-phenylalanine on a column packed with β-cyclodextrin-containing resins

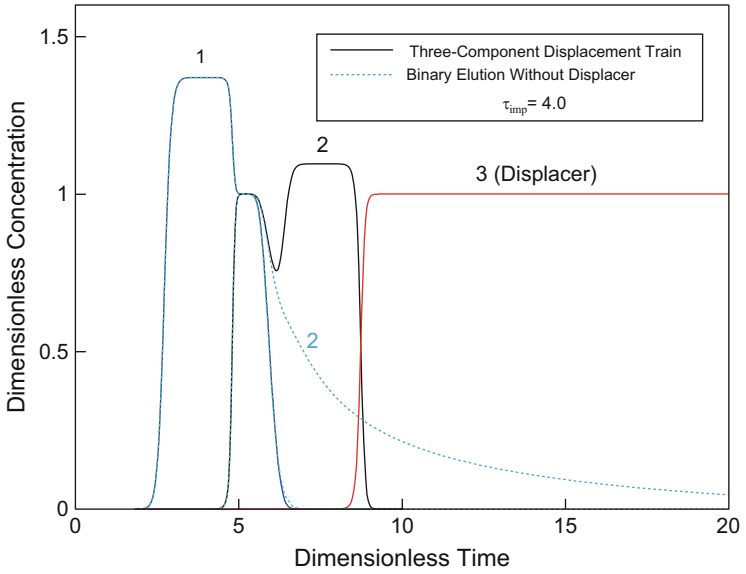

Fig. 6.3 Three-component displacement system

Figure 6.1 illustrated that the concentration front of the displacer is diffused by component 1 in the displacement process. The concentration profile of component 2 is actually its breakthrough curve under the interference of component 1. As compared with the breakthrough curve of pure component 2 (double-dotted line in Fig. 6.1), the concentration front of component 2 becomes diffused due to the influence of component 1.

The concentrating effect and roll-up phenomenon in displacement chromatography with negligible mass transfer effects have been predicted by the ideal theories including the interference theory [1, 9–12]. The general model presented here describes the roll-up phenomenon under mass transfer conditions.

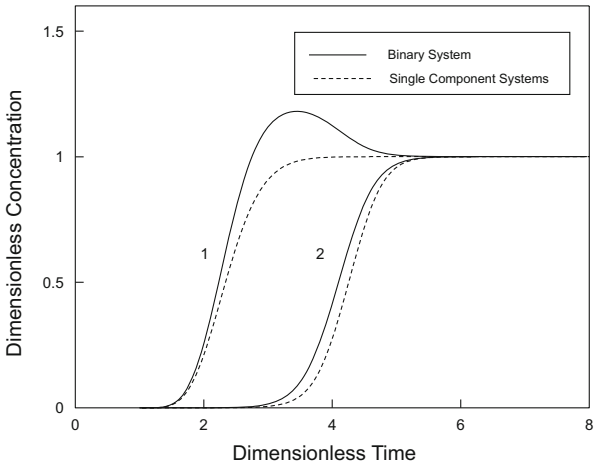

Fig. 6.4 Binary frontal adsorption with a roll-up peak

6.2.2 Frontal Adsorption Mode

Figure 6.4 shows a simulated chromatogram of a binary frontal adsorption process, in which component 1 has a weaker affinity than component 2 ($b_1 < b_2$). The concentration profile of component 1 reaches a maximum that is larger than its feed concentration before leveling off. This roll-up phenomenon is the result of a displacement effect. The concentration front of component 1, which has a weaker affinity, migrates faster than the concentration front of component 2 inside the column. Component 1 takes advantage of the relative absence of component 2 and initially occupies a disproportionate share of binding sites. When the concentration front of component 2 catches up, it displaces some portion of component 1 from the stationary phase such that the concentration of component 1 may exceed its feed value causing the roll-up. The column finally reaches adsorption equilibrium, and each component occupies its share of binding sites according to the governing multicomponent isotherms. Experimental observations and simulations for the roll-up in frontal adsorption with mass transfer effects have been reported by many researchers [3, 13–20].

A comparison of the breakthrough curves of the binary system and their corresponding pure component breakthrough curves in Fig. 6.4 indicates earlier breakthrough for both components in the binary system. This suggests that the dimensionless holdup capacity of each component in the column is lower compared to the corresponding pure component case.

Figure 6.5 shows a ternary system in which a third component, which has a stronger affinity than the other two, is added to the binary system shown in Fig. 6.4. Two roll-up peaks appear and, by the same token, they can be explained by the displacement effect. The last component, which has the strongest affinity, does not roll-up in any isothermal frontal adsorption case. It is worthwhile to note that the component in the middle (component 2) displaces component 1, while it is displaced by component 3.

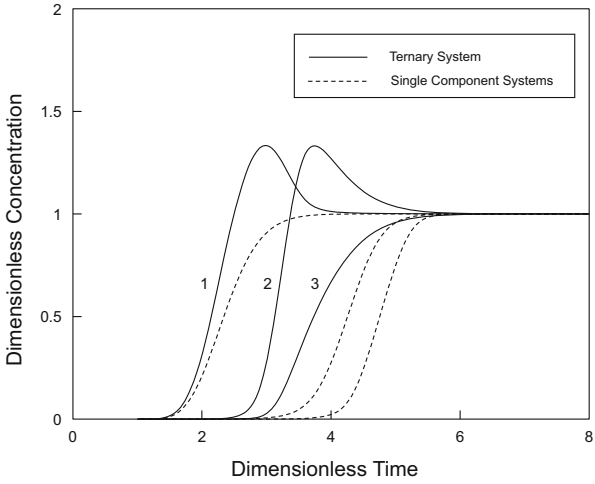

Fig. 6.5 Ternary frontal adsorption with two roll-up peaks

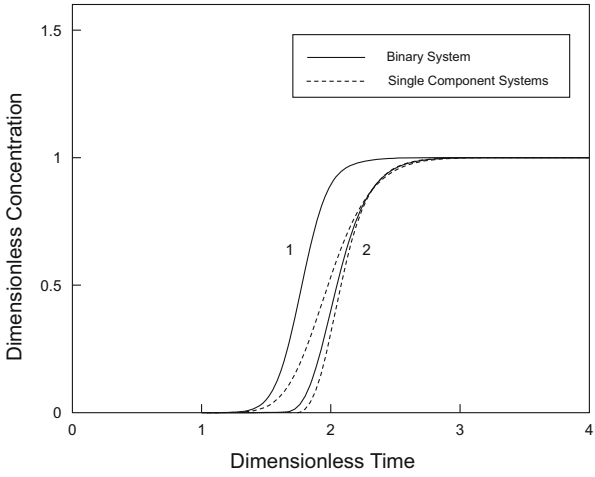

Fig. 6.6 Binary frontal adsorption with no roll-up peak

Roll-up peaks do not always exist or are noticeable in frontal adsorptions, especially when the saturation capacities of the components are low, or the components have very similar physical properties. Figure 6.6 has the same conditions as Fig. 6.4, except that its b_i values are ten times of those for Fig. 6.4; thus, the saturation capacity ($C_i^{\infty} = a_i/b_i$) values for Fig. 6.6 are 1/10 of those for Fig. 6.4. In Fig. 6.6, the roll-up phenomenon is not noticeable, but the displacement effect is still evident.

6.2.3 Elution Mode

Multicomponent elution with an inert mobile phase results in a shortened retention time for each component (Fig. 6.7). The retention times here are based on the first

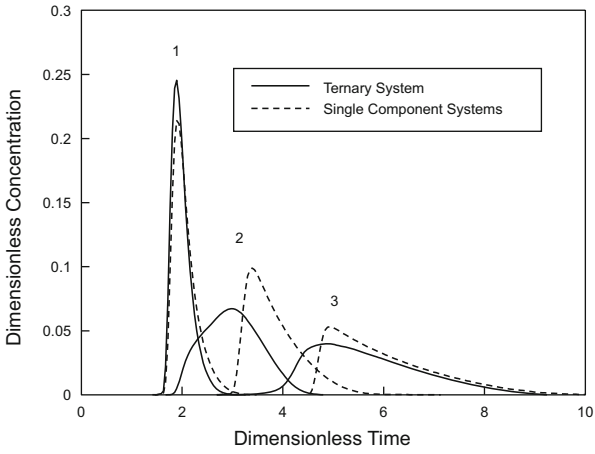

Fig. 6.7 Ternary elution

moments rather than the positions of peak maxima. The peak height of component 1, which has a weaker affinity than component 2, is increased, indicating that less band spreading occurs as compared with the corresponding single-component case. For the component 2 peak, its front is diffused and tail reduced. Conversely, the peak height of component 3 is significantly decreased and its front is severely diffused.

These observations again can be explained by the displacement effect. When the three components are migrating inside the column with different speeds depending primarily on their adsorption affinities, they separate from each other. Since component 2 has a higher affinity than component 1, it travels behind and displaces and concentrates component 1, thus reducing the tail of the component 1 peak. This results in a slightly shorter retention time, a larger peak height, and less band spreading for component 1. The displacement effect in such a case has been mentioned by other researchers [5, 11].

Mutual displacement causes the portion of component 2 that is in the mixing zone with component 1 to migrate faster than for the single-component case inside the column, while the unmixed portion of component 2 migrates with the same speed as the single-component case. This causes the diffusion of the front of the component 2 peak. In comparison, the displacement effect of component 3 on component 2 reduces the tail of the component 2 peak. In return, component 2 diffuses the front of the component 3 peak. Since component 3 elutes last, the tail's end-point hardly changes as compared to its single-component case. The effect of surrounding components is further illustrated by component 2 in Fig. 6.7 where the diffusion effect of component 1 reduces the peak height of component 2, while the displacement effect of component 3 tends to do the opposite. Therefore, the net effect of these two influences will determine the relative peak height of component 2.

The influence of the displacement effect on nonlinear multicomponent elution is summarized in Table 6.2, with the understanding that the effects listed in the table may not always be noticeable depending on the severity of the displacement effect.

Table 6.2 Summary of multicomponent elution (compared with single-component elutions)

Peak position in chromatogram	Retention time (first moment)	Peak height	Front flank	Tailing
First peak	Decreases	Increases	Sharpens	Decreases
Middle peak(s)	Decreases	Increases or decreases	Diffuses	Decreases
Last peak	Decreases	Decreases	Diffuses	[a]

[a]The tail end-point does not change much while the tail may become flatter (see Figs. 6.7 and 6.9)

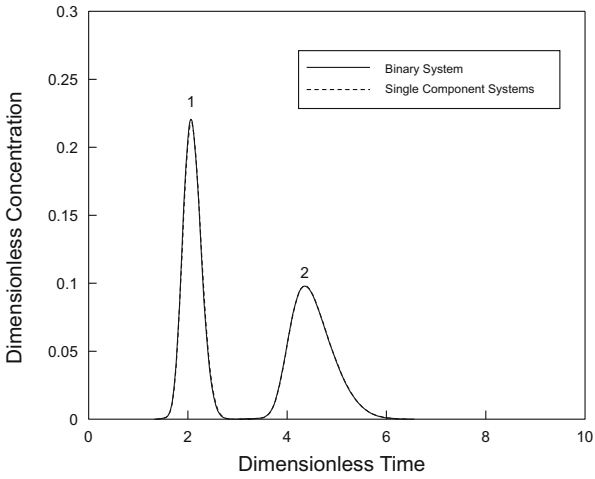

Fig. 6.8 Binary elution showing almost no displacement effect

The severity of the displacement effect depends on the level of competition among all the components and the nonlinearity of the system. In multicomponent elution, five factors have impacts on the displacement effect.

6.2.3.1 Adsorption Equilibrium Constants

As the values of b_i increase, the nonlinearity of the Langmuir isotherm and the competition for binding sites also increase. This escalates the displacement effect. If the values of b_i in a binary elution system are similar, the contact time between the two components is maximized as they migrate through the column and separate from each other. This increases the displacement effect. Figure 6.8 has the same conditions as Fig. 6.9, except that in Fig. 6.9, the affinity of component 1 (b_1) is larger, thus closer to that of component 2 (see Table 6.1). Compared with Fig. 6.8, the displacement effect in Fig. 6.9 is obviously more pronounced as evidenced by the increased differences between the solid lines and dashed lines. Note that in both Figs. 6.8 and 6.9, molar-based $C_i^{\infty}(= a_i/b_i)$ values are kept the same for both components as required by the thermodynamic consistency of the Langmuir isotherm.

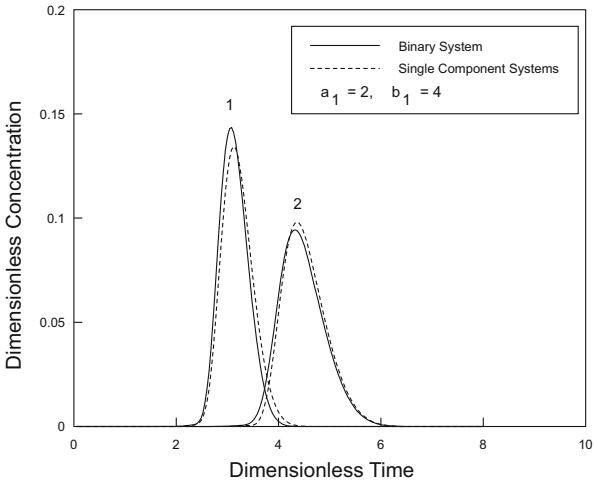

Fig. 6.9 Binary elution with increased a_1 and b_1 values

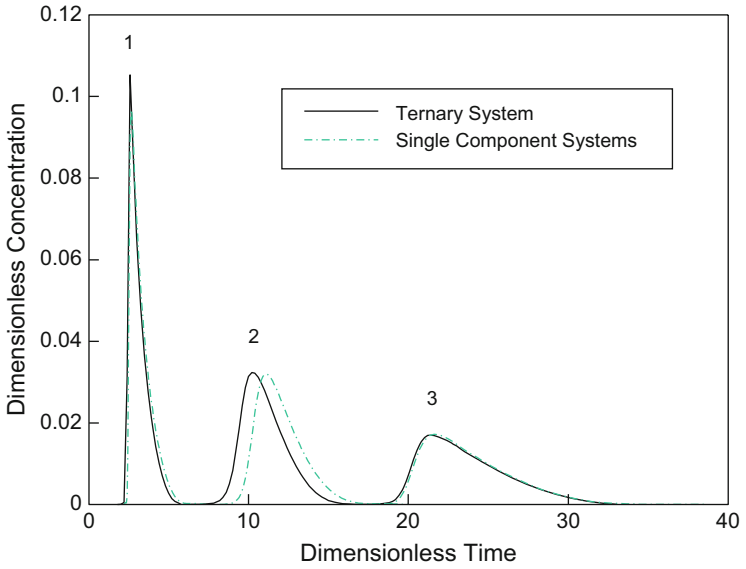

Fig. 6.10 Ternary elution with increased saturation capacity

6.2.3.2 Low Adsorption Saturation Capacity

A lower saturation capacity means fewer binding sites, and often increased competition for binding sites, especially in a system with large b_i values. In Fig. 6.7, a system with a small saturation capacity $\left(C_i^{\infty}\right)$ was used in order to show a case with pronounced displacement effects. Figure 6.10 is obtained from Fig. 6.7 by

increasing the values of a_i for the three components by fourfold. The displacement effect is more noticeable in Fig. 6.7 than in Fig. 6.10.

6.2.3.3 High Sample Feed Concentration (Concentration Overload)

Increasing C_{0i} is equivalent to increasing b_i and reducing C_i^{∞} proportionally, as is shown by the isotherm expression, Eqs. (3.21a) and (3.21b). Thus, the displacement effect escalates when the feed concentrations of the sample are increased.

6.2.3.4 Large Sample Size (Volume Overload)

When a large sample size is used, the contact time between the components will increase, thus making the displacement effect more noticeable. Figures 6.8 and 6.11 have the same conditions except that in Fig. 6.11, the sample size ($\tau_{\text{imp}} = 2.5$) is much larger than that in Fig. 6.8 ($\tau_{\text{imp}} = 0.1$). The first half of the effluent history in Fig. 6.11 actually represents the concentration profiles of the frontal adsorption curves with a roll-up peak, due to severe volume overload.

The use of large sample sizes in elution is becoming more common. In order to promote column throughput, the column is often overloaded in terms of either sample size or sample concentration [21–25]. Overload generally increases the nonlinearity of the system and thus the displacement effect.

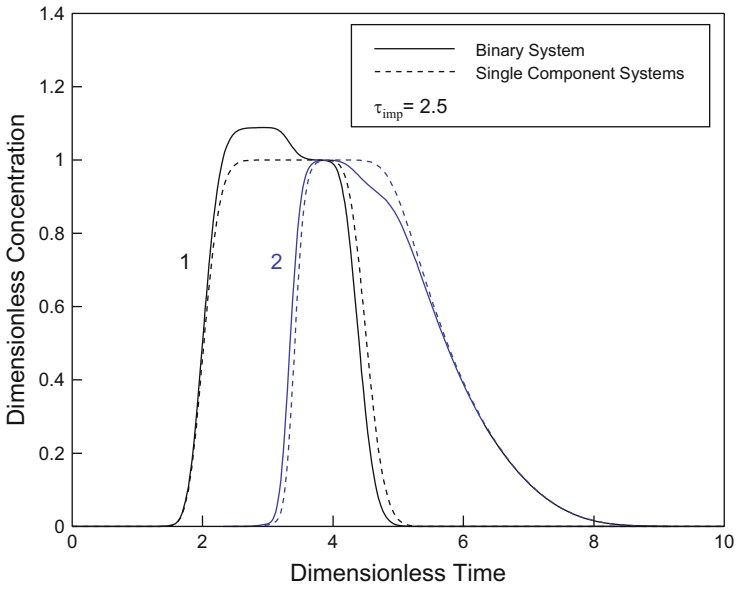

Fig. 6.11 Binary elution with a large sample size

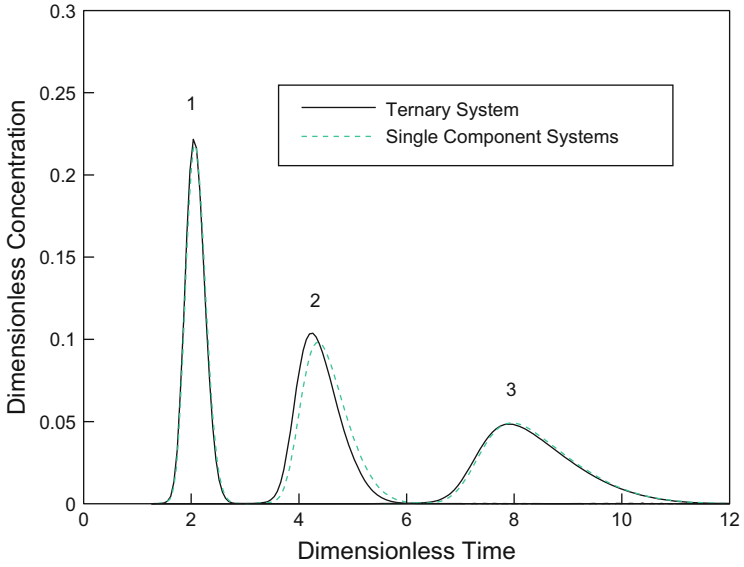

Fig. 6.12 Effect of an added component in the sample

6.2.3.5 More Component(s)

Adding more component(s) in the sample will increase the competition for binding sites among components. It also increases the nonlinearity of the isotherms, thus escalating the displacement effect. The increased displacement effect in Fig. 6.12 is obtained by adding one more component to the case presented in Fig. 6.8.

When an additional component is present as a competing modifier in the mobile phase, the displacement effect becomes rather complicated. The peaks corresponding to the concentration profile of the modifier in a chromatogram are often referred to as system peaks, which will be discussed in Chap. 7.

6.3 Summary

For multicomponent LC involving competitive isotherms, the dominating interference effect can be attributed to the displacement effect, which occurs not only in the displacement mode but also in the other two major modes of chromatography: frontal and elution. Five factors that may escalate the displacement effect in elution chromatography have been investigated. In short, these five factors either promote competition for binding sites among components or prolong such competition, or both. From a mathematical point of view, these factors can be interpreted as being able to either increase or prolong the nonlinearity of the isotherms. It has also been

shown that roll-up exists not only in frontal adsorption and displacement but also in elution. It has been demonstrated that the displacement effect tends to reduce peak tails of the displaced components, while the concentration front of the displacer's peak is diffused by the displaced components in all the three major modes of chromatography.

The use of a general nonlinear multicomponent rate model allows a systematic study of interference effects in multicomponent LC. The model accounts for various diffusional and mass transfer effects. The graphical representation of the results aids the visualization of multicomponent interactions and thereby promotes a better understanding of the primary causes of the interference effects. The discussion presented here may also be useful in the optimization of LC separation processes.

References

1. Helfferich FG, Klein G (1970) Multicomponent chromatography: theory of interference. Dekker, New York
2. Rhee H-K, Aris R, Amundson NR (1970) On the theory of multicomponent chromatography. Philos Trans R Soc Lond A Math Phys Sci 267:419–455
3. Rhee H, Amundson NR (1974) Shock layer in two solute chromatography: effect of axial dispersion and mass transfer. Chem Eng Sci 29:2049–2060
4. Yu Q, Yang J, Wang N-HL (1987) Multicomponent ion-exchange chromatography for separating amino acid mixtures. React Polym Ion Exch Sorbents 6:33–44. doi:10.1016/0167-6989(87)90205-4
5. Tiselius A (1940) A new method for adsorption analysis of solutions. Ark Kemi Mineral Geol 14B:1
6. Wankat PC (1986) Large-scale adsorption and chromatography. CRC Press, Boca Raton, FL
7. Gu T (1990) Inclusion chromatography using cyclodextrin-containing resins and studies of nonlinear chromatographic theories. Purdue University, West Lafayette
8. Helfferich F (1962) Ligand exchange. II. Separation of ligands having different coordinative values. J Am Chem Soc 84:3242–3245
9. Ruthven DM (1984) Principles of adsorption and adsorption processes. Wiley, New York
10. Glueckauf E (1949) Theory of chromatography. Part VII. The general theory of two solutes following non-linear isotherms. Discus Faraday Soc 7:12–25
11. Antia FD, Horváth C (1989) Operational modes of chromatographic separation processes. Ber Bunsenges Phys Chem 93:961–968. doi:10.1002/bbpc.19890930907
12. Tiselius A (1943) Displacement development in adsorption analysis. Ark Kemi Mineral Geol 16A:1
13. Santacesaria E, Morbidelli M, Servida A, Storti G, Carra S (1982) Separation of xylenes on Y zeolites. 2. Breakthrough curves and their interpretation. Ind Eng Chem Process Des Dev 21:446–451
14. Carra S, Santacesaria E, Morbidelli M, Storti G, Gelosa D (1982) Separation of xylenes on Y zeolites. 3. Pulse curves and their interpretation. Ind Eng Chem Process Des Dev 21:451–457
15. Liapis AI, Rippin DWT (1978) The simulation of binary adsorption in activated carbon columns using estimates of diffusional resistance within the carbon particles derived from batc. Chem Eng Sci 33:593–600. doi:10.1016/0009-2509(78)80021-9
16. Gu T, Tsao GT, Tsai G-J, Ladisch MR (1990) Displacement effect in multicomponent chromatography. AIChE J 36:1156–1162

17. Gu T, Tsai G-J, Tsao GT (1991) Multicomponent adsorption and chromatography with uneven saturation capacities. AIChE J 37:1333–1340
18. Thomas WJ, Lombardi JL (1971) Binary adsorption of benzene-toluene mixtures. Trans Inst Chem Eng 49:240
19. Hsieh JSC, Turian RM, Tien C (1977) Multicomponent liquid phase adsorption in fixed bed. AIChE J 23:263–275. doi:10.1002/aic.690230308
20. Liapis AI, Litchfield RJ (1980) Ternary adsorption in columns. Chem Eng Sci 35:2366–2369
21. Eble JE, Grob RL, Antle PE, Snyder LR (1987) Simplified description of high-performance liquid chromatographic separation under overload conditions, based on the Craig distribution model. III. Computer simulations for two co-eluting bands assuming a Langmuir isotherm. J Chromatogr A 405:1–29
22. Pieri G, Piccardi P, Muratori G, Cavallo L (1983) Scale-up for preparative liquid-chromatography of fine chemicals. Chim Ind 65:331–336
23. Giddings JC (1965) Dynamics of chromatography. Part 1. Principles and theory. Dekker, New York
24. Bauman WC, Wheaton RM, Simpson DW (1956) Ion Exclusion. In: Nachod FC, Schubert J (eds) Ion exchange technology. Academic, New York
25. Eble JE, Grob RL, Antle PE, Snyder LR (1987) Simplified description of high-performance liquid chromatographic separation under overload conditions, based on the Craig distribution model. I. Computer simulations for a single elution band assuming a Langmuir isotherm. J Chromatogr A 384:25–44

Chapter 7
System Peaks in Multicomponent Elution

7.1 Introduction

In isocratic elution chromatography, a modifier is often added to the mobile phase in order to compete with sample solutes for binding sites in the stationary phase [1]. This helps to reduce the retention time and band spreading of the sample solutes.

Peaks attributed to the modifier in an elution chromatogram are called system peaks [2–4]. A positive system peak, which is above the baseline value of the modifier concentration, is called a displacement peak [5, 6]. A negative one, which is below the baseline value, is called a vacancy peak [6]. Solms et al. [5] used a plate model to simulate three cases of single-component elution with a mobile phase containing a competing modifier. Another group of researchers [7, 8] simulated binary elutions with a competing modifier using a semi-ideal model with nonlinear multicomponent Langmuir isotherms. They also performed experiments that qualitatively proved some of their model predictions.

Two different types of samples are used for elution chromatography with the mobile phase containing a modifier. The first type, named Type I sample in this chapter, consists of those samples that are prepared by dissolving sample solutes in a solution that has the same composition as the mobile phase; thus the feed stream to the column contains the competing modifier with a constant concentration. This kind of system is a strictly isocratic elution process if the modifier concentration in the feed is constant. Modeling of system peaks with Type I samples was first carried out by Solms et al. [5]. The second type of sample, Type II sample, consists of those samples that are prepared based on an inert (blank) solution, i.e., the samples contain no modifier. In such cases, system peaks have different patterns from those with Type I samples because of the deficit of a modifier introduced during the sample injection. Experiments with both types of samples were carried out by Levin and Grushka [4]. They also investigated elution systems containing more than one modifier in the mobile phase.

© Springer International Publishing Switzerland 2015

T. Gu, *Mathematical Modeling and Scale-Up of Liquid Chromatography*,
DOI 10.1007/978-3-319-16145-7_7

This chapter extends the previous theoretical studies in the literature on elution chromatography with a competing modifier, which has a constant concentration in the mobile phase, using the general rate model for adsorption observing the Langmuir isotherm described in Chap. 3. The effect of modifier on the elution performance of binary-solute systems with a Type I or Type II sample will be studied, and system peak patterns will be summarized for both cases. Binary elution with two modifiers in the mobile phase will also be briefly discussed.

7.2 Boundary Conditions for the General Rate Model

The modifier is treated as one of the components in the governing equations of the rate model. The multicomponent Langmuir isotherm is used, in which the modifier is considered as one of the competing components.

The following boundary conditions are needed for the modifier. For a modifier in systems with Type I sample,

$$C_{\mathrm{fi}}(\tau)/C_{0i} = 1. \tag{7.1}$$

For a modifier in systems with Type II sample,

$$C_{\mathrm{fi}}(\tau)/C_{0i} = \begin{cases} 0 & 0 \le \tau \le \tau_{\mathrm{imp}} \\ 1 & \text{else} \end{cases} \tag{7.2}$$

7.3 Results and Discussion

The RATE model module for adsorption LC with a Langmuir isotherm is used for simulation in this chapter to study system peaks. Parameter values used for simulation are listed in Table 7.1, or mentioned during discussions. Since the competing modifier is considered as a competing component in the multicomponent Langmuir isotherm, a binary elution with a competing modifier in the mobile phase constitutes a three-component system. The last component is designated as the modifier in the simulation parameters.

7.3.1 Modifier Is Weaker Than Sample Solutes

Figure 7.1 (solid lines) shows a simulated effluent history (chromatogram) of a binary elution with Type I sample and a competing modifier (component 3) in the mobile phase. Components 1 and 2 are the two sample solutes. The binding affinity of the modifier (with the stationary phase) is smaller than those of the sample components. For a multicomponent Langmuir isotherm with the same molar

Table 7.1 Parameter values used for simulation in Chap. 7[a]

Figure(s)	Species	Physical parameters					Numerical parameters	
		Pe_{Li}	η_i	Bi_i	a_i	$b_i \times C_{0i}$	N_e	N
7.1 and 7.2	1	300	8	20	5	2.5×0.2	8	2
	2	400	9	12	10	5×0.2		
	3	350	9.5	9	2	1×0.1		
7.3 and 7.4	1	300	8	20	5	2.5×0.2	8	2
	2	400	9	12	10	5×0.2		
	3	350	9.5	9	7	3.5×0.1		
7.5 and 7.6	1	300	8	20	5	2.5×0.2	7	2
	2	400	9	12	10	5×0.2		
	3	350	9.5	9	20	10×0.1		
7.7	1	300	8	20	5	2.5×0.2	8	2
	2	400	9	12	10	5×0.2		
	3	350	9.5	9	40	20×0.1		
7.8	1	300	8	20	5	2.5×0.2	8	2
	2	400	9	12	10	5×0.2		
	3	350	9.5	9	100	50×0.1		
7.11, 7.12, and 7.13	1	300	8	20	5	5×0.4	9	2
	2	300	8	20	20	20×0.4		
	3	300	8	20	40	40×0.2		
7.15	1	300	8	20	5	2.5×0.2	8	2
	2	400	9	12	6.6	3.3×0.2		
	3	350	9.5	9	2	1×0.1		
7.16	1	300	8	20	1	0.5×0.2	9	2
	2	400	9	12	10	5×0.2		
	3	350	9.5	9	100	50×0.1		
7.17	1	300	8	20	5	2.5×0.2	8	2
	2	400	9	12	6.6	3.3×0.2		
	3	350	9.5	9	7	3.5×0.48		
7.19 and 7.20	1	200	6	9	6	3×0.25	8	2
	2	200	6	9	20	10×0.2		
	3	200	6	9	2	1×0.2		
	4	200	6	9	20	10×0.2		

[a]In all runs, $\varepsilon_p = \varepsilon_b = 0.4$ and $\tau_{imp} = 0.1$, unless specified otherwise

saturation capacity for all components, binding affinities of the components are reflected by their dimensionless $b_i \times C_{0i}$ values. Note that the scale for the modifier concentration shown in Fig. 7.1 (as well as in all other figures) is $(c_{b3} - 1)$. The actual baseline value for the modifier concentration is $(c_{b3} = 1)$. By transforming the baseline value to zero (i.e., $c_{b3} - 1 = 0$), the effluent history becomes more presentable. A negative system peak does not indicate negative concentrations, but rather concentration values that are below the baseline value.

The case shown in Fig. 7.1 gives one positive system peak and two negative system peaks that are due to the displacement effect of two sample solutes on the modifier. A mass balance of each species has been checked to evaluate the accuracy of the numerical solution. For the modifier, the numerical integration of the

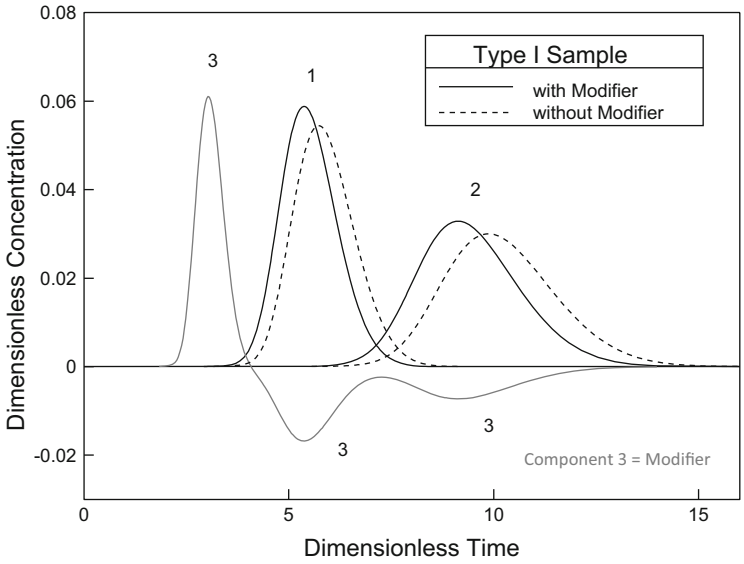

Fig. 7.1 Binary elution with a weak modifier (Type I sample)

concentration profile of the modifier ($c_{b3} - 1$) in Fig. 7.1, which consists of 400 data points, from $\tau = 1$ to $\tau = 15$ gives a value of 0.0000, which is in agreement with its theoretical value zero. For the sample solutes, mass balances are also satisfied.

Figure 7.1 (dashed lines) also shows the corresponding binary elution case in the absence of the modifier. It is evident that the use of a modifier results in the decrease of the retention time and the spreading of the band and the increase of peak height of each sample solute. Figure 7.2 shows an effluent history with a Type II sample. Other conditions for Fig. 7.2 are the same as in Fig. 7.1. It can be seen that in Fig. 7.2, there are three negative system peaks and no positive ones. The numerical integration of the concentration for the modifier (component 3) of the three system peaks over dimensionless time has been found to be -0.1000. This negative value indicates the deficit of the modifier introduced during sample injection. The deficit quantity is equivalent to the sample size, $\tau_{imp} = 0.1$. In Fig. 7.2, the peak at the front is a negative system peak, instead of a positive one shown in Fig. 7.1, because the large negative system peak induced by the deficit of the modifier during sample injection negates the positive system peak. This can be easily verified by examining the concentration profile of the modifier when a blank sample, which contains only an inert carrier liquid, is employed. This is shown in Fig. 7.2 (dashed line). It gives only a single large negative peak, and the peak area is found to be equal to the injection pulse size, $\tau_{imp} = 0.1$, by numerical integration.

Positive system peaks do occur involving a Type II sample, if the positive system peak overcomes the negative one due to sample introduction, as shown below. The number and direction (positive/negative, i.e., upward/downward) of

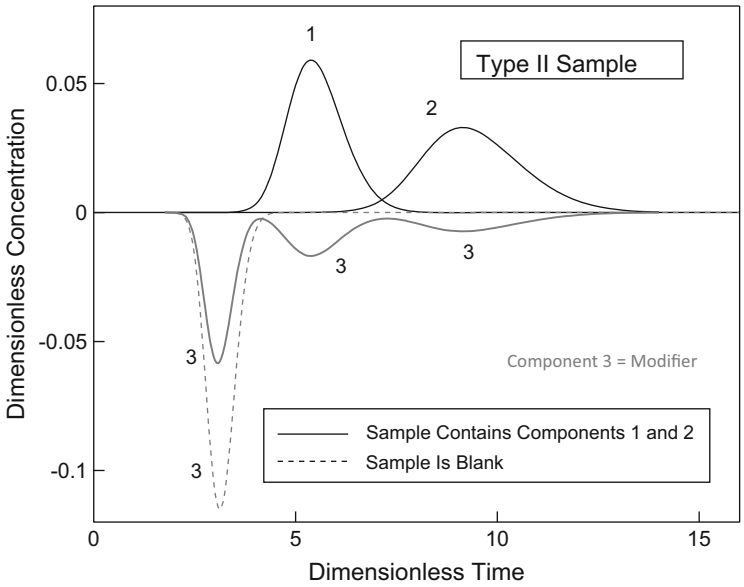

Fig. 7.2 Binary elution with a weak modifier (Type II sample)

system peaks for the modifier are determined primarily by the sample type and their relative affinity to those of the sample solutes and of course, the number of sample solutes.

7.3.2 Modifier Affinity Is Between Those of Sample Solutes

Figure 7.3 gives the effluent history for the case shown in Fig. 7.1 except that the affinity of the modifier is between those of the two sample solutes. Figure 7.3 shows one positive system peak and two negative ones, which are similar to those in Fig. 7.1. However, the retention time of the positive system peak is prolonged and the peak is sharpened. Both changes are due to the increase of the affinity of the modifier. Because of the increase, there are more modifier molecules adsorbed onto the stationary phase that can be dislodged by the sample solutes. If the modifier has no affinity to the column packing, its concentration profile will be flat. On the other hand, if the affinity of the modifier further increases, when its affinity is already not far from the leveling off range of the Langmuir isotherm, the increase of a modifier's loading in the stationary phase can be overshadowed by the affinity increase that could make it too difficult to be dislodged by the sample solutes. In such cases, the increase of modifier affinity may result in a reduced positive system peak at the front.

Figure 7.4 has the same conditions as Fig. 7.3, except that a Type II sample is used in Fig. 7.4. The effluent history shown in Fig. 7.4 gives one positive and two

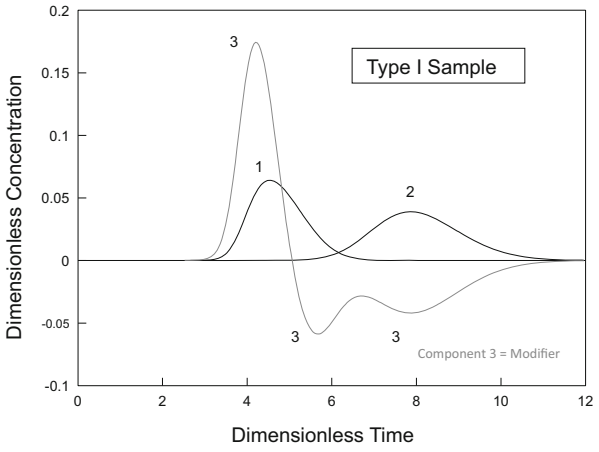

Fig. 7.3 Modifier affinity is between those of sample solutes (Type I sample)

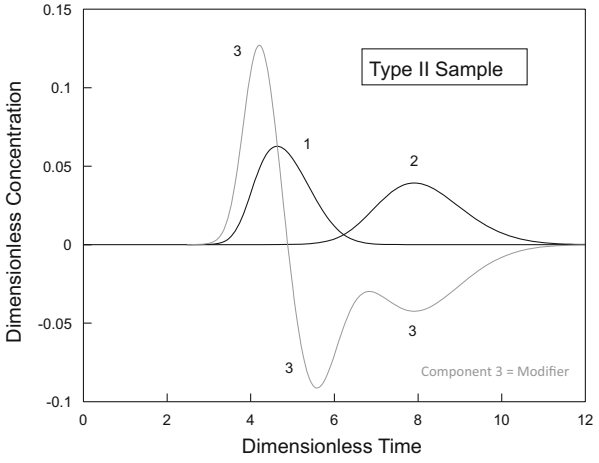

Fig. 7.4 Modifier affinity is between those of sample solutes (Type II sample)

negative system peaks, quite different from the case shown in Fig. 7.2, which has the same conditions as Fig. 7.4, except that Fig. 7.4 has a stronger modifier. This is because the displacement effects from components 1 and 2 cause a larger positive system peak, and it overcomes the negative system peak that is caused by the deficit of a modifier in the sample. The observation that the positive system peak in Fig. 7.4 is smaller than the one in Fig. 7.3 is in agreement with this argument.

7.3.3 Modifier Is Stronger Than Sample Solutes

Figure 7.5 shows a case in which the affinity of the modifier is stronger than both sample solutes. There are two positive system peaks and one negative one in the

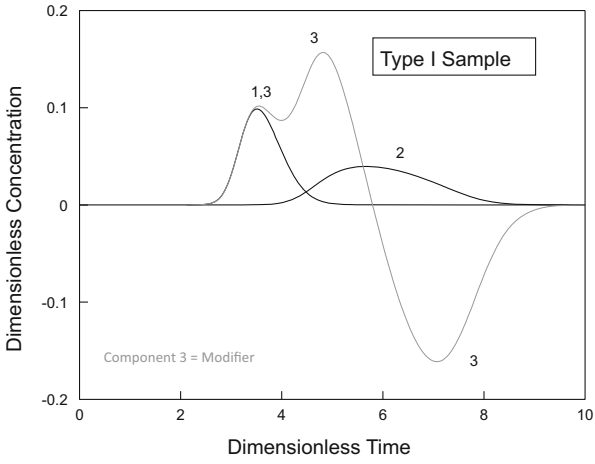

Fig. 7.5 Binary elution with a strong modifier (Type I sample)

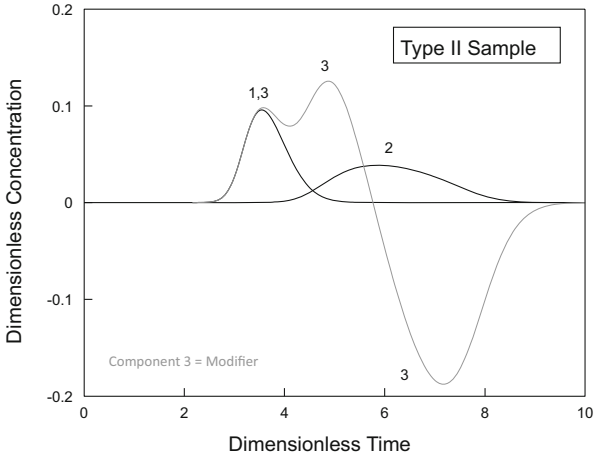

Fig. 7.6 Binary elution with a strong modifier (Type II sample)

figure. The first positive system peak partially overlaps with the component 1 peak, and it departs from the component 1 peak when the component 2 peak starts to take off. The corresponding case with a Type II sample is shown in Fig. 7.6 that gives a similar system peak pattern.

In Fig. 7.5, if the affinity of the modifier is further increased, the first positive system peak will no longer overlap the component 1 peak, as is shown clearly in Fig. 7.7. Figure 7.8 shows a degenerated case that is obtained by simply increasing the affinity of the modifier shown in Fig. 7.7 furthermore. It is obvious that the merger of two positive system peaks in Fig. 7.8 is due to the partial overlapping of the component 1 peak with the component 2 peak.

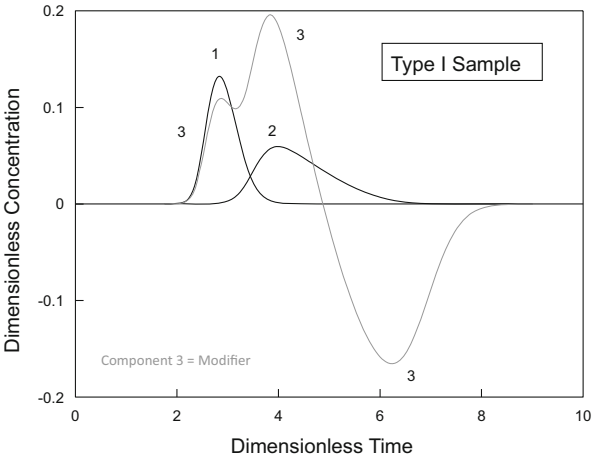

Fig. 7.7 Same conditions as Fig. 7.5, except that the modifier affinity is stronger

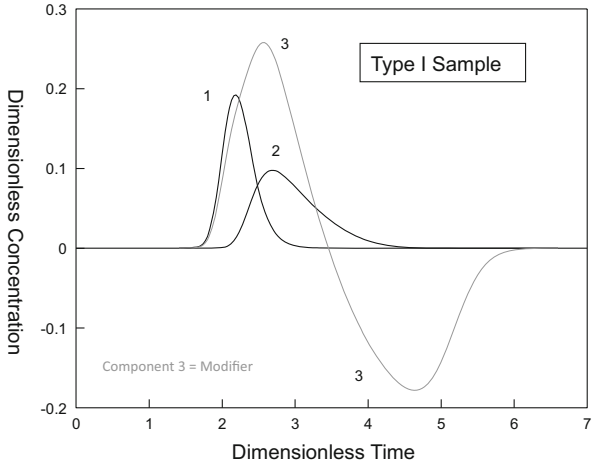

Fig. 7.8 Same conditions as Fig. 7.7, except that the modifier affinity is increased further

7.3.4 Effect of Modifier Concentration on System Peak Patterns

The modifier's concentration change actually results in the change of the modifier's affinity ($b_i \times C_{0i}$). In LC operations other than hydrophobic interaction chromatography, an increase in the modifier's concentration reduces the retention times of the sample solutes because the modifier competes with sample solutes for binding sites. It also affects system peaks. Figure 7.9 shows a case in which the modifier concentration is ten times higher than that in Fig. 7.3. Comparing Fig. 7.3 with Fig. 7.9, it can be seen that the system peaks in Fig. 7.9 are much smaller than those in Fig. 7.3. This means that the disturbance caused by the sample solutes to the concentration profile of the modifier becomes smaller if the concentration of the

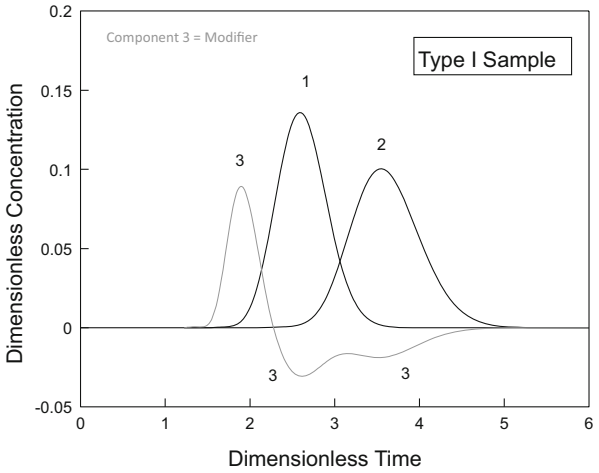

Fig. 7.9 Same conditions as Fig. 7.3, except higher modifier concentration ($C_{03} = 1.0$)

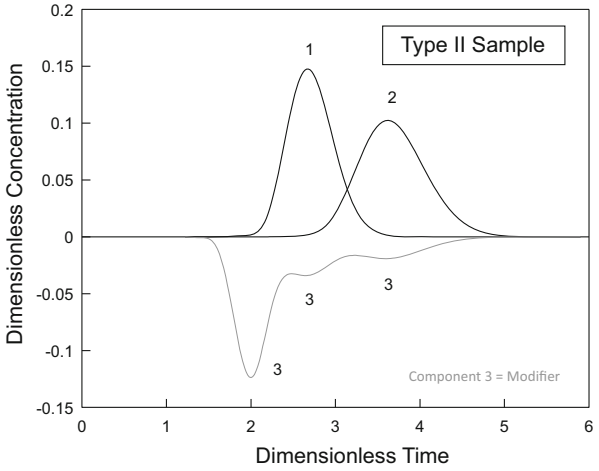

Fig. 7.10 Same conditions as Fig. 7.4, except higher modifier concentration ($C_{03} = 1.0$)

modifier increases. It also implies that if the modifier concentration is sufficiently large, its concentration in the system can be considered as a constant. This simplifies the simulation. Note that in all figures the concentration scale is dimensionless. Thus, a smaller peak does not necessarily mean a smaller dimensional concentration.

Figure 7.10 shows a case with a Type II sample, in which the modifier concentration is ten times higher than in Fig. 7.4. The increase in the modifier's concentration changes the first system peak from a positive one (Fig. 7.4) to a negative one (Fig. 7.10). The reversal of the peak direction occurs because when the modifier's concentration is increased the negative system peak, which is caused by the deficit of the modifier during sample injection, overcomes the positive system peak caused by the displacement effect from the sample solutes on the modifier.

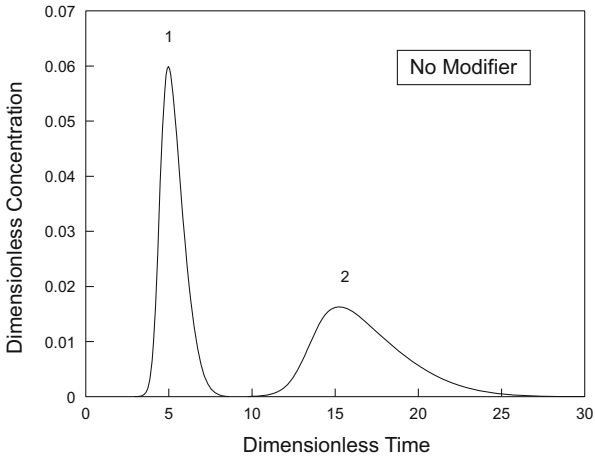

Fig. 7.11 Binary elution without modifier

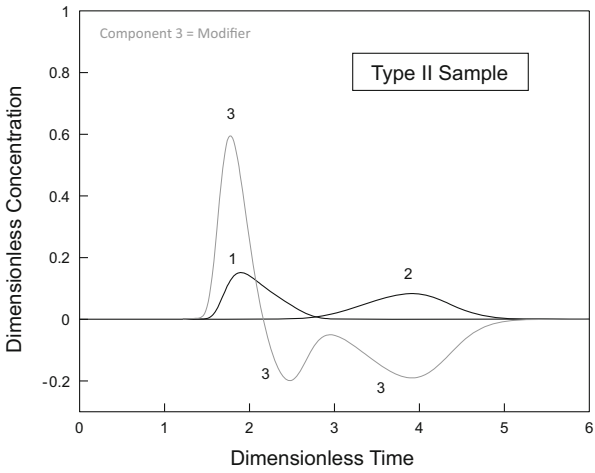

Fig. 7.12 Effect of an added modifier (Type II sample)

7.3.5 Effect of Modifier on Sample Solutes

The retention time and resolution of the two solute peaks are both unnecessarily high in Fig. 7.11 for a complete separation of the two components. Adding a proper modifier may reduce the process duration while still achieving a baseline separation. Figure 7.12 shows the effect of an added modifier. The baseline separation of the two sample solutes is achieved, while the elution duration is cut by four-fifths. The concentrations of the peaks are much higher and the band spreading of these peaks is largely reduced when the modifier is used. This is because of the displacement effect from the modifier. Figure 7.13 has the same conditions as Fig. 7.12, except that in Fig. 7.13 a Type I sample is employed. The result shown in Fig. 7.13 is similarly desirable.

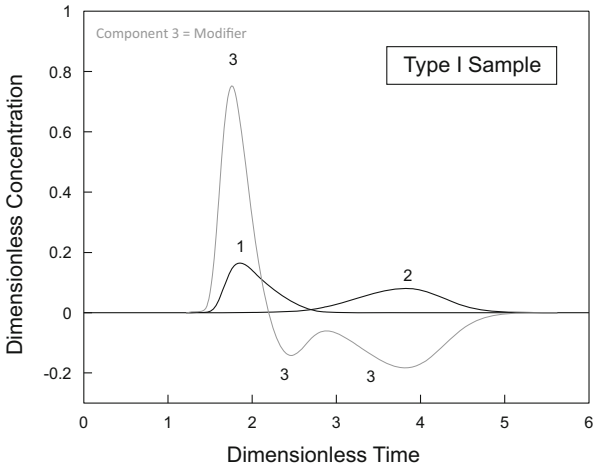

Fig. 7.13 Effect of an added modifier (Type I sample)

Figures 7.12 and 7.13 show that at low modifier concentration levels, the phenomenon of peak shape reversal also occurs if the adsorption equilibrium constant of the modifier (b_3) is high enough and the adsorption capacity is low. Interestingly, in the two figures, component 1 peak still retains its Langmuir-type peak shape, while the peak shape of component 2 becomes anti-Langmuirian type (i.e., tail is smaller than front flank).

7.3.6 Effect of Sample Type

The difference in the system peak pattern due to sample type is quite obvious. Sample type may affect the direction, size, and location of system peaks. These effects have been shown during the previous discussion. On the other hand, sample type also affects the elution pattern of sample solutes. By comparing some of the figures shown in this chapter, one may quickly find that the influence of sample type on sample solutes is usually quite small. This situation may change if the sample size is large. Figures 7.3 and 7.4 have the same conditions except the type of sample. The sample size in both cases is $\tau_{imp} = 0.1$. Their corresponding cases with $\tau_{imp} = 1.0$ are shown in Fig. 7.14. It is clear that the difference in the concentration profiles of the two sample solutes is not small when a large sample size is used.

7.3.7 Effect of Sample Solutes on the Modifier

In the discussion above, it has been pointed out that system peaks are the result of the displacement effects of the sample solutes on the modifier arising from

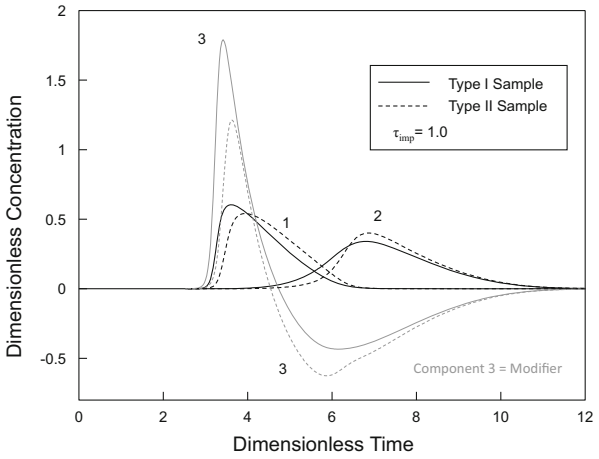

Fig. 7.14 Effect of type of sample at a large sample size

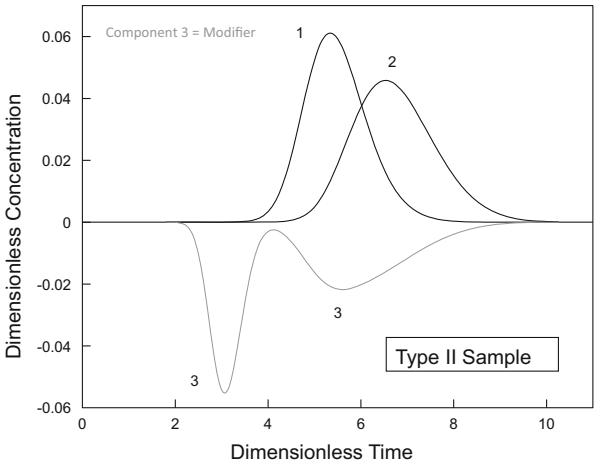

Fig. 7.15 Same conditions as Fig. 7.2, except that component 2 has a weaker affinity

competition for binding sites. This was also revealed by other researchers [5, 7]. If a Type II sample is used, the deficit of a modifier during sample introduction also plays a role that may cause a negative system peak at the front (Fig. 7.2) or reduce the size of the positive system peak at the front (Fig. 7.14). It may even negate the positive system peak (Fig. 7.15).

The relative affinities of sample solutes also affect system peaks as shown in Fig. 7.15. Figure 7.15 has the same conditions as Fig. 7.2, except that in Fig. 7.15 the affinity of component 2 is smaller, thus closer to that of component 1. Figure 7.15 (with a Type II sample) shows that when component 1 and component 2 peaks overlap to some degree, the two corresponding negative system peaks will degenerate into a single one. The comparison of Fig. 7.8 with Fig. 7.16 proves that a partial overlapping of the peaks for sample solutes may also cause the merger of positive system peaks.

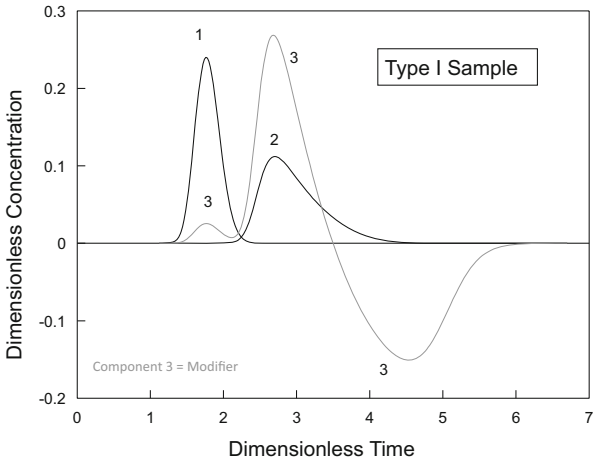

Fig. 7.16 Same conditions as Fig. 7.8, except that component 1 has a weaker affinity

Table 7.2 Possible system peak combinations in binary elutions

Sample	System peak combinations (positive peak(s)/negative peak(s))					
	I	II	III	IV	V	VI
Type I	1/2 (Fig. 7.1)	1/1 (Fig. 7.8)	2/1 (Fig. 7.5)			
Type II	0/3 (Fig. 7.2)	0/2 (Fig. 7.15)	0/1 (Fig. 7.17)	1/1 (Fig. 7.18)	2/1 (Fig. 7.6)	1/2 (Fig. 7.4)

7.3.8 Summary of System Peak Patterns

Table 7.2 summarizes all possible combinations of system peak patterns for binary elutions with a competing modifier. There are twice as many combinations for cases with a Type II sample than those with a Type I sample. This table also gives indications for system peak combinations in a single-component elution since degenerated cases are included in the table. It is interesting to point out that Fig. 7.17 gives a severely degenerated case in which the overlapping of the peaks of components 1 and 2 causes the degeneration of their corresponding negative system peaks. The positive displacement peak and the peak that is due to the deficit of a modifier during sample introduction negated each other. Figure 7.18 has the same conditions as Fig. 7.17, except that the modifier concentration is $C_{0i} = 0.1$ mol/L, which is lower than that in Fig. 7.17. Because of the decrease in the modifier's concentration, the previously degenerated peak (in Fig. 7.17) becomes very prominent in Fig. 7.18.

In general, both sample types, I and II, can have a maximum of only three system peaks for binary elutions with one competing modifier. For binary elutions with a Type I sample, the minimum number of system peaks should be two because the existence of a positive system peak necessitates a negative system peak in order to meet the mass balance, which requires the sum of peak areas of positive system peaks equal the sum of peak areas of negative system peaks. On the other hand, this

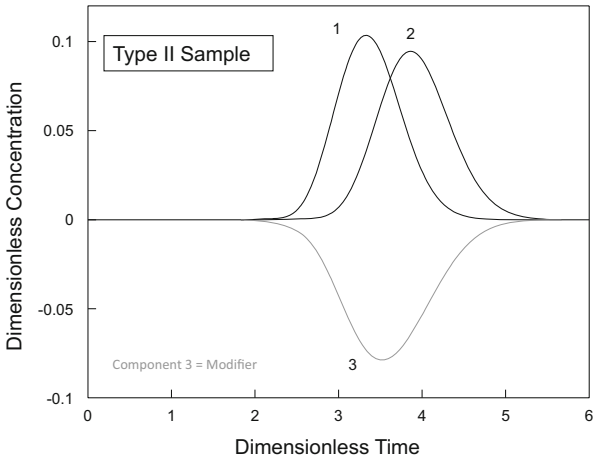

Fig. 7.17 Binary elution showing only one system peak (Type II sample)

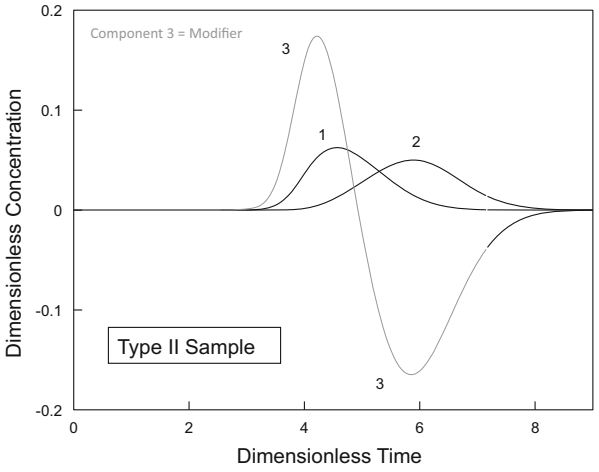

Fig. 7.18 Binary elution showing two system peaks, one positive and one negative

requirement does not apply to cases with a Type II sample. In such cases, the minimum number of system peaks is one as shown in Fig. 7.17.

7.3.9 Binary Elution with Two Different Modifiers

As the discussion above indicates, system peak behavior can be very complex and elusive. The situation can be further complicated if there is more than one modifier in the mobile phase. In practice, multiple modifier cases are not rare. Experiments by Levin and Grushka [4] showed that each modifier gave a different set of system peaks.

Figure 7.19 shows a case involving two sample solutes (components 1 and 2) and two different modifiers (components 3 and 4). The first modifier (component 3) has

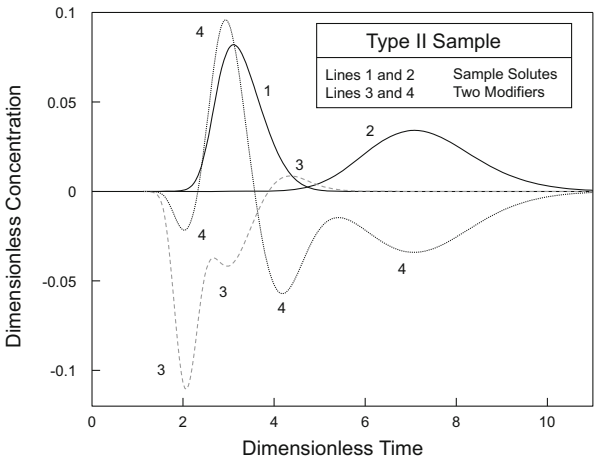

Fig. 7.19 Binary elution with two modifiers (Type II sample)

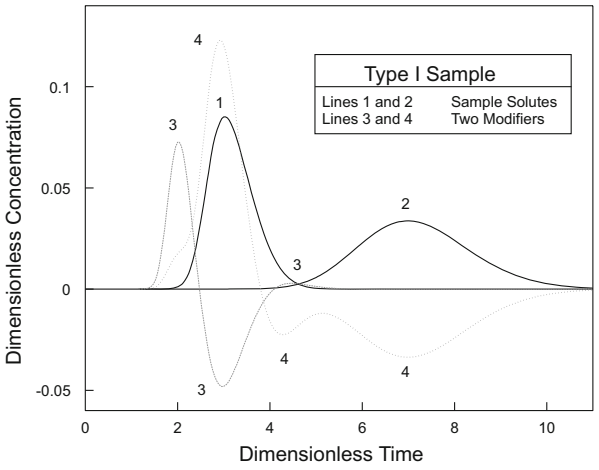

Fig. 7.20 Binary elution with two modifiers (Type I sample)

a weaker affinity than the second modifier (component 4). Figure 7.20 has the same conditions as Fig. 7.19, except that a Type I sample is employed. There is a positive system peak at the tail of the concentration profile of the first modifier (component 3) in both figures. This kind of tail has never been observed in simulations for single modifier systems. Its presence is likely due to the involvement of a second modifier in the system.

7.4 Concluding Remarks

The interrelationship between sample solutes and the modifier(s) in elution chromatography has been investigated through computer simulation using a general rate model. It has been concluded that for binary elutions with one competing modifier

in the mobile phase, there are three system peak patterns if Type I samples are used, and six if Type II samples are used. In addition, a binary elution system with two different competing modifiers has been discussed briefly.

This study shows that system peaks can be very complex and may not be fully explained by qualitative arguments, although the ultimate cause behind system peaks may be simply attributed to the displacement effect due to the competitive nature of the isotherms involving all the components in the system including the modifier, and the deficit of a modifier during sample introduction if a Type II sample is used.

In gradient elutions, the modifier's concentration can be continuously changed during the elution process. The situation in gradient elutions is more complicated since the modifiers used in gradient elutions usually cannot be considered as competing with sample solutes for binding sites. They can actually change the binding affinities of the sample solutes with the stationary phase, which is a much more efficient mechanism for the retention time control. The mutual interaction is quite complex. System peaks are especially noticeable in IEC involving the stoichiometric mass action isotherm. In Chap. 13, some simulated ion-exchange chromatograms clearly show system peaks.

References

1. Snyder LR, Kirkland JJ, Glajch JL (2012) Practical HPLC method development. Wiley, New York
2. Dreux M, Lafosse M, Pequignot M (1982) Separation of inorganic anions by ion-pair, reverse phase liquid chromatography monitored by indirect photometry. Chromatographia 15:653–656. doi:10.1007/BF02279494
3. Cassidy RM, Fraser M (1984) Equilibria effects in the dynamic ion-exchange separation of metal ions. Chromatographia 18:369–373. doi:10.1007/BF02262483
4. Levin S, Grushka E (1987) System peaks in liquid chromatography: their relation to the adsorption isotherm. Anal Chem 59:1157–1164. doi:10.1021/ac00135a019
5. Solms DJ, Smuts TW, Pretorius V (1971) Displacement peaks in liquid elution chromatography. J Chromatogr Sci 9:600–603
6. McCormick RM, Karger BL (1980) Role of organic modifier sorption on retention phenomena in reversed-phase liquid chromatography. J Chromatogr A 199:259–273. doi:10.1016/S0021-9673(01)91378-0
7. Golshan-Shirazi S, Guiochon G (1989) Theoretical study of system peaks and elution profiles for large concentration bands in the case of a binary eluent containing a strongly sorbed additive. J Chromatogr A 461:1–18. doi:10.1016/S0021-9673(00)94271-7
8. Golshan-Shirazi S, Guiochon G (1989) Experimental study of system peaks and elution profiles for large concentration bands in the case of a binary eluent containing a strongly sorbed additive. J Chromatogr A 461:19–34. doi:10.1016/S0021-9673(00)94272-9

Chapter 8
Modeling and Scale-Up of Size-Exclusion Chromatography

Size-exclusion chromatography (SEC) is ubiquitous in the downstream processing of a protein product in modern biotechnology. It is also known as gel filtration chromatography because its separation mechanism relies on the differences in molecular size and shape of solutes, and the separation media are often soft gels. Large molecules elute out of an SEC column first because they cannot penetrate small macropores in particles. Small molecules elute out of an SEC column later because it takes time for them to diffuse in and out of small macropores. In gradient elution of reverse phase, affinity, ion-exchange, or hydrophobic interaction LC, the feed volume can be many times of the column volume [1–3] due to the fact that the gradient operation has a concentrating effect. Because SEC separation does not rely on any binding, gradient elution using an eluitor in the mobile phase to elute out the solutes in the sample is not applicable. Thus, peak bands will invariably diffuse over time due to a lack of any concentrating effect. This means the feed loading volume can only be a small fraction of column volume, leading to the need for very large SEC columns in industrial separations [4–6]. In fact, in the separation of a small molecule from a large molecule, such as in solvent exchange or desalting SEC operations, the feed volume may be up to several percent of the column volume [7], while only a fraction of a percent is possible for the purification of different proteins because protein separation is more difficult [4]. Soft gels are less expensive and thus cost-effective in large-scale SEC [8]. One drawback of soft gels is that scale-up of SEC has to often increase column diameter, rather than column length, because a large pressure drop caused by bed height increase could compress the gels too much.

Electronic supplementary material The online version of this chapter (doi:10.1007/978-3-319-16145-7_8) contains supplementary material, which is available to authorized users.

© Springer International Publishing Switzerland 2015

T. Gu, *Mathematical Modeling and Scale-Up of Liquid Chromatography*,
DOI 10.1007/978-3-319-16145-7_8

8.1 Size-Exclusion Modeling

Several mathematical models have been proposed for size-exclusion chromatography [9–12]. The model proposed by Kim and Johnson [9] is similar to the general rate model described in this work, except that their model considers size exclusion in single-component systems without any adsorption. They introduced an "accessible pore volume fraction" to account for the size-exclusion effect.

In this book, a symbol ε_p^a is used to denote the accessible porosity (i.e., accessible macropore volume fraction) for a particular species. For small molecules with no size-exclusion effect, $\varepsilon_p^a = \varepsilon_p$, and for large molecules that are completely excluded from the particle macropores, $\varepsilon_p^a = 0$. For medium-sized molecules, $0 < \varepsilon_p^a < \varepsilon_p$. It is convenient to define a size-exclusion factor of $0 \leq F^{ex} \leq 1$ such that $\varepsilon_p^a = F^{ex}\varepsilon_p$. $F^{ex} = 1$ means no size exclusion, while $F^{ex} = 0$ means complete size exclusion.

Based on Eq. (4.16), the retention time of a solute that is partially excluded by the SEC gel is

$$t_R = t_d\left[1 + \frac{(1-\varepsilon_b)\varepsilon_p^a}{\varepsilon_b}\right] \tag{8.1}$$

This accessible macropore concept is similar to the pore volume fraction concept used by Kim and Johnson [9]. Li et al. [10] demonstrated that the F^{ex} value is actually equal to the distribution coefficient in SEC (K_{SEC}), which can be obtained from elution volumes or retention times of a solute of interest, a small molecule, and a completely excluded molecule from the following equation:

$$K_{SEC} = \frac{V_{e,R} - V_{e,d}}{V_{e,0} - V_{e,d}} = \frac{t_R - t_d}{t_0 - t_d} \tag{8.2}$$

By inserting Eq. (8.1) and Eq. (4.16) into the equation above, one obtains

$$K_{SEC} = \frac{\varepsilon_p^a}{\varepsilon_p} = F^{ex} \tag{8.3}$$

For a completely excluded solute that is nonbinding, its elution volume is obviously

$$V_{e,d} = V_b\varepsilon_b = \left(\pi d_c^2/4\right) L\varepsilon_b \tag{8.4}$$

in which V_b is the bed volume of the column. For a nonbinding solute that penetrates all macropores inside the particles, its elution volume is larger because particle macropore volume must be included:

$$V_{e,0} = V_{e,d}\left[1 + \frac{(1-\varepsilon_b)\varepsilon_p}{\varepsilon_b}\right] \tag{8.5}$$

For a nonbinding solute that is partially excluded from macropores, its elution volume is

$$V_{e,R} = V_{e,d}\left[1 + \frac{(1-\varepsilon_b)\varepsilon_p^a}{\varepsilon_b}\right] \tag{8.6}$$

which is smaller than $V_{e,0}$. These three equations above can be used to evaluate ε_b and ε_p for a column and ε_p^a for different solutes.

To model SEC, the general rate model in Chap. 3 can be modified. The bulk-fluid phase Eq. (3.9) is unchanged. The particle phase Eq. (3.10) is modified by replacing the particle porosity with the accessible porosity to yield the following PDE system:

$$-\frac{1}{Pe_{Li}}\frac{\partial^2 c_{bi}}{\partial z^2} + \frac{\partial c_{bi}}{\partial z} + \frac{\partial c_{bi}}{\partial \tau} + \xi_i\left(c_{bi} - c_{pi,r=1}\right) = 0 \tag{8.7a}$$

$$\frac{\partial}{\partial \tau}\left[\left(1-\varepsilon_p\right)c_{pi}^* + \varepsilon_{pi}^a c_{pi}\right] - \eta_i\left[\frac{1}{r^2}\frac{\partial}{\partial r}\left(r^2\frac{\partial c_{pi}}{\partial r}\right)\right] = 0 \tag{8.8a}$$

in which $\eta_i = \varepsilon_{pi}^a D_{pi} L/\left(R_p^2 v\right)$. Keep in mind that the molar saturation capacities for solutes with different accessible porosity values will likely differ if there is binding in the presence of size exclusion (see Chap. 11). This particle phase PDE requires that the adsorption saturation capacity is based on the particle skeleton volume. One needs to avoid the mistake of using the particle skeleton that lumps in the inaccessible pore volume when a solute with size-exclusion effect is used to estimate ε_p experimentally. Such an adsorption saturation capacity is smaller and it does not match the $\left(1-\varepsilon_p\right)$ term in Eq. (8.8a). Its value should be corrected by multiplying it with $\left(1-\varepsilon_{pi}^a\right)/\left(1-\varepsilon_p\right)$ before it can be used in Eq. (8.8a).

Usually in SEC, binding is a side effect to be prevented by using a salt (for ion-exchange binding) and solvent (for hydrophobic interaction binding) in the mobile phase. When binding is dropped from the model, there is no need to write the model for a multicomponent system because it is assumed that there is no interaction among different solutes in SEC modeling. The following two equations form the rate model for SEC without binding:

$$-\frac{1}{Pe_L}\frac{\partial^2 c_b}{\partial z^2} + \frac{\partial c_b}{\partial z} + \frac{\partial c_b}{\partial \tau} + \xi\left(c_b - c_{p,r=1}\right) = 0 \tag{8.7b}$$

$$\frac{\varepsilon_p^a}{\eta}\frac{\partial c_p}{\partial \tau} = \frac{1}{r^2}\frac{\partial}{\partial r}\left(r^2\frac{\partial c_p}{\partial r}\right) \tag{8.8b}$$

with the following initial and boundary conditions needed for the model PDEs:

Initial conditions (at $\tau = 0$):

$$c_b = c_b(0, z) = 0 \tag{8.9a}$$

$$c_p = c_p(0, r, z) = 0 \tag{8.9b}$$

Boundary conditions:

$$\text{at } z = 0, \quad \partial c_b/\partial z = \text{Pe}_L[c_b - C_f(\tau)/C_0] \tag{8.10}$$

$$\text{and at } z = 1, \quad \partial c_b/\partial z = 0 \tag{8.11}$$

$$\text{At } r = 0, \quad \partial c_p/\partial r = 0 \tag{8.12}$$

$$\text{and at } r = 1, \quad \partial c_p/\partial r = \text{Bi}\left(c_b - c_{p,r=1}\right) \tag{8.13}$$

The dimensionless feed profile for an elution with a dimensionless pulse size of τ_{imp} is

$$C_f(\tau)/C_0 = \begin{cases} 1 & 0 \le \tau \le \tau_{imp} \\ 0 & \text{else} \end{cases} \tag{8.14}$$

There is no need to write the model system in a multicomponent form, because the solute species are considered independent during their migration inside the SEC column without any interaction.

8.2 Numerical Methods and Parameter Estimation

The numerical strategy used to solve the SEC model system is identical to that in Fig. 3.3. Peclet number estimation is the same as that presented in Chap. 4. The dimensionless η number is estimated based on its definition

$$\eta = \frac{\varepsilon_p^a D_p L}{R_p^2 v} \tag{8.15}$$

which requires the intraparticle diffusivity (D_p). D_p is calculated from the following experimental correlation [13]:

$$D_p = \frac{D_m}{\tau_{tor}}\left(1 - 2.1044\lambda + 2.089\lambda^3 - 0.948\lambda^5\right) \tag{8.16}$$

where τ_{tor} is the particle tortuosity. It is usually unavailable from the vendor. Its value ranges from 2 to 6 for many commercial porous media [14]. A median value of 4 may be used for simulation, or τ_{tor} can be used as an adjustable parameter for curve fitting [10]. D_m estimation has been discussed in Chap. 4. λ can be calculated from the following relationship for SEC [15]:

$$\lambda = \frac{d_m}{d_p} = 0.35\left(\frac{\text{MW of solute molecule}}{\text{MW of upper exclusion limit}}\right)^{1/3} \tag{8.17}$$

The Biot number for mass transfer is then readily calculated from its definition

$$\text{Bi} = \frac{kR_p}{\varepsilon_p^a D_p} \tag{8.18}$$

The estimation of k, the interfacial film mass transfer coefficient, has been discussed in Chap. 4.

8.3 Scale-Up Example

Li et al. [10] presented a systematic procedure for parameter estimation and scale-up prediction using the SEC model above. They used the commercial Bio-Rad P60 gel to separate ovalbumin from myoglobin. A small column (1.5 cm × 30 cm) packed with SEC gel was first used to obtain the elution volume data for various solutes. The column was found to have a bed voidage of $\varepsilon_b = 0.27$ using blue dextran (nonbinding and completely excluded). Its particle porosity was found to be $\varepsilon_p = 0.66$ using L-tryptophan (a very small solute). The MW of upper exclusion limit was set to the MW of bovine serum albumin (BSA) (MW = 66,463) for the gel in Eq. (8.17) because tests showed that BSA had a very limited access to the pores of the SEC gel. The gel's vendor indicated a size-exclusion range of 3,000–60,000. If 60,000 is used instead of 66,463 in Eq. (8.17), the changes in η, and Bi values will be very small, without a significant impact on simulated chromatograms. The accessible particle porosities were also calculated from that data in Table 8.1. In Table 8.2, D_m was calculated from Eq. (4.27) and D_p from Eq. (4.35). The particle radius, R_p, value was from vendor specifications. Assuming that this small column and other columns packed with the same gel had the same gel's consistency, it could be assumed that ε_b, ε_p, and ε_p^a values remained the same. This assumption required that the bed compression level did not change. The Microsoft Excel spreadsheet Table 8.3 can be used to obtain Pe_L, η, and Bi values for all the simulated myoglobin and ovalbumin SEC chromatograms in this chapter. The

Table 8.1 Elution volume data from 1.5 cm × 30 cm SEC column (data from [10])

Solute	Elution volume (ml)	MW
L-tryptophan	39.8	204
Myoglobin	23.2	16,890
Ovalbumin	17.4	43,500
BSA	15.5	67,000
Blue dextrin	14.3	2,000,000

Table 8.2 Physical properties (data from [10])

Proteins	ε_p[a]	F^{ex}	$D_m \times 10^{11}$ ($m^2\ s^{-1}$)	$D_p \times 10^{11}$ ($m^2\ s^{-1}$)	ε_b	ε_p	$R_p \times 10^6$ (m)
Myoglobin	0.23	0.35	10.7	2.98	0.27	0.66	67.5
Ovalbumin	0.08	0.12	7.8	1.65			

fourth column values are listed for users to verify their calculation results in the second column.

As a mass transfer parameter, τ_{tor} does not impact the retention time. When its value increases, the peak gets more diffused. τ_{tor} was found to be 2.0 by fitting myoglobin elution peak with model prediction with τ_{tor} as the adjustable parameter for a 1.5 cm × 27.3 cm column packed with 48.2 ml P60 gel as shown in Fig. 8.1 [10]. Figure 8.2a shows Chromulator KINETIC simulator screenshot of simulated chromatogram with dimensionless time and dimensionless concentration. This simulator uses the second-order kinetics. It is discussed in detail in Chap. 10. The binding-related parameters must be set to zero. This is why adsorption saturation capacity (C^{∞}) and Damköhler numbers for adsorption and desorption (Da^a and Da^d) are set to zero. The size-exclusion factor, F^{ex} (ExF), is set to 0.35 for myoglobin according to Table 8.2. In SEC modeling, C_0 value does not impact the simulated dimensionless chromatogram due to nondimensionalization. It can be set to unity for convenience.

Multiplying the dimensionless time in Fig. 8.2a by 13.03 ml (total bed void volume $V_b\varepsilon_b$ not including particle macropores) gave the elution volume in Fig. 8.1. This conversion factor was based on the following relationship between dimensionless time and elution volume:

$$V_e = (V_b\varepsilon_b)\tau \tag{8.19}$$

In LC simulation, $\tau = 1$ leads to $V_e = V_b\varepsilon_b$. $\tau = 1$ is the time needed for a nonbinding eluite to elute out the column without penetrating any particle macropores (e.g., blue dextran time). The dimensionless concentration in Fig. 8.2a was first converted to dimensional concentration using the sample concentration 8.9×10^{-5} mol/L and then converted to absorbance based on the absorbance–concentration calibration curve for myoglobin. In this case, the dimensionless concentration in Fig. 8.2a multiplied by 2.25 gave the absorbance in Fig. 8.1 assuming that the concentration was in the linear UV absorbance range.

Table 8.3 Microsoft excel sheet for the calculation of Pe_L, η, and Bi values in Fig. 8.1

A	*B*	*C*	*D*	
Raw data		Eq.	Results	1
MW	16,890			2
Q (ml/min)	0.289			3
L (cm)	27.3			4
Column diameter, d_c (cm)	1.5			5
Particle radius, R_p (cm)	0.00675			6
ε_b (bed voidage)	0.27			7
Particle tortuosity, τ_{tor}	2			8
Pore diameter, d_p (Å)	300			9
ε_p (particle porosity)	0.66			10
$\varepsilon_p{}^a$ (accessible ε_p)	0.23			11
				12
Calculated				13
Bed volume, V_b (ml)	=(1/4) * PI() * B5 * B5 * B4		48.243	14
v (cm/s) (interstitial)	=B3/60 * B4/(B14 * B7)	(4.11)	0.010095	15
λ (d_m/d_p)	=0.35 * (B2/66,463)^(1/3)	(8.17)	0.22169	16
D_m (cm^2/s)	=0.0000274 * B2^(−1/3)	(4.27)	1.06792E−06	17
D_p (cm^2/s)	=B17 * (1 − 2.104 * B16 + 2.09 * B16^3 − 0.95 * B16^5)/B8	(4.35)	2.96788E−07	18
k (cm/s)	=0.687 * (B15^(1/3)) * ((B17/(B7 * B6))^(2/3))	(4.38)	0.0010397	19
Pe	=0.1 * B4/(B6 * B7)	(4.32)	1497.94	20
η	=B11 * B18 * B4/(B6 * B6 * B15)	(4.34)	4.0515	21
Biot	=B19 * B6/(B11 * B18)	(4.37)	102.81	22
				23
τ to t conversion factor				24
L/v (min)	=B4/B15/60			25

It is actually not essential to convert the y-axis in LC scale-up because it has peak bottom width rather than peak height that really matters when judging peak sepataions. On top of that, due to peak area balance (bounded by the total amount of solute in the sample), when peak bottom width and peak shape are predicted by Chromulator, the peak height can be estimated provided that the solute concentration is in the linear absorbance range.

In Chromulator software, SEC simulation uses the KINETIC simulator that considers the size-exclusion factor. Up to four different solutes can be simulated

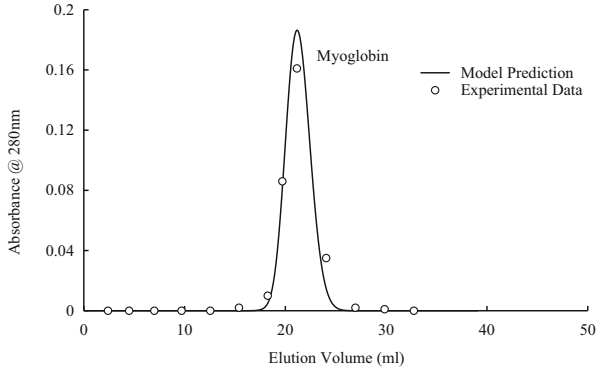

Fig. 8.1 Curve fitting of myoglobin elution peak for τ_{tor} evaluation (experimental data from [10])

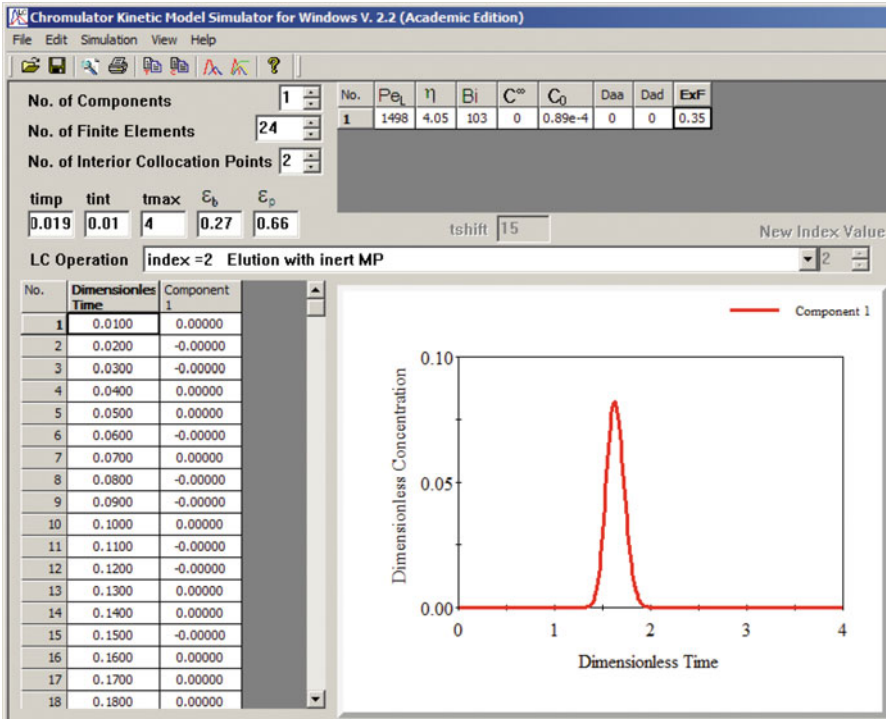

Fig. 8.2a Screenshot of KINETIC simulator for the simulation of Fig. 8.1 before axis conversions

in multicomponent elution in the same run. Figure 8.2b shows that the same chromatogram can be produced using Chromulator RATE simulator by setting Langmuir isotherm parameters a and b to zero (i.e., no binding in SEC) and by setting particle porosity to accessible particle porosity. One must not use this particle porosity substitution method to study F^{ex} when there is binding because the $\left(1-\varepsilon_p\right)$ term will be misrepresented in Eq. (8.8). Figure 8.2b again shows that

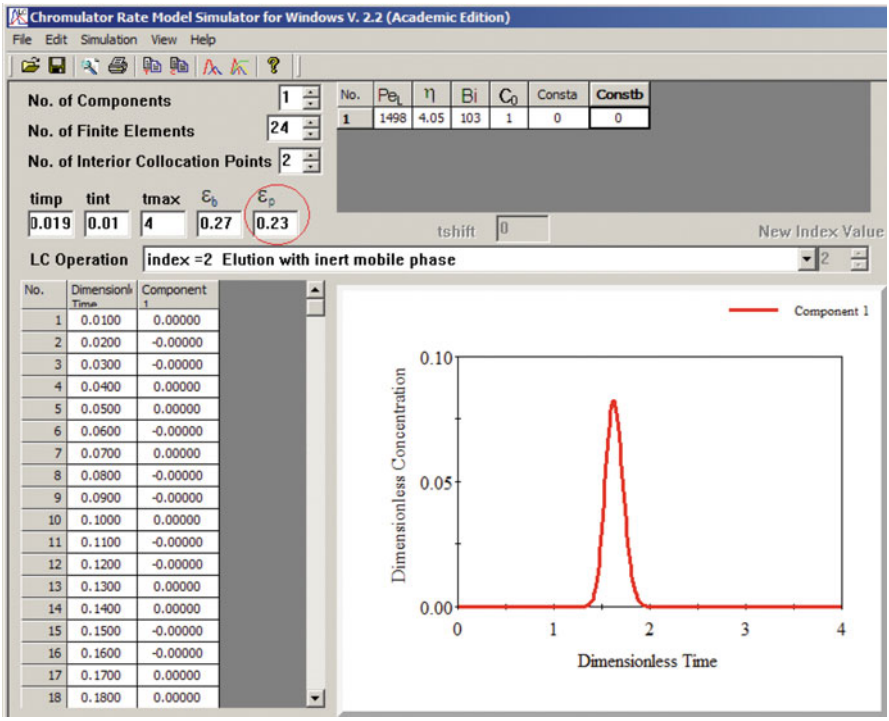

Fig. 8.2b Reproduction of the chromatogram in Fig. 8.2a using the RATE simulator

C_0 value does not impact the simulated dimensionless chromatogram. It is set to one for convenience. Because the RATE simulator has only one field to enter particle porosity, it can only simulate a single-component elution in a single run. For multicomponent elution, each component may be simulated in separate runs because the SEC model in this chapter does not consider interactions among different components in the same sample. Chromatogram output data for all the solutes can be copied to a spreadsheet and then plotted. This is not as convenient as using the KINETIC simulator which can simulate a multicomponent system in a single run. Another option for multicomponent SEC simulation is to use the dedicated SEC simulator for cored beads, in Chap. 9, by setting $\beta = 0$ to signify conventional solid beads without cores. However, this simulator is currently not in the standard academic version of Chromulator. Figure 8.2c is a reproduction of Figs. 8.2a and 8.2b using the dedicated SEC simulator that can simulate both fully porous beads ($\beta = 0$) and cored beads ($\beta > 0$). More details are available in Chap. 9. All the three simulators produced identical results above despite the fact that they are designed to solve different particle phase PDEs.

Li et al. found that using the parameters in Table 8.4 and $\tau_{tor} = 2.0$, the model predicted a binary elution of myoglobin and ovalbumin on the 1.5 cm × 27.3 cm column very well [10]. They subsequently used the parameters for scale-up

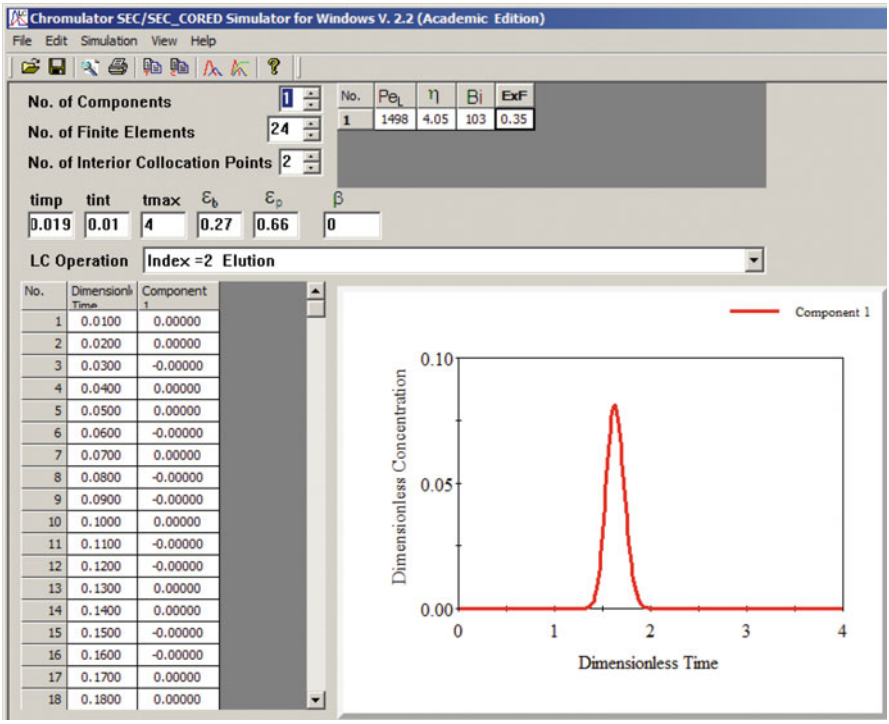

Fig. 8.2c Reproduction of the chromatogram in Fig. 8.2a using the SEC simulator that can simulate both regular fully porous beads ($\beta = 0$) and cored beads

Table 8.4 Parameters in addition to those in Table 8.2 (experimental data from [10])

		Operating parameters				Simulation parameters			
Figures	Proteins	d (m)	L (m)	$v \times 10^4$ (m s^{-1})	$C_0 \times 10^5$ (mol L^{-1})	Pe_L	Bi[a]	η	τ_{imp}
8.1, 8.2	Myoglobin	0.015	0.273	1.01	8.9	1,498	103	4.1	0.019
8.3	Myoglobin	0.050	0.295	0.76	5.9	1,619	93.3	5.8	0.013
	Ovalbumin				3.9	1,619	397	1.1	
8.4	Myoglobin	0.050	0.420	0.54	5.9	2,305	83.3	11.7	0.045
	Ovalbumin				2.3	2,305	354	2.2	

[a]In Ref. [10], the definition of Re missed ε_b in the numerator, leading to larger Bi values. Since the Bi values here are already very large, this error does not noticeably change simulation results

prediction of two other larger columns as shown in Figs. 8.3 and 8.4 for the separation of the two proteins. In both cases, the a priori predictions were excellent. The column–volume ratio of the 5.0 cm × 42 cm column (Fig. 8.4) to the 1.5 cm × 30 cm column (small column used for parameter estimation) reached 15.6:1, which means a scale-up factor of 15.6 for column volume.

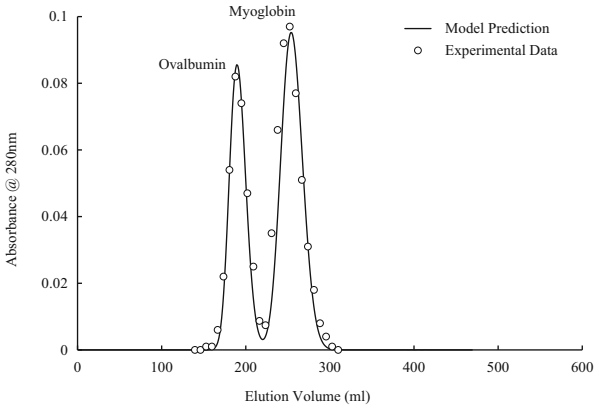

Fig. 8.3 Prediction of binary elution on a 5.0 cm × 29.5 cm column packed with P60 gel (experimental data from [10])

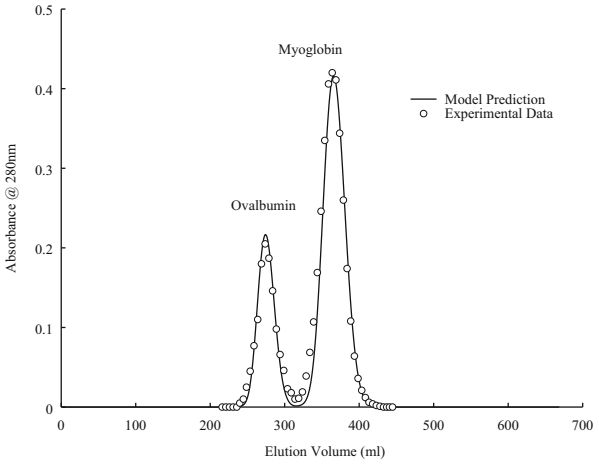

Fig. 8.4 Prediction of binary elution on a 5.0 cm × 42.0 cm column packed with P60 gel (experimental data from [10])

8.4 Summary

The comprehensive SEC model presented in this chapter uses the concept of size-exclusion factor for each species in the sample. It has the same value as the size-exclusion distribution coefficient. The scale-up example in this work showed that the model predicted myoglobin and ovalbumin separation on a preparative SEC column very well. This is not surprising in view of the fact that the model considers all the essential mass-transfer mechanisms: axial dispersion, interfacial film mass transfer, and intraparticle diffusion. Because SEC separation involves only mass transfer without specific binding, it is expected that the model can be reliably used for scale-up if there is no significant flow maldistribution in large columns.

A recent theoretical development in SEC is the predicted use of cored beads for improved SEC separation by replacing an inert core in a bead to reduce radial distance for mass transfer. Chapter 9 shows that cored beads are superior to conventional fully porous beads for SEC separation.

Because affinity LC often involves macromolecules that may be excluded by small pores in the stationary phase, the SEC effect in affinity LC is discussed in Chap. 10. If adsorption LC or other LC operations involve specific binding, the size-exclusion effect may reduce the saturation capacity of a species due to inaccessible binding sites. This effect is discussed in Chap. 10 (see Fig. 10.10).

References

1. Yamamoto S, Nomura M, Sano Y (1987) Adsorption chromatography of proteins: determination of optimum conditions. AIChE J 33:1426–1434. doi:10.1002/aic.690330903
2. Zhou W, Bi J, Janson J-C, Dong A, Li Y, Zhang Y, Huang Y, Su Z (2005) Ion-exchange chromatography of hepatitis B virus surface antigen from a recombinant Chinese hamster ovary cell line. J Chromatogr A 1095:119–125. doi:10.1016/j.chroma.2005.08.006
3. Gu T, Zheng Y (1999) A study of the scale-up of reversed-phase liquid chromatography. Sep Purif Technol 15:41–58. doi:10.1016/S1383-5866(98)00083-5
4. Bérot S, Compoint JP, Larré C, Malabat C, Guéguen J (2005) Large scale purification of rapeseed proteins (*Brassica napus* L.). J Chromatogr B 818:35–42. doi:10.1016/j.jchromb.2004.08.001
5. Stickel JJ, Fotopoulos A (2001) Pressure-flow relationships for packed beds of compressible chromatography media at laboratory and production scale. Biotechnol Prog 17:744–751. doi:10.1021/bp010060o
6. Hofmann M (2003) Use of ultrasound to monitor the packing of large-scale columns, the monitoring of media compression and the passage of molecules, such as monoclonal antibodies, through the column bed during chromatography. J Chromatogr A 989:79–94. doi:10.1016/S0021-9673(03)00006-2
7. Terry DE, Umstot E, Desiderio DM (2004) Optimized sample-processing time and peptide recovery for the mass spectrometric analysis of protein digests. J Am Soc Mass Spectrom 15:784–794. doi:10.1016/j.jasms.2004.02.005
8. Afeyan NB, Fulton SP, Regnier FE (1991) Perfusion chromatography packing materials for proteins and peptides. J Chromatogr A 544:267–279. doi:10.1016/S0021-9673(01)83991-1
9. Kim DH, Johnson AF (1984) Computer model for gel permeation chromatography of polymers. ACS Symp Ser 245:25–45
10. Li Z, Gu Y, Gu T (1998) Mathematical modeling and scale-up of size-exclusion chromatography. Biochem Eng J 2:145–155
11. Koo Y-M, Wankat PC (1988) Modeling of size exclusion parametric pumping. Sep Sci Technol 23:413–427
12. Yau WW, Kirkland JJ, Bly DD (1979) Modern size-exclusion liquid chromatography. Wiley, New York, p 89
13. Anderson JL, Quinn JA (1974) Restricted transport in small pores: a model for steric exclusion and hindered particle motion. Biophys J 14:130–150. doi:10.1016/S0006-3495(74)70005-4
14. Geankoplis C (2003) Transport processes and separation process principles (includes unit operations), 4th edn. Prentice Hall, Upper Saddle River, NJ
15. Stegeman G, Kraak JC, Poppe H (1991) Hydrodynamic and size-exclusion chromatography of polymers on porous particles. J Chromatogr A 550:721–739. doi:10.1016/S0021-9673(01)88577-0

Chapter 9
Modeling of Liquid Chromatography with Cored Beads

In typical LC operations, the Biot numbers for mass transfer are much larger than 2. This means intraparticle diffusion is typically the limiting step, while interfacial film mass transfer between the bulk-fluid phase and the particle phase is relatively fast. Due to its spherical structure, the center section of a particle has a disproportionately small volume, but it presents a relatively large radial distance for diffusional mass transfer. To the other extreme, nonporous beads offer no intraparticle diffusion due to a lack of macropores. These beads have found success in fast analytical LC that uses very small sample sizes. In the absence of intraparticle diffusion, they offer sharp peaks [1, 2]. However, they have insufficient binding sites per unit volume without the macropores and thus they are unsuitable for preparative- and large-scale LC.

As a compromise between fully porous beads and nonporous beads, cored beads have been created to offer decent binding capacities without the long radial distance for diffusion. Cored beads are also known as pellicular beads [3–6] and superficially porous beads [7] with an inert impenetrable solid core to block fluids. A heavy silica or stainless steel core may be used to achieve this objective. For gel beads, the solid core can significantly improve the rigidity of the beads. The core can also be used to adjust the density of beads, which is useful in expanded bed adsorption. Because solid cores with uniform diameters (e.g., silica beads) can be selected and then coated with shells, cored beads can be manufactured with a good spherical shape and a narrow particle size distribution [8]. These beads have desirable hydrodynamic performances such as reduced nonideal flow and pressure drop [9, 10]. They have been used in various LC separations including ion exchange [3, 11, 12]. Some commercially available cored beads were reviewed and compared experimentally by Cabooter et al. [13].

Figure 9.1 shows a schematic diagram of a cored bead in which parameter β is defined as the core radius fraction (R_{core}/R_p). For fully porous beads, β is equal to zero, while $\beta = 1$ means that an inert core occupies the entire bead. To model the impact of the β value on LC performance, it is necessary to do an axis transformation with the following relationship:

© Springer International Publishing Switzerland 2015

T. Gu, *Mathematical Modeling and Scale-Up of Liquid Chromatography*,
DOI 10.1007/978-3-319-16145-7_9

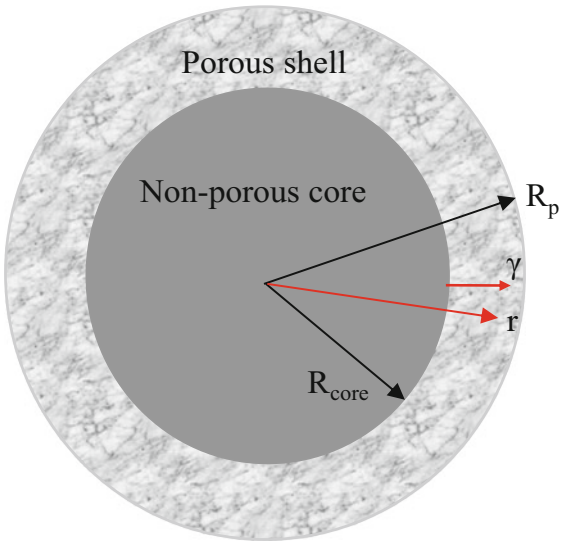

Fig. 9.1 Schematic diagram of a cored bead with an inert core (after [6])

$$\gamma = \frac{r - \beta}{1 - \beta} \tag{9.1}$$

such that $0 \leq \gamma \leq 1$. For modeling nonporous beads, one should use a number such as $\beta = 0.9999$ instead of $\beta = 1$ to avoid singularity in the equation above. The dimensionless γ-axis is used to describe the radial distance for porous shell. Figure 9.2 shows a theoretical relationship between β and the core volume fraction for cored beads. It shows that a small core radius fraction does not reduce the core volume fraction much. For example, a core radius fraction of 0.5 leads to a shell volume fraction ($1 - \beta^3$) of 0.875. This means that a radial distance reduction of 50 % for mass transfer surprisingly leads to only 12.5 % of volume loss (or binding capacity loss) in the shell. For $\beta = 0.6$, the shell volume fraction is 0.785 that is still quite large. To investigate the impact of β on LC performances, it is highly desirable to solve a mathematical model for cored beads with the ability to adjust β in the simulation of LC operations using the cored beads.

9.1 General Rate Model and Numerical Methods

The following dimensionless model equations first presented in Chap. 3 for conventional fully porous beads can be used for cored beads by modifying the particle phase PDE and the boundary condition:

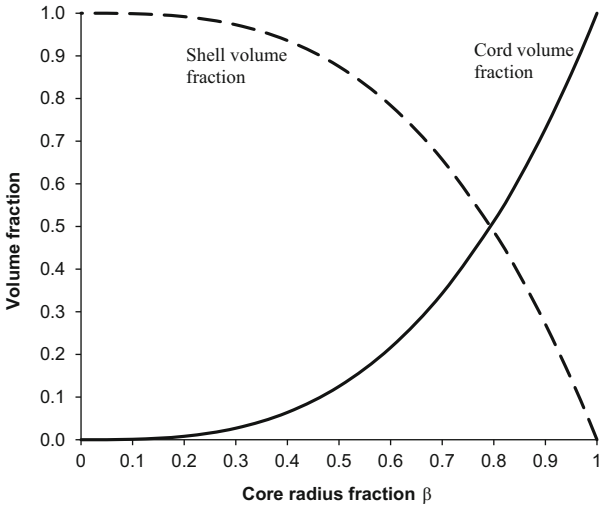

Fig. 9.2 Theoretical relationship between core radius fraction and core volume (after [6])

$$-\frac{1}{\mathrm{Pe}_{\mathrm{L}i}}\frac{\partial^2 c_{\mathrm{b}i}}{\partial z^2}+\frac{\partial c_{\mathrm{b}i}}{\partial z}+\frac{\partial c_{\mathrm{b}i}}{\partial \tau}+\xi_i\left(c_{\mathrm{b}i}-c_{\mathrm{p}i,r=1}\right)=0 \tag{9.2}$$

$$\left(1-\varepsilon_{\mathrm{p}}\right)\frac{\partial}{\partial \tau}c_{\mathrm{p}i}^{*}+\varepsilon_{\mathrm{p}}\frac{\partial c_{\mathrm{p}i}}{\partial \tau}-\eta_i\frac{1}{r^2}\frac{\partial}{\partial r}\left(r^2\frac{\partial c_{\mathrm{p}i}}{\partial r}\right)=0 \tag{9.3}$$

Inserting $r=\gamma(1-\beta)+\beta$ into Eq. (9.3) yields

$$\begin{aligned}&\left(1-\varepsilon_{\mathrm{p}}\right)\frac{\partial}{\partial \tau}c_{\mathrm{p}i}^{*}+\varepsilon_{\mathrm{p}}\frac{\partial c_{\mathrm{p}i}}{\partial \tau}\\&\quad-\eta_i\left[\frac{1}{(1-\beta)^2}\frac{\partial^2 c_{\mathrm{p}i}}{\partial \gamma^2}+\frac{2}{\gamma(1-\beta)+\beta}\cdot\frac{1}{1-\beta}\frac{\partial c_{\mathrm{p}i}}{\partial \gamma}\right]\\&\quad=0\end{aligned} \tag{9.4}$$

Initial conditions:

$$\text{At } \tau=0,\quad c_{\mathrm{b}i}=c_{\mathrm{b}i}(0,z)=0,\quad c_{\mathrm{p}i}=c_{\mathrm{p}i}(0,r,z)=0.$$

Boundary conditions:

$$\text{At } z=0,\quad \partial c_{\mathrm{b}i}/\partial z=\mathrm{Pe}_{\mathrm{L}i}[c_{\mathrm{b}i}-C_{\mathrm{f}i}(\tau)/C_{0i}] \tag{9.5}$$

$$\text{and at } z=1,\quad \partial c_{\mathrm{b}i}/\partial z=0 \tag{9.6}$$

$$\text{At } \gamma = 0, \quad \partial c_{\mathrm{p}i}/\partial \gamma = 0 \tag{9.7}$$

$$\text{and at } \gamma = 1, \quad \partial c_{\mathrm{p}i}/\partial \gamma = \mathrm{Bi}_i\left(c_{\mathrm{b}i} - c_{\mathrm{p}i,r=1}\right) \tag{9.8}$$

These initial and boundary conditions are the same as those used for the RATE model in Chap. 3, except that for the particle phase boundary conditions, r is replaced by γ. This general rate model for cored beads here is labeled as RATECORED model. When there is no core (i.e., $\beta = 0$, and thus $r = \gamma$), RATECORED degenerates into the RATE model as expected.

Because the bulk-fluid phase-governing PDF remains untouched, its discretization using the finite element method is the same as that used for the RATE model. The particle phase governing PDE, Eq. (9.4), must be discretized differently because now the particle center γ starts at the core surface (R_{core}) rather than the center of the particle. Gu et al. [6] used the following approach. The orthogonal collocation method is used to discretize the first- and second-order $c_{\mathrm{p}i}$ derivatives with respect to γ in Eq. (9.4) in a way different from that used for the RATE model. The general purpose (i.e., good for different geometries, not just for spheres) **A**, **B** matrices calculated with the polynomial roots on p. 77 must be used instead of the **A**, **B** matrices calculated using the polynomial roots for spherical particles on p. 96 in Finlayson's book [14] for these two derivatives, respectively for interior collocation points. The following two equations from Finlayson's book are used for the evaluation of **A**, **B** matrices:

$$\mathbf{A} \equiv \mathbf{C}\mathbf{Q}^{-1}, \tag{9.9a}$$

$$\mathbf{B} \equiv \mathbf{D}\mathbf{Q}^{-1} \tag{9.9b}$$

in which matrices **Q**, **C**, and **D** are evaluated using the following equations:

$$Q_{ji} = x_j^{i-1} \tag{9.10a}$$

$$C_{ji} = (i-1)x_j^{i-2} \tag{9.10b}$$

$$D_{ji} = (i-1)(i-2)x_j^{i-3} \tag{9.10c}$$

The polynomial roots x_j are given for the number of interior collocation points (N) from 1 to 6 in Table 4.3 of Finlayson's book. For example, $x_j = 0.2113248654$ and 0.7886751346 for $N = 2$ in the table. Note that $x_j = 0$ and 1 are two exterior collocation points for the discretization of a dimensionless x-axis. At each interior collocation point m ($m = 1, 2, \ldots, N$), the two derivatives in Eq. (9.4) are evaluated from the following two equations:

$$\left(\frac{\partial^2 c_{pi}}{\partial \gamma^2}\right)_m = \sum_{k=1}^{N+2} B_{m,k}\left(c_{pi}\right)_k = B_{m,1}\left(c_{pi}\right)_l + B_{m,N+2}\left(c_{pi}\right)_{N+2} + \sum_{k=2}^{N+1} B_{m,k}\left(c_{pi}\right)_k \tag{9.11}$$

$$\left(\frac{\partial c_{pi}}{\partial \gamma}\right)_m = \sum_{k=1}^{N+2} A_{m,k}\left(c_{pi}\right)_k = A_{m,1}\left(c_{pi}\right)_l + A_{m,N+2}\left(c_{pi}\right)_{N+2} + \sum_{k=2}^{N+1} A_{m,k}\left(c_{pi}\right)_k \tag{9.12}$$

The m index values correspond to the interior collocation point positions specified by the x_j values. They do not include the two derivatives at the two exterior collocation points (at $\gamma = 1$ and $\gamma = 0$), which are evaluated using the two corresponding boundary conditions. Plugging Eq. (9.12) into Eqs. (9.7) and (9.8) that are boundary conditions, the following two equations can be obtained for the particle phase concentration at the bead surface ($\gamma = 1$) and the core surface ($\gamma = 0$):

$$\left(c_{pi}\right)_{N+2} = c_{pi,\gamma=1} = \frac{A_{N+2,1}\sum_{k=2}^{N+1} A_{1,k}\left(c_{pi}\right)_k - A_{1,1}\sum_{k=2}^{N+1} A_{N+2,k}\left(c_{pi}\right)_k + (1-\beta)A_{1,1}\mathrm{Bi}_i c_{bi}}{(1-\beta)A_{1,1}\mathrm{Bi}_i - A_{N+2,1}A_{1,N+2} + A_{1,1}A_{N+2,N+2}} \tag{9.13}$$

$$\left(c_{pi}\right)_1 = c_{pi,\gamma=0} = -\frac{1}{A_{1,1}}\left(\sum_{k=2}^{N+1} A_{1,k}\left(c_{pi}\right)_k + A_{1,N+2}\left(c_{pi}\right)_{N+2}\right) \tag{9.14}$$

The two values are needed to evaluate Eqs. (9.11) and (9.12), which are needed for Eq. (9.4).

The discretization of the z-axis in Eq. (9.2) uses exactly the same finite element approach as described in Chap. 3 for fully porous beads because the bulk-fluid phase PDE does not change. The first-order ODE system resulted from the discretization of Eqs. (9.2) and (9.4) is solved together using DVODE with the help of the isotherm equation in Eq. (3.21) similar to solving the RATE model. A software simulator called RATECORED has been created for cored bead LC simulation analogous to RATE simulator for fully porous bead LC simulation.

9.2 How to Use the RATECORED Simulator

The RATECORED simulator is not in the standard package of Chromulator 2.2 However, it may still be obtained free of charge for most academic applications by contacting the author. Its graphical user interface is identical to that of RATE, except the added entry for the core radius fraction β. Despite the fact that the orthogonal collocation method in RATECORED and RATE uses different polynomial roots, RATECORED with $\beta = 0$ has been verified to produce the same simulation results as RATE.

Figure 9.3 shows a screenshot of the RATECORED simulation for the comparison of a single-component breakthrough operation using fully porous beads ($\beta = 0$) vs. cored beads ($\beta = 0.5$). The software allows the overlapping of two sets of simulated chromatograms. The second set is shown as dashed lines with its input parameters displayed in the table above the simulated chromatograms. The parameter table for the solid lines has been embedded in Fig. 9.3 manually.

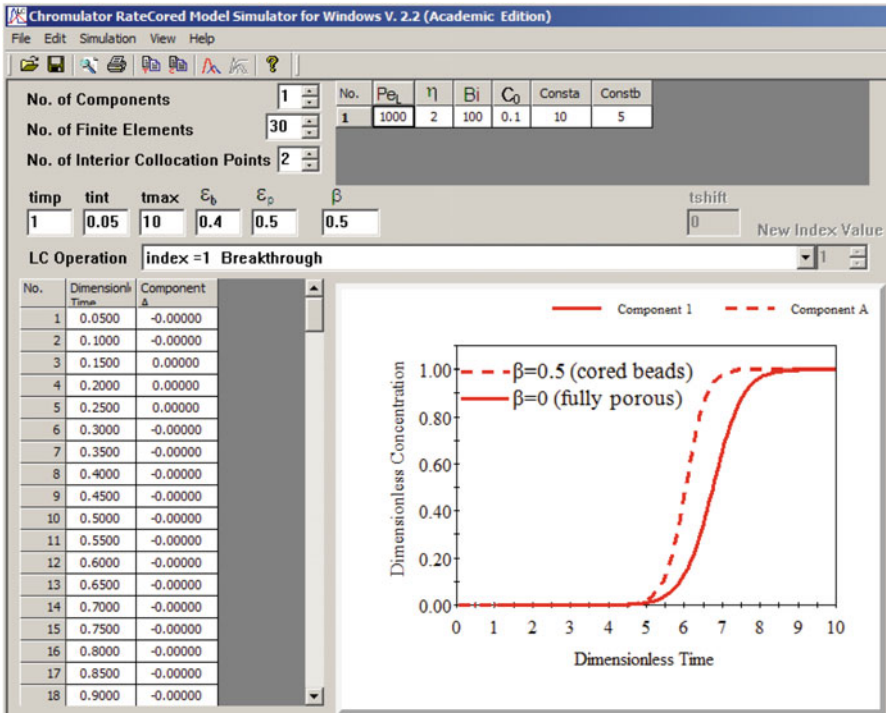

Fig. 9.3 RATECORED simulator screen shot showing comparison of single-component breakthrough curves: *solid line* for $\beta = 0$ (fully porous beads) and *dashed line* for $\beta = 0.5$ (cored beads)

9.3 Effects of Core Radius Fraction

Figure 9.4 demonstrates that when β increases, the column hold-up capacity decreases, while the breakthrough curve becomes sharper. The loss of column hold-up capacity is relatively small when β increases from 0 to 0.5 and 0.7. However, the loss accelerates when β gets larger progressively. The parameters used for simulating the single-component breakthrough analysis with Langmuir isotherm in Fig. 9.4 are listed in Fig. 9.3 with a variation in β only. The dimensionless column hold-up capacity is represented by the capacity area (CA) in a dimensionless breakthrough curve that is bordered by the x and y-axes, the breakthrough curve and the horizontal breakthrough leveling off line (Fig. 4.1). For cored beads, the CA value for species i in multicomponent breakthrough can be calculated based on the following equation:

$$\mathrm{CA}_i = 1 + \frac{1}{\varepsilon_\mathrm{b}}\left(1-\beta^3\right)\left[\left(1-\varepsilon_\mathrm{b}\right)\left(1-\varepsilon_\mathrm{p}\right)\frac{b_i C^\infty}{1+\sum_{j=1}^{N_\mathrm{s}} b_j C_{0j}} + \left(1-\varepsilon_\mathrm{b}\right)\varepsilon_\mathrm{p}\right] \tag{9.15}$$

which reduces to the following equation for single-component breakthrough:

$$\mathrm{CA} = 1 + \frac{1}{\varepsilon_\mathrm{b}}\left(1-\beta^3\right)\left[\left(1-\varepsilon_\mathrm{b}\right)\left(1-\varepsilon_\mathrm{p}\right)\frac{a}{1+bC_0} + \left(1-\varepsilon_\mathrm{b}\right)\varepsilon_\mathrm{p}\right] \tag{9.16}$$

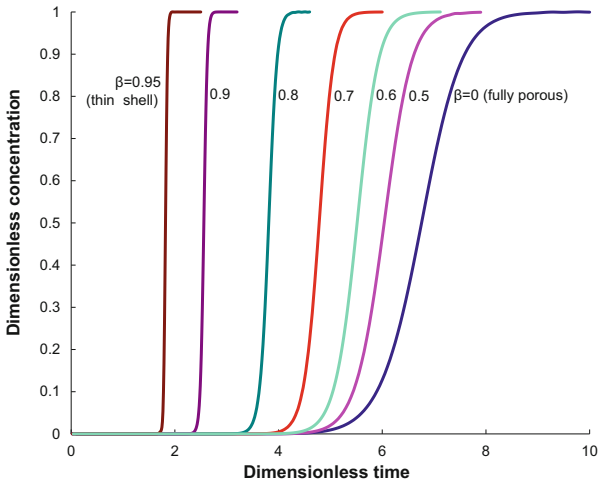

Fig. 9.4 Effect of core radius fraction on breakthrough analysis. Parameters for simulation are shown in Fig. 9.3

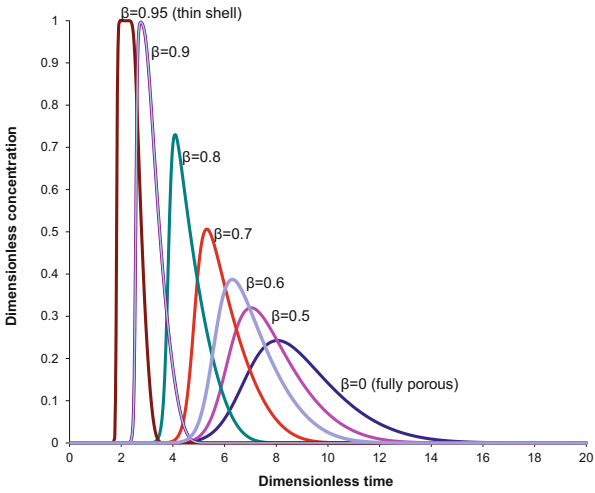

Fig. 9.5 Effect of core radius fraction (β) on isocratic elution with a pulse size of $\tau_{imp} = 1$

For elution with a preparative-scale sample size of $\tau_{imp} = 1$ that is equivalent to 40 % of the bed volume (calculated from $\tau_{imp}.\varepsilon_b$), Fig. 9.5 indicates that increasing β makes the peak sharper while reducing its retention time. The parameters for simulation of Fig. 9.5 can be found in Fig. 9.3 with the exception of operation index and β variation. Figure 9.6 is a screenshot showing the effect of β on binary elution. The output chromatogram data are replotted in Fig. 9.7. It shows that with fully porous beads, the two peaks (dashed lines) overlap slightly around dimensionless time 12.8, while cored beads with $\beta = 0.7$ (solid lines) can achieve almost baseline separation with much sharper peaks. The overall elution time marked by the end of the second peak reduces from 40 to around 24.

When β further increases to 0.93, Fig. 9.8 shows that the overall elution time can be terminated at around dimensionless time 7. However, the retention time range of 0–7 is insufficient for the two peaks to resolve. There is a significant peak overlap around dimensionless time 3.1. This is because the cored beads have much reduced loading capacity and are thus incapable of coping with the preparative sample load ($\tau_{imp} = 1$). Figure 9.9 suggests that when the load is reduced by half ($\tau_{imp} = 0.5$), baseline separation can be achieved with the same cored beads ($\beta = 0.93$). Gu et al. also demonstrated the advantages of cored beads with a ternary elution example. They showed that even when β reached 0.99 (very thin shell), baseline separation could still be achieved if the sample size was $\tau_{imp} = 0.01$ that is too small for preparative LC [6]. This provided theoretical proof that cored beads can be used in fast analytical LC (small τ_{imp}), which has been practiced in the form of fused-core beads [15]. In reality, cored beads need to compete with very small silica beads and also nonporous beads that are very small. All these beads are designed for fast mass transfer without the worry of low loading capacity because they are used for analytical LC rather than preparative LC.

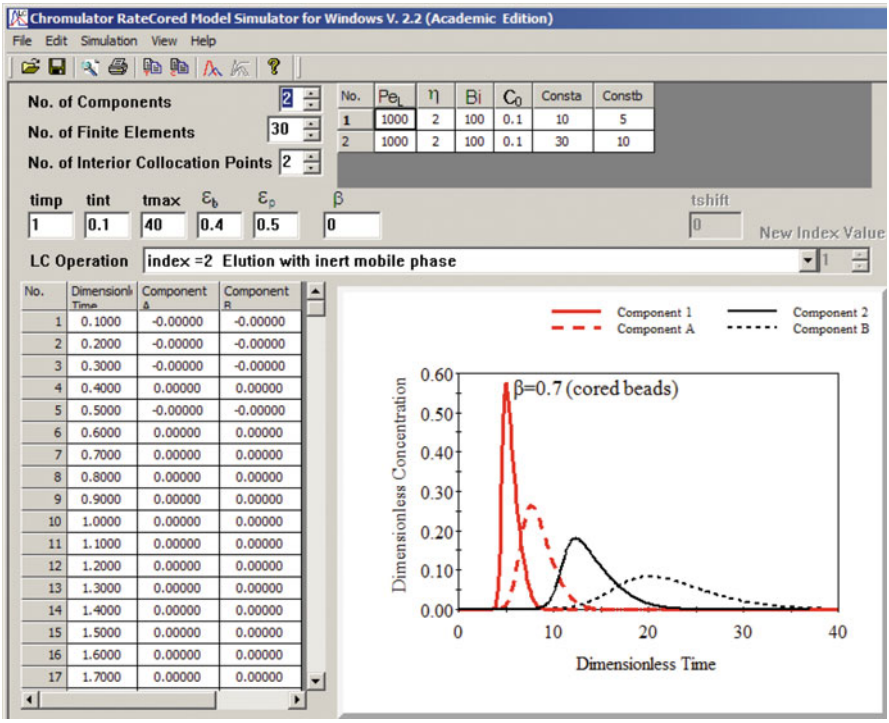

Fig. 9.6 Screenshot of binary elution (pulse size $\tau_{imp} = 1$) using fully porous beads (*dashed lines*) and cored beads with $\beta = 0.7$ (*solid lines*)

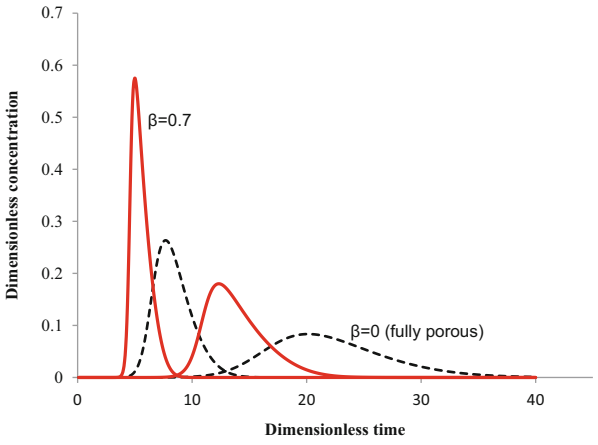

Fig. 9.7 Binary elution (pulse size $\tau_{imp} = 1$) using fully porous beads (*dashed lines*) and cored beads with $\beta = 0.7$ (*solid lines*) reproduced from data in Fig. 9.6

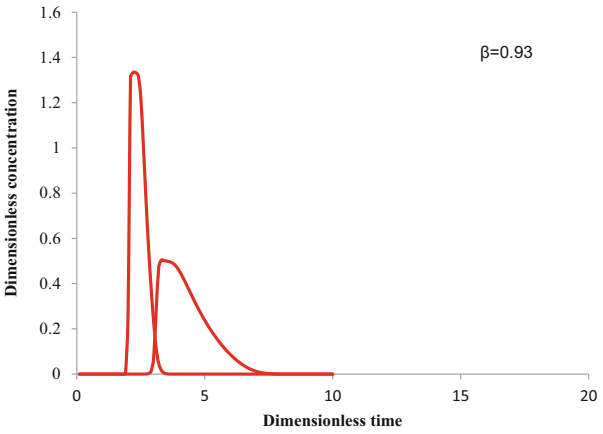

Fig. 9.8 Binary elution (pulse size $\tau_{imp} = 1$) using cored beads with $\beta = 0.93$

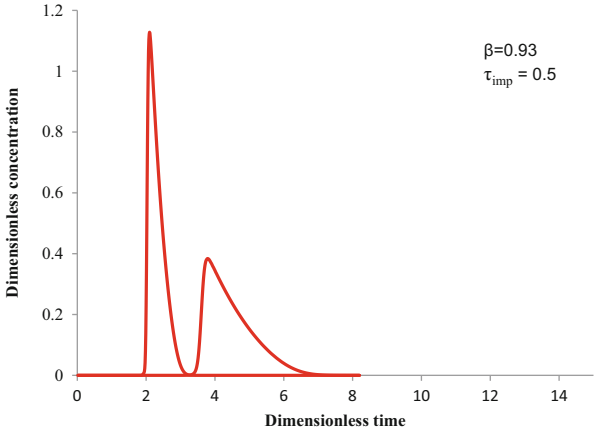

Fig. 9.9 Binary elution using cored beads ($\beta = 0.93$) with a reduced pulse size $\tau_{imp} = 0.5$

9.4 General Rate Model for SEC Using Cored Beads

As discussed in Chap. 8, SEC separation relies on the difference in intraparticle diffusion. Smaller molecules can penetrate more macropores, and thus their diffusion in and out of the particles takes more time, resulting in longer retention times. On the other hand, larger molecules have fewer macropores that are large enough for them to diffuse in and out. Thus, they have shorter retention times. A macromolecule such as blue dextran has the shortest retention time if it does not have any binding as a side effect. A small molecule such as a solvent molecule or salt ion will penetrate all the macropores in the particles. They have the longest retention time. All eluites will elute out between these two retention times unless they have nonspecific binding as a side effect. Because of the lack of a specific binding mechanism, peaks coming out of SEC columns are always diffused. When peaks are wider, peak resolution suffers. Improved mass transfer can reduce band

broadening and thus enhance resolution. Cored beads improve mass transfer inside particles because the radial distance for diffusion is greatly reduced. However, their solid cores reduce the amount of utilizable macropores for molecules to separate. Thus, an optimal core radius fraction exists for a particular SEC separation system.

Although cored beads have not been reported in the literature for actual SEC applications, it is reasonable to believe that cored beads offer performance enhancements. The general rate model for SEC using fully porous beads has been presented in Chap. 8. Its particle phase dimensionless PDE needs to be modified as below for SEC modeling:

$$\frac{\varepsilon_p^a}{\eta}\frac{\partial c_p}{\partial \tau} = \frac{1}{(1-\beta)^2}\cdot\frac{\partial^2 c_p}{\partial \gamma^2} + \frac{2}{\gamma(1-\beta)^2+\beta(1-\beta)}\cdot\frac{\partial c_p}{\partial \gamma} \tag{9.17}$$

with the following boundary conditions:

$$\text{at } \gamma = 0, \quad \partial c_p/\partial \gamma = 0 \tag{9.18}$$

$$\text{and at } \gamma = 1, \quad \partial c_p/\partial \gamma = \mathrm{Bi}\left(c_b - c_{p,r=1}\right) \tag{9.19}$$

Equation (9.17) is the same as Eq. (9.4) with the binding term removed and particle porosity changed to the accessible particle porosity defined for SEC in Chap. 8. There is no need for multicomponent formulation here because it is assumed that there is no interference among the different eluites in SEC. The numerical solution methods are similar to those discussed earlier in this chapter without the need for Langmuir isotherm. The SEC/SEC_CORED simulator has been created. It is available by contacting the author. By setting $\beta = 0$, this simulator is used as the SEC simulator for conventional fully porous beads as shown in Chap. 8.

9.5 Enhanced SEC Separation Using Cored Beads Predicted by Modeling

Luo et al. reported their theoretical findings that proved the hypothesis that cored beads enhance SEC separations [16]. They imagined that the commercial Bio-Rad P60 gel discussed in Chap. 8 could be made into cored beads for the separation of myoglobin (MW = 16,890) and ovalbumin (MW = 43,500). The physical parameters for the Bio-Rad P60 gel listed in Table 8.2 in Chap. 8 remain the same when a core is inserted into the beads. Figure 9.10 is a screenshot of the simulation of the separation of myoglobin from ovalbumin using a 5 cm × 30 cm SEC column. The solid lines are for fullyporous Bio-Rad P60 gel beads ($\beta = 0$) that are commercially available, and the dashed lines are for cored beads ($\beta = 0.8$) with Bio-Rad P60 gel shell that are not yet created in the lab as of the year 2014. The size exclusion factor F^{ex} (ExF in Fig. 9.10) values of 0.35 and 0.12 are from Table 8.2 in Chap. 8. The Pe_L, η, and Bi values in Fig. 9.10 can be obtained using the same parameter

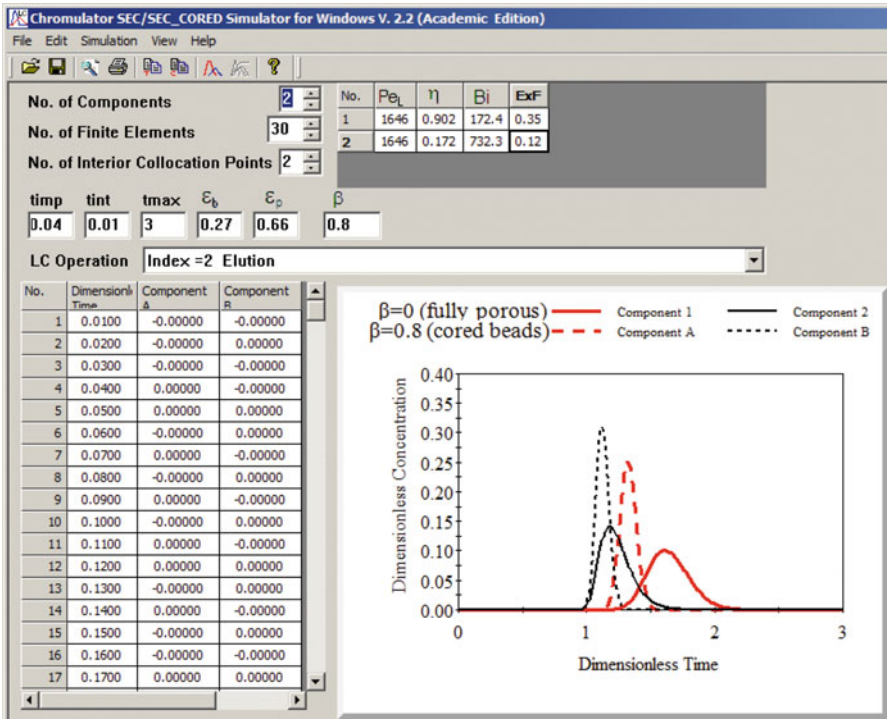

Fig. 9.10 Screenshot of SEC_CORED simulated for the comparison of binary SEC separation of myoglobin from ovalbumin on a 5 cm × 30 cm column packed with Bio-Rad P60 gel with a flow rate of 15.9 ml/min ($v = 0.05$ ml/s). *Dashed lines* are for cored beads with $\beta = 0.8$ (product not yet made), while *solid lines* are for fully porous beads. The first component is myoglobin and the second ovalbumin (eluted out earlier)

estimated methods discussed in Chaps. 4 and 8 as demonstrated by Luo et al. [16]. Table 8.3 can be directly used to obtain Pe_L, η, and Bi values for all the simulated myoglobin and ovalbumin SEC chromatograms in this chapter by plugging in new Q, L, d_c and MW values as needed.

For convenience and better views in comparison, the simulation solid lines are replotted in Fig. 9.11 (dashed lines) by converting dimensionless time to elution volume. Dimensionless time τ can be converted to elution volume V_e (ml) using the conversion formula $V_e = (V_b\varepsilon_b)\tau$, which is Eq. (8.19). For Fig. 9.11, the conversion relationship is $V_e = 159\tau$ ml because $\varepsilon_b = 0.27$ (Table 8.2) and $V_b = 589$ ml (Table 8.4).

Figure 9.10 shows that by using cored beads with $\beta = 0.8$ (reflecting a core volume fraction of 0.512), the separation time can be reduced from 2.1 to 1.5 (dimensionless), a saving of 29 % of time. The cored beads also give much sharper peaks. However, the two peaks still overlapped considerably. One strategy to improve the separation is to increase the column length. The dark black solid line

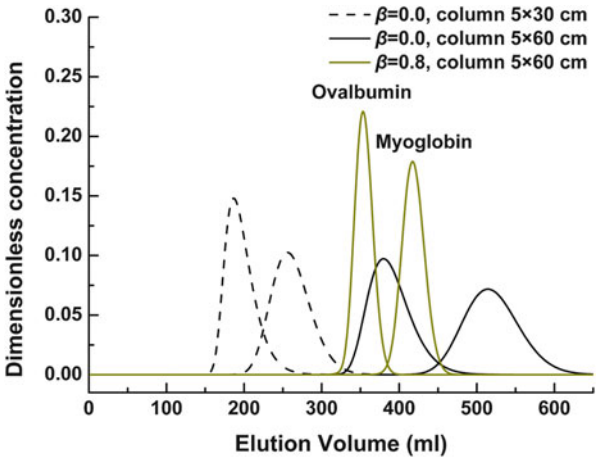

Fig. 9.11 Comparison of cored beads and fully porous beads, all with $v = 0.05$ cm/s and 6.36 ml sample size (from [16] with permission)

peaks in Fig. 9.11 indicate that peak overlapping is significantly reduced when the column length is increased from 30 to 60 cm without changing the flow rate. Consequently, the separation time is also increased by 82 % (calculated from elution volumes of 620 and 340 ml). In practice, doubling the bed length may present excessive bed compression due to increased pressure drop. This is why pancake-shaped columns are common in large-scale SEC applications. They suffer from flow distortion, resulting in deterioration of separation outcome. Because cored beads have a rigid solid cores that maintain their shape under pressure better, this results in column pressure drops several times lower than a column packed with fully porous beads [3]. This means the columns packed with cored beads have more room for axial direction scale-up. The two sharper peaks (lighter colored solid peaks that are the two tallest) in Fig. 9.11 demonstrate that when the column length increases from 30 to 60 cm for cored beads with $\beta = 0.8$, there is only a minor overlap between the ovalbumin and myoglobin peaks. In the meantime, separation time is decreased by 26 % compared with the column packed with fully porous beads of the same length (based on elution volume reduction from 620 to 460 ml).

Figure 9.12 is a screenshot with two sets of simulated chromatograms corresponding to the two cases in Fig. 9.11 with a column size of 5 cm × 60 cm (1,178 ml bed volume). In this case, dimensionless time τ is converted to elution volume using $V_e = (V_b\varepsilon_b)\tau = 318\tau$ ml. Note that, compared with Fig. 9.10 for the column size of 5 cm × 30 cm, the longer column case has Peclet and η numbers that are doubled, because their values are proportional to column length L according to Eqs. (4.32) and (4.34), respectively. In the meantime time, the sample pulse size is halved from 0.04 in Fig. 9.10 to 0.02 in Fig. 9.12 because of the following relationship:

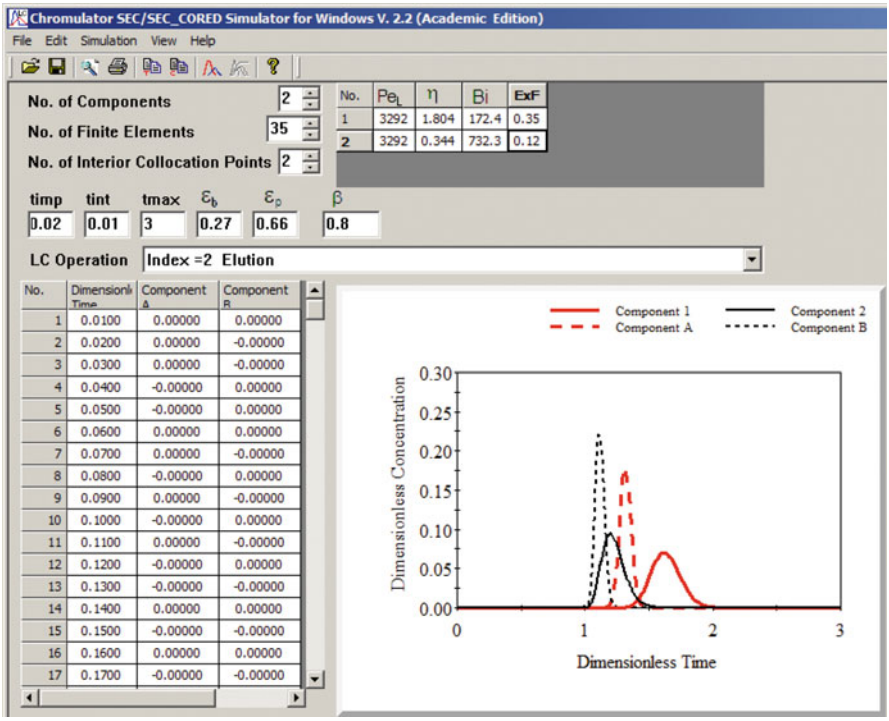

Fig. 9.12 Screenshot for the simulation of the two *solid-line* cases with 5×60 cm columns in Fig. 9.11

$$\tau_{\text{imp}} = \left(V_{\text{samp}}/Q\right)/(L/v) = 4V_{\text{samp}}/\left(\pi d^2 L \varepsilon_{\text{b}}\right) \tag{9.20}$$

which says τ_{imp} is inversely proportional to column length with a fixed dimensional sample volume (in ml). All the peaks in Fig. 9.11 have the same peak area, leading to the same sample volume of 6.36 ml.

Because cored beads exhibit bed pressure drops that are several times lower than fully porous beads with the same column dimensions [3], it is possible to scale up a column packed with cored beads by doubling the column length while using a flow rate that is twice as large. Figure 9.13 shows the comparison of ovalbumin separation from myoglobin using fully porous beds (dashed lines) and core beads (solid lines). The dashed lines are the same as the dashed lines in Fig. 9.11. Figure 9.13 demonstrates that by using cored beads with $\beta = 0.8$, better separation is achieved with a sample volume (12.7 ml) twice as large. Note that in Fig. 9.13, the peak areas for cored beads are twice as large as those for fully porous beads. Because the flow rate is doubled for cored beads, even though the elution volume increased from 340 to 470 ml, the real time for cored beads is still about 30 % shorter.

Figure 9.14 shows a screenshot for the simulation of the solid lines in Fig. 9.13. Compared with Fig. 9.10, the Peclet numbers in Fig. 9.14 are twice as large because

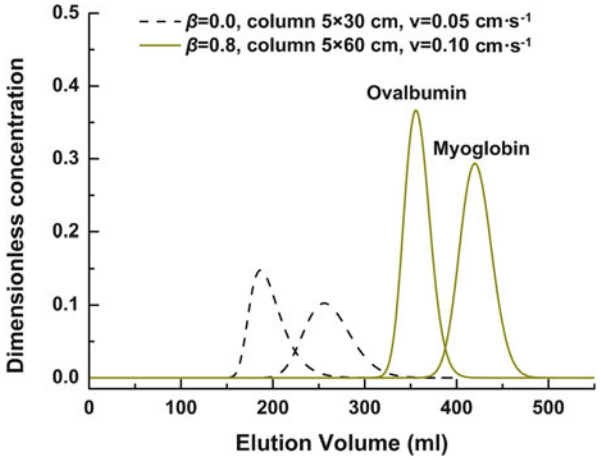

Fig. 9.13 Comparison of cored beads and fully porous beads using a doubled column length and doubled flow rate for cored beads (from [16] with permission)

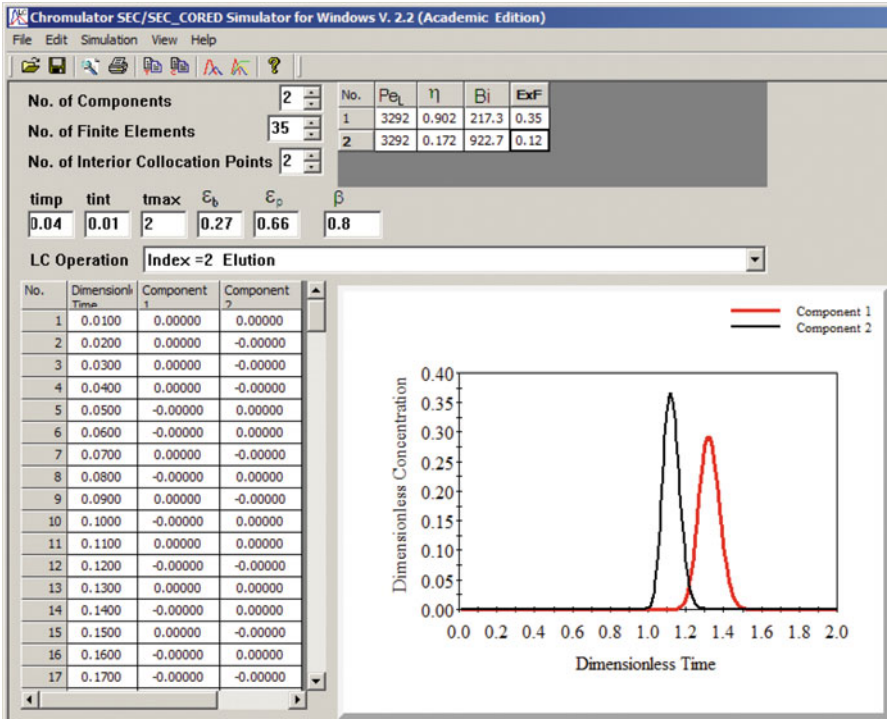

Fig. 9.14 Screenshot showing parameters used to simulate the *solid lines* in Fig. 9.13

of the doubling of column length according to Eq. (4.32). Because η is proportional to L/v, the doubling of both L and v values does change η values for both proteins. The Biot numbers for the two proteins increase by a factor of $2^{1/3}$ because they are proportional to k, that is in turn proportional to $v^{1/3}$ according to Eq. (4.38). One can verify the parameter changes by using the Microsoft Excel sheet in Table 8.3 for Pe_L, η, and Bi values in SEC.

9.6 Summary

Although cored beads remove a portion of effective separation media, its improved mass transfer provides sharper peaks and reduced separation time. Theoretical simulation results for both adsorption LC with Langmuir isotherm and SEC have demonstrated superiority of cored beads over fully porous beads. In practice, cored beads have been tested for adsorption LC and IEC, but not yet for SEC. The parameters used for SEC separation with cored beads are the same as those from the experimental work in Chap. 8. Because SEC separation is based on mass transfer only, computer simulation in Chap. 8 has indicated that simulation results fit preparative SEC chromatograms very well. Thus, it is reasonable to believe the theoretical predictions for cored beads. The simulation in this work will encourage vendors to create cored beads for SEC application. They will likely have a market advantage if their costs are not much higher than conventional fully porous beads.

References

1. Lee W-C (1997) Protein separation using non-porous sorbents. J Chromatogr B Biomed Sci Appl 699:29–45. doi:10.1016/S0378-4347(97)00179-5
2. Fekete S, Ganzler K, Fekete J (2010) Facts and myths about columns packed with sub-3 μm and sub-2 μm particles. J Pharm Biomed Anal 51:56–64. doi:10.1016/j.jpba.2009.08.003
3. Wang C, Soice NP, Ramaswamy S, Gagnon BA, Umana J, Cotoni KA, Bian N, Cheng K-SC (2007) Cored anion-exchange chromatography media for antibody flow-through purification. J Chromatogr A 1155:74–84. doi:10.1016/j.chroma.2007.04.030
4. Coutinho FM, Carvalho D, La Torre Aponte M, Barbosa CC (2001) Pellicular ion exchange resins based on divinylbenzene and 2-vinylpyridine. Polymer 42:43–48. doi:10.1016/S0032-3861(00)00343-8
5. Zhou X, Shi Q-H, Bai S, Sun Y (2004) Dense pellicular agarose–glass beads for expanded bed application: fabrication and characterization for effective protein adsorption. Biochem Eng J 18:81–88. doi:10.1016/S1369-703X(03)00169-4
6. Gu T, Liu M, Cheng K-SC, Ramaswamy S, Wang C (2011) A general rate model approach for the optimization of the core radius fraction for multicomponent isocratic elution in preparative nonlinear liquid chromatography using cored beads. Chem Eng Sci 66:3531–3539. doi:10.1016/j.ces.2011.04.021
7. Kirkland JJ, Truszkowski FA, Dilks CH Jr, Engel GS (2000) Superficially porous silica microspheres for fast high-performance liquid chromatography of macromolecules. J Chromatogr A 890:3–13. doi:10.1016/S0021-9673(00)00392-7

8. Liang P, Fan M, Cao X, Huang X, Wang C (2007) Composition and measurement of the apparent internal resistance in microbial fuel cell. Chin J Environ Sci 28:1894
9. Fanigliulo A, Cabooter D, Bellazzi G, Tramarin D, Allieri B, Rottigni A, Desmet G (2010) Comparison of performance of high-performance liquid chromatography columns packed with superficially and fully porous 2.5 μm particles using kinetic plots. J Sep Sci 33:3655–3665. doi:10.1002/jssc.201000463
10. Pietrogrande MC, Dondi F, Ciogli A, Gasparrini F, Piccin A, Serafini M (2010) Characterization of new types of stationary phases for fast and ultra-fast liquid chromatography by signal processing based on AutoCovariance function: a case study of application to *Passiflora incarnata* L. extract separations. J Chromatogr A 1217:4355–4364. doi:10.1016/j.chroma.2010.04.048
11. Horvath CG, Preiss BA, Lipsky SR (1967) Fast liquid chromatography. Investigation of operating parameters and the separation of nucleotides on pellicular ion exchangers. Anal Chem 39:1422–1428. doi:10.1021/ac60256a003
12. Ning J, Kong F, Li D, Du Y (1998) Preparation of monodisperse agglomerated pellicular anion-exchange resins compatible with high-performance liquid chromatography solvents for ion chromatography. J Chromatogr A 793:193–197. doi:10.1016/S0021-9673(97)00889-3
13. Cabooter D, Fanigliulo A, Bellazzi G, Allieri B, Rottigni A, Desmet G (2010) Relationship between the particle size distribution of commercial fully porous and superficially porous high-performance liquid chromatography column packings and their chromatographic performance. J Chromatogr A 1217:7074–7081. doi:10.1016/j.chroma.2010.09.008
14. Finlayson BA (2003) Nonlinear analysis in chemical engineering. Ravenna Park Publishing, Seattle
15. Manchón N, D'Arrigo M, García-Lafuente A, Guillamón E, Villares A, Ramos A, Martínez JA, Rostagno MA (2010) Fast analysis of isoflavones by high-performance liquid chromatography using a column packed with fused-core particles. Talanta 82:1986–1994. doi:10.1016/j.talanta.2010.08.050
16. Luo J, Zhou W, Su Z, Ma G, Gu T (2013) Comparison of fully-porous beads and cored beads in size exclusion chromatography for protein purification. Chem Eng Sci 102:99–105

Chapter 10
Modeling of Slow Kinetics and Affinity Chromatography

10.1 Introduction

Affinity chromatography is a powerful tool for the purification of enzymes, antibodies, antigens, and many other proteins and macromolecules that are important in scientific research and development of novel biological drugs. Affinity chromatography not only purifies a product, but also concentrates the product to a great extent [1]. Over the years, this subject has been reviewed by many people, including Chase [1] and Liapis [2]. Affinity chromatography is also called biospecific adsorption, since it utilizes the biospecific binding between solute molecules and immobilized ligands that is often compared with the fitting of a lock and its key. The monovalent binding between a ligand and a solute macromolecule is generally treated as second-order kinetics.

A class of monoclonal antibody used in affinity chromatography is immunoglobulin G, which has two identical antigen-binding sites. If the binding of one antigen does not interfere with the binding of another antigen onto the other binding site of the same antibody, then bindings can be considered as two monovalent bindings. If the antigen has more than one binding site that can be recognized by the antibody, multivalent bindings are possible. This was discussed by Chase [1]. There are two kinds of bindings in affinity chromatography, specific and nonspecific. The specific binding involves only the target macromolecule and the ligand. Nonspecific binding is an undesirable, but often unavoidable side effect. It can be caused by unintended ion exchange or hydrophobic interaction.

The operational stages of affinity chromatography often include adsorption, washing, and elution. The column is regenerated after each cycle. The adsorption stage is carried out in the form of a frontal adsorption similar to breakthrough analysis. In order to obtain a sharp concentration front for the target macromolecule, a small flow rate is often used [1]. The washing stage right after the adsorption

Electronic supplementary material The online version of this chapter (doi:10.1007/978-3-319-16145-7_10) contains supplementary material, which is available to authorized users.

© Springer International Publishing Switzerland 2015

T. Gu, *Mathematical Modeling and Scale-Up of Liquid Chromatography*,
DOI 10.1007/978-3-319-16145-7_10

stage is aimed at removing the impurities in the bulk fluid and in the stagnant fluid inside particle macropores and impurities bonded to the stationary phase via nonspecific binding such as ion exchange and hydrophobic interaction which are considered side effects [1].

The elution stage removes the bonded target macromolecules from the ligands. Elution can be carried out by using a soluble ligand that can be the same chemical as that immobilized in the stationary phase or its analog, provided that the soluble ligand is present in a higher concentration and is relatively inexpensive. The other method is called nonspecific desorption, which uses a variety of eluting agents, such as pH, protein denaturants, chaotropic agents, polarity-reducing agents, and temperature [1] to weaken the binding between the macromolecules and immobilized ligands. Elution in affinity chromatography has a different meaning from that used in other forms of chromatography, such as reversed phase and ion exchange, in which elution means impulse analysis. To avoid confusion, impulse analysis in affinity chromatography is referred as zonal analysis [3–5]. The Langmuir isotherm for biospecific binding, which is derived from the second-order kinetics at equilibrium, is characterized by a very large b (representing affinity), and a very small saturation capacity (C^{∞}), indicating that the ligand density of an affinity matrix is often quite low. Because of the large b value, the isotherm can be nonlinear even if the concentration of macromolecules is very low.

General rate models were developed by Arve and Liapis [6, 7] for affinity chromatography. Their models consider various mass transfer mechanisms and the second-order kinetics between the immobilized ligands and the macromolecules, and between the soluble ligands and the macromolecules during elution.

10.2 Effect of Reaction Kinetics

In the multicomponent rate model for adsorption in Chap. 3, it is assumed that there exists a local equilibrium for each component between the stagnant fluid phase inside macropores and the solid phase of the particles. This assumption may not be satisfied if the adsorption and desorption reaction rates are not high, or the mass transfer rates are relatively much faster. In such cases, isotherm expressions cannot be directly inserted into Eq. (3.10) to replace $c_{\mathrm{p}i}^{*}$. Instead, a second-order kinetics expression can be used. It has been widely adopted to account for reaction kinetics in the study of affinity chromatography [1, 4, 8–12]. A rate model with second-order kinetics was applied to affinity chromatography by Arve and Liapis [12].

The second-order kinetics assumes the following reversible binding and dissociation reactions:

$$\mathrm{P}_i + \mathrm{L} \underset{k_{\mathrm{d}i}}{\overset{k_{\mathrm{a}i}}{\rightleftharpoons}} \mathrm{P}_i\mathrm{L} \tag{10.1}$$

where P_i is component i in the fluid (often a protein) and L represents immobilized ligands. $k_{\mathrm{a}i}$ and $k_{\mathrm{d}i}$ are the adsorption and desorption reaction rate constants

for component i, respectively. The binding kinetics is of second order and the dissociation first order. The rate equation for Eq. (10.1) is expressed as follows:

$$\frac{\partial C^*_{\mathrm{p}i}}{\partial t} = k_{\mathrm{a}i} C_{\mathrm{p}i} \left(C^\infty - \sum_{j=1}^{N_\mathrm{s}} C^*_{\mathrm{p}i} \right) - k_{\mathrm{d}i} C^*_{\mathrm{p}i} \tag{10.2}$$

The rate constant $k_{\mathrm{a}i}$ has units of concentration over time while the rate constant $k_{\mathrm{d}i}$ has units of inverse time. If the reaction rates are relatively large compared to mass transfer rates, then instant adsorption/desorption equilibrium can be assumed such that the left-hand side of Eq. (10.2) can be set to zero, which subsequently gives the Langmuir isotherm with the equilibrium constant $b_i = k_{\mathrm{a}i}/k_{\mathrm{d}i}$ for component i.

Introducing dimensionless groups $\mathrm{Da}^i_{\mathrm{a}} = L(k_{\mathrm{a}i} C_{0i})/v$ and $\mathrm{Da}^{\mathrm{d}}_i = L k_{\mathrm{d}i}/v$ that are defined as the Damköhler numbers [13] for adsorption and desorption, respectively, Eq. (10.2) can be nondimensionalized as follows:

$$\frac{\partial c^*_{\mathrm{p}i}}{\partial \tau} = \mathrm{Da}^{\mathrm{a}}_i c_{\mathrm{p}i} \left(c^\infty - \sum_{j=1}^{N_\mathrm{s}} \frac{C_{0j}}{C_{0i}} c^*_{\mathrm{p}j} \right) - \mathrm{Da}^{\mathrm{d}}_i c^*_{\mathrm{p}i} \tag{10.3}$$

If the molar saturation capacities are the same for all the components in order to achieve thermodynamic consistency [14], at equilibrium, Eq. (10.3) gives $b_i C_{0i} = \mathrm{Da}^{\mathrm{a}}_i / \mathrm{Da}^{\mathrm{d}}_i$ and $a_i = C^\infty b_i = c^\infty \mathrm{Da}^{\mathrm{a}}_i / \mathrm{Da}^{\mathrm{d}}_i$ which leads to the multicomponent Langmuir isotherm.

Equation (10.3), which is an ODE, replaces the Langmuir isotherm and it does not complicate the numerical procedure for the solution of the model since the discretization process is untouched. One only has to combine Eq. (10.3) with the ODE system resulted from the discretization of Eqs. (3.9) and (3.10). This is an initial-value ODE problem. With the trial values of $c_{\mathrm{b}i}$, $c_{\mathrm{p}i}$, and $c^*_{\mathrm{p}i}$ in the function subroutine in the Fortran 77 code, their derivatives can be readily evaluated from the three ODE expressions. If Ne elements and N interior collocation points are used for the discretization of Eqs. (3.9) and (3.10), there will be $N_\mathrm{s}(2N_\mathrm{e}+1)(2N+1)$ ODEs in the final ODE system, which are $N_\mathrm{s}(2N_\mathrm{e}+1)N$ more than in the equilibrium case [15]. These extra ODEs come from Eq. (10.3) at each element node and each interior collocation point for each component. N_e quadratic elements correspond to $(2N_\mathrm{e}+1)$ element nodes.

A general rate model with second-order kinetics has been solved in the Fortran 77 code named KINETIC.FOR by the author. Size exclusion effect is included in the model by replacing Eq. (3.10) with Eq. (8.8), i.e., replacing the particle porosity with the accessible particle porosity. It has been compiled into KINETIC.DLL Fortran dynamic link library file and interfaced with a C++ GUI in Chromulator 2.2. Figure 10.1 (added) is a screenshot for the simulation of a single-component breakthrough curve with slow kinetics. In Fig. 10.1, the size exclusion factor F^{ex} (ExF in the screenshot) is set to unity (i.e., no size exclusion effect). The KINETIC simulator can be used to study kinetic effects for slow binding and dissociation. The three breakthrough curves in Fig. 10.2 show the effect of reaction rates in three different

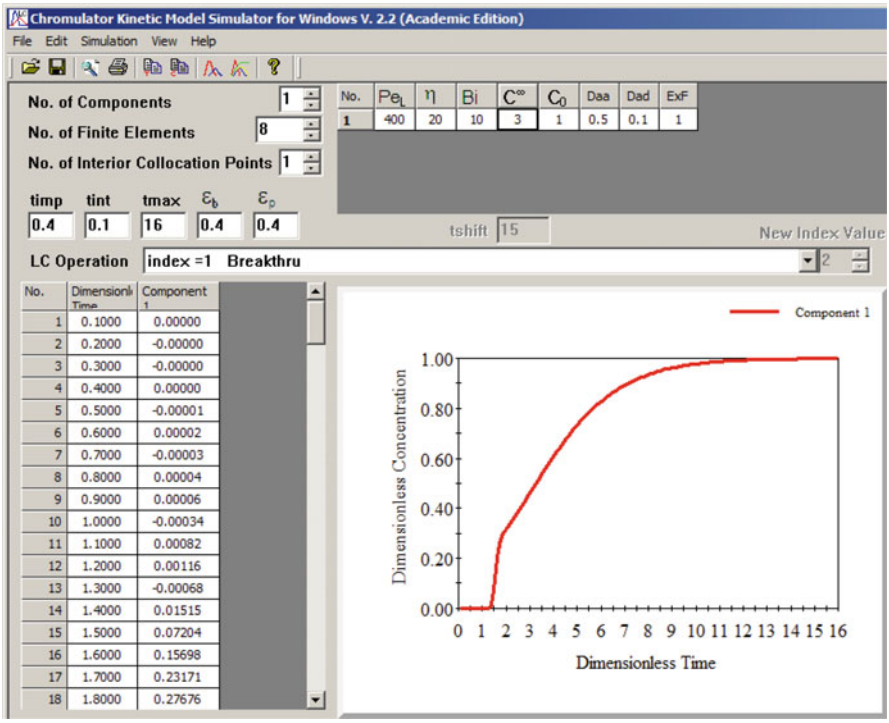

Fig. 10.1 Screenshot of KINECTIC simulator for the simulation of breakthrough of a compound with slow kinetics for binding and dissociation

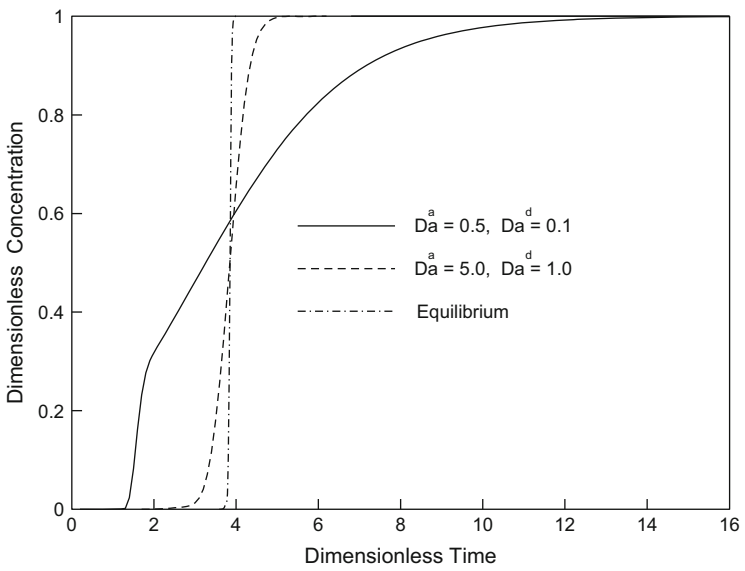

Fig. 10.2 Effect of reaction rates in frontal analysis

single-component systems. The solid line (data from Fig. 10.1) shows that when the Damköhler numbers for binding and dissociation are low, the breakthrough curve takes off sharper and earlier. It levels off later slowly. This is due to slow reaction rates.

Figure 10.3 shows that when the reaction rates increase to some extent, the breakthrough curves will be very close to that of the equilibrium case. In fact, the equilibrium case is the asymptotical limit of the results obtained from the kinetic model with large Damköhler numbers. The simulation input parameters for Fig. 10.3 are the same as in Fig. 10.1 except the Damköhler numbers.

Figure 10.4 shows the effect of reaction rates in a single-component zonal elution case. The solid line shows that the elution peak appears early with a very sharp front, but it has a very long tail. This indicates that when the reaction rates are very low, a large portion of the solute molecules do not have a chance to bind with the ligands and they are eluted out quite quickly. On the other hand, those molecules that do bind with the ligands are dissociated very slowly, causing a long tail. This is partially reflected by the breakthrough curve shown as the solid line in Fig. 10.2 since the two operational modes are interrelated. Figure 10.4 also shows that the peak front appears later, and the peak height becomes lower when the reaction rates increase. When the reaction rates further increase, the appearance of the peak front is delayed even more, and the peak height increases. The increase of reaction rates reduces the tailing effect and sharpens the peak front (Fig. 10.4). Figure 10.5 (added figure) shows the screenshot for the simulation of the solid line in Fig. 10.4.

In Fig. 10.6, the solid line is the same as that in Fig. 10.2. Figure 10.6 shows that the slow reaction rates are the rate-limiting steps in this case. Changing mass transfer parameters Pe_L, η, and Bi does not yield significant differences in the breakthrough curve. Changing the number of interior collocation point (N) from 1 to 3 does not yield significant differences either. On the contrary, Fig. 10.7a shows

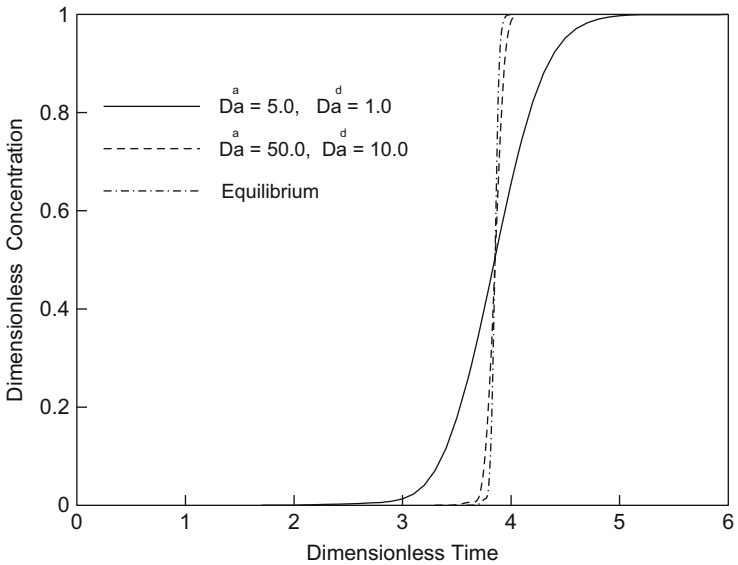

Fig. 10.3 Fast reaction rates vs. equilibrium

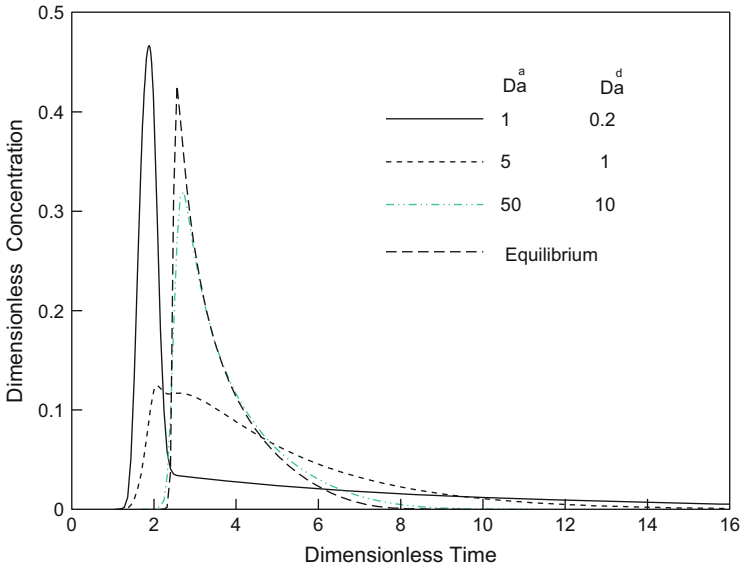

Fig. 10.4 Effect of reaction rates in zonal analysis

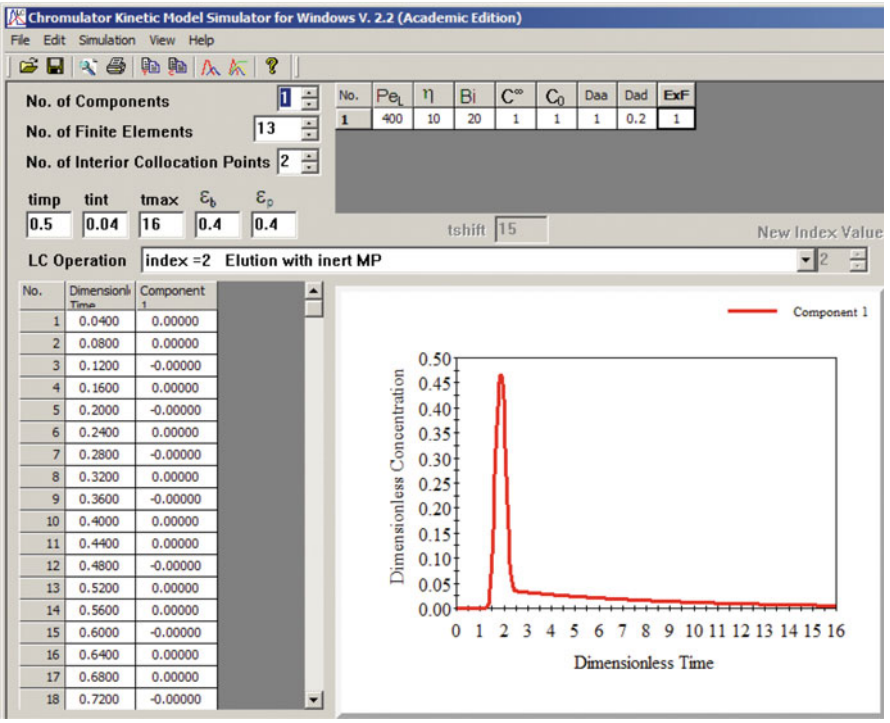

Fig. 10.5 Screenshot of KINECTIC simulator for the simulation of zonal analysis with slow kinetics

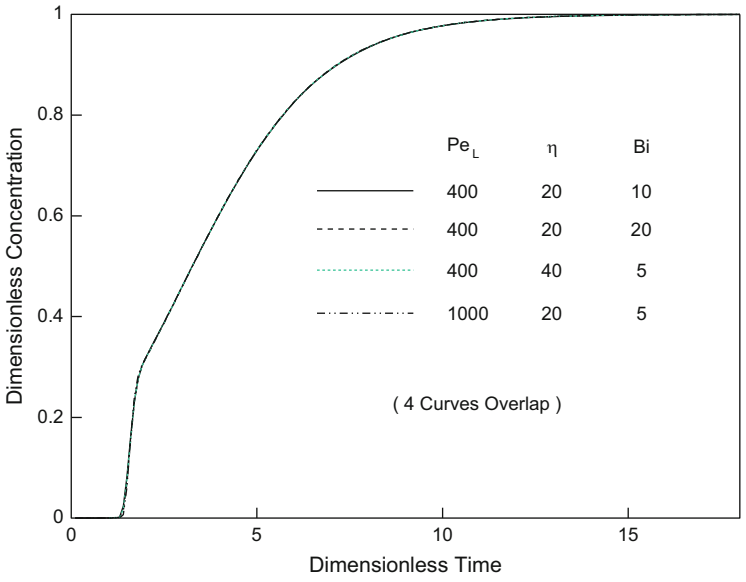

Fig. 10.6 Slow kinetics as rate-limiting step in frontal analysis

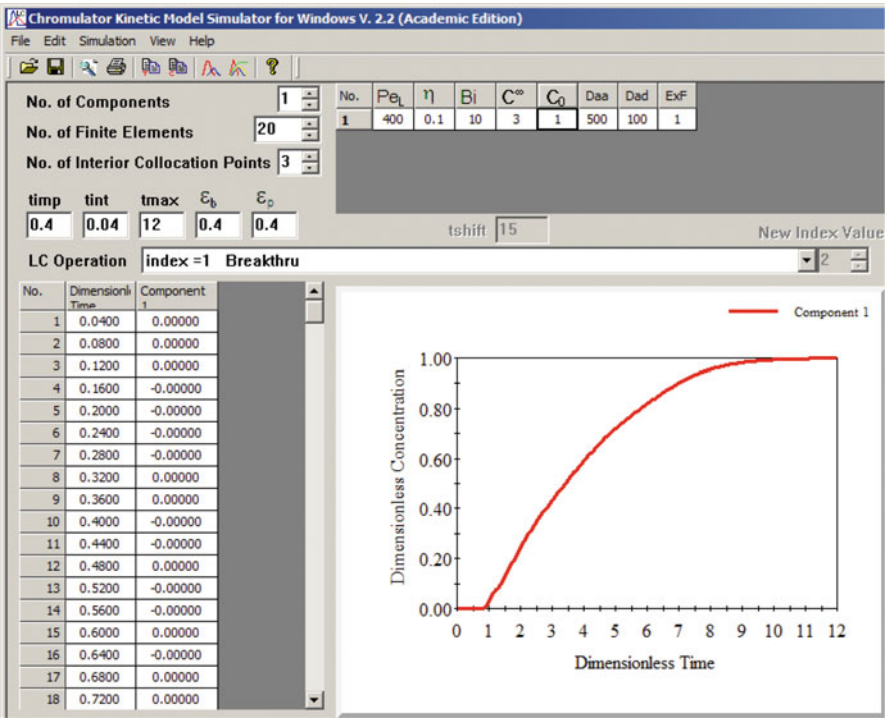

Fig. 10.7 (**a**) Screenshot of KINECTIC simulator for the simulation of breakthrough of slow mass transfer case using $N = 3$. (**b**) Screenshot of KINECTIC simulator for the simulation of breakthrough of slow mass transfer case using $N = 2$

a case in which the mass transfer rates are rate limiting, since the reaction rates in the figure are relatively much higher than the mass transfer rates. Increasing Da^a and Da^d values 10 times would not cause any significant change in the breakthrough curve. However, when N is set to 2, Fig. 10.7b shows two small humps, suggesting that $N = 2$ is insufficient for this slow mass transfer case because the particle phase concentration profile is more sophisticated than $N = 2$ can handle accurately.

The breakthrough curve of an adsorption system with slow mass transfer rates is somewhat similar to that with slow reaction rates. Both take off sharper and earlier and then level off later slowly. Figure 10.8 shows simulated breakthrough curve with slow kinetics (dashed line) superimposed on the simulated curve of slow mass transfer (solid line with parameter table embedded in the screenshot. The two cases differ in a revealing way. For the slow mass transfer case, the breakthrough curve takes off earlier (at τ slightly less than 1) than in the case with slow reaction rates, since in the former case, a significant portion of solute molecules do not enter the particles, while in the latter case they do. The slow mass transfer here means that both the external film mass transfer and intraparticle diffusion rates are low. The solid line in Fig. 10.9a shows that the take-off of the breakthrough curve is very sharp if the film mass transfer coefficient is small even through the intraparticle diffusion coefficient is not, since many solute molecules do not have a chance to penetrate the liquid film into the macropores of the particles. The parameters for simulation for the solid line in Fig. 10.9a can be found in Fig. 10.9b.

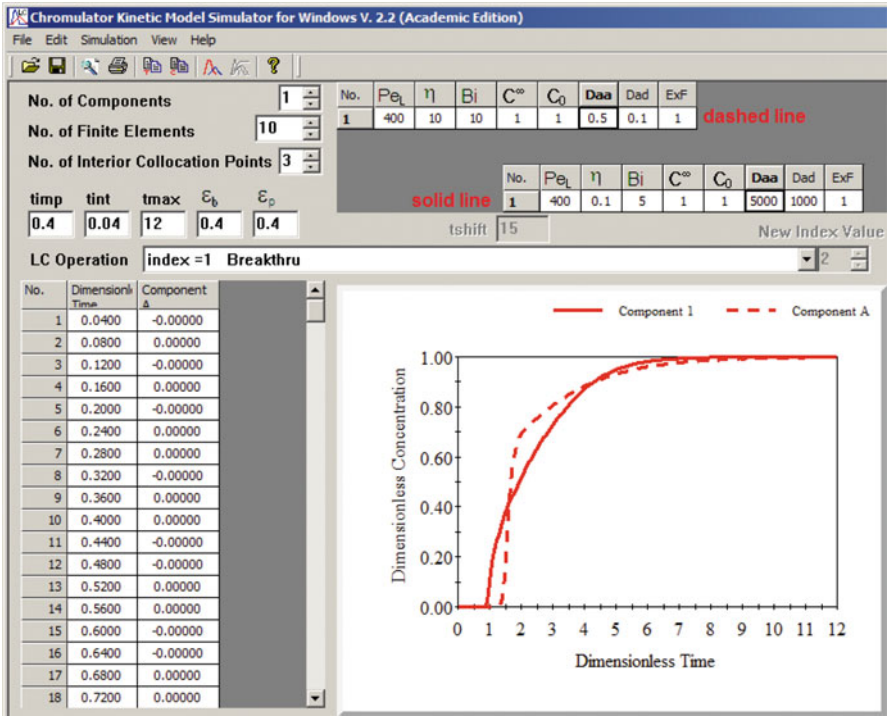

Fig. 10.8 Comparison slow kinetics (*dashed lines*) with slow mass transfer (*solid lines*)

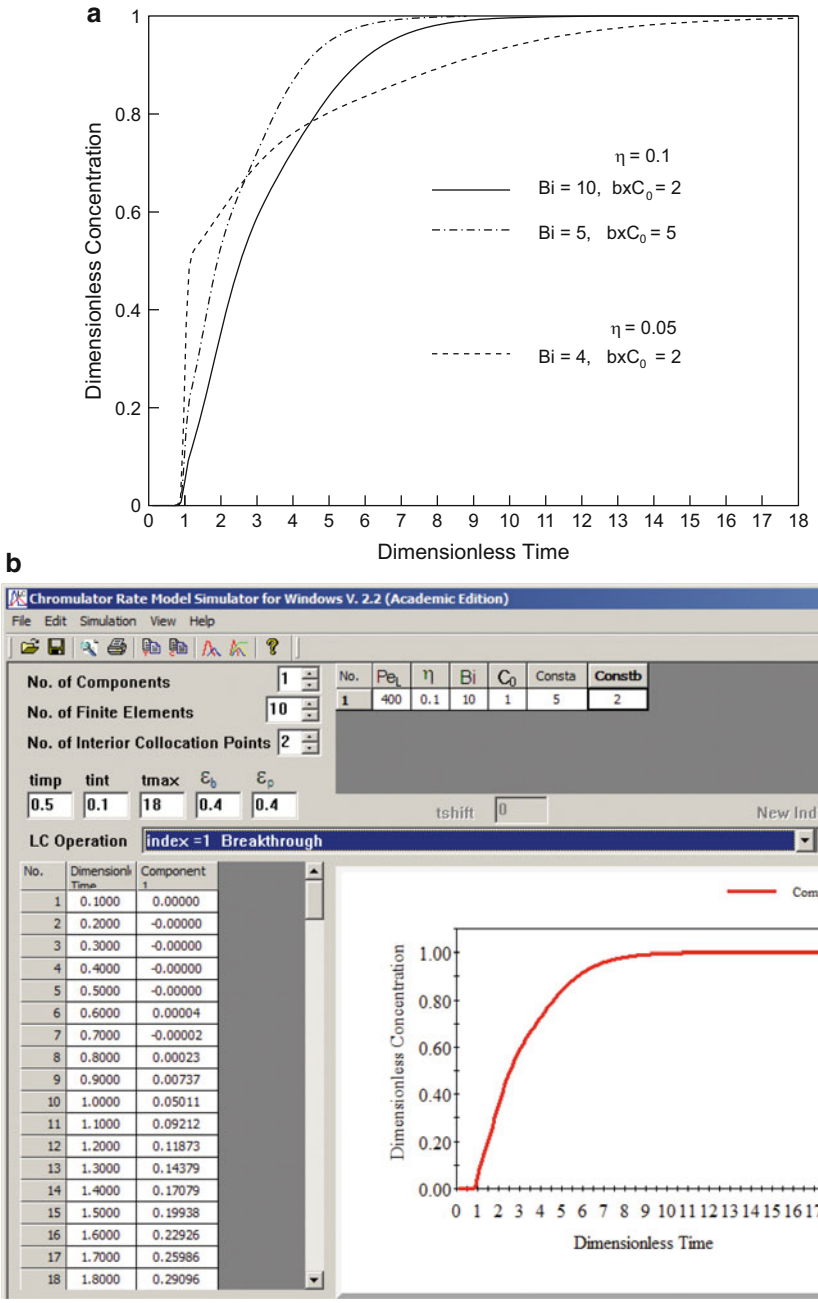

No.	Dimensionless Time	Component 1
1	0.1000	0.00000
2	0.2000	-0.00000
3	0.3000	-0.00000
4	0.4000	-0.00000
5	0.5000	-0.00000
6	0.6000	0.00004
7	0.7000	-0.00002
8	0.8000	0.00023
9	0.9000	0.00737
10	1.0000	0.05011
11	1.1000	0.09212
12	1.2000	0.11873
13	1.3000	0.14379
14	1.4000	0.17079
15	1.5000	0.19938
16	1.6000	0.22926
17	1.7000	0.25986
18	1.8000	0.29096

Fig. 10.9 (**a**) Effect of slow intraparticle diffusion and film mass transfer. (**b**) Screenshot of breakthrough simulation for the slow mass transfer case in Fig. 10.9a (*solid line*)

10.3 Effect of Size Exclusion

The effect of size exclusion on adsorption saturation capacity has been discussed in Chap. 8. The reduction of the column hold-up capacity due to the effect of size exclusion is clearly shown in Fig. 10.10. The two single-component breakthrough curves have the same conditions except that the dashed line case has a size exclusion effect such that half of the particle porosity is inaccessible, i.e., $F^{ex} = \varepsilon_p^a/\varepsilon_p = 0.5$. The capacity in the size exclusion case has been set to half of that of the case without size exclusion (solid line). Figure 10.10 shows that in the case of size exclusion, the breakthrough curve tends to be sharper. This is also true for a system with no adsorption as shown in Fig. 10.11. In both Figs. 10.10 and 10.11, the column hold-up capacity area (CA) can be calculated from the following equation which is from Eq. (4.18) by replacing ε_p with ε_p^a:

$$\mathrm{CA} \cdot \varepsilon_b = \varepsilon_b + (1-\varepsilon_b)\varepsilon_p^a + (1-\varepsilon_b)\left(1-\varepsilon_p\right)\frac{bC^\infty}{1+bC_0} \tag{10.4}$$

The third term on the right-hand side of Eq. (10.4) uses ε_p instead of ε_p^a, because C^∞ is based on particle skeleton. The first breakthrough curve on the left of Fig. 10.11 shows a case with complete size exclusion ($F^{ex} = 0$). It has the smallest

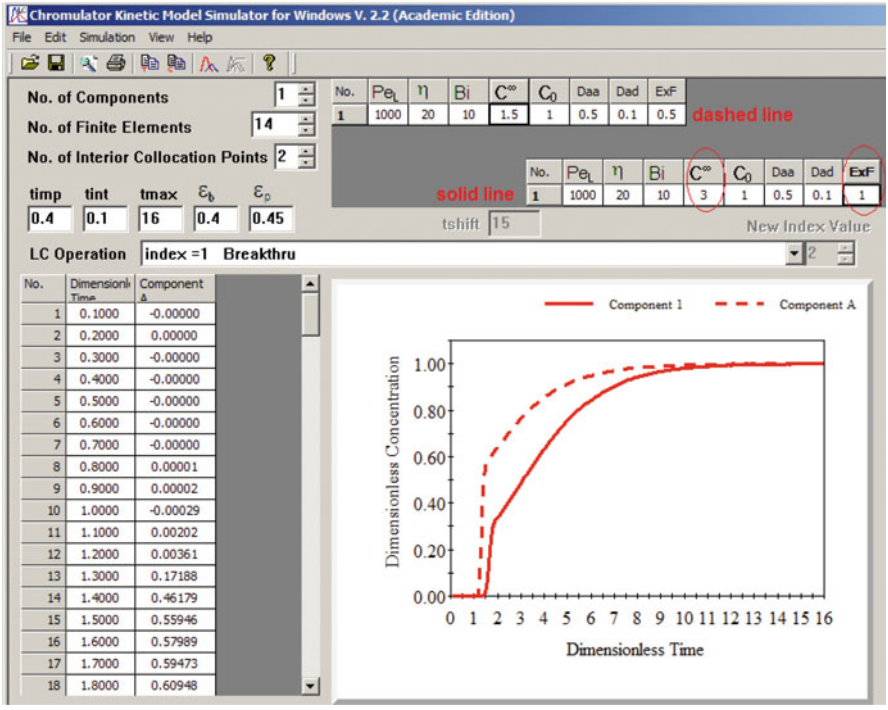

Fig. 10.10 Breakthrough without size exclusion effect (*solid line*) compared with breakthrough having size exclusion effect with 50 % reduction of saturation capacity (*dashed line*)

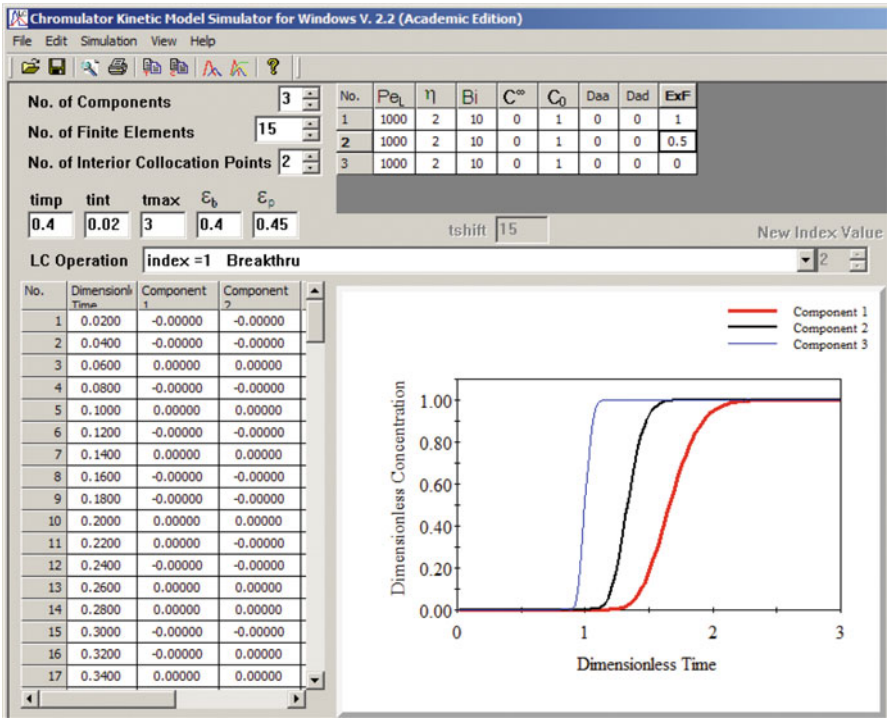

Fig. 10.11 Size exclusion effect in the absence of binding

CA value of unity from the integration of the breakthrough curve, which is consistent with Eq. (10.4) after dropping the second term and third term on the right-hand side. One may expect this kind of case when using a totally nonpenetrating and nonbinding substance (e.g., blue dextran) to measure the bed void volume fraction based on Eq. (4.3). The three breakthrough curves in Fig. 10.11 demonstrate that when the size exclusion effect is more severe, the column holds less solute than expected. It should be noted that in Fig. 10.11, there is no interference among the three components in the absence of any binding, which makes the simulation run equivalent to three separate one-component runs.

10.4 Interaction Between Soluble Ligand and Macromolecule

Soluble ligands can be used to elute the adsorbed macromolecules in the elution stage, if the ligands are not expensive and can be easily separated from the macromolecules after elution [1]. A rate model involving soluble ligand used for the elution of a single adsorbate was reported by Arve and Liapis [6, 16] for finite bath and fixed-bed (i.e., column) operations.

10.4.1 Modeling of Reaction in the Fluid

The kinetic rate model above can be extended to include a binding reaction in the bulk fluid and the stagnant fluid inside macropores of the particles between macromolecule P (component 1) and soluble ligand I (component 2). The complex formed from the binding of P and I is PI (component 3).

$$\mathrm{P} + \mathrm{I} \underset{k_{\mathrm{d2}}}{\overset{k_{\mathrm{a2}}}{\leftrightarrows}} \mathrm{PI} \tag{10.5}$$

In Eq. (10.5), k_{a2} and k_{d2} are the association and dissociation reaction rate constants for P and I, respectively. The binding between the macromolecule and the immobilized ligand L forms PL,

$$\mathrm{P} + \mathrm{L} \underset{k_{\mathrm{d1}}}{\overset{k_{\mathrm{a1}}}{\leftrightarrows}} \mathrm{PL} \tag{10.6}$$

It is assumed that each macromolecule can bind with only one ligand, I or L, and there is no interaction between the two different ligands, I and L.

Size exclusion effect in a system that involves large molecules, such as P, PL, and possibly L, may not be negligible. If so, they should be included in the model. For simplicity, only a three-component system is discussed here, since a generalized system in this case is cumbersome to present. The extension of the kinetic rate model can be carried out as follows:

1. Bulk-Fluid Phase-Governing Equation
   where $f(i) = -1$ is for components 1 and 2 ($i = 1,2$), and $f(i) = 1$ for component 3 ($i = 3$).

$$\begin{aligned} &-D_{\mathrm{b}i}\frac{\partial^2 C_{\mathrm{b}i}}{\partial Z^2} + v\frac{\partial C_{\mathrm{b}i}}{\partial Z} + \frac{\partial C_{\mathrm{b}i}}{\partial t} + \frac{3k_i(1-\varepsilon_{\mathrm{b}})}{\varepsilon_{\mathrm{b}}R_{\mathrm{p}}}\left(C_{\mathrm{b}i} - C_{\mathrm{p}i,R=R_{\mathrm{p}}}\right) \\ &\quad - f(i)\left(k_{\mathrm{a2}}C_{\mathrm{b1}}C_{\mathrm{b2}} - k_{\mathrm{d2}}C_{\mathrm{b3}}\right) \\ &\quad = 0 \end{aligned} \tag{10.7}$$

$$\begin{aligned} &g(i)\left(1-\varepsilon_{\mathrm{p}}\right)\frac{\partial C^*_{\mathrm{p}i}}{\partial t} + \varepsilon^{\mathrm{a}}_{\mathrm{p}i}\frac{\partial C_{\mathrm{p}i}}{\partial t} - \varepsilon^{\mathrm{a}}_{\mathrm{p}i}D_{\mathrm{p}i}\left[\frac{1}{R^2}\frac{\partial}{\partial R}\left(R^2\frac{\partial C_{\mathrm{p}i}}{\partial R}\right)\right] \\ &\quad - f(i)\varepsilon^{\mathrm{a}}_{\mathrm{p}i}\left(k_{\mathrm{a2}}C_{\mathrm{p1}}C_{\mathrm{p2}} - k_{\mathrm{d2}}C_{\mathrm{p3}}\right) \\ &\quad = 0 \end{aligned} \tag{10.8}$$

2. Particle Phase-Governing Equation

$$\frac{\partial C^*_{\mathrm{p1}}}{\partial t} = k_{\mathrm{a1}}C_{\mathrm{p1}}\left(C^{\infty}_{\mathrm{l}} - C^*_{\mathrm{p1}}\right) - k_{\mathrm{d1}}C^*_{\mathrm{p1}} \tag{10.9}$$

in which $g(i) = 1$ for $i = 1$, and $g(i) = 0$ for $i = 2,3$, since only component 1 binds with the immobilized ligand. The use of sign changers, $f(i)$ and $g(i)$, is purely for the compactness of the model system in its written form. Note that C^*_{p1} represents concentration [PL] in the stationary phase.

The model system presented here is more general than a similar one presented by Arve and Liapis [6] since size exclusion is included. This model seems to be more like a model for a fixed-bed reactor than a model for chromatography, because there is a new component (PI) forming and leaving the column.

Defining the following dimensionless constants:

$$c_{\mathrm{b}i} = C_{\mathrm{b}i}/C_{0i}, \quad c_{\mathrm{p}i} = C_{\mathrm{p}i}/C_{0i}, \quad c^*_{\mathrm{p}i} = C^*_{\mathrm{p}i}/C_{0i}, \quad c_1^{\infty} = C_1^{\infty}/C_{01}, \quad r = R/R_{\mathrm{p}}, \quad z = Z/L$$
$$\mathrm{Pe}_{\mathrm{L}i} = vL/D_{\mathrm{b}i}, \quad \mathrm{Bi}_i = k_i R_{\mathrm{p}}/\left(\varepsilon^{\mathrm{a}}_{\mathrm{p}i} D_{\mathrm{p}i}\right), \quad \eta_i = \varepsilon^{\mathrm{a}}_{\mathrm{p}i} D_{\mathrm{p}i} L/(Rv), \quad \xi_i = 3\mathrm{Bi}_i \eta_i (1-\varepsilon_{\mathrm{b}})/\varepsilon_{\mathrm{b}}$$
$$\tau = vt/L, \quad \mathrm{Da}_1^{\mathrm{a}} = L(k_{\mathrm{a}1}C_{01})/v, \quad \mathrm{Da}_1^{\mathrm{d}} = Lk_{\mathrm{d}1}/v, \quad \mathrm{Da}_2^{\mathrm{a}} = L(k_{\mathrm{a}2}C_{01})/v, \quad \mathrm{Da}_2^{\mathrm{d}} = Lk_{\mathrm{d}2}/v$$

the PDE system can be expressed in dimensionless forms as follows:

$$-\frac{1}{\mathrm{Pe}_{\mathrm{L}i}}\frac{\partial^2 c_{\mathrm{b}i}}{\partial z^2} + \frac{\partial c_{\mathrm{b}i}}{\partial z} + \frac{\partial c_{\mathrm{b}i}}{\partial \tau} + \xi_i\left(c_{\mathrm{b}i} - c_{\mathrm{p}i,r=1}\right) - f(i)\left(\mathrm{Da}_2^{\mathrm{a}} c_{\mathrm{b}1}\frac{C_{02}}{C_{0i}}c_{\mathrm{b}2} - \mathrm{Da}_2^{\mathrm{d}}\frac{C_{03}}{C_{0i}}c_{\mathrm{b}3}\right) = 0 \tag{10.10}$$

$$g(i)\left(1-\varepsilon_{\mathrm{p}}\right)\frac{\partial c^*_{\mathrm{p}i}}{\partial \tau} + \varepsilon^{\mathrm{a}}_{\mathrm{p}i}\frac{\partial c_{\mathrm{p}i}}{\partial \tau} - f(i)\varepsilon^{\mathrm{a}}_{\mathrm{p}i}\left(\mathrm{Da}_2^{\mathrm{a}} c_{\mathrm{p}1}\frac{C_{02}}{C_{0i}}c_{\mathrm{p}2} - \mathrm{Da}_2^{\mathrm{d}}\frac{C_{03}}{C_{0i}}c_{\mathrm{p}3}\right) - \eta_i\frac{1}{r^2}\frac{\partial}{\partial r}\left(r^2\frac{\partial c_{\mathrm{p}i}}{\partial r}\right) = 0 \tag{10.11}$$

$$\frac{\partial c^*_{p1}}{\partial \tau} = \mathrm{Da}_1^{a} c_{\mathrm{p}1}\left(c_1^{\infty} - c^*_{\mathrm{p}1}\right) - \mathrm{Da}_1^{\mathrm{d}} c^*_{\mathrm{p}1} \tag{10.12}$$

Since C_{03} is not known before simulation, it is replaced by C_{01} for the nondimensionalization of the concentrations of component 3 such that $C_{\mathrm{b}3} = c_{\mathrm{b}3}C_{01}$ and $C_{\mathrm{p}3} = c_{\mathrm{p}3}C_{01}$. For convenience, $\mathrm{Da}_2^{\mathrm{a}}$ definition uses C_{01} instead of C_{02}. This brings a benefit when investigating the effect of an increase of soluble ligand (component 2) on elution because $\mathrm{Da}_2^{\mathrm{a}}$ will remain unchanged. Note that Gu et al. [17] used C_{02} instead of C_{01} in the definition of $\mathrm{Da}_2^{\mathrm{a}}$; they had C_{01}/C_{0i} instead of C_{02}/C_{0i} in Eqs. (10.10) and (10.11). Only the following two lines are different in the Fortran source code AFFINITY.FOR:

if C_{01} is used in the definition of Da_2^a (this book chapter):
rb(i) = daa(2)*cb(i,1)***c0(2)***cb(i,2) − dad(2)*c0(3)*cb(i,3)
rp(j) = daa(2)*cp(j,1)***c0(2)***cp(j,2) − dad(2)*c0(3)*cp(j,3);
if C_{02} is used in the definition of Da_2^a (Gu et al. [17]):
rb(i) = daa(2)*cb(i,1)***c0(1)***cb(i,2) − dad(2)*c0(3)*cb(i,3)
rp(j) = daa(2)*cp(j,1)***c0(1)***cp(j,2) − dad(2)*c0(3)*cp(j,3)

10.4.2 Solution Strategy

The numerical procedure for the kinetic model can be modified to implement the fluid phase reaction. For the bulk-fluid phase, the finite element vector (**AFB**$_i$) should now include the last term of Eqs. (10.10) and (10.13) should be used to replace Eq. (3.28).

$$(\mathbf{AFB}_i)_m^{\mathrm{e}} = \int \left[\xi_i \phi_m c_{\mathrm{p}i,r=1} + \phi_m f(i) \left(\mathrm{Da}_2^{\mathrm{a}} c_{\mathrm{b}1} \frac{C_{02}}{C_{0i}} c_{\mathrm{b}2} - \mathrm{Da}_2^{\mathrm{d}} \frac{C_{03}}{C_{0i}} c_{\mathrm{b}3} \right) \right|_{\mathrm{e}} \mathrm{d}z \quad (10.13)$$

The modification of the particle phase-governing equation is straightforward. Details are omitted here. The simulator based on the model system is called

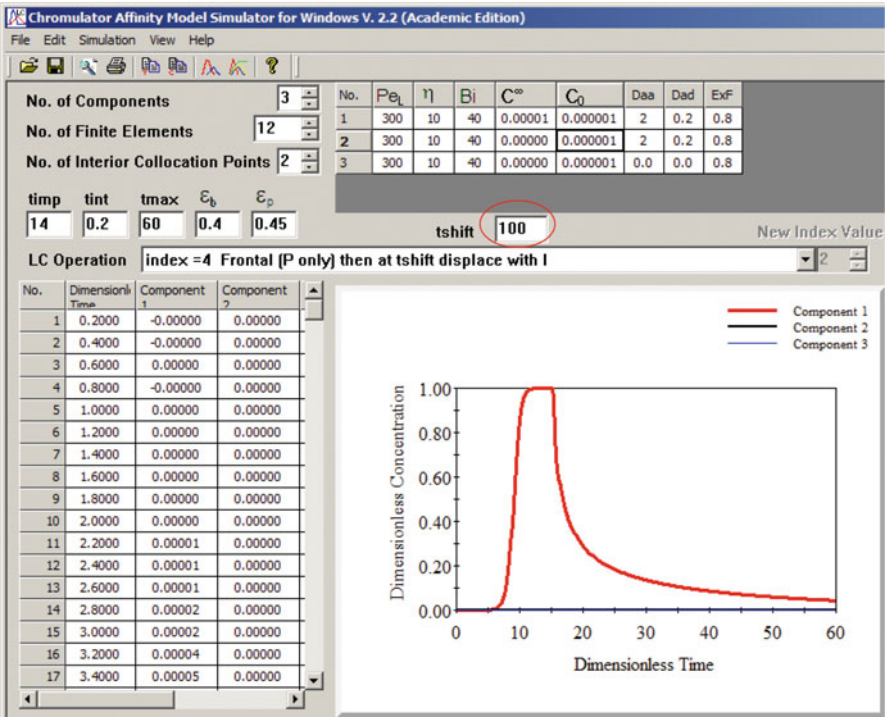

Fig. 10.12 Frontal adsorption stage combined with wash stage in affinity chromatography

AFFINITY simulator. In the simulator, index = 4 is for frontal adsorption lasting *timp* dimensionless time followed by a wash stage with a mobile phase to remove solutes adsorbed on the stationary phase with nonspecific binding. At *tshift* (dimensionless time), soluble ligand is introduced into the column to start the elution stage. The wash stage time duration is the difference between *tshift* and *timp*.

10.5 Modeling of the Three Stages in Affinity Chromatography

Figure 10.12 shows an affinity chromatographic separation with a wash stage after the frontal adsorption stage is terminated at $\tau = 14$. The nonspecifically bound impurities are not included in the simulation. Their effluent histories can be simulated in a separate run and then superimposed onto the current figure, since they do not interact with the macromolecule. Because no soluble ligand or other active eluting agent is used for the elution, the simulated chromatogram shows a very long tail. It indicates that the recovery of the macromolecule is difficult and not efficient.

Figure 10.13 has the same condition as Fig. 10.12, except that soluble ligands are used for elution at $\tau = 15$ after the wash stage that started at $\tau = 14$ and ended at $\tau = 15$. Compared with Fig. 10.12, it is obvious that elution using soluble ligands

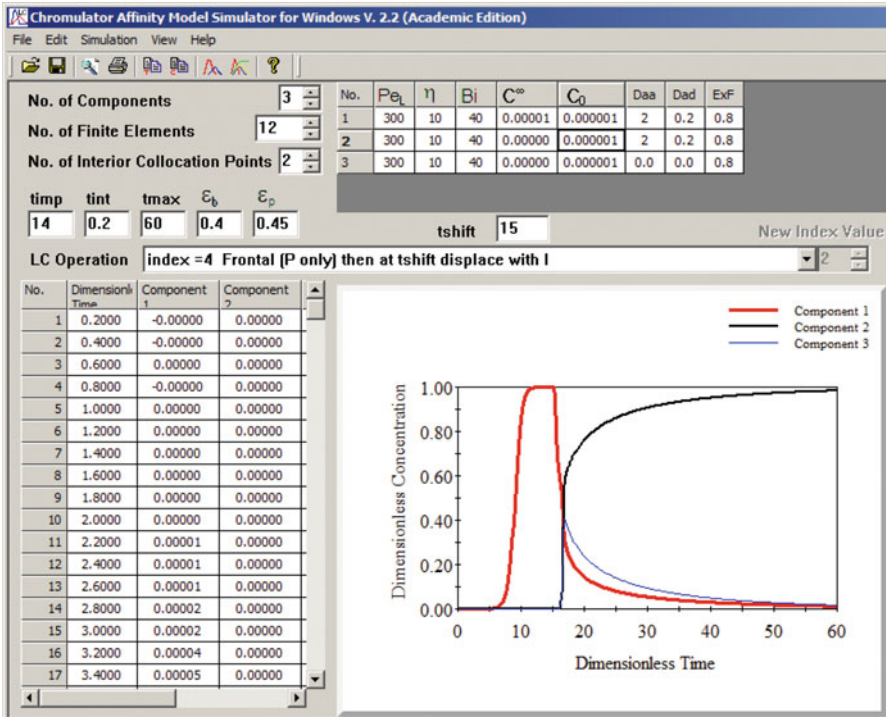

Fig. 10.13 Effect of using a soluble ligand in the elution stage of affinity chromatography

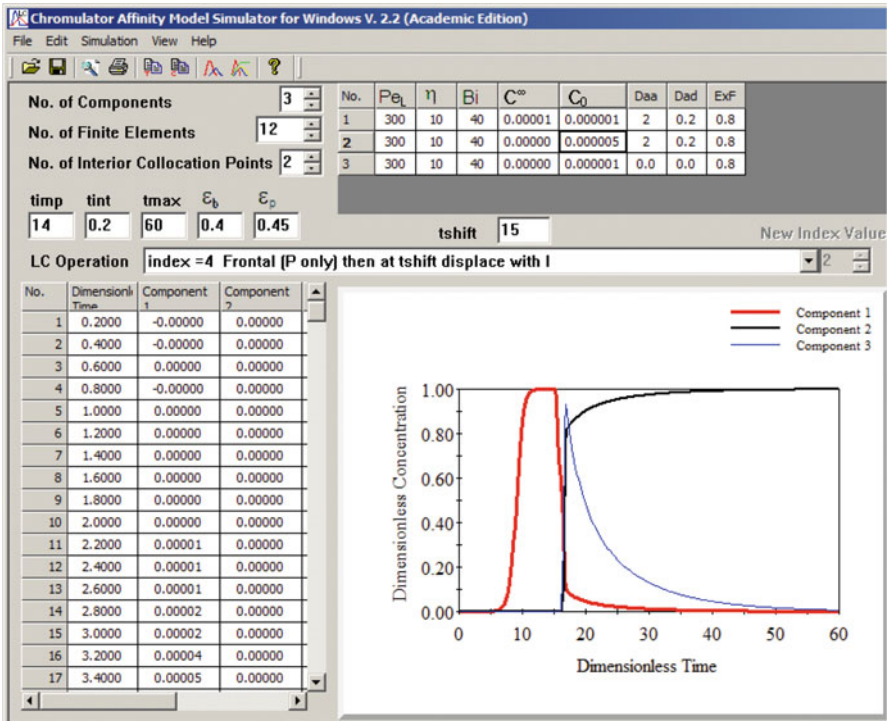

Fig. 10.14 Screenshot of AFFINITY simulator simulating the effect of increasing the soluble ligand concentration by five times than that in Fig. 10.13

helps reduce tailing and the time needed for the recovery of the product. If a higher concentration of soluble ligand is used for elution, the elution stage will be shorter, and the recovered product will have a higher concentration. This is demonstrated by Fig. 10.14, in which the soluble ligand concentration in the feed is five times that in Fig. 10.13. In Fig. 10.13, $\tau_{\text{imp}} = 14$ ("timp" = 14) input indicates the duration that the protein (component 1) solution is fed to the column. At $\tau = 15$ ("tshift" = 15), the column feed is switched to the soluble ligand (component 2) solution for elution. The difference between the two dimensionless times is $\Delta\tau = 1$, which is the time for the wash stage. In the output data, component 3 is complex PI. By setting index = 2 or 3, the affinity LC simulator can be used to simulate a zonal elution with a soluble ligand serving as an inhibitor in the mobile phase. If the injected sample contains the soluble ligand, index = 2. If not, index = 3.

10.6 Affinity Chromatography Scale-up Example

Gu et al. [17] predicted the chromatograms of a 98.2-ml (20 cm × 2.5 cm) column and a 501-ml (31.5 cm × 4.5 cm) column for lysozyme and also bovine serum albumin (BSA) single-component systems a priori by using essential parameters

obtained from a 7.85-ml (10 cm × 1 cm) column. Mass transfer parameters Pe_L, η, and Bi were estimated using existing correlations in Chap. 4. All the columns were packed with the same Affi-Gel containing 4.5 μmol/cm^3 Cibacron Blue F-3GA immobilized ligands on agarose gel. Using the 7.83-ml column, bed voidage and particle porosity were obtained using zonal analysis with a mixture of blue dextran (large nonbinding molecule that does not penetrate particle macropores) and glycine (small nonbinding molecule that penetrates all particle macropores) to obtain elution volumes $V_{e,\,d}$ and $V_{e,0,}$ respectively. The values of ε_b and ε_p calculated from Eqs. (8.4) and (8.5) were 0.41 and 0.58, respectively. By integrating the two breakthrough curves with 1 mg/ml and 2 mg/ml lysozyme on the 7.83-ml column to obtain corresponding column capacity areas, C_1^{∞} and b_1 values (for component 1, i.e., the protein to be separated) were calculated from Eq. (4.18) and found to be 4.41×10^{-3} mol/l particle skeleton and 1.18×10^6 mol/l, respectively. Size exclusion effect was not considered in their work. Tortuosity (τ_{tor}) was set to a typical value of 4. The 1 mg/ml breakthrough curve above was also used for curve-fitting using the AFFINITY simulator to find Da_1^a and Da_1^d values. Only one of them is adjusted because the following relationship leads to the other:

$$Da_1^a/Da_1^d = (k_{a1}/k_{d1})C_{01} = b_1C_{01}. \tag{10.14a}$$

If curve-fitting result is poor in this kind of situation, one may consider using a different tortuosity value.

The Langmuir isotherm parameter b_2 for the soluble ligand (component 2) was set to b_1 value approximately because the soluble ligand was the same as the immobilized ligand (Cibacron Blue). Da_2^a was found by curve-fitting of protein-soluble ligand complex effluent concentration profile in the elution stage. The soluble ligand effluent curve was insensitive for curve-fitting in this system. Da_2^d was calculated using the following relationship:

$$Da_2^a/Da_2^d = (k_{a2}/k_{d2})C_{01} = b_2C_{01} \tag{10.14b}$$

Note that C_{01} is used here instead of C_{02} as discussed earlier in this chapter. Gu et al. found that Da_2^d value was quite insensitive when Da_2^a was fixed [17]. Thus, b_2 value estimation did not have to be very stringent.

Figure 10.15 shows the curve-fitting results using experimental data on the small 7.85-ml column at a flow rate of 0.1 ml/min. The Pe_L, η, and Bi values can be easily calculated using the Microsoft Excel sheet in Table 4.1. The parameters for simulation are listed in Table 10.1, and they are used in Fig. 10.16 to produce the simulated chromatogram in Fig. 10.15. The best fit was achieved as shown in Fig. 10.15 by using $Da_2^a = 2.00$. Note that Gu et al. [17] showed $Da_2^a = 55.71$

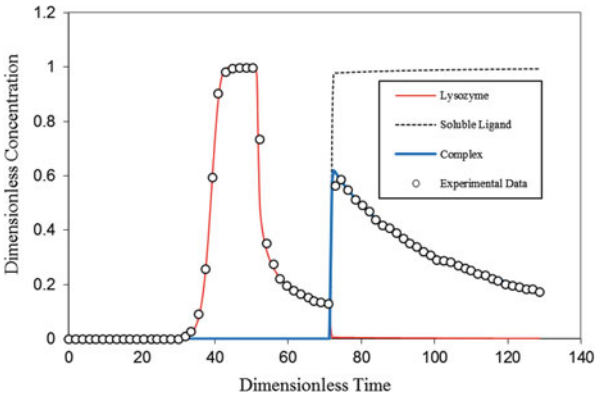

Fig. 10.15 Experimental and simulated chromatogram for affinity LC of lysozyme on the small 7.85-ml column at a flow rate of 0.1 ml/min (reproduced with data in Table 10.1 from [17] with permission)

Table 10.1 Parameter values for Fig. 10.15 (experimental data portion from [16])

Parameters	Column data	Lysozyme ($i=1$)	Cibacron blue ($i=2$)	Complex ($i=3$)	Source
L (cm)	10				Vendor
d_c (cm)	1				Vendor
V_b (cm^3)	7.85				
R_p (μm)	112.5				Vendor
τ_{tor}	4				Typical value
ε_b	0.41				Eq. (8.4)
ε_p	0.58				Eq. (8.5)
d_p (Å)	300				Arve and Liapis [16]
Q (ml/s)	0.1				
v (cm/s)	0.311				Eq. (4.11)
τ_{imp}	50				$\tau = t(v/L)$
τ_{shift}	70				$\tau = t(v/L)$
MW_i		13,930	772	14,702	
C_i^{∞} (M)		4.41×10^{-3}	–	–	Eq. (4.18)
b_i (M^{-1})		1.18×10^{6}	Set $b_2 = b_1$	–	Eq. (4.18)
C_{0i} (M)		7.18×10^{-5}	0.002	7.18×10^{-5}	
d_{mi} (Å)		34.65	13.21	35.28	Eq. (4.36)
D_{mi} (cm^2/s)[a]		1.14×10^{-6}	2.99×10^{-6}	1.12×10^{-6}	Eq. (4.27)
D_{pi} (cm^2/s)		2.16×10^{-7}	6.78×10^{-7}	2.11×10^{-7}	Eq. (4.35)
k_i (cm/s)		4.68×10^{-4}	8.89×10^{-4}	4.62×10^{-4}	Eq. (4.38)
Da_i[a]		1.830	2.003	0	Curve-fitting
Da_i[d]		0.022	0.024	0	Eq. (8.14a, b)
Pe_{Li}		217	217	217	Eq. (4.32)
η_i		1.92	6.00	1.87	Eq. (4.34)
Bi_i		41.91	25.46	42.40	Eq. (4.37)

[a]Gu et al. [17] used a more complicated formula than Eq. (4.27) for the evaluation of D_{m2} because Cibacron Blue is a small molecule, rather than a large protein. They showed a value 10 % higher. This, however, does not cause any noticeable differences in simulated chromatograms. Thus, Eq. (4.27) that is simpler is used here instead

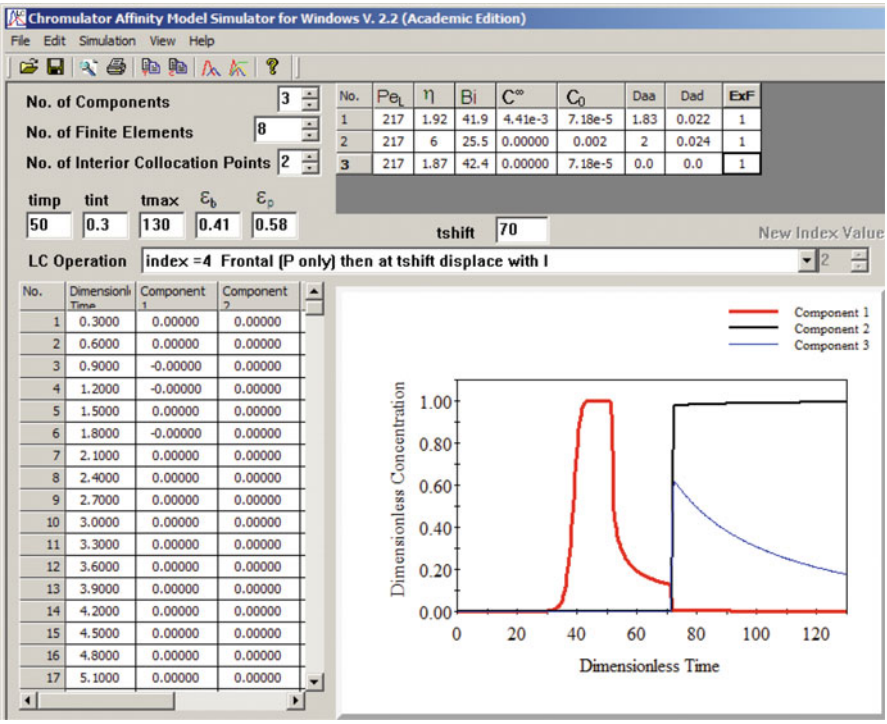

Fig. 10.16 Screenshot of AFFINITY simulator for the simulated chromatogram in Fig. 10.15

instead of 2.000 because they used C_{02} instead of C_{01} for the definition of Da_2^a as discussed before. Their simulator was different in this regard from the one used in this book. The Da_1^a value was obtained from curve-fitting using a breakthrough curve. Figure 10.15 shows that the simulated frontal breakthrough section matched the experimental data very well. Had the Da_1^a value not obtained separately, it would also be practical to use Fig. 10.15's frontal adsorption stage (before the lysozyme concentration started to drop below one) for curve-fitting to estimate these two parameters.

With the parameters obtained from the small column, a priori scale-up predictions could be made for larger columns before the columns were even purchased or built. Figure 10.17a shows that the predicted chromatogram matched experimental data very well for the 98.2-ml column packed with the same affinity gel as the small 7.83-ml column. The flow rate was increased from 0.1 ml/min to 1 ml/min. Other parameters are listed in Table 10.2 and the Chromulator screenshot for the simulation of Fig. 10.17a is shown in Fig. 10.17b. Figure 10.18a again shows that the a priori scale-up prediction fits the experimental data very well for a 501-ml

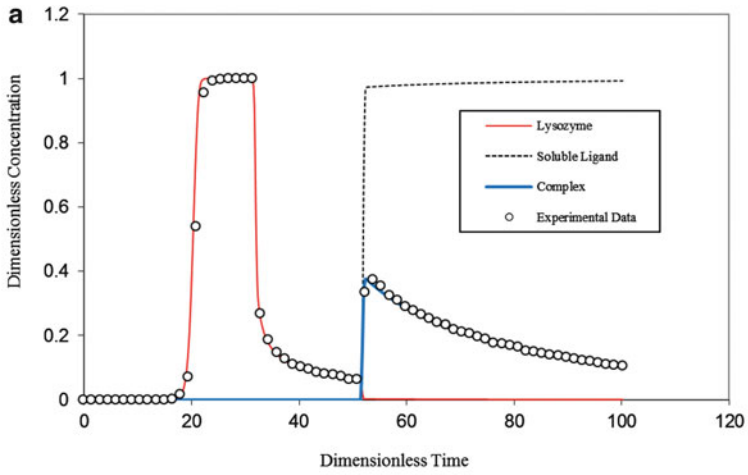

Fig. 10.17 (**a**) Experimental and simulated chromatogram for affinity LC of lysozyme on the 98.2-ml preparative column with a frontal loading time of $\tau_{imp} = 30$ followed by a washing period lasting 20 before elution at $\tau = 50$ at a flow rate of 1 ml/min (reproduced with data in Table 10.2 from [17] with permission). (**b**) Screenshot of the simulated chromatogram in Fig. 10.17a. Parameters' sources as listed in Table 10.2

Table 10.2 Parameter values for Fig. 10.17b

Parameters	Column data	Lysozyme ($i=1$)	Cibacron blue ($i=2$)	Complex ($i=3$)
L (cm)	20			
d_c (cm)	2.5			
V_b (cm^3)	98.17			
R_p (μm)	112.5			
τ_{tor}	4			
ε_b	0.41			
ε_p	0.58			
d_p (Å)	300			
Q (ml/s)	1			
v (cm/s)	0.00828			
τ_{imp}	30			
τ_{shift}	50			
MW_i		13,930	772	14,702
C_i^{∞} (M)		4.41×10^{-3}	–	–
b_i (M^{-1})		1.18×10^{6}	Set $b_2 = b_1$	–
C_{0i} (M)		1.44×10^{-4}	0.002	1.44×10^{-4}
d_{mi} (Å)		34.65	13.21	35.28
D_{mi} (cm^2/s)		1.14×10^{-6}	2.99×10^{-6}	1.12×10^{-6}
D_{pi} (cm^2/s)		2.16×10^{-7}	6.78×10^{-7}	2.11×10^{-7}
k_i (cm/s)		5.47×10^{-4}	1.04×10^{-3}	5.40×10^{-4}
Da_i^a		4.589	5.021	0
Da_i^d		0.0270	0.0296	0
Pe_{Li}		434	434	434
η_i		2.40	7.50	2.34
Bi_i		49.0	29.8	49.6

column (64 times larger than the 7.83-ml column) with a flow rate of 8 ml/min. Simulation parameters are listed in Table 10.3 and a screenshot for the simulator output is shown in Fig. 10.18b. As long as the same gel is used for larger columns and the bed packing structure is similar (no extra compression and no channeling or short circuiting in flow), scale-up prediction is expected to be reliable for even bigger columns. This scale-up example did not add impurities to the lysozyme in the experiment and in the simulation. In reality, impurities would be washed off during the washing stage between the dimensionless times τ_{imp} and τ_{shift} because impurities are retained in the column during sample loading through loose nonspecific binding.

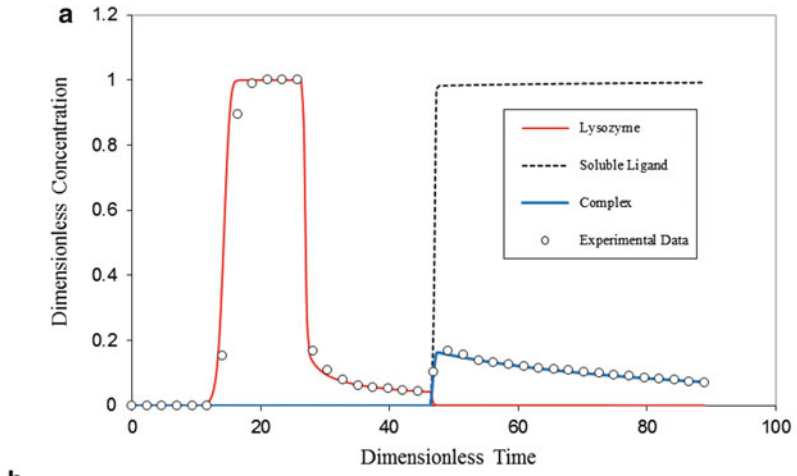

b

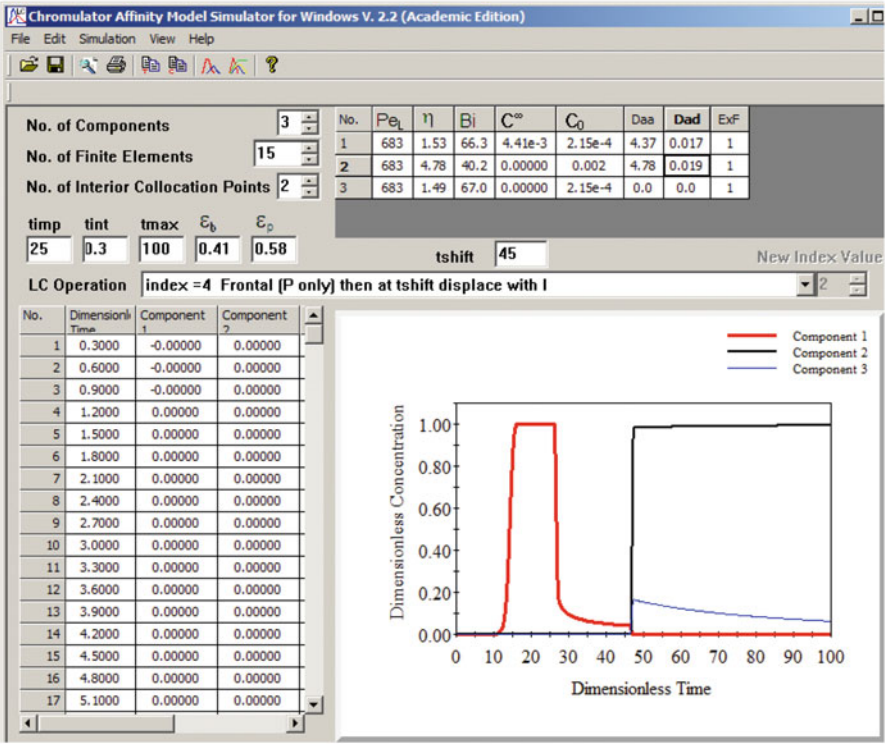

Fig. 10.18 (**a**) Experimental and simulated chromatogram for affinity LC of lysozyme on the 501-ml preparative column with a frontal loading time of $\tau_{imp} = 25$ followed by a washing period lasting 20 before elution at a flow rate of 8 ml/min (reproduced with data in Table 10.3 from [17] with permission). (**b**) Screenshot of the simulated chromatogram in Fig. 10.18a. Parameter sources at listed in Table 10.3

Table 10.3 Parameter values for Fig. 10.18b

Parameters	Column data	Lysozyme ($i = 1$)	Cibacron blue ($i = 2$)	Complex ($i = 3$)
L (cm)	31.5			
d_c (cm)	4.5			
V_b (cm^3)	501.0			
R_p (μm)	112.5			
τ_{tor}	4			
ε_b	0.41			
ε_p	0.58			
d_p (Å)	300			
Q (ml/s)	8			
v (cm/s)	0.0204			
τ_{imp}	25			
τ_{shift}	45			
MW_i		13,930	772	14,702
C_i^{∞} (M)		4.41×10^{-3}	–	–
b_i (M^{-1})		1.18×10^{6}	Set $b_2 = b_1$	–
C_{0i} (M)		2.15×10^{-4}	0.002	2.15×10^{-4}
d_{mi} (Å)		34.65	13.21	35.28
D_{mi} (cm^2/s)		1.14×10^{-6}	2.99×10^{-6}	1.12×10^{-6}
D_{pi} (cm^2/s)		2.16×10^{-7}	6.78×10^{-7}	2.11×10^{-7}
k_i (cm/s)		7.39×10^{-4}	1.41×10^{-3}	7.30×10^{-4}
Da_i^a		4.370	4.782	0
Da_i^d		0.0172	0.0188	0
Pe_{Li}		683	683	683
η_i		1.53	4.78	1.49
Bi_i		66.3	40.2	67.0

10.7 Summary

In this chapter, various aspects of affinity chromatography, including the effects of reaction kinetics, mass transfer, and size exclusion have, been discussed using computer simulation. The KINETIC model has been used to study the effects of slow kinetics and compared with slow mass transfer as well as the size exclusion effect. The KINETIC model has been modified to describe the reaction between macromolecules and soluble ligands in the bulk fluid and in stagnant fluid inside particle macropores to yield the AFFINITY model. The role of a soluble ligand in the elution stage in affinity chromatography has been investigated. The affinity LC scale-up example in this chapter shows how parameters could be evaluated using a small column to predict performances of larger columns a priori using the AFFINITY simulator.

References

1. Chase HA (1984) Affinity separations utilising immobilised monoclonal antibodies—a new tool for the biochemical engineer. Chem Eng Sci 39:1099–1125. doi:10.1016/0009-2509(84)85074-5
2. Liapis AI (1989) Theoretical aspects of affinity chromatography. J Biotechnol 11:143–160. doi:10.1016/0168-1656(89)90116-8
3. Lee W-C (1989) PhD thesis. Purdue University, West Lafayette, IN
4. Arnold FH, Schofield SA, Blanch HW (1986) Analytical affinity chromatography: I. Local equilibrium theory and the measurement of association and inhibition constants. J Chromatogr A 355:1–12. doi:10.1016/S0021-9673(01)97299-1
5. Lee W-C, Tsai G-J, Tsao GT (1990) Radial-flow affinity chromatography for trypsin purification. ACS Symp Ser 427:104–117
6. Arve BH, Liapis AI (1987) The modeling and analysis of the elution stage of biospecific adsorption in fixed beds. Biotechnol Bioeng 30:638–649. doi:10.1002/bit.260300508
7. Arve BH, Liapis AI (1988) Biospecific adsorption in fixed and periodic countercurrent beds. Biotechnol Bioeng 32:616–627
8. Chase HA (1984) Prediction of the performance of preparative affinity chromatography. J Chromatogr A 297:179–202. doi:10.1016/S0021-9673(01)89041-5
9. Arnold FH, Blanch HW, Wilke CR (1985) Analysis of affinity separations: I: Predicting the performance of affinity adsorbers. Chem Eng J 30:B9–B23. doi:10.1016/0300-9467(85)80016-2
10. Arnold FH, Blanch HW, Wilke CR (1985) Analysis of affinity separations II: The characterization of affinity columns by pulse techniques. Chem Eng J 30:B25–B36. doi:10.1016/0300-9467(85)80017-4
11. Arnold FH, Blanch HW (1986) Analytical affinity chromatography: II. Rate theory and the measurement of biological binding kinetics. J Chromatogr A 355:13–27. doi:10.1016/S0021-9673(01)97300-5
12. Arve BH, Liapis AI (1987) Modeling and analysis of biospecific adsorption in a finite bath. AIChE J 33:179–193. doi:10.1002/aic.690330203
13. Froment GF, Bischoff KB, De Wilde J (1990) Chemical reactor analysis and design. Wiley, New York
14. Ruthven DM (1984) Principles of adsorption and adsorption processes. Wiley, New York
15. Gu T (1990) Inclusion chromatography using cyclodextrin-containing resins and studies of nonlinear chromatographic theories. Purdue University, West Lafayette
16. Arve BH, Liapis AI (1988) Modeling and analysis of elution stage of biospecific adsorption in finite bath. Biotechnol Bioeng 31:240–249. doi:10.1002/bit.260310310
17. Gu T, Hsu KH, Syu MJ (2003) Scale-up of affinity chromatography for purification of enzymes and other proteins. Enzym Microb Technol 33:430–437

Chapter 11
Multicomponent Adsorption Chromatography with Uneven Saturation Capacities

11.1 Introduction

In chromatographic separations of large biomolecules, such as proteins, using porous adsorbents, a size exclusion effect may be significant. Some large molecules either cannot access part of the small macropores in the adsorbent particles or all the macropores. This is especially possible in chromatographic separations of large proteins or other macromolecules. For a multicomponent system involving components with very different molecular sizes, the extent of size exclusion is not the same for all components. This causes uneven adsorption saturation capacities (based on moles) for the components. The least excluded component tends to have the highest saturation capacity.

In size exclusion chromatography (SEC) with globular sample components, the component that has a larger molecular size has a smaller chance to penetrate the macropores of the particles; thus, it has a smaller retention time. A size exclusion stationary phase should have very little adsorption ability, since adsorption is considered an undesirable side-effect in size exclusion chromatography that causes band broadening. It disrupts the retention sequence dictated by molecular size distribution of the components. In practice, a salt (or solvent) solution is used as the mobile phase to reduce ion-exchange (or reversed-phase) binding of solutes. Ammonia carbonate is a preferred salt because it can be evaporated. Ironically, size exclusion becomes a side-effect in other forms of chromatography, such as affinity or adsorption chromatography.

In this book, the saturation capacities are based on the molar amount of solutes per unit volume of particle skeleton. The differences in saturation capacities can be caused by size exclusion (a steric hindrance effect) or by sample solutes' chiral discrimination of binding sites. Uneven saturation capacities caused by size exclusion or other reasons bring serious complications in mathematical modeling. The topic of uneven saturation capacities deserves special attention because they are not uncommon. The multicomponent Langmuir isotherm is widely used because of its

© Springer International Publishing Switzerland 2015

T. Gu, *Mathematical Modeling and Scale-Up of Liquid Chromatography*,
DOI 10.1007/978-3-319-16145-7_11

simplicity and lack of other choices. Unfortunately, it violates the Gibbs–Duhem law of thermodynamics if the saturation capacities are not even [1, 2]. Although it can be considered only as an experimental expression used for correlation, it may not be used for extrapolation over a wider concentration range [1].

In this chapter, an isotherm system has been presented for multicomponent systems with uneven saturation capacities induced either by size exclusion or by chiral discrimination of binding sites. The crossover of the isotherms has been studied. A general rate model has been used with the new isotherm system to demonstrate the "peak reversal" phenomenon in multicomponent elution and the crossover of breakthrough curves.

11.2 Kinetic and Isotherm Models

A mathematical treatment is presented here for adsorption systems with uneven saturation capacities due to size exclusion. It is assumed that one molecule can occupy only one binding site, and its binding or size exclusion does not block the availability of other vacant binding sites. One molecule can only take one binding site is a reasonable assumption for affinity chromatography involving low-density immobilized ligands.

Based on these basic assumptions, the second-order kinetics can be modified by inserting θ_{ij} to give the following kinetic expression [3] that is going to be coupled with the particle phase governing equation, Eq. (3.2):

$$\frac{\partial C_{\mathrm{p}i}^{*}}{\partial t} = k_{\mathrm{a}i} C_{\mathrm{p}i} \left(C_i^{\infty} - \sum_{j=1}^{N_{\mathrm{s}}} \theta_{ij} C_{\mathrm{p}j}^{*} \right) - k_{\mathrm{d}i} C_{\mathrm{p}i}^{*} \tag{11.1}$$

where constants $\theta_{ij}\left(0 \le \theta_{ij} \le 1\right)$ are named "discount factors," and $k_{\mathrm{a}i}$ and $k_{\mathrm{d}i}$ are rate constants for component i for binding and dissociating reactions, respectively. The θ_{ij} values are used to discount the values of $C_{\mathrm{p}j}^{*}$ that belong to the components with a lower degree of size exclusion when doing the calculation of a current component, i.e.,

$$\theta_{ij} = \begin{cases} 1 & i = j \quad \text{or} \quad C_i^{\infty} \ge C_j^{\infty} \\ < 1 & C_i^{\infty} < C_j^{\infty} \end{cases} \tag{11.2}$$

Equation 11.2 means that, when calculating the $\partial C_{\mathrm{p}i}^{*}/\partial t$ value in Eq. (11.1) for a component with a large molecular size, the $C_{\mathrm{p}j}^{*}$ values for smaller solutes should be discounted, since some of the binding sites for the small solutes are not available to the large solute anyway. For a component with an accessible porosity of $\varepsilon_{\mathrm{p}i}^{\mathrm{a}}$ (a fraction of particle porosity ε_{p}), its size exclusion factor is defined by the relationship $F_i^{\mathrm{ex}} = \varepsilon_{\mathrm{p}i}^{\mathrm{a}}/\varepsilon_{\mathrm{p}}$. Details on the physical meaning of the accessible porosity are discussed in Chap. 8 in this book. It is obvious that for component

i with a higher degree of size exclusion, its F_i^{ex} value is smaller, and so is its saturation capacity C_i^{∞}. For example, if the system has two components competing for binding sites and component 1 cannot access 60 % of the binding sites due to size exclusion while component 2 can access all binding sites, one may set $\theta_{11} = 1$ and $\theta_{12} = C_1^{\infty}/C_2^{\infty} = 0.4$. Thus, $\theta_{12} = 0.4$ is used discount $C_{\mathrm{p}2}^*$ because only 40 % of $C_{\mathrm{p}2}^*$ belongs to the binding sites that are accessible to component 1. It is reasonable to assume that $\theta_{ij} = C_i^{\infty}/C_j^{\infty}$ for those θ_{ij} values that are apparently not equal to unity. If those θ_{ij} values are obtained from experimental correlations, the modified second-order kinetics model in this work then becomes semiempirical.

If an adsorption equilibrium is assumed, Eq. (11.1) becomes

$$b_i C_{\mathrm{p}i}\left(C_i^{\infty} - \sum_{j=1}^{N_{\mathrm{s}}} \theta_{ij} C_{\mathrm{p}\,j}^*\right) - C_{\mathrm{p}i}^* = 0 \tag{11.3}$$

Rearrangement gives

$$b_i C_{\mathrm{p}i} C_i^{\infty} - \sum_{j=1}^{N_{\mathrm{s}}} b_i C_{\mathrm{p}i} \theta_{ij} C_{\mathrm{p}\,j}^* - C_{\mathrm{p}i}^* = 0 \tag{11.4}$$

Equation 11.4 can be rewritten in a matrix form below,

$$[\mathbf{A}] - [\mathbf{B}]\left[C_{\mathbf{p}}^*\right] - \left[C_{\mathbf{p}}^*\right] = 0 \tag{11.5}$$

which gives the following *extended multicomponent Langmuir isotherm:*

$$\left[\mathbf{C}_{\mathbf{p}}^*\right] = ([\mathbf{B}] + [\mathbf{I}])^{-1}[\mathbf{A}] \tag{11.6}$$

where

$$\mathrm{A}_i = b_i C_{\mathrm{p}i} C_i^{\infty}, \quad \mathrm{B}_{ij} = b_i C_{\mathrm{p}i} \theta_{ij}, \quad \text{and} \quad \mathrm{I}_{ij} = \begin{cases} 1 & i = j \\ 0 & \text{else} \end{cases}$$

For a binary system in which component 1 has a higher degree of size exclusion than component 2, one obtains $\theta_{11} = \theta_{22} = \theta_{21} = 1$ and $\theta_{12} < 1$. The extended binary Langmuir isotherm becomes

$$C_{\mathrm{p}1}^* = \frac{b_1 C_{\mathrm{p}1}\left[\left(1 + b_2 C_{\mathrm{p}2}\right) C_1^{\infty} - \theta_{12} b_2 C_{\mathrm{p}2} C_2^{\infty}\right]}{1 + b_1 C_{\mathrm{p}1} + b_2 C_{\mathrm{p}2} + (1 - \theta_{12}) b_1 C_{\mathrm{p}1} b_2 C_{\mathrm{p}2}} \tag{11.7}$$

$$C_{\mathrm{p2}}^{*} = \frac{b_2 C_{\mathrm{p2}}\left[\left(1 + b_1 C_{\mathrm{p1}}\right) C_2^{\infty} - b_1 C_{\mathrm{p1}} C_1^{\infty}\right]}{1 + b_1 C_{\mathrm{p1}} + b_2 C_{\mathrm{p2}} + (1 - \theta_{12}) b_1 C_{\mathrm{p1}} b_2 C_{\mathrm{p2}}} \tag{11.8}$$

It is obvious that the two isotherm expressions above reduce to the common Langmuir isotherm expressions if $C_1^{\infty} = C_2^{\infty}$ and $\theta_{12} = 1$. The extended binary Langmuir isotherm has only one extra constant θ_{12} apart from $C_1^{\infty} \neq C_2^{\infty}$ compared with the standard Langmuir isotherm. θ_{12} may be reasonably set to $C_1^{\infty}/C_2^{\infty} (< 1)$. Thus, no new parameter is in the new binary isotherm compared with the standard Langmuir isotherm, except $C_1^{\infty} \neq C_2^{\infty}$. (For systems with more than two components, the determination of θ_{ij} values may not be that simple.) In view of the arguments above using the binary isotherm example and the rationale behind Eq. (11.1), it is not difficult to understand why it has been proven that $C_1^{\infty} \neq C_2^{\infty}$ in the standard Langmuir isotherm is thermodynamically inconsistent [1]. It is also physically unreasonable. However, the introduction of θ_{12} rationalizes the uneven adsorption saturation capacity values.

In some multicomponent systems, uneven saturation capacities do not arise from different degrees of size exclusion, but they are induced by an adsorption mechanism at the molecular level. For example, for a binary system, suppose the binding sites (or ligands) are a chiral mixture and they make no difference to component 2, but only some of them are active and usable for component 1; thus, component 1 has a lower saturation capacity than component 2. The mathematical treatment for such a system with a chiral discrimination of binding sites is the same as that for systems with uneven saturation capacities that are induced by size exclusion. Another type of uneven binding capacities could be caused by a macromolecule binding with one binding site but covering (without binding) additional ones due to its large footprint. This steric hindrance has led to the so-called steric mass-action isotherm in IEC [4, 5] as discussed in Chap. 13 of this book.

11.3 Isotherm Crossover

With uneven saturation capacities, an isotherm "crossover" may occur. In this chapter, the isotherm concentration crossover point $C_{\mathrm{p}}^{\mathrm{c}}$ is defined as the concentration in the stagnant fluid inside macropores for a pair of components, at which the corresponding solid phase concentrations ($C_{\mathrm{p}i}^{*}$) are equal.

The concentration crossover point for the binary isotherms, given by Eqs. (11.7) and (11.8), can be derived by subtracting the two isotherm expressions and setting $C_{\mathrm{p1}} = C_{\mathrm{p2}} = C_{\mathrm{p}}^{\mathrm{c}}$, which gives

$$C_{p1}^{*} - C_{p2}^{*} = \frac{\left(b_1 C_1^{\infty} - b_2 C_2^{\infty}\right) C_p^c + b_1 b_2 \left[2C_1^{\infty} - (1+\theta_{12}) C_2^{\infty}\right] \left(C_p^c\right)}{1 + b_1 C_p^c + b_2 C_p^c + (1-\theta_{12}) b_1 C_p^c b_2 C_p^c} \tag{11.9}$$

The superscript c indicates the crossover point. Setting the left-hand side of Eq. (11.9) to zero, one obtains

$$0 = \left(b_1 C_1^{\infty} - b_2 C_2^{\infty}\right) C_p^c + b_1 b_2 \left(C_p^c\right)^2 \left[2C_1^{\infty} - (1-\theta_{12}) C_2^{\infty}\right] \tag{11.10}$$

which gives a nontrivial solution,

$$C_p^c = \frac{b_1 C_1^{\infty} - b_2 C_2^{\infty}}{b_1 b_2 \left[(1+\theta_{12}) C_2^{\infty} - 2C_1^{\infty}\right]} \tag{11.11}$$

If $\theta_{12} = C_1^{\infty}/C_2^{\infty}$,

$$C_p^c = \frac{b_1 C_1^{\infty} - b_2 C_2^{\infty}}{b_1 b_2 \left(C_2^{\infty} - C_1^{\infty}\right)} \tag{11.12}$$

The denominator of Eq. (11.12) is positive since $C_1^{\infty} < C_2^{\infty}$. Thus, the binary isotherm has a crossover point if and only if the crossover concentration has a positive value, which requires

$$b_1 C_1^{\infty} > b_2 C_2^{\infty} \quad \text{or} \quad b_1/b_2 > C_2^{\infty}/C_1^{\infty} \tag{11.13}$$

An isotherm concentration crossover signals a selectivity change. The selectivity crossover point may be defined as the critical concentration $C_p^c = C_{p1} = C_{p2}$, which is obtained by setting the relative selectivity of the two components to unity, i.e.,

$$\frac{\partial C_{p1}^{*} / \partial C_{p1}}{\partial C_{p2}^{*} / \partial C_{p2}} = 1 \tag{11.14}$$

This leads to Eq. (11.15),

$$\partial C_{p1}^{*} / \partial C_{p1} - \partial C_{p2}^{*} / \partial C_{p2} = 0 \tag{11.15}$$

from which the following critical selectivity crossover concentration can be easily obtained from Eqs. (11.7) and (11.8) with $C_{p1} = C_{p2} = C_p^c$ and $C_1^{\infty}/C_2^{\infty}$:

$$C_{\mathrm{p}}^{\mathrm{c}} = \frac{1}{b_1} + \frac{1}{b_2}\sqrt{\frac{C_1^{\infty}(b_1 - b_2)}{b_2\left(C_2^{\infty} - C_1^{\infty}\right)}} \tag{11.16}$$

In Eq. (11.16), $C_{\mathrm{p}}^{\mathrm{c}} > 0$ only if $C_1^{\infty}(b_1 - b_2)/\left[b_2\left(C_2^{\infty} - C_1^{\infty}\right)\right] > 1$. This leads to Eq. (11.13). Thus, both the concentration crossover and the selectivity crossover require the satisfaction of Eq. (11.13).

It has been known that selectivity depends on the concentration range, and selectivity reversal may occur in the operational concentration range [6]. A selectivity reversal may cause the reversal of the retention time sequence of elution peaks since the migration speed of a component is primarily determined by the $\partial C_{\mathrm{p}i}^{*}/\partial C_{\mathrm{p}i}$ value [7].

Figure 11.1 shows two simulated binary elution cases in which component 1 has a smaller saturation capacity and a higher adsorption equilibrium constant than component 2. Parameter values used for the simulation are listed in Table 11.1. The simulation was carried out using the KINETIC simulator module with a simple modification to account for θ_{ij} in Eq. (11.1). For the binary system used to discuss the isotherm crossover above, θ_{12} is set to $C_1^{\infty}/C_2^{\infty}$, and $\theta_{11} = \theta_{22} = \theta_{21} = 10$. In the input data file for the computer code, a large value (such as 1,000) is assigned to $\mathrm{Da}_i^{\mathrm{a}}$ (to force the second-order kinetics to degenerate into equilibrium), and a value is then given to $\mathrm{Da}_i^{\mathrm{d}}$ to yield the appropriate values for b_i and a_i according to relationships: $b_i C_{0i} = \mathrm{Da}_i^{\mathrm{a}}/\mathrm{Da}_i^{\mathrm{d}}$ and $a_i = C_i^{\infty} b_i$. This code will then produce the same results as the one using the extended Langmuir isotherm expressed by

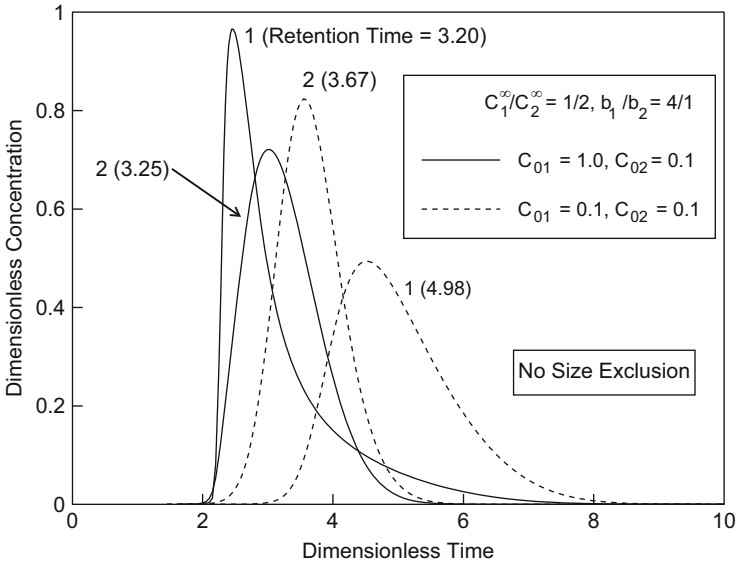

Fig. 11.1 Peak reversal due to increased component 1 concentration

Table 11.1 Parameter values used for simulation in this chapter[a]

Figure(s)	Species	Physical parameters					Numerical parameters	
		Pe_{Li}	η_i	Bi_i	a_i	$b_i \times C_{0i}$	N_e	N
11.1, 11.2, 11.3, 11.4	1	300	4	20	4	4×	12–22	2
	2	300	4	20	2	1×		
11.5	1	300	1	40	4	4×	8	2
	2	300	1	40	2	1×		
11.6	1	300	1	20	4	4×	8	2
	2	300	1	20	1	0.5×		
11.7	1	300	1	20	4	4×	10	2
	2	300	4	20	1	0.5×		

[a]In all cases, $\varepsilon_b = \varepsilon_p = 0.4$. For all elution cases, $\tau_{imp} = 1.0$, except for Fig. 11.4 ($\tau_{imp} = 0.05$).

Eqs. (11.7) and (11.8). The RATE simulator module is not modified for use here, since it does not consider the size exclusion effect needed for the discussion below.

The dashed lines in Fig. 11.1 show that component 2 has a smaller retention time than component 1 when the feed concentration of component 1 is low. The solid lines show that component 2 has a higher retention time when the feed concentration of component 1 is increased by tenfold. In Fig. 11.1 (solid lines) the tail end of the component 1 peak is behind that of the component 2 peak. Apparently, at low concentrations, component 1 is retained longer than component 2.

Figure 11.2 has the same conditions as Fig. 11.1, except that in the solid line case the concentrations of components 1 and 2 are both 2 moles/l in Fig. 11.2. The peak reversal phenomenon is also present in Fig. 11.2. If the uneven saturation capacities are not induced by chiral discrimination of binding sites, but induced by size exclusion, peak reversal still can be present. Figure 11.3 clearly shows such a case in which component 1 has a size exclusion factor of $F_i^{ex} = 0.5$.

In Figs 11.1, 11.2, 11.3, the sample size is quite large ($\tau_{imp} = 1.0$) such that the sample is not diluted too much during its migration inside the column. Otherwise, the dilution of the sample will quickly change the general working concentration range in the isotherm from that over the isotherm crossover point to that below the point. In such a case, peak reversal may not occur at all. Figure 11.4 has the same conditions as Fig. 11.3, except that in Fig. 11.4, the sample size is much smaller ($\tau_{imp} = 0.05$). There is no peak reversal in Fig. 11.4 (solid lines) because the concentrations of the two sample components are below the isotherm crossover point most of the time during their migration inside the column. Their concentrations are quickly diluted after the initial stage of migration because of the small sample size.

The selectivity reversal is also interesting in frontal adsorptions. The solid lines in Fig. 11.5 show that the breakthrough curves cross over each other when the feed concentrations are high. Figure 11.6 (with size exclusion) shows a crossover of breakthrough curves (solid lines). The crossover of breakthrough curves depends on not only the isotherm characteristics and feed concentration but also mass transfer conditions. Figure 11.7 has the same conditions as Fig. 11.6, except that $\eta_2 = 4$ in Fig. 11.7 instead of $\eta_2 = 1$ in Fig. 11.6. There is a reversal of sequence of

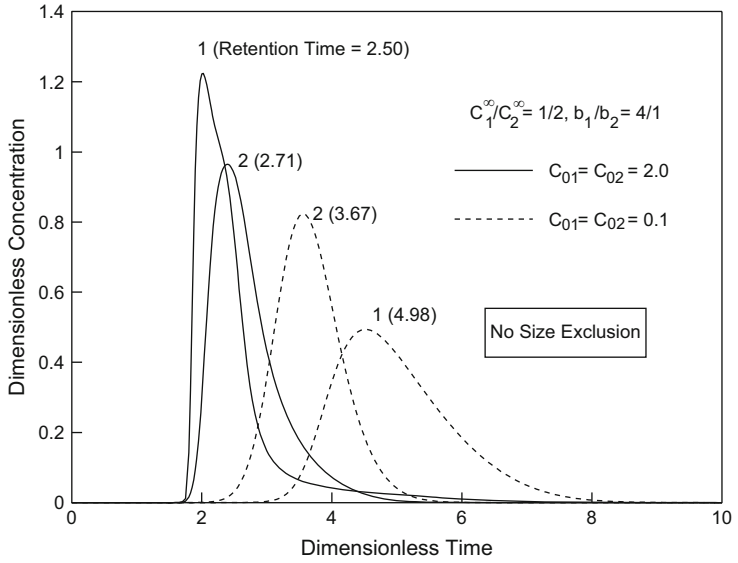

Fig. 11.2 Peak reversal in binary elution without size exclusion

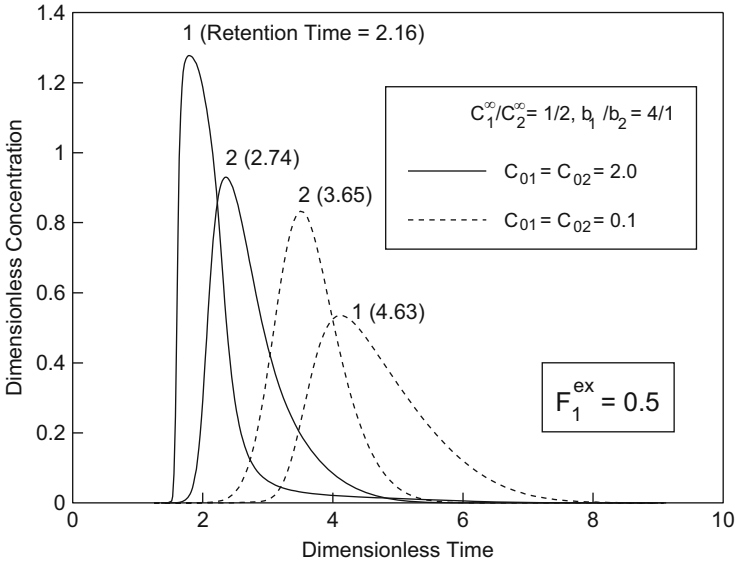

Fig. 11.3 Peak reversal with size exclusion

breakthrough curves when the feed concentrations are increased, but there is no crossover of the two curves. The absence of a crossover of the two breakthrough curves is apparently because of the change of relative positions of the concentration

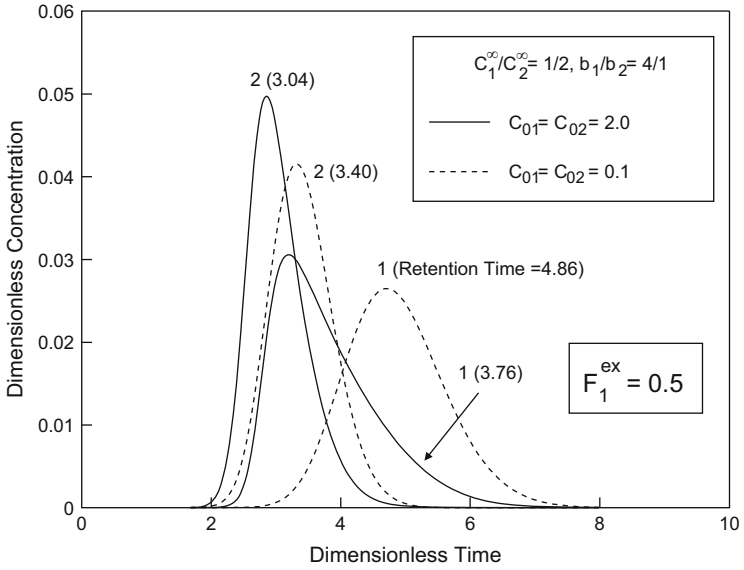

Fig. 11.4 No peak reversal due to a small sample size

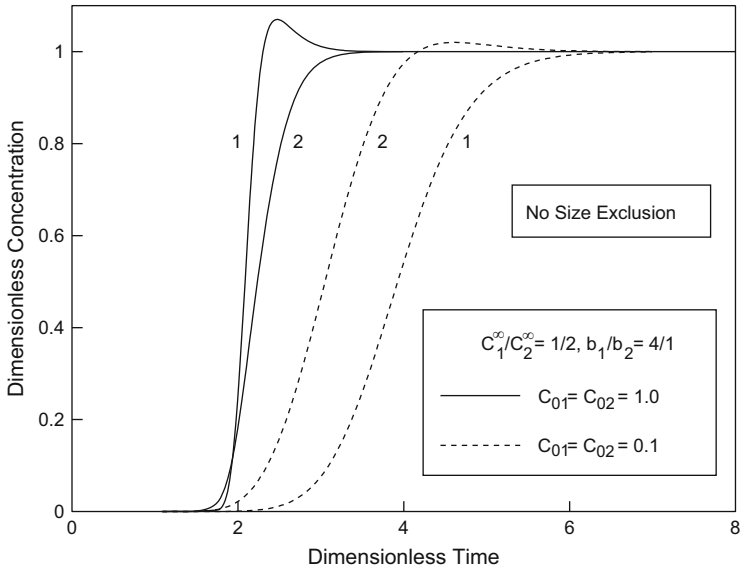

Fig. 11.5 Crossover of breakthrough curves (no size exclusion)

fronts of the two components arising from a change in mass transfer conditions for component 2.

A detailed treatment of peak reversals due to isotherm selectivity crossover is considerably more difficult, which involves complicated arguments. A peak

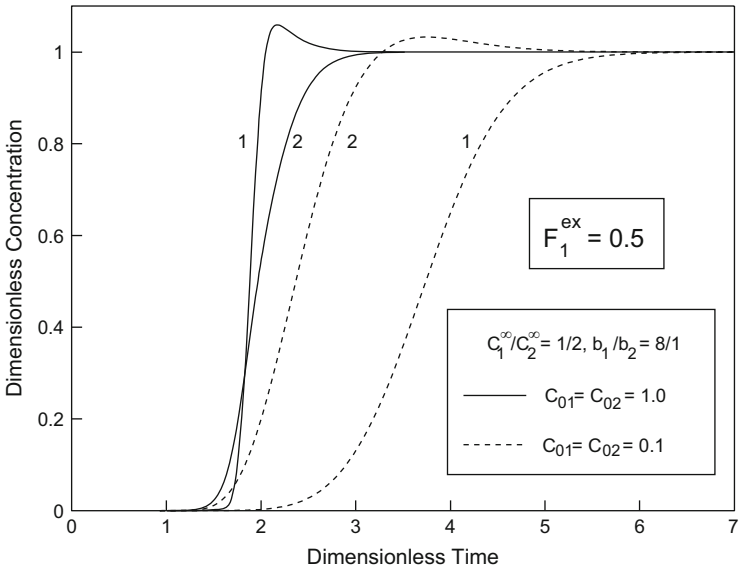

Fig. 11.6 Crossover of breakthrough curves (with size exclusion)

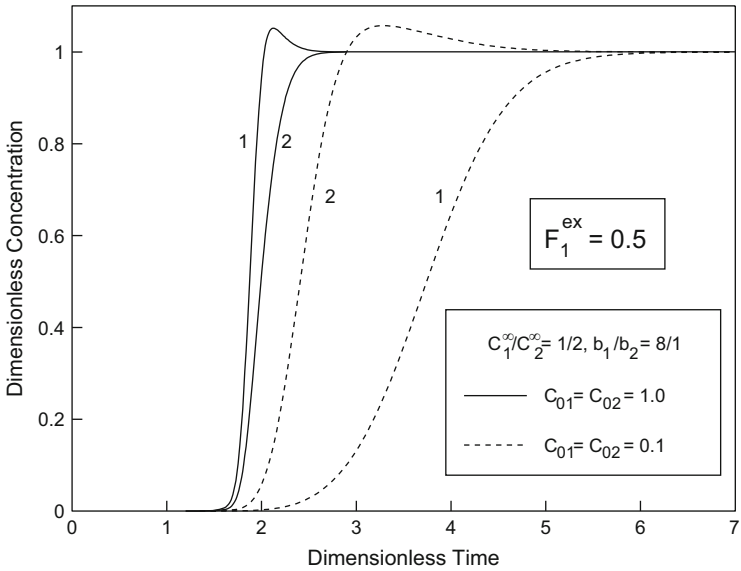

Fig. 11.7 Reversal of the sequence of breakthrough curves without crossover of the curves

reversal is not necessarily the consequence of a selectivity reversal, although a selectivity reversal facilitates a peak reversal.

11.4 Summary

An isotherm system has been presented for multicomponent systems with uneven saturation capacities induced by either size exclusion or chiral discrimination of the binding sites. The mathematical criteria for isotherm crossover in terms of concentration and selectivity have been derived and discussed for the isotherm. The isotherm system serves as a valuable model for experimental correlation of isotherm data showing uneven saturation capacities. Using a general rate model that counts for an extended binary Langmuir isotherm system, the peak reversal phenomenon in elutions and the crossover of breakthrough curves in frontal adsorptions have been demonstrated. The methodology demonstrated here for systems with uneven saturation capacities can be readily applied to common stoichiometric ionexchange systems.

References

1. Ruthven DM (1984) Principles of adsorption and adsorption processes. Wiley, New York
2. Kemball C, Rideal EK, Guggenheim EA (1948) Thermodynamics of monolayers. Trans Faraday Soc 44:948–954
3. Gu T, Tsai G-J, Tsao GT (1991) Multicomponent adsorption and chromatography with uneven saturation capacities. AIChE J 37:1333–1340
4. Brooks CA, Cramer SM (1992) Steric mass-action ion exchange: displacement profiles and induced salt gradients. AIChE J 38:1969–1978
5. Mehay A, Gu T (2014) A general rate model of ion-exchange chromatography for investigating ion-exchange behavior and scale-up. J Microb Biochem Technol 6:216–222
6. Antia FD, Horváth C (1989) Operational modes of chromatographic separation processes. Berichte der Bunsengesellschaft für physikalische Chemie 93:961–968. doi:10.1002/bbpc.19890930907
7. Helfferich FG, Klein G (1970) Multicomponent chromatography: theory of interference. Dekker, New York

Chapter 12
Modeling of Multicomponent Gradient Elution

12.1 Introduction

Gradient elution chromatography is a very important method in chromatographic separations, especially for proteins, because they have a wide range of retentivity. In gradient elution, a modulator is added to the mobile phase to adjust eluent strength. The modulator can be acetonitrile in reversed phase chromatography, ammonium sulfate in hydrophobic interaction chromatography, or sodium chloride in ion-exchange chromatography. In ion-exchange chromatography, a pH gradient is also used. This kind of pH gradient elution is covered in the ion-exchange chapter of this book. The modulator concentration in the mobile phase is increased (or decreased as in hydrophobic interaction chromatography) continuously with time. This change in the strength of the modulator allows gradient elution to separate components with widely different retentivity. In preparative- or large-scale operations, gradient elution can concentrate a sample while achieving purification at the same time. It is possible to reduce the sample volume by many folds. In isocratic elution, a sample is always diluted to a certain degree. Because of this, gradient elution is often desired when handling large volumes of dilute samples.

Gradient elution in analytical HPLC involves small and dilute samples separated on a high-efficiency column. In preparative- and large-scale gradient elution chromatography, the column is often overloaded in terms of feed volume and/or concentration, or both. The column may not be a high-efficiency column due to scale and cost factors. Larger particle sizes are typically used for column packing to reduce cost and pressure drop. Thus, interference effects, axial dispersion, and mass transfer resistance such as interfacial film mass transfer and intraparticle diffusion may become important. The scale-up of protein purification using gradient elution was often carried out empirically [1]. The theoretical basis of gradient elution in nonlinear chromatography has not been fully established [2]. Because of the complications involved in the modeling of gradient elution, very few existing models considered mass transfer resistance or kinetic resistance, although some

© Springer International Publishing Switzerland 2015

T. Gu, *Mathematical Modeling and Scale-Up of Liquid Chromatography*,
DOI 10.1007/978-3-319-16145-7_12

considered axial dispersion [1–4]. Existing mathematical models in the literature for gradient elution were reviewed by Gu et al. [5].

Melander et al. [6] proposed an eluite–modulator relationship, which is suitable for both electrostatic and hydrophobic interactions. This relationship was supported by some thermodynamic arguments. In this chapter, a general rate model for multicomponent elution chromatography is presented. In the model, it is assumed that the eluites follow the multicomponent Langmuir isotherm with a uniform (molar) saturation capacity, C^{∞}. The Langmuir isotherm parameter b_i values are a function of the modulator concentration following the eluite–modulator relationship proposed by Melander et al. The gradient model in this work is capable of simulating various gradient operations with linear, nonlinear, and stepwise linear gradients.

12.2 General Rate Model for Multicomponent Gradient Elution

The modulator is designated as the last component in a multicomponent model system, which is component N_s. The eluite–modulator relationship proposed by Melander et al. [6] can be written for component i as follows:

$$\log_{10} b_i = \alpha_i - \beta_i \log_{10} C_m + \gamma_i C_m \tag{12.1}$$

in which α_i, β_i, and γ_i are experimental correlation parameters. Note that Melander et al. used retention factor k' (also known as the capacity factor whose evaluation is described in Chap. 4) instead of the adsorption equilibrium constant in the Langmuir isotherm, b_i. But $k'_i = \varphi C^{\infty} b_i$ according to Eq. (4.14), and the constant value of φC^{∞} can be separated from $\varphi C^{\infty} b$ and lumped into the α term in Eq. (12.1), leading to

$$\log_{10} k'_i = \alpha'_i - \beta_i \log_{10} C_m + \gamma_i C_m \tag{12.2}$$

in which

$$\alpha'_i = \alpha_i + \log_{10} \varphi C^{\infty} \tag{12.3}$$

In Eq. (12.3), the phase ratio φ can be evaluated from bed voidage and particle porosity based on Eq. (4.22)

For simplicity, it is assumed that eluites do not interfere with each other's correlation parameters. The molar saturation capacities for all the eluites are the same and they are not affected by the modulator concentration. This Melander et al. correlation implies that when the modulator concentration is zero, the b_i values for eluites are infinity, indicating irreversible bindings. In practice, a column

is usually presaturated with a small nonzero modulator concentration C_{m0}. This also means that during simulation a sample should have a background concentration of the modulator to prevent $\log_{10}0$ situation in simulation software. Thus, in this work, samples in all simulation runs are treated as having a modulator concentration of C_{m0} in its background solution during simulation. Usually, C_{m0} is insufficient to elute the eluites inside the column at a significant peak migration speed. Thus, it is permissible to assume this in the simulation, while in reality the sample may not have any modulator in its background solution. This practice should not cause significant errors in retention time and peak shapes as long as C_{m0} corresponds to very large b_i values.

The model requires the following initial conditions:

$$\begin{aligned}&\text{At } \tau = 0, \quad c_{bi} = c_{pi} = c^*_{pi} = 0 \quad \text{for the eluites} \quad (i = 1, 2, \ldots, N_s - 1), \quad \text{and}\\ &\text{at } \tau = 0, \quad c_{bi} = c_{pi} = C_{m0}/C_{0i} = c_{m0}, \quad \text{and} \quad c^*_{pi} \equiv 0\\ &\quad \text{for the modulator} \quad (\text{i.e., } i = N_s)\end{aligned}$$

The dimensionless feed concentration profiles for the boundary conditions at the column inlet are as follows:

For the eluites ($i = 1, 2, \ldots, N_s - 1$),

$$C_{fi}(\tau)/C_{0,i} = \begin{cases} 1 & 0 \le \tau \le \tau_{imp} \\ 0 & \tau_{imp} \end{cases} \tag{12.4}$$

For the modulator ($i = N_s$),

$$C_{fi}(\tau)/C_{0i} = \begin{cases} = C_{m0}/C_{0i} & -\infty < \tau \le \tau_{imp} \\ \ge (\text{or} \quad \le) C_{m0}/C_{0i} & \tau > \tau_{imp} \end{cases} \tag{12.5}$$

The concentration of an eluite before injection is taken as their reference concentration value, C_{0i}. For the modulator, its reference concentration value can take any convenient value. For example, 1 can be used to indicate 100 % (v/v) of a solvent. In this case, modulator concentration uses volume fraction of the modulator for convenience. Unlike the eluites (often proteins), there is no need to use molar concentration since the modulator will not bind with the stationary phase $\left(c^*_{pi} \equiv 0\right)$. The gradient profile of a modulator concentration is described in Eq. (12.5). It can take any shape after a sample injection (i.e. after $\tau > \tau_{imp}$). If the takeoff of the modulator concentration after a sample injection is of nonlinear nature, i.e., $C_{f,N_s}(\tau)/C_{0,N_s}$ vs. τ is nonlinear for $\tau > \tau_{imp}$, the process is sometimes known as nonlinear gradient elution.

12.3 Numerical Solution

The gradient model is numerically solved using Fortran 77 to get GRADIENT.FOR for Chromulator 1.0. The code was obtained by modifying the existing code KINETIC.FOR that was written for the kinetic rate model described in Chap. 10. The Fortran code was compiled to get GRADIENT.DLL for Chromulator 2.2 which has a C++ GUI for Microsoft Windows.

The use of the kinetic rate model instead of an equilibrium rate model gives a special advantage in dealing with gradient elution with variable b_i values for the eluites. In the equilibrium rate model, the multicomponent Langmuir isotherm is directly inserted into the particle phasegoverning equation to eliminate c_{pi}^{*} in Eq. (3.10). This makes the left-hand side of Eq. (3.10) too complicated for the evaluation of time derivatives of particle phase concentrations in gradient elution, since a_i and b_i in the multicomponent Langmuir isotherm are also timedependent variables because of Eq. (12.1). Fortunately, all the complications are not present if the kinetic model is used.

The asymptotic limit of the kinetic model is the equilibrium rate model. To use the kinetic model as an equilibrium rate model for gradient elution, one only has to set the Damköhler number for the desorption (or adsorption) of eluites (i=1, 2, . . ., N_s-1) in the kinetic model to a large arbitrary value (say, no less than 1,000) and then calculate the Damköhler number for adsorption (or desorption) from the relationship $\mathrm{Da}_i^{a}/\mathrm{Da}_i^{d} = b_i C_{0i}$, where b_i is obtained from Eq. (12.1). By doing so, Eq. (12.1) is combined with the kinetic model with ease. The incorporation of Eq. (12.5) in the initial conditions in the Fortran code required for gradient elution is straightforward.

12.4 How to Use the GRADIENT Simulator

To demonstrate the capability of the simulator, two simulation cases are presented below. In both cases, the sample size is $\tau_{imp} = 0.3$, and $\varepsilon_p = \varepsilon_b = 0.4$. It is assumed that the adsorption of the modulator onto the stationary phase is negligible. This is done by setting the right-hand side of Eq. (10.3) to zero for component N_s because the last component is designated as the modulator in all simulation cases.

Figure 12.1 shows a simulated chromatogram of a gradient elution of three proteins with a modulator (component 4). The eluite–modulator relationships are shown in Fig. 12.2. Two consecutive linear gradients are used to achieve a complete baseline separation within a short period of time. In Fig. 12.1, the meanings of some of the parameter symbols are as follows: C_0 = the concentration in the sample for components 1–4 (C_{04} is conveniently set to 1, i.e., 100 % of a solvent for the modulator), $timp = \tau_{imp}$, $tint = \tau$ interval in chromatogram, $tmax$ = maximum τ in the chromatogram, cnsp0 = dimensionless initial concentration of the modulator inside the column before sample injection $(= C_{m0}/C_{0,N_s} = C_{m0}/C_{04} = c_{m0})$,

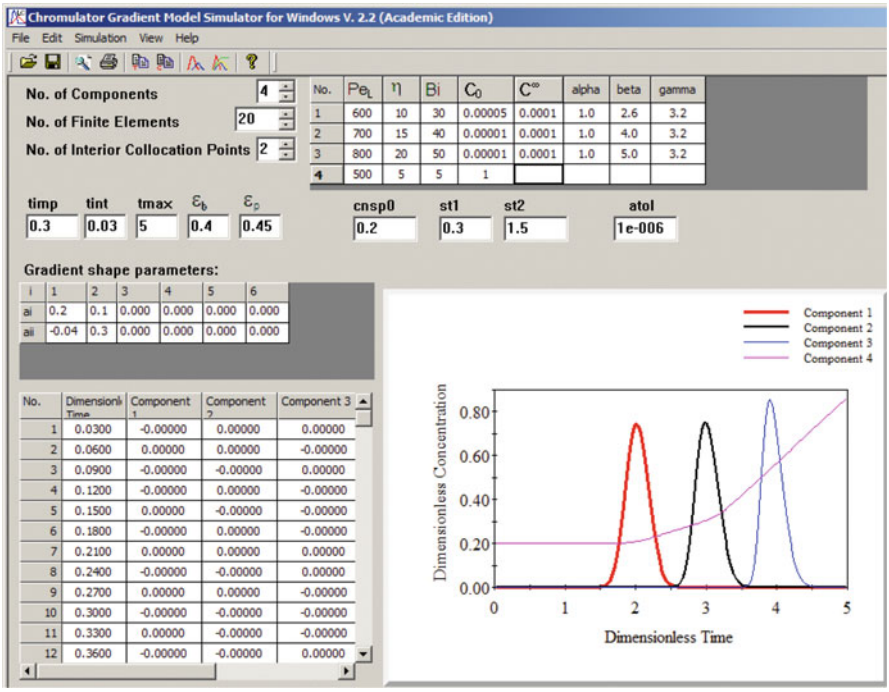

Fig. 12.1 Screenshot of GRADIENT simulator for the elution of three components using two consecutive linear gradients in the mobile phase. The first gradient takes off in the mobile phase tubing right after the sample pulse. The second gradient takes off 1.5 (dimensionless time) after the sample pulse starts to enter the column inlet

st1 = dimensionless time for the first gradient front to reach the column inlet, and st2 = dimensionless time for the second gradient front to reach the column inlet. The *a*1–*a*6 and *a*11–*a*66 values are the coefficients used to describe the two linear gradient profiles. If there is no second gradient, st2 can be set to a value larger than tmax. If so, the software does not read parameters *a*11–*a*66 in the input data file. It is assumed that the pulse sample always has a modifier concentration of cnsp0 in its background solution to prevent singularity in computation as discussed earlier in this chapter. The st1 value must be set to a value equal or higher than *timp* because the gradient front cannot enter the column before the sample is completely inside the column unless two pumps are run simultaneously in an unlikely arrangement: one for sample, and another for mobile phase at the same time. In Fig. 12.1, st1 is equal to *timp*. This means that the gradient front follows the end of sample pulse. Note that the Chromulator assumes that the pulse feed starts to enter the column at $\tau = 0$. The atol input is used to adjust the absolute tolerance of the VODE ODE solver in the software. A smaller tolerance value such as atol $= 10^{-8}$ may solve a stiff case that crashes with atol $= 10^{-6}$ or 10^{-7} at a cost of increased computation time. However, if atol is too small, the ODE solver may be trapped in an infinite loop, resulting in ODE solver error as well. Other Chromulator simulators have a

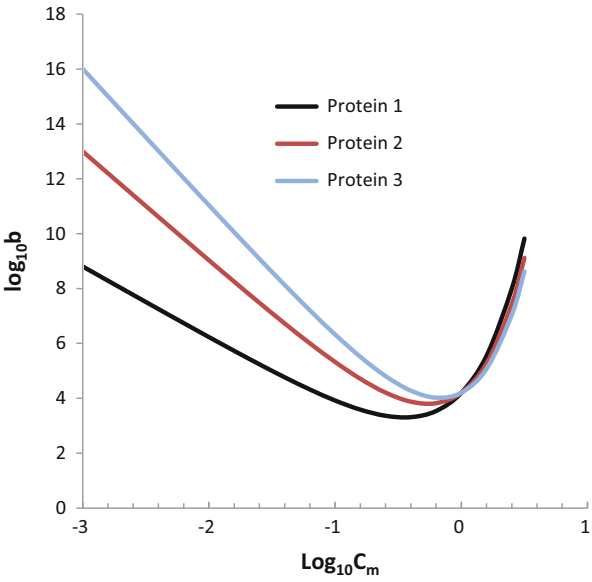

Fig. 12.2 Eluite–modulator relationship used in Fig. 12.1

fixed atol value of 10^{-6}. This is because the GRADIENT simulator crashes in stiff cases due to numerical difficulties, while other simulators usually don't crash. The use of Eq. (12.1) with log terms may be a major factor. Users may also artificially reduce mass transfer parameters to avoid excessive stiffness in case of crashes. N_e and N values can also be adjusted to avoid crashes. Another tweak is to use a smaller tint step size. A very small tint will increase calculation and plotting times considerably, but it makes the ODE solver more robust.

When $\tau < \mathrm{st1}$, the dimensionless modulator feed concentration is automatically maintained at cnsp0 by the simulator. When $\tau = \mathrm{st1}$, the first gradient starts with the following profile:

$$C_{\mathrm{f},N_s}(\tau)/C_{0,N_s} = a1 + a2 \cdot (\tau - \tau_{\mathrm{imp}}) + a3 \cdot (\tau - \tau_{\mathrm{imp}})^2 + a4 \cdot (\tau - \tau_{\mathrm{imp}})^3 + a5 \cdot \exp[a6 \cdot (\tau - \tau_{\mathrm{imp}})] \tag{12.6}$$

This means that at $\tau = \mathrm{st1}$, the gradient front reaches the column inlet. When $\tau = \mathrm{st2}$, the second gradient front with the following profile reaches the column inlet:

$$C_{\mathrm{f},N_s}(\tau)/C_{0,N_s} = a11 + a22 \cdot (\tau - \tau_{\mathrm{imp}}) + a33 \cdot (\tau - \tau_{\mathrm{imp}})^2 + a44 \cdot (\tau - \tau_{\mathrm{imp}})^3 + a55 \cdot \exp[a66 \cdot (\tau - \tau_{\mathrm{imp}})] \tag{12.7}$$

In Fig. 12.1, the first gradient front reaches the column inlet at $\tau = \mathrm{st1} = \tau_{\mathrm{imp}} = 0.3$, immediately following the sample pulse with a modulator concentration profile of

$C_{f,N_s}(\tau)/C_{0,N_s} = 0.2 + 0.1(\tau - \tau_{imp})$. At $\tau = st2 = 1.5$, the second gradient front reaches the column inlet. It has an increased slope of 0.3 instead of 0.1. At $\tau = st2$, the two $C_{f,N_s}(\tau)/C_{0,N_s}$ expressions above must have the same value to achieve continuity of the modifier concentration feed into the column. This means that for the two linear gradients to connect in the case shown in Fig. 12.1 at $\tau = st2$, $a1$, $a2$, $a11$ and $a22$ values must satisfy $a1 + a2 \cdot (st2 - \tau_{imp}) = a11 + a22 \cdot (st2 - \tau_{imp})$. This requires $a11 = -0.04$. In the modulator output effluent profile shown in Fig. 12.1, there is a delay compared to times when the gradient fronts reach the column inlet due to column bed voidage and porosity. The delay is equal to the dimensionless "solvent time" of $\tau_0 = 1.675$ as calculated by Eq. (4.17). Thus, the first gradient takes off at 1.975 ($= st1 + \tau_0$) and the second gradient takes off 3.175 ($= st2 + \tau_0$) in the modulator effluent profile in Fig. 12.1 compared to 0.3 ($= st1$) and 1.5 ($= st2$) in the feed. The gradient profile is slightly diffused at the two connection points due to mass transfer effects inside the column.

In the two gradient profiles above, $C_{f,N_s}(\tau)$ is the modulator concentration at the column inlet at dimensionless time τ. $\tau = 0$ is the moment when the sample first enters the column inlet. Ideally, the gradient front immediately follows the end of the injected sample stream;thus we have $(\tau - \tau_{imp})$ instead of τ in the gradient profiles as shown in Eq. (12.6) above. In reality, the sample leaves the sample loop at $\tau = 0$, and it enters the column soon after. The delay time between the injector exit and the column inlet is usually negligible. On the other hand, the gradient front begins at the gradient mixer at $\tau = 0$, not at the end of the sample stream especially when the sample loop is not full. For example, a 2 ml sample loop may be filled with only 0.1 ml sample and the rest is still the mobile phase. The gradient front has to travel through the sample loop to reach the column inlet. There is usually a distance between the gradient front and the end of the sample stream. This creates a lag time, during which the modulator concentration is still its initial concentration, cnsp0. A failure to consider this factor may lead to wrong gradient profile input parameters. Although in Eq. (12.6), τ_{imp} was used as the default delay in the simplest case, longer delays are allowed. Users just have to match the actual gradient profile with time zero at the moment the sample starts to enter the column inlet with Eq. (12.6). Let's consider a simple case in which a gradient elution has a single linear gradient with a dimensionless modulator concentration change of Δc_{N_s} (i.e., the gradient starts from cnsp0 to cnsp0 $+ \Delta c_{N_s}$) in a dimensionless time period of $\Delta\tau$. The dimensionless sample pulse size is τ_{imp}. At time $\tau = 0$, the sample starts to enter the column inlet and the gradient front starts to leave the gradient mixer. Assume that it takes the gradient front a dimensionless time of τ_{delay} to travel from the mixer to the column inlet via the sample loop. Then, we should have $st1 = \tau_{delay}$, and the gradient profile should be

$$C_{f,N_s}(\tau)/C_{0,N_s} = \left[cnsp0 - (\Delta c_{N_s}/\Delta\tau)(\tau_{delay} - \tau_{imp})\right] + (\Delta c_{N_s}/\Delta\tau)(\tau - \tau_{imp}) \quad (12.8)$$

which means that for the gradient input parameters,

$$a1 = \text{cnsp0} - \left(\Delta c_{N_s}/\Delta\tau\right)\left(\tau_{\text{delay}} - \tau_{\text{imp}}\right) \tag{12.9a}$$

and

$$a2 = \Delta c_{N_s}/\Delta\tau \tag{12.9b}$$

The gradient delay volume V_{delay} is defined as the volume of the liquid between the gradient front and the column inlet because simulation time zero is the time when the sample starts to enter the column inlet. The time it takes to move this much liquid to reach the column inlet is V_{delay}/Q, corresponding to a dimensionless gradient delay time of $\tau_{\text{delay}} = \left(V_{\text{delay}}/Q\right)/(L/v)$. For very thin stainless steel tbings, the liquid volume between the sample loop exit (column end) and the column inlet is often negligible compared to the sample loop volume. The liquid volume between the gradient mixture and the tail end of the sample loop is also negligible for thin tubings. In this kind of cases, $V_{\text{delay}} = V_{\text{loop}}$ (sample loop volume). Obviously, $a2$ is the gradient slope. Usually, a sample loop is not completely filled; only the exit end (near the column) is filled with a sample by displacing some preexisting mobile phase liquid, while the rest is still filled with the preexisting mobile phase. $\tau_{\text{delay}} = \tau_{\text{imp}}$ would require the sample loop to be completely filled with the sample. If the system has $\tau_{\text{delay}} = \tau_{\text{imp}}$, meaning the gradient front immediately follows the end of injected sample stream, then $\text{st1} = \tau_{\text{delay}} = \tau_{\text{imp}}$, and Eq. (12.8) simplifies to

$$C_{\text{f},N_s}(\tau)/C_{0,N_s} = \text{cnsp0} + \left(\Delta c_{N_s}/\Delta\tau\right)\left(\tau - \tau_{\text{imp}}\right) \tag{12.10}$$

Thus, $a1$ is equal to cnsp0 in the input in this simplest case. Eq. (12.10) shows that the gradient concentration starts from cnsp0 and ends with $\text{cnsp0} + \Delta c_{N_s}$ for the time duration of 0 to $\Delta\tau + \tau_{\text{imp}}$. Of cause, a chromatographer may choose to start a gradient with a different concentration than cnsp0. If so, $a1$ is different from cnsp0.

Figure 12.2 shows the eluite–modulator relationships for the three proteins in Fig. 12.1. It indicates that on the left-hand side, there are big differences in affinity (Langmuir isotherm parameter b value), while on the right-hand side the b values almost overlap. An increased modulator concentration gradient results in reduced b values for the three curves on the left-hand side. Figure 12.1 simulates the scenario of two linear gradients with an increasing solvent concentration from 20 % (= $\text{cnsp0} = a1$) to 86 % (at $\tau = 3.325$) in the influent. 86 % is seen at $\tau = 5$ in Fig. 12.1 (effluent) due to a delay of $\tau_0 = 1.675$. In hydrophobic interaction chromatogram, the right-hand side b values in Fig. 12.2 would have big differences, such that a decreasing salt concentration would be used to gradually weaken binding.

In Fig. 12.3, the following quadratic gradient is used to replace the two linear gradients in Fig. 12.1 to yield a similar baseline separation outcome:

$$C_{\text{f},N_s}(\tau)/C_{0,N_s} = 0.2 + 0.07\left(\tau - \tau_{\text{imp}}\right)^2 \quad \text{for} \quad \tau \geq \tau_{\text{imp}} \tag{12.11}$$

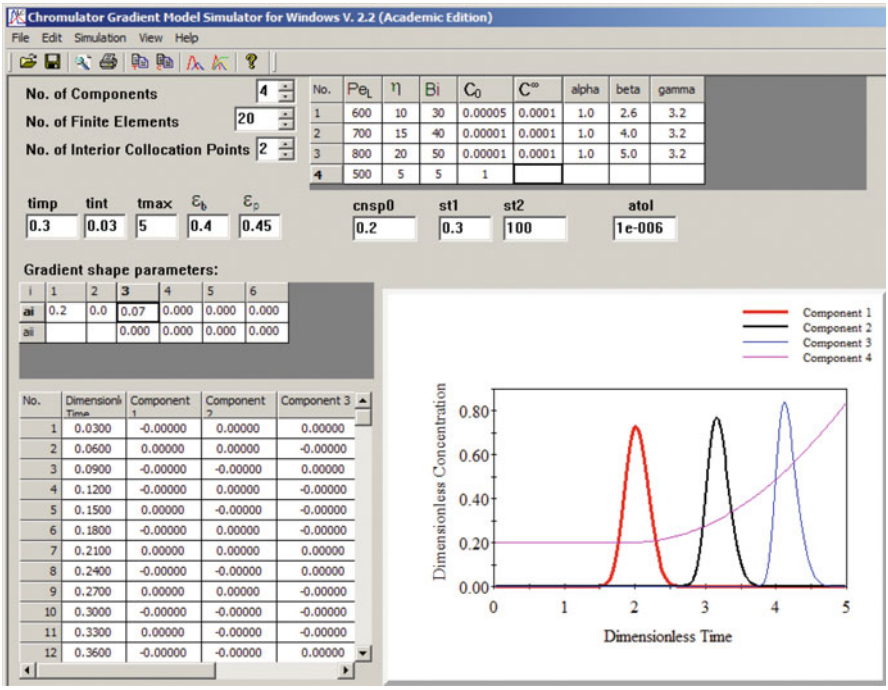

Fig. 12.3 Screenshot of GRADIENT simulator for the elution of three components using a nonlinear gradient of $0.015 + 0.0007(\tau - \tau_{\text{imp}})$ for the modulator in the mobile phase

In the input data, the st2 value is set to an arbitrary value greater than $t_{\max}$. This signals the simulator to use the first gradient until it terminates at $t_{\max}$. The second gradient never has a chance to take off and thus $a$ii values in the input data are not needed in Fig. 12.3.

Users must be fully aware that $a11$, $a22$, and st2 values cannot be arbitrarily specified to test run chromatogram simulation. Users are advised to draw the feed gradient profiles on a chart to see whether the sections connect as desired. The gradient input parameters have enough flexibility to cope with many situations. For example, a washing step after a sample is injected can be described as either a flat gradient curve or as extra delay time if it uses cnsp0 concentration in the mobile phase. If the user wants a different gradient scheme that cannot be described by the current setup, the GRADIENT.FOR code can be easily modified.

12.5 Parameter Estimation for Gradient Elution Simulation

The estimation of mass transfer parameters has been discussed in Chap. 4. For gradient elution, the estimation of α, β, γ, and C^{∞} are discussed here. For simplicity, eluite–modulator relationship in Eq. (12.1) and Eq. (12.2) donot consider

interactions through Langmuir isotherm parameter b among different eluites. The eluites are related through the Langmuir isotherm parameter C^{∞}. For each eluite, a small column is used to run several isocratic elutions using different fixed modulator concentrations in the mobile phase to obtain the corresponding retention factor k' values. For some systems, the β term can be dropped. Thus, Eqs. (12.1) and (12.2) are simple linear relationships. A minimum of two k' vs. C_{m} (modulator concentration) data points are needed to obtain α' and γ values. If there are more than two data points, linear regression can be performed. If the β term cannot be dropped, multilinear regression can be used because Eq. (12.2) follows the $y = a1x_1 + a2x_2 + a3x_3$ format. MATLAB from mathworks.com may be used to perform this type of regression easily. The α' value for an eluite must be converted to α for use by Chromulator using $\alpha = \alpha' - \log_{10}\varphi C^{\infty}$ in which the phase ratio φ is calculated from ε_{b} and ε_{p} according to Eq. (4.15).

Several methods for the estimation of adsorption saturation capacity are discussed in Chap. 4. Gu and Zheng [7] described a different procedure to obtain C^{∞} using gradient elution based on the method introduced by Snyder and Stadalius [8] making use of a small retention time difference, Δt_{R} (min), from two gradient runs for an eluite, one with a small sample and another with a large (overload) sample. Based on Snyder and Stadalius [8] correlations, the following equation was derived by Gu and Zheng [7] to obtain w_{s} (mg of eluite) that is the saturation capacity for the entire column:

$$\frac{w_{\mathrm{s}}}{w_{\mathrm{x}}} = \frac{2.5}{\left(1 - 10^{-0.48\,\mathrm{MW}^{0.44}\Delta t_R \Delta C_{\mathrm{m}}/t_{\mathrm{G}}}\right)^2} \tag{12.12}$$

in which MW is the molecular weight of a protein ($600 \le \mathrm{MW} \le 80{,}000$), and ΔC_{m} is the change in volume fraction of the organic modulator such as acetonitrile (ACN) in the mobile phase during a gradient time period of t_{G} (min). For example, a linear ACN gradient of 40 % (v/v) to 80 % in 30 min would yield $\Delta C_{\mathrm{m}} = 0.8 - 0.4 = 0.4$ for $t_{\mathrm{G}} = 30$ min. In Eq. (12.12), w_{x} is the amount of eluite (mg) in the large sample. With w_{s} obtained, C^{∞} (mmol per unit volume of particle skeleton) can be calculated using the following relationship:

$$C^{\infty} = \frac{(w_{\mathrm{s}}/\mathrm{MW})}{(1 - \varepsilon_{\mathrm{b}})(1 - \varepsilon_{\mathrm{p}})V_{\mathrm{b}}} \tag{12.13}$$

in which $(1 - \varepsilon_{\mathrm{b}})(1 - \varepsilon_{\mathrm{p}})\,V_{\mathrm{b}}$ is the total particle skeleton volume for a column with a bed volume of V_{b}.

12.6 Application Example

Gu and Zheng [7] predicted HPLC chromatograms for human growth hormone (hGH) and a human growth hormone antagonist called hGHG120R (MW = 22 k). The discovery of hGHG120R, an analogy of hGH with a replacement of a single amino acid at the amino acid position 120 [9], led to the prescription drug SOMAVERT®. The two proteins can be separated on a preparative C4 reverse phase Vydac 214TP510 RP-HPLC column (25 cm × 1 cm, 19.63-ml bed volume, 5-μm particles with 300-Å pores) with an acetonitrile (ACN) gradient [7]. A smaller 25 cm × 0.46 cm analytical RP-HPLC column (Vydac 214TP54) with the same packing material was used to obtain some physical parameters for simulation. In all the LC operations for the two columns discussed in this chapter, the mobile had a constant 0.1 % (v/v) trifluoroacetic acid (TFA) concentration, which is routinely used to suppress the ion-exchange side effect and to minimize silica dissolution exacerbated by higher mobile phase pH.

The analytical column yielded a solvent time of $t_0 = 2.78$ min at a mobile phase flow rate of 1 ml/min. Based on $\varepsilon_b = 0.4$ that is typical for beds with 5-μm silica beads [10], $V_b = 4.155$ ml and $Q = 1$ ml/min, Eq. (4.15) gives $\varepsilon_p = 0.45$. A very small hGHG120R sample was injected into the analytical column and eluted out using a 40 % (v/v) ACN to 80 % ACN gradient ($\Delta C_m = 80\ \% - 40\ \% = 0.4$) in 30 min at 1 ml/min. This run was repeated with a relatively large sample size of $w_x = 2.176$ mg hGHG120R. The hGHG120R retention times in these two runs were 22.50 and 20.48 min, respectively. These data led to $w_s = 6.55$ mg based on Eq. (12.10). After conversion, this value gives $C^{\infty} = 2.2 \times 10^{-4}$ mol/l (particle skeleton) based on Eq. (12.11). The same value is used for hGH to keep the molar-based adsorption saturation capacity the same, which is required by the thermodynamic consistency for the Langmuir isotherm. On the analytical column, three isocratic elution runs were carried out to obtain t_R values corresponding to 56.99 %, 61.83 %, and 62.02 % ACN in the mobile phase. Figure 12.4 shows the relationship of $\log_{10} k'$ vs. C_m. The two straight lines suggest $\beta_i = 0$ for both hGH and hGHG10R. The α_i' values from Fig. 12.4 for hGH and hGHG120R are 14.4935 and 13.6875, respectively, while the γ_i values are −22.9190 and −22.3863, respectively. The α_i' values correspond to α_i values of 18.456 and 17.650 for hGH and hGHG120R, respectively based on Eq. (12.3) with a phase ratio of $\varphi = 0.493$.

Figure 12.5 simulates the gradient elution of a 40 μl binary sample containing 5.7×10^{-7} mol/l hGH and 5.5×10^{-6} mol/l hGHG120R on the preparative C4 column using a gradient of 40 % ACN + 0.1 % TFA to 80 % ACN + 0.1 % TFA in 30 min at a flow rate of 2 ml/min. Sources for the parameters used in the simulation are listed in Table 12.1. The Pe_L, η, and Bi values can be easily calculated by using the Microsoft Excel spreadsheet in Table 4.1. C_0 for the last component is set to 1 (i.e., 100 % ACN) and ACN concentration is expressed conveniently in volume fraction rather than mol/l throughout this chapter. Because the Peclet number of 25,000 is extremely stiff, it is replaced by 1,000 for simulation. Using a less stiff Peclet number will not change peak width much in this kind of stiff cases because

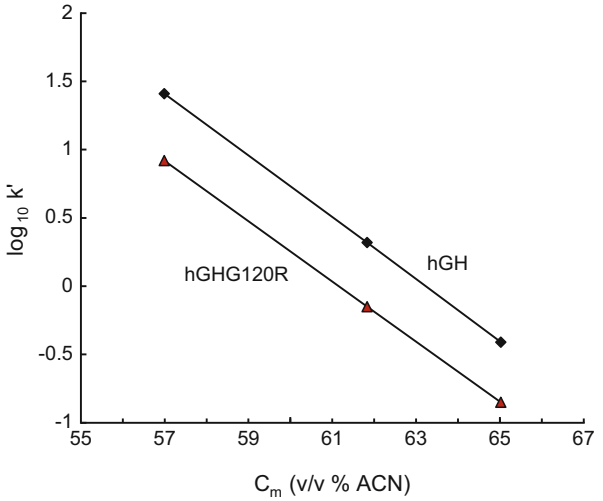

Fig. 12.4 Retention factor vs. ACN concentration for the determination of α_i', β_i, and γ_i in the eluite–modulator relationship (experimental data from [7])

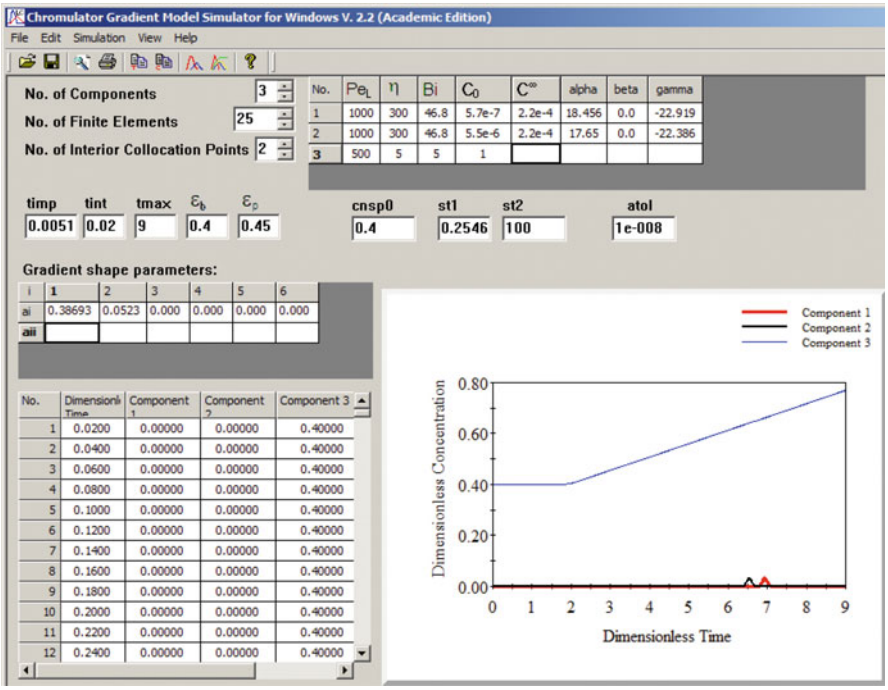

Fig. 12.5 Screenshot of gradient elution simulation for a 40 µl binary sample (first component hGH and second hGHG120R) separated on a 25 cm × 10 mm Vydac 214TP510 C4 preparative RP-HPLC column using a linear gradient of 40 % ACN + 0.1 % TFA to 80 % ACN + 0.1 % TFA in 30 min at 2 ml/min (after [7])

Table 12.1 Simulation parameters for the two proteins in Fig. 12.5 (data from [7])

Direct raw data:		
L (column length, cm)	25	
d_c (column diameter, cm)	1	
Q (flow rate, ml/min)	2	
V_{imp} (sample pulse volume, ml)	40×10^{-3}	
C_{sample} (sample concentration, M)	5.5×10^{-7} for hGH and 5.5×10^{-7} for hGHG120R	
Molecular weight	22×10^3	
C_{m0} (initial modulator fraction)	0.4 (=40 % ACN)	
ΔC_m (gradient modulator fraction change)	0.4 (=80 %−40 % for ACN)	
V_{loop} (sample loop size, ml)	2	
V_{delay} (gradient delay volume, ml)	2	$=V_{loop}$ in this case
R_p (cm)	2.5×10^{-4}	
d_p (particle macropore size, Å)	300	
t_G (gradient time duration, min)	30	
ε_b (bed voidage)	0.4	
τ_{tor} (particle tortuosity)	4	
Calculated data:		
V_b (bed volume, ml)	19.63	
v (interstitial velocity, cm/s)	0.106	$Q/(\varepsilon_b \cdot V_b/L)$
ε_p (particle porosity)	0.45	Eq. (4.15)
τ_{imp} (dimensionless sample pulse time)	5.09×10^{-3}	$(V_{imp}/Q)/(L/v) = V_{imp}/(V_b\varepsilon_b)$
τ_{delay} (dimensionless delay time, =st1)	0.2546	$(V_{delay}/Q)/(L/v)$
$\Delta\tau$ (dimensionless gradient time duration)	7.637	$t_G/(L/v)$
$a1 = C_{m0} - a2(\tau_{delay} - \tau_{imp})$	0.38693	Eq. (12.9a)
$a2 = \Delta C_m/\Delta\tau$	0.05236	Eq. (12.9b)
d_m (molecular diameter, Å)	40.35	Eq. (4.36)
$\lambda = d_m/d_p$	0.1345	
D_m (molecular diffusivity, cm^2/s)	9.78×10^{-7}	Eq. (4.27)
D_p (effect. intraparticle diffusivity, cm^2/s)	1.77×10^{-7}	Eq. (4.35)
k (film mass transfer coeff., cm/s)	0.0148	Eq. (4.38)
Pe_L (Peclet number)	25,000	Eq. (4.32)
$\eta = \varepsilon_p D_p L/(R_p{}^2 v)$	299.5	Eq. (4.34)
$Bi = kR_p/(\varepsilon_p D_p)$	46.8	Eq. (4.37)
L/v (time conversion factor, min)	3.928	

Peclet beyond 1,000 is insensitive. There is no need to evaluate the Peclet number, η, and Bi numbers for ACN because its profile is not stiff. Figure 12.5 used 500, 5, and 5, respectively, for these three parameters. Users can always rerun the

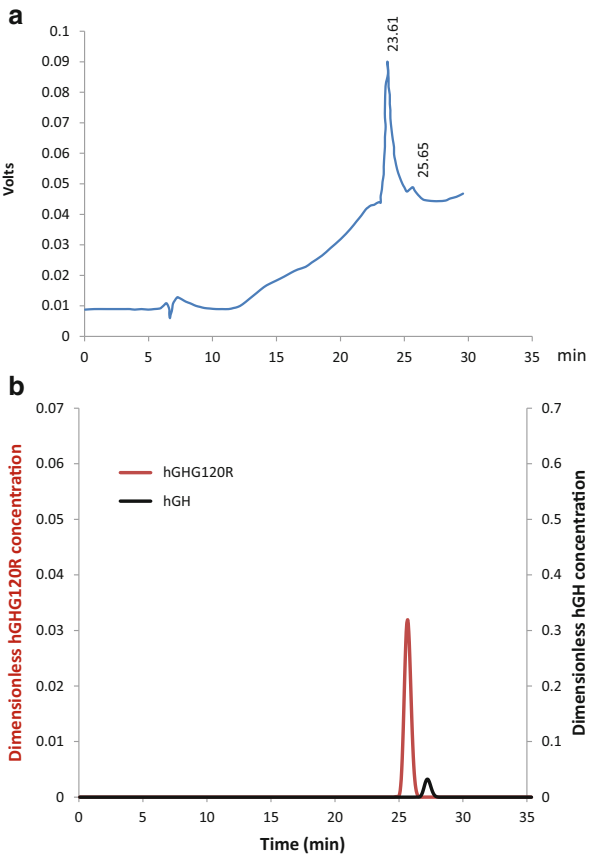

Fig. 12.6 Comparison of experimental and simulated binary gradient elution. Subplot (**b**) is based on Fig. 12.5 data (experimental data from [7])

simulation by changing an input parameter to see whether the chromatogram is sensitive to the change or not.

Figure 12.6 shows a comparison of the experimental chromatogram and the simulated chromatogram. Figure 12.6b is based on the data of Fig. 12.5 with the dimensionless time converted (dimensionless time of 1 is equivalent to 3.928 min in this case as shown in Table 12.1). Because the hGH sample concentration is actually an order of magnitude smaller than that of hGHG120R (see Table 12.1), to achieve a better visual comparison, the hGH peak height is reduced by using a larger *y*-axis range on the right. In practice, it is the peak width rather than height that really matters in scale-up. Retention time also matters. Figure 12.6 shows that simulated results are useful in predicting retention time and peak width in this rather complicated gradient elution case. This proves that the software is useful in gradient LC scale-up.

Figure 12.7 shows the simulation of the gradient elution separation of a relatively pure and large hGHG120R sample (50 ml) using the preparative C4 column as its final separation step in an actual research project to obtain hGHG120R for lab

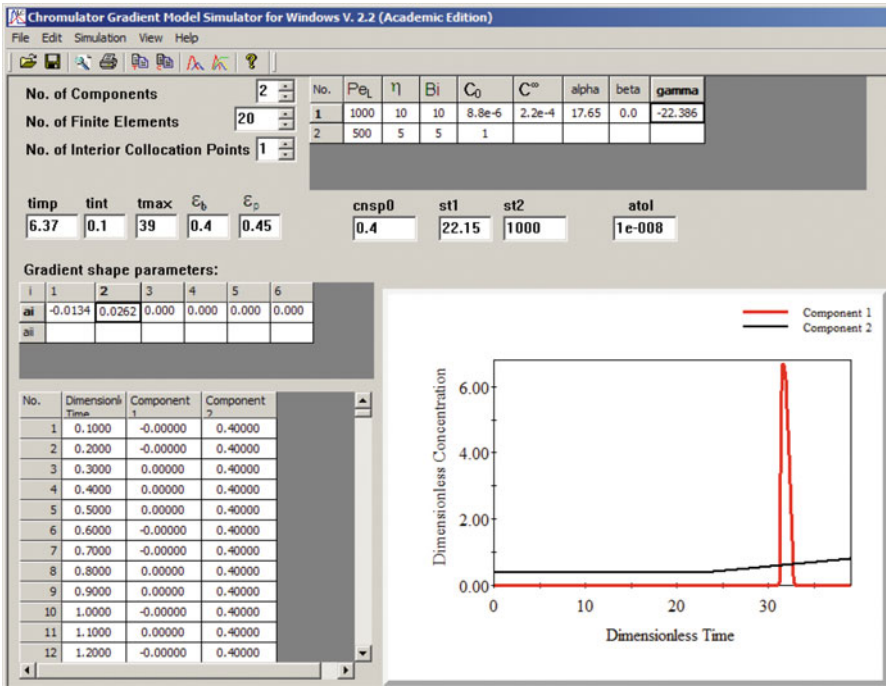

Fig. 12.7 Screenshot of the simulation of 50 ml hGH sample eluted from Vydac 214TP510 C4 column using a linear gradient of 40 % ACN + 0.1 % TFA to 80 % ACN + 0.1 % TFA in 60 min at 2 ml/min

testing on mice [9]. Parameters for simulation are listed in Table 12.2. In the actual experiment, the column was presaturated with 40 % ACN + 0.1 % TFA. A 50 ml semipurified hGHG120R sample was pumped into the column without using a sample loop because it was much smaller than 50 ml. It was followed by a washing stage using 120 ml 40 % ACN + 0.1 % TFA. After pumping in the 120 ml mobile phase, a 40 % ACN + 0.1 % TFA to 80 % ACN + 0.1 % TFA in 60 min linear gradient was started in the gradient mixer. There was 4 ml mobile phase between the column inlet and the gradient mixer. This means that the gradient front had a total 174 ml liquid ahead of it at the moment when the sample started to enter the column inlet (i.e., time zero in simulation). The flow rate throughout this experimental run was 2 ml/min. For this very stiff case, the protein's Peclet, η, and Biot numbers were artificially reduced from those in Table 12.2 to 1,000, 10, and 10, respectively. Increasing these numbers will not change the peak width significantly, but they may cause the program to crash due to numerical difficulties encountered by the tolerance check of the ODE solver in the software.

Figure 12.8 shows the comparison of experimental and simulated chromatograms. The experimental retention time of 38.14 min matches the model prediction well. Peak widths also match well. Figure 12.8b is based on the data of Fig. 12.7 with its dimensionless time converted to real time. In the experiment, the 50 ml

Table 12.2 Simulation parameters for hGH in Fig. 12.7 (data from [7])

Direct raw data:	
L (column length, cm)	25
d_c (column diameter, cm)	1
Q (flow rate, ml/min)	2
V_{imp} (sample pulse volume, ml)	50
C_{sample} (sample concentration, M)	8.8×10^{-6}
Molecular weight	22×10^3
C_{m0} (initial modulator fraction, =cnsp0)	0.4 (=40 % ACN)
ΔC_m (gradient modulator fraction change)	0.4 (=80 % − 40 % for ACN)
V_{delay} (gradient delay volume, ml)	174
R_p (cm)	2.5×10^{-4}
d_p (particle macropore size, Å)	300
t_G (gradient time duration, min)	60
ε_b (bed voidage)	0.4
τ_{tor} (particle tortuosity)	4
Calculated data:	
V_b (bed volume, ml)	19.63
v (interstitial velocity, cm/s)	0.106
ε_p (particle porosity)	0.45
τ_{imp} (dimensionless sample pulse time)	6.37
t_{delay} (delay time, min)	87
τ_{delay} (dimensionless delay time, =st1)	22.15
$\Delta\tau$ (dimensionless gradient time duration)	15.27
$a1 = C_{m0} - a2(\tau_{delay} - \tau_{imp})$	−0.134
$a2 = \Delta C_m/\Delta\tau$	0.0262
d_m (molecular diameter, Å)	40.35
$\lambda = d_m/d_p$	0.1345
D_m (molecular diffusivity, cm^2/s)	9.78×10^{-7}
D_p (effect. intraparticle diffusivity, cm^2/s)	1.77×10^{-7}
k (film mass transfer coeff., cm/s)	0.0148
Pe_L (Peclet number)	25,000
$\eta = \varepsilon_p D_p L/(R_p{}^2 v)$	299.5
$Bi = kR_p/(\varepsilon_p D_p)$	46.8
L/v (time conversion factor, min)	3.928

sample size was more than twice as large as the column volume (19.63 ml). It was an overload LC case. The flat top of the peak in Fig. 12.8a was due to its large concentration that was out of the UV detector response range. Due to gradient elution, hGHG120R in the effluent was much more concentrated as indicated by the dimensionless peak concentration height of 6.6 (i.e., 6.6 times of the feed concentration at the peak tip). In Fig. 12.8a, the experimental chromatogram's time (in min) did not start when the sample started to enter the column. The chart recorder was started when the 50 ml sample and 120 ml washing mobile phase had been pumped into the column. This means Fig. 12.8a time was cut short by

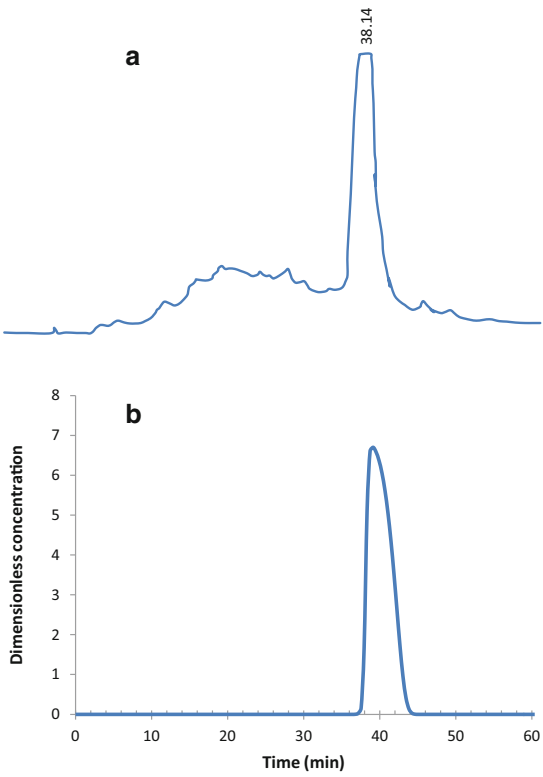

Fig. 12.8 Comparison of experimental (**a**) and simulated (**b**) chromatograms for a large hGH sample. Subplot (**b**) is based on Fig. 12.7 data (experimental data from [7])

85 min at a flow rate of 2 ml/min. Thus, the dimensionless time in Fig. 12.7 should be converted to real time using the following formula:

$$t = \tau(L/v) - t_{\text{adj}} \tag{12.14}$$

in which $t_{\text{adj}} = 85$ min because simulation time zero is ahead of chart recording time zero by 85 min. The experimental chromatogram in Fig. 12.8a shows that there were obviously numerous impurities before the hGHG120R peak. It is impractical to include these impurities in the simulation because their parameter estimation would be too demanding. In scale-up, one may use hGHG120R as the product compound and another compound as a key impurity that affects the separation outcome most. It is then worthwhile to devote efforts toward parameter estimation of the key impurity.

The simulation examples above all use an increasing solvent concentration gradient to elute out proteins. In hydrophobic interaction LC, however, a decreasing salt gradient is used to weaken protein binding. This is because proteins bind more strongly through hydrophobic interaction with ion-exchange resins when the resins are coated with a salt solution layer. When the salt solution layer is removed, proteins will be dislodged. This binding behavior is covered by the eluite–modulator relationship proposed by Melander et al. as discussed earlier in this chapter.

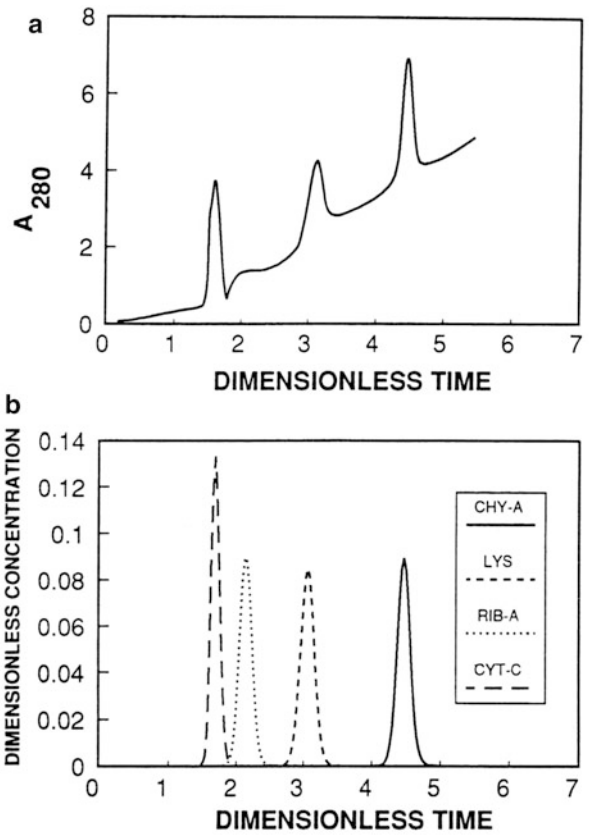

Fig. 12.9 Comparison of experimental and simulated chromatography for a quaternary protein sample containing α-chymotrypsinogen A, lysozyme, ribonuclease A, and cytochrome C separated using a 4 min linear gradient of ammonium sulfate from 1.7 to 0.6 mol/l on a Zorbax Bio-Series WCX-300 (80 mm × 6.2 mm) ion-exchange column (reproduced from [11] with permission)

Truei et al. [11] demonstrated that the GRADIENT simulator predicted the gradient elution separation of four proteins (α-chymotrypsinogen A from bovine pancrease, lysozyme from chicken egg white, ribonuclease A from bovine pancrease, and cytochrome C from horse hear) on Zorbax Bio-Series WCX-300 (80 mm × 6.2 mm) ion-exchange column remarkably well as shown in Fig. 12.9. The four proteins were separated using a decreasing linear gradient of ammonium sulfate from 1.7 to 0.6 mol/l in 4 min. For comparison, the experimental chromatogram was replotted by converting real time to dimensionless time. The UV optical density at 280-nm wave length in the *y*-axis was not converted because peak height comparison is not important in scale-up. It is retention time and peak width that matter most.

12.7 Summary

In this chapter, a general rate model for gradient elution has been presented for the study of gradient elution in nonlinear chromatography. The model is suitable for preparative- and large-scale chromatography since various mass transfer effects,

such as axial dispersion, film mass transfer, and intraparticle diffusion, are considered. The eluite–modulator relationship in the model accounts for both electrostatic and hydrophobic interactions. The software based on the model provides a useful tool for studying various aspects of gradient elution chromatography, including process optimization and scale-up. The scale-up example given in this chapter demonstrates the methodology in parameter estimation and how to match simulated chromatograms with experimental chromatograms.

References

1. Furusaki ES, Haruguchi E, Nozawa AT (1987) Separation of proteins by ion-exchange chromatography using gradient elution. Bioprocess Eng 2:49–53
2. Antia FD, Horváth C (1989) Operational modes of chromatographic separation processes. Berichte der Bunsengesellschaft für physikalische Chemie 93:961–968. doi:10.1002/bbpc.19890930907
3. Pitt WW (1976) Gradient-elution ion exchange chromatography: a digital computer solution of the mathematical model. J Chromatogr Sci 14:396–404
4. Kang K, McCoy BJ (1989) Protein separation by ion exchange chromatography: a model for gradient elution. Biotechnol Bioeng 33:786–790
5. Gu T, Truei YH, Tsai GJ, Tsao GT (1992) Modeling of gradient elution in multicomponent nonlinear chromatography. Chem Eng Sci 47:253–262
6. Melander WR, El Rassi Z, Horváth C (1989) Interplay of hydrophobic and electrostatic interactions in biopolymer chromatography: effect of salts on the retention of proteins. J Chromatogr A 469:3–27
7. Gu T, Zheng Y (1999) A study of the scale-up of reversed-phase liquid chromatography. Sep Purif Technol 15:41–58. doi:10.1016/S1383-5866(98)00083-5
8. Snyder LR, Stadalius MA (1986) Gradient elution. High-performance liquid chromatography-advances and perspectives, C. Horvath. Academic Press, New York, p 195
9. Gu T, Zheng Y, Gu Y, Haldankar R, Bhalerao N, Ridgway D, Wiehl PE, Chen WY, Kopchick JJ (1995) Purification of a pyrogen-free human growth hormone antagonist. Biotechnol Bioeng 48:520–528
10. Unger KK (1979) Porous silica: its properties and use as support in column liquid chromatography. Elsevier, Amsterdam, p 170
11. Truei Y-H, Gu T, Tsai G-J, Tsao G (1992) Large-scale gradient elution chromatography. In: Tsao GT (ed) Bioseparation. Springer, Berlin, pp 1–44

Chapter 13
Modeling of Ion-Exchange Chromatography

13.1 Introduction

Ion-exchange chromatography (IEC) is one of the most popular LC separation methods. It has a higher loading capacity compared with RP-LC. Although RP-LC typically has high resolution, IEC is more compatible with proteins because the strong solvents in RP-LC can denature proteins, which is undesirable for preparative- and large-scale LC. Analytical RP-HPLC does not suffer when proteins are denatured since effluent is not fractionated any way. Thus, due to its high resolution and better reproducibility, RP-HPLC is widely used in analytical applications. SEC is good for protein stability, but its loading capacity is only a small fraction of its column volume. To elute proteins from an ion-exchange column, a gradient of salt and/or pH is required because proteins have a wide range of retentivity.

Proteins are zwitterions with an isoelectric point at which they do not carry a net charge. They can be either positively charged or negatively charged if the solution pH differs from the isoelectric points. Thus, the mobile phase pH affects binding. Modeling gradient IEC with a pH gradient is rather complicated especially when sorption of H^+ or OH^- is involved [1]. At all locations inside the column's particle phase, a charge balance must be performed for all ions. When buffers are present, a set of implicit equations must be solved for the H^+ or OH^- concentration. Ghose and coworkers [2] demonstrated that the sorption of H^+ or OH^- could lead to pH dips or spikes as large as 1 pH unit in the effluent of IEC columns. Although IEC has been modeled by a few research groups such as Wang's group [3] and Frey and coworkers [4], so far, only Mehay and Gu included the calculation of pH in the presence of a buffer solution [1].

© Springer International Publishing Switzerland 2015

T. Gu, *Mathematical Modeling and Scale-Up of Liquid Chromatography*,
DOI 10.1007/978-3-319-16145-7_13

13.2 General Rate Model for Gradient Elution IEC

The general rate model for IEC presented by Mehay and Gu [1] considers axial dispersion, interfacial film mass transfer resistance, and intraparticle diffusion. The dimensionless governing equations are shown below for the bulk-fluid phase and the particle phase, respectively:

$$-\frac{1}{\mathrm{Pe}_{\mathrm{L}i}}\frac{\partial^2 c_{\mathrm{b}i}}{\partial z^2}+\frac{\partial c_{\mathrm{b}i}}{\partial z}+\frac{\partial c_{\mathrm{b}i}}{\partial \tau}+\xi_i\left(c_{\mathrm{b}i}-c_{\mathrm{p}i,r=1}\right)=0 \tag{13.1}$$

$$\left(1-\varepsilon_{\mathrm{p}}\right)\frac{\partial q_i}{\partial \tau}+\varepsilon_{\mathrm{p}}\frac{\partial c_{\mathrm{p}i}}{\partial \tau}-\eta_i\frac{1}{r^2}\frac{\partial}{\partial r}\left(r^2\frac{\partial c_{\mathrm{p}i}}{\partial r}\right)=0 \tag{13.2}$$

With the following boundary conditions:

$$\text{at } z=L,\quad \frac{\partial c_{\mathrm{b}i}}{\partial z}=0; \tag{13.3}$$

$$\text{at } z=0,\quad \frac{\partial c_{\mathrm{b}i}}{\partial z}=\mathrm{Pe}\left[c_{\mathrm{b}i}-c_{\mathrm{f}i}(\tau)\right], \tag{13.4}$$

$$\text{and at } r=0,\quad \frac{\partial c_{\mathrm{p}i}}{\partial r}=0; \tag{13.5}$$

$$\text{At } r=1,\quad \frac{\partial c_{\mathrm{p}i}}{\partial r}=\mathrm{Bi}_i\left(c_{\mathrm{b}i}-c_{\mathrm{p}i,r=1}\right). \tag{13.6}$$

The model equations above are basically the same as the general rate model for adsorption LC presented in Chap. 3, except that q is used instead of c_{p}^{*} to describe particle phase concentration in order to be consistent with commonly used IEC terminology. The dimensionless feed profile $c_{\mathrm{f}i}(\tau)$ for the modulator ($i=1$, the first component) in this gradient elution IEC model determines what kind of elution profile is used, including isocratic elution, step-change displacement, or gradient elution. In adsorption LC, the Langmuir isotherm is typically used. In IEC, stoichiometric ion-exchange isotherm is used instead. If a protein follows the Langmuir isotherm on an ion-exchange column, it will be treated like adsorption LC or hydrophobic interaction LC. These two LC modes are covered in Chap. 12. This IEC chapter covers ion-exchange that actually involves exchange of ion on the stationary phase with another ion in the mobile phase as the primary separation mechanism. The following reaction is an example of cation exchanger in which the replacement of initially sorbed Na^{+} on the ion-exchange resin is replaced by Ca^{2+} in the feed solution,

$$2\mathrm{Na}^{+}_{(\mathrm{s})}+\mathrm{Ca}^{2+}_{(\mathrm{aq})}\rightleftharpoons \mathrm{Ca}^{2+}_{(\mathrm{s})}+2\mathrm{Na}^{+}_{(\mathrm{aq})} \tag{13.7}$$

Similar to Na^+ ion, a protein's positively charged region can bind with a cation-exchange resin by replacing the sorbed Na^+. The following reaction describes an anion exchanger for SO_4^{2-} in the mobile phase to replace sorbed Cl^- in the particle phase,

$$2Cl^-_{(s)} + SO^{2-}_{4(aq)} \rightleftharpoons SO^{2-}_{4(s)} + 2Cl^-_{(aq)} \tag{13.8}$$

In the case of a protein sample in the mobile phase, a protein's negatively charged region can bind with an anion-exchange resin by replacing the sorbed Cl^-. Equation (13.9) summarizes both cation exchange and anion exchange, in which species i in the solution replaces the initially sorbed species j,

$$\upsilon_i Q_j + \upsilon_j C_{pi} \rightleftharpoons \upsilon_j Q_i + \upsilon_i C_{pj}. \tag{13.9}$$

For simplicity, this reaction is treated as an elementary reaction. To distinguish solid-phase concentration (for the sorbed species) from the concentration in the fluid phase (in the fluid inside the particle macropores), Q and C are used, respectively. The solid-phase concentration Q is based on the particle skeleton volume according to Eq. (13.2), while the fluid phase concentration C is based on liquid volume. The subscript p in Eq. (13.9) suggests that ion-exchange reaction happens in the particle phase. The υ_i and υ_j values are stoichiometric coefficients. They correspond to the number of charges carried by species i and j, respectively. Absolute values are used in the case of anion exchange for υ.

The following equation describes the mass action isotherm. For simplicity, concentrations are used instead of the more accurate activity coefficients,

$$K_{ij} = \left(\frac{C_{pj}}{Q_j}\right)^{\upsilon_i} \left(\frac{Q_i}{C_{pi}}\right)^{\upsilon_j} \tag{13.10}$$

in which K_{ij} is the dimensionless mass action equilibrium concentration referenced to species j, i.e.,

$$K_{ij} = \frac{k_{ij}}{k_{ji}} \tag{13.11}$$

where k_{ij} is the forward reaction rate constant for the exchange of species i in solution with species j in the sorbed phase, and k_{ji} is the backward reaction rate constant for the exchange of species j in the solution with species i in the sorbed phase. For convenience, a salt ion such as Na^+ or Cl^-, which is usually the sorbed species initially on an ion exchanger, is designated as species 1 to serve as the reference for all of the equilibrium constants. K_{i1} values are needed as input parameter for simulation. All equilibrium constants can be calculated from the $N_s - 1$ independent equilibrium constants from the following relationship:

$$K_{ij} = K_{ik}^{\upsilon_j/\upsilon_k} K_{kj}^{\upsilon_i/\upsilon_k} \tag{13.12}$$

The exchange capacity Λ for the ion-exchange isotherm is calculated from the following equation:

$$\Lambda = \sum_{i=1}^{N_s} \upsilon_i Q_i \tag{13.13}$$

in which N_s is the number of species in the system. This kind of isotherm is inherently implicit. It is difficult to use it to obtain $\partial q_i/\partial\tau$ in Eq. (13.2). Instead of using the ion-exchange equilibrium isotherm, the following nonequilibrium kinetic expression is used:

$$\frac{\partial Q_i}{\partial t} = \left(k_{ij} C_{\mathrm{p}i}^{\upsilon_j} Q_j^{\upsilon_i} - k_{ji} C_{\mathrm{p}j}^{\upsilon_i} Q_i^{\upsilon_j}\right)/\upsilon_j \tag{13.14}$$

A similar approach has been used in Chap. 12 for gradient elution. Equation (13.14) is the rate expression for the reversible ion-exchange reaction with species j as the initially sorbed species. This Q expression yields the following dimensionless rate expression which can be inserted into Eq. (13.2):

$$\frac{\partial q_i}{\partial \tau} = \left(\mathrm{Da}_{ij} c_{\mathrm{p}i}^{\upsilon_j} q_j^{\upsilon_i} - \frac{C_{0j}}{C_{0i}} \mathrm{Da}_{ji} c_{\mathrm{p}j}^{\upsilon_i} q_i^{\upsilon_j}\right)/\upsilon_j \tag{13.15}$$

in which Da_{ij} and Da_{ji} are Damköhler numbers (dimensionless) defined by the following equations:

$$\mathrm{Da}_{ij} = C_{0i}^{\upsilon_j - 1} C_{0j}^{\upsilon_i} \frac{L}{v} k_{ij} \tag{13.16}$$

$$\mathrm{Da}_{ji} = C_{0j}^{\upsilon_i - 1} C_{0_i}^{\upsilon_j} \frac{L}{v} k_{ji} \tag{13.17}$$

When the Damköhler numbers are very large, the ion-exchange reaction approaches equilibrium. For each species, using the kinetic expression instead of an equilibrium isotherm will introduce one additional parameter. This extra parameter can be obtained by artificially degenerating the kinetic expression into equilibrium through setting Da_{ij} values sufficiently large (e.g., 1000). This means an artificially large k_{ij} value is set for each protein. The corresponding Da_{ji} values can then be calculated from Eq. (13.17). This trick solves the implicit isotherm problem at a cost of increased ODE system size for the model equation system after discretization.

Unlike ion exchange involving only small salt ions, steric hindrance can occur when large protein molecules are involved. A protein molecule can replace a sorbed salt ion and then blocks more proteins from accessing ion-exchange sites

underneath it. This steric hindrance reduces the available ion-exchange sites for macromolecules. The so-called steric mass action (SMA) isotherm [5] is based on this scenario. To include the steric hindrance effect, Q_j in Eq. (13.10) and Eq. (13.15) is replaced with $\overline{Q}_1$ by setting j = 1. $\overline{Q}_1$ is calculated from the following equation using σ_i as the steric factor for species i (excluding the salt, i.e., $i \neq 1$):

$$\overline{Q}_1 = Q_1 - \sum_{i=2}^{N_s} \sigma_i Q_i. \tag{13.18}$$

in which species 1 is the initially sorbed salt ion and σ_i is the steric factor for species i ($i = 2, \ldots N_s$). $\overline{Q}_1$ is the concentration of salt ion sorbed on the stationary phase available for ion exchange after steric hindrance. It is smaller than Q_1, which does not consider steric hindrance. Equation (13.15) can be modified accordingly to include the steric hindrance effect.

Mehay and Gu used the approach of varying the equilibrium constant and the characteristic charge for each protein with fluid pH to model the elution of proteins with pH gradients. The pH at each location is calculated from the following equation:

$$\mathrm{pH} = \begin{cases} -\log_{10}\left(\Delta C_{\mathrm{H^+(strong\,acid)}} + \Delta C_{\mathrm{H^+(strong\,base)}} + \Delta C_{\mathrm{H^+(buffer)}} + \Delta C_{\mathrm{H^+(water)}}\right), & \mathrm{pH} \leq 7 \\ 14 - \log_{10}\left(-\Delta C_{\mathrm{H^+(strong\,acid)}} - \Delta C_{\mathrm{H^+(strong\,base)}} - \Delta C_{\mathrm{H^+(buffer)}} + \dfrac{10^{-14}}{\Delta C_{\mathrm{H^+(water)}}}\right), & \mathrm{pH} > 7 \end{cases} \tag{13.19}$$

13.3 Numerical Solution to the IEC Model

The numerical solution strategy is identical to that used for the GRADIENT simulator. Finite element and orthogonal collocation are used for discretization. VODE is used as the ODE solver. Chromulator-IEX is the result of software implementation of the IEC simulator using C++ by Aaron Mehay. Unlike the standard Chromulator package with Fortran library DLL and simulator DLL coupled with C++ GUI EXE file, Chromulator-IEX software contains only one executable file for Microsoft Windows. It is not included in the standard Chromulator software that is free to academic users. Due to the complexity of IEC modeling, it is intended for specialists only.

13.4 How to Use the IEC Simulator for Modeling of IEC

Figure 13.1 is a screenshot of an isocratic elution of two proteins (species 2 and 3) using a salt solution (species 1). C_0 is the reference concentration used for nondimensionalization. c_i is the dimensionless concentration initially inside the

column before sample injection. In this simulation, the column is presaturated with 0.1 mol/L of the salt while the proteins are absent. Cation-exchange "capacity" of the stationary phase is 0.2 in equivalents per L of particle skeleton. The sample impulse time is $\tau_{imp} = 0.2$ in dimensionless time. In Fig. 13.1, the sample does not contain the salt ("Species 1 in sample" unchecked). The first salt peak with a peak height slightly larger than 1.6 is due to the displacement of sorbed salt ions by the two proteins in the sample. The two protein peaks both have a peak area of 0.2, corresponding to $\tau_{imp} = 0.2$. It is interesting to note that the first salt peak has an area of 0.2 instead of 0.4 (combined peak area for the two proteins). This is because the sample has a deficit of the salt in exactly the same amount. Figure 13.2 has the same simulation parameters, except that the sample contains that salt at 0.1 mol/L,

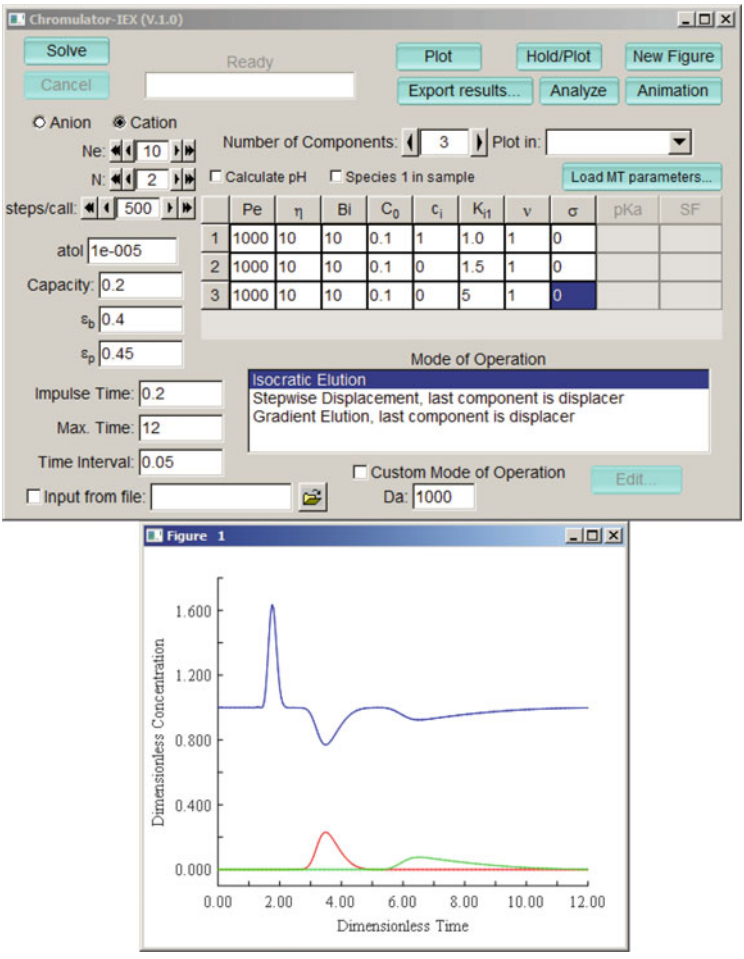

Fig. 13.1 Screenshot of an isocratic cation-exchange elution using a salt solution to elute two other species injected in a pulse sample without the salt in the background solution

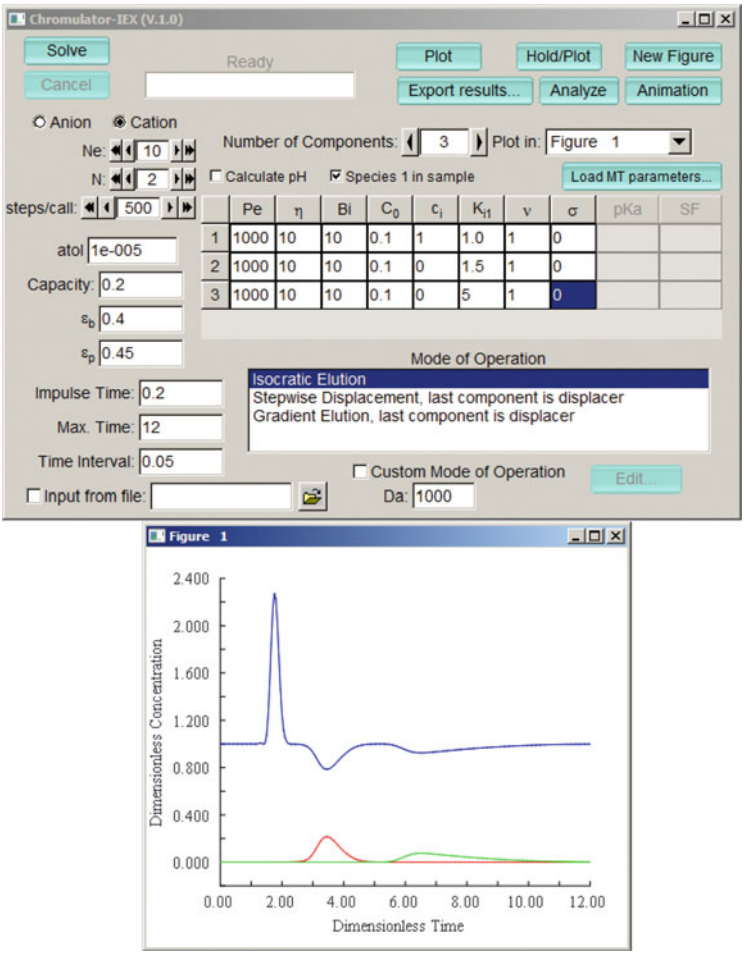

Fig. 13.2 Screenshot of an isocratic cation-exchange elution using a salt solution to elute two other species injected in a pulse sample with the salt in the background solution

that is, the concentration presaturating the column. In this case, the first salt peak is twice as large with a peak area of 0.4, which equals areas of the two protein peaks combined. In Figs. 13.1 and 13.2, the salt concentration profile has two "negative" peaks below the baseline, each of them having a peak area of 0.2. Obviously, they are due to the displacement of the two protein peaks by the salt, resulting in a deficit of salt in the effluent. All these salt peaks can be explained by mass balance.

For easy comparison, the software allows overlapping of two simulation runs by using the Hold/Plot button instead of the Plot button to plot the second run after the input setting has been modified and the Solve button has been executed. Figure 13.3 shows the comparison of Figs. 13.1 and 13.2. The second run (dashed lines) is for

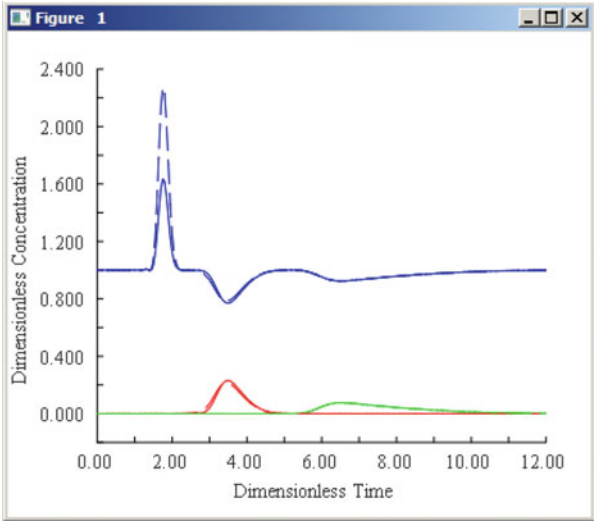

Fig. 13.3 Chromatograms in Figs. 13.1 and 13.2 plotted in the same figure using the Hold/Plot button for easy comparison

the case with salt in the sample background solution. If "Calculate pH" is checked in Fig. 13.2, pK_a and SF (salt fraction) values must be entered.

Figure 13.4 has the same parameters as Fig. 13.1, except that the elution is carried out using a salt gradient of 1 to 4 dimensionless salt concentration in a dimensionless time frame of 8. Dimensionless salt concentration of 4 means 0.4 mol/L because $C_{01} = 0.1$ mol/L is used for nondimensionalization. Again, the first salt peak is due to protein replacement of sorbed salt ions. The second and third salt peaks are negative peaks (dips) on the sloped salt effluent profile.

To allow different feed profiles, the simulator allows the input of profiles of all species to be specified individually in stepwise, pulse, ramp shapes. Figure 13.5 specifies a salt gradient entering the column inlet right after a sample that does not contain the salt. Right after the sample is pumped into the column, a gradient takes off from 1 to 4 in a dimensionless concentration between dimensionless times of 0.2 and 4. Keep in mind that it is impractical to have a gradient takeoff at dimensionless time 0 because a salt gradient has to wait after the impulse sample has completely entered the column. One unusual exception is that a chromatographer pumps the sample into the column using one pump, while a salt gradient is also pumped into the column using separate pump(s) at the same time by mixing the streams. Species 2 and 3 feed profiles are specified by indicating that their dimensionless concentrations are 1 (i.e., dimensional concentrations C_{02} and C_{03}) between dimensionless times 0 and 0.2. Figure 13.4 demonstrates that by using a salt gradient, separation of the two protein peaks can be carried out in about 7 instead of 10 dimensionless time shown in Fig. 13.1.

One useful feature of the IEC simulator is the animation of the dimensionless concentration profiles inside the column using a movie. Figure 13.6 contains screenshots of the movie at dimensionless times 2.65 and 3.20 for the simulation

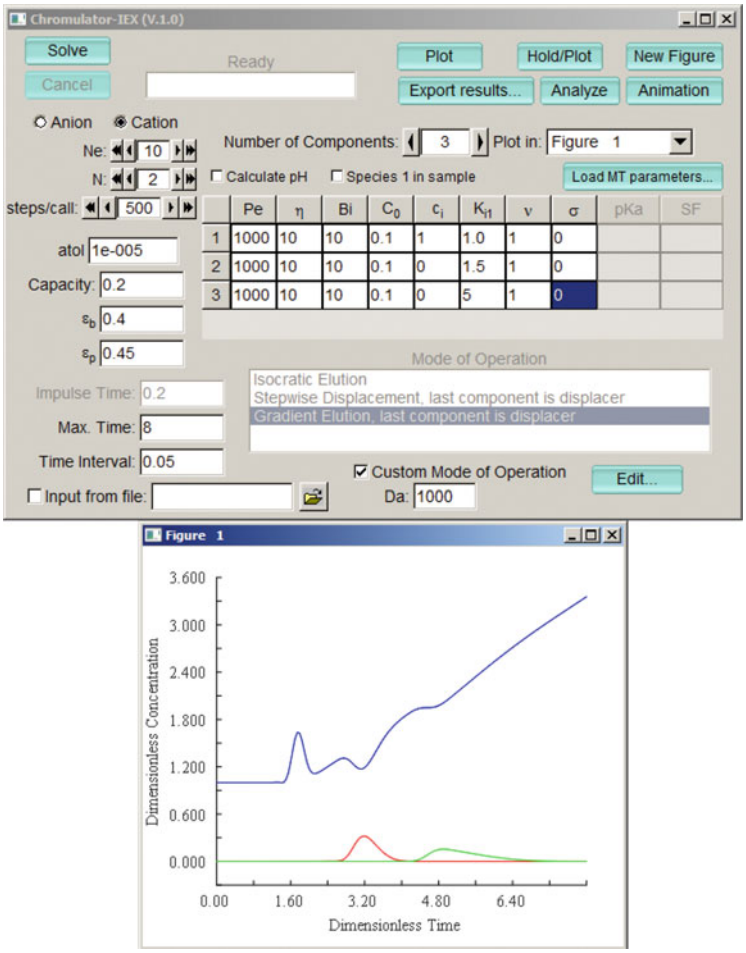

Fig. 13.4 Screenshot of a cation-exchange elution using a linear salt gradient to elute two other species injected in a pulse sample without the salt in the background solution

case shown in Fig. 13.1. The concentrations in Fig. 13.6 at $z = 1$ (column exit) correspond to those in Fig. 13.1 at dimensionless times 2.65 and 3.20. Note that the peaks inside the columns appear to have a diffused left flank and sharper right flank (elute out earlier than the left flank), Thus, when they elute out of the column exit, they will have a sharper front (left flank) and diffused tail.

In Fig. 13.7, Mehay and Gu [1] demonstrated the Chromulator-IEX simulated experimental data [6] on an ion-exchange column well. The 15 mm × 47 mm column was packed with 225-mm-diameter Dowex 50 resin particles in H^+ form. Figure 13.7 shows that the experimental concentration profiles are predicted by the model quite well.

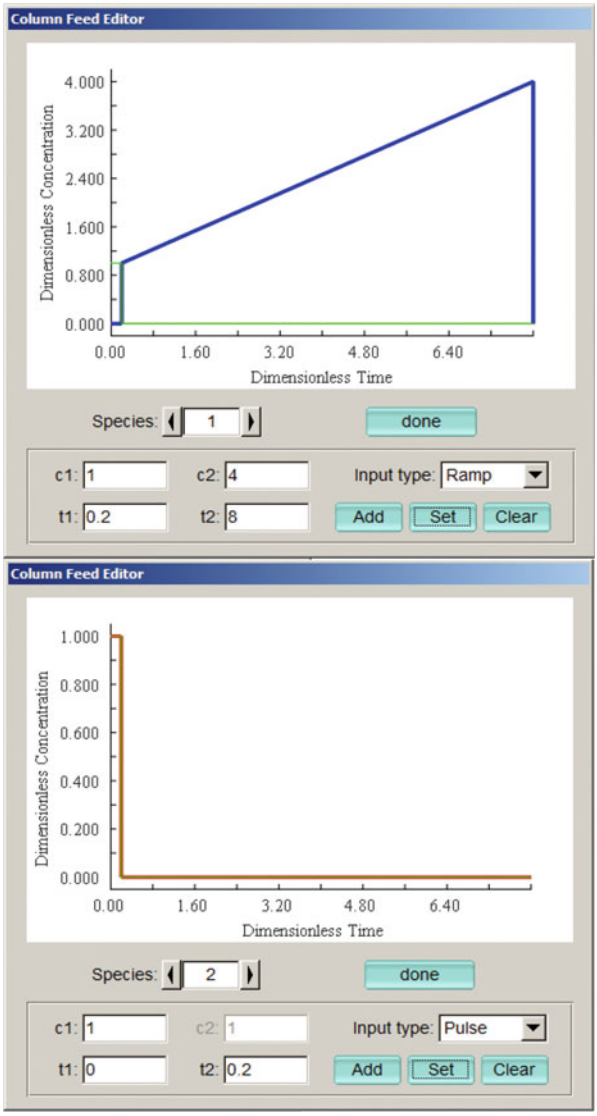

Fig. 13.5 Screenshot of feed profile setup for the linear salt gradient following sample injection and the impulse shape of species 2 during sample injection

An interesting and important phenomenon was revealed by Ghose et al. [2] experimentally for ion-exchange columns, suggesting that pH spikes and dips as large as 1 pH unit are possible in the effluent due to step changes in NaCl concentration in the mobile phase feed solution. This unintentional pH fluctuation is sufficient to cause significant bioactivity losses for some pH-sensitive proteins [2]. To avoid this, computer simulation would be a very useful tool if it can accurately predict this unusual IEC behavior. Figure 13.8 shows the experimental chromatogram from Ghose et al. [2] and simulated chromatogram from

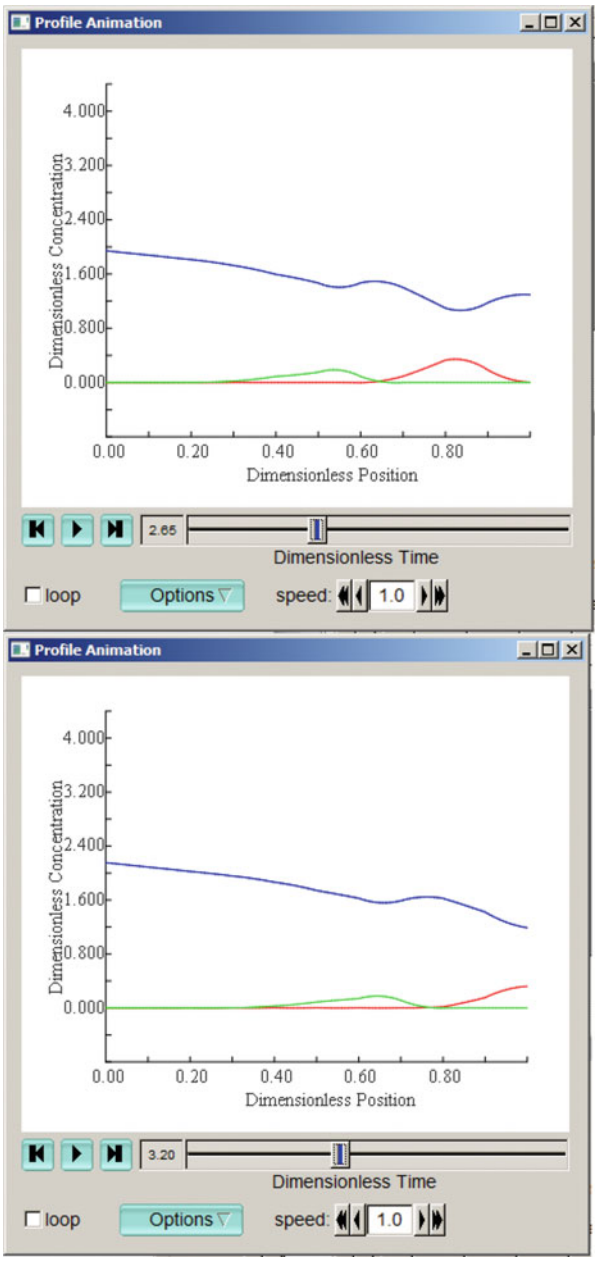

Fig. 13.6 Concentration profiles inside the column at two difference times

Chromulator-IEX for a blank run without eluites by using a mobile phase containing a 25 mM sodium citrate buffer at pH 5.5 with step changes of the NaCl concentration in the mobile phase feed solution. The column was packed

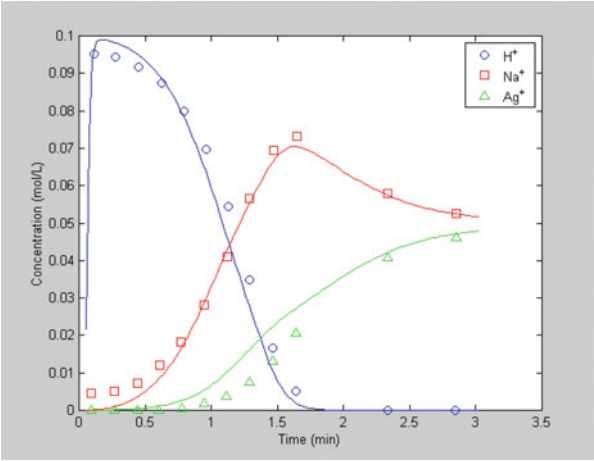

Fig. 13.7 Simulation results (lines) vs. experimental ion-exchange chromatography data from Dranoff and Lapidus [6] (reprinted from [1], permission not required)

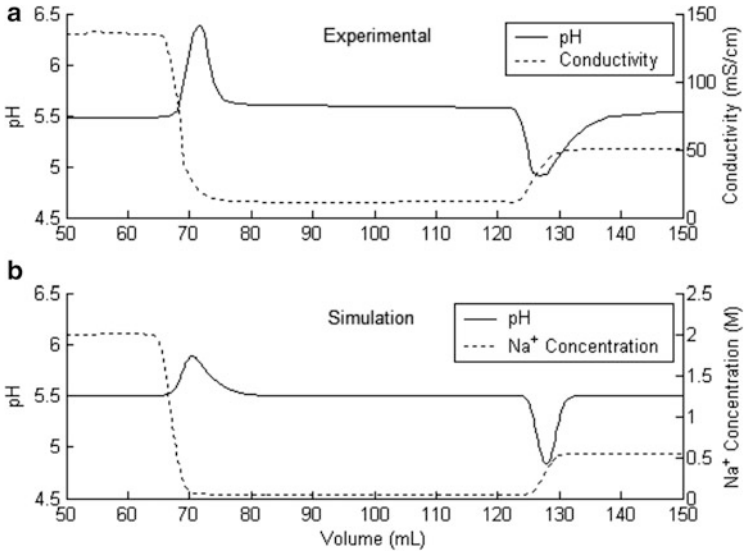

Fig. 13.8 Simulation prediction and comparison with experimental data for a pH spike and a pH dip in the effluent of an cation-exchange column in a blank run using only a sodium citrate buffer (reprinted from [1], permission not required)

with 40–90-μm Fractogel EMD (M) gel, which is a strong cation exchanger with a functional group of SO_3^-. Figure 13.8 demonstrates that the simulation successfully depicts a pH spike and a pH dip in the effluent.

13.5 Summary

By using the kinetic reversible ion-exchange reaction expression and then artificially degenerating it to equilibrium, the difficulty of processing the implicit ion-exchange isotherm for use in the general rate model for gradient elution IEC is avoided. The examples demonstrated in this chapter show that the IEC simulator is flexible in the feed concentration profiles to tackle various feed scenarios. The simulator allows for easy comparison of different simulation runs for parameter studies. Concentration profiles inside a column can be viewed as a movie for visualization. The IEC simulator is a useful tool for studying various IEC behaviors. It is also a useful tool in the scale-up of IEC.

References

1. Mehay A, Gu T (2014) A general rate model of ion-exchange chromatography for investigating ion-exchange behavior and scale-up. J Microb Biochem Technol 6:216–222
2. Ghose S, McNerney TM, Hubbard B (2002) pH Transitions in ion-exchange systems: role in the development of a cation-exchange process for a recombinant protein. Biotechnol Prog 18:530–537
3. Ernest MV, Whitley RD, Ma Z, Wang N-HL (1997) Effects of mass action equilibria on fixed-bed multicomponent ion-exchange dynamics. Ind Eng Chem Res 36:212–226
4. Frey DD, Barnes A, Strong J (1995) Numerical studies of multicomponent chromatography using pH gradients. AIChE J 41:1171–1183
5. Brooks CA, Cramer SM (1992) Steric mass-action ion exchange: displacement profiles and induced salt gradients. AIChE J 38:1969–1978
6. Dranoff J, Lapidus L (1961) Ion exchange in ternary systems. Ind Eng Chem 53:71–76. doi:10.1021/ie50613a040

Chapter 14
Multicomponent Radial Flow Chromatography

14.1 Introduction

Radial flow chromatography (RFC) was introduced into the commercial market in the mid-1980s [1] as an alternative to the conventional axial flow chromatography (AFC) for preparative- and large-scale applications. Figure 14.1 shows a schematic of an RFC column with inward radial flow. Compared to AFC, the RFC geometry in Fig. 14.2 provides a relatively large flow area and a short flow path. It allows a higher volumetric flow rate with a lower bed pressure compared to longer AFC columns. If soft gels or affinity matrix materials are used as separation media, the low-pressure drop of RFC helps prevent bed compression [2, 3]. An experimental case study of the comparison of RFC and AFC was carried out by Saxena and Weil [4] for the separation of ascites using the QAE cellulose packing. They reported that by using a higher flow rate, the separation time for RFC was one-fourth of that needed for a longer AFC column with the same bed volume. It was claimed that by using RFC instead of AFC, separation productivity can be improved quite significantly [1]. Lay et al. tested and modeled a continuous RFC system for protein separation [5]. Recently, Yan et al. successfully used a commercially available 500-mL RFC column packed with ion-exchange resins to separate antiproliferative polysaccharides from *Hypsizigus marmoreus*. Numerous other experimental studies have also been reported using RFC columns. Both prepacked and unpacked RFC columns, with a size range from 50 mL to 200 L in bed volume, are commercially available. A comprehensive review was provided by Gu in 2013 [6].

Mathematical modeling of RFC presents certain challenges. Since the linear flow velocity (v) in the RFC column changes continuously along the radial coordinate of the column, the radial dispersion and external mass transfer coefficients may no longer be treated as constant. This important feature was sometimes not considered in the mathematical modeling of RFC in the literature for convenience. Extensive theoretical studies have been reported for single-component ideal RFC, which neglects radial dispersion, intraparticle diffusion, and external mass transfer

© Springer International Publishing Switzerland 2015

T. Gu, *Mathematical Modeling and Scale-Up of Liquid Chromatography*,
DOI 10.1007/978-3-319-16145-7_14

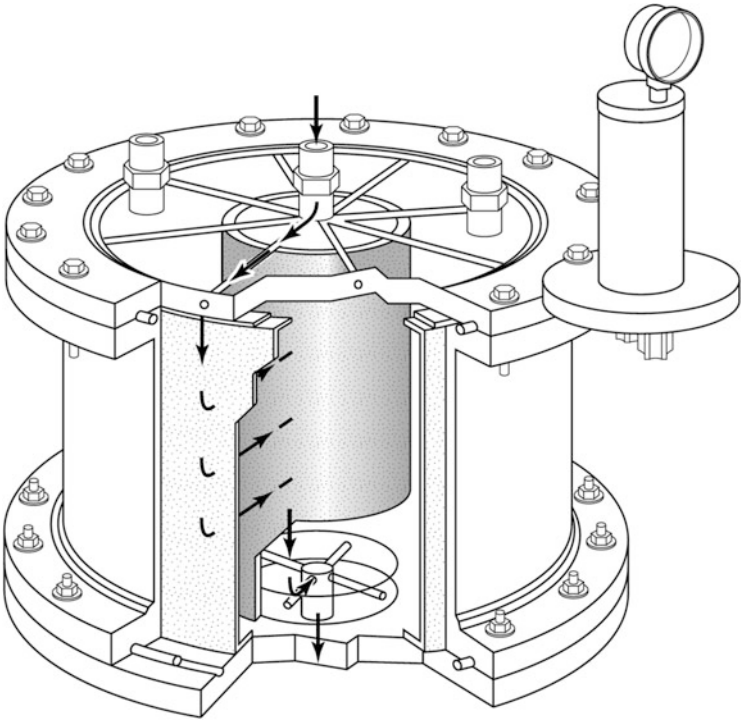

Fig. 14.1 Schematic of a commercial RFC column with inward flow (Courtesy of Sepragen Corp.)

resistance. In such studies, a local equilibrium assumption and linear isotherms are often assumed. The earliest theoretical treatment of RFC was made by Lapidus and Amundson [7]. A similar study was carried out by Rachinskii [8]. Later, Inchin and Rachinskii [9] included bulk-fluid phase molecular diffusion in their modeling. Lee et al. [10] proposed a unified approach for moments in chromatography, both AFC and RFC. They used several single-component rate models for the comparison of statistical moments for RFC and AFC. Their models included radial dispersion, intraparticle diffusion, and external mass transfer effects. Kalinichev and Zolotarev [11] also carried out an analytical study on moments for single-component RFC in which they treated the radial dispersion coefficient as a variable.

A rate model for nonlinear single-component RFC was solved numerically by Lee [12] by using the finite difference and orthogonal collocation methods. His model considered radial dispersion, intraparticle diffusion, external mass transfer, and nonlinear isotherms. It used averaged radial dispersion and mass transfer coefficients instead of treating them as variables. A nonlinear model of this kind of complexity has no analytical solution and must be solved numerically. Rhee et al. [13] discussed the extension of their multicomponent chromatography theory for ideal AFC with Langmuir isotherms to RFC. With today's powerful personal

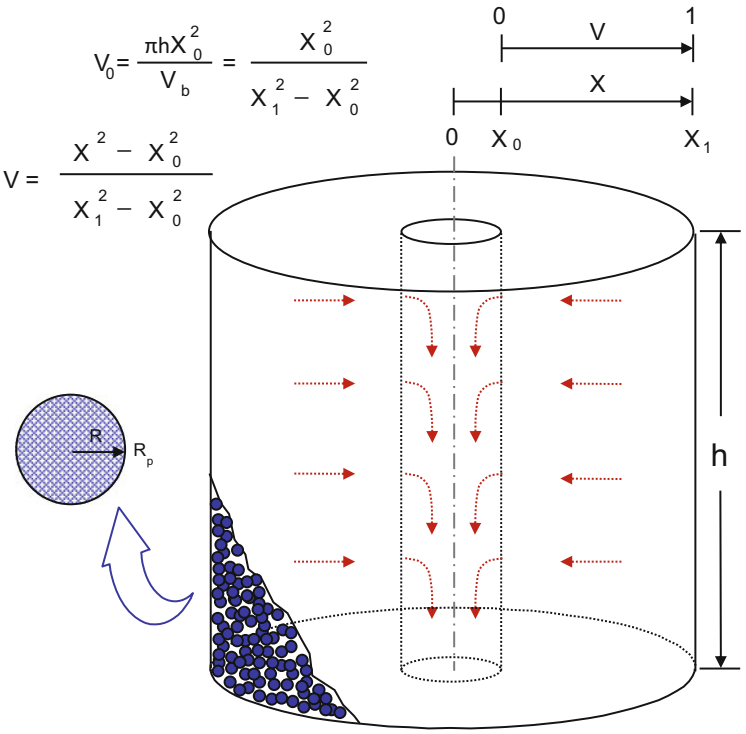

Fig. 14.2 RFC column schematic showing inward flow

computers and efficient numerical methods, more complicated treatment of multicomponent RFC modeling is attainable. A general model for multicomponent RFC can provide some useful information. In this chapter, a numerical procedure is presented for solution to a general rate model for multicomponent RFC. The model is solved by using the same basic approach presented in Chap. 3 for the corresponding AFC model. The solution of the model enables the discussion of several important issues concerning the characteristics and performance of RFC and its differences from AFC and the question of whether one should treat dispersion and mass transfer coefficients as variables.

14.2 General Multicomponent Rate Model for RFC

Figure 14.2 shows the structure of a cylindrical RFC column. The following basic assumptions are needed for the formulation of a unified general model for RFC.

(1) The chromatographic process is isothermal. There is no temperature change during a run.

(2) The porous particles in the bed are spherical and uniform in diameter.
(3) The concentration gradients in the axial direction are negligible. This means that the maldistribution of radial flow is ignored.
(4) The fluid inside particle macropores is stagnant, i.e., there is no convective flow inside macropores.
(5) An instantaneous local equilibrium exists between the macropore surfaces and the stagnant fluid in the macropores.
(6) The film mass transfer theory can be used to describe the interfacial mass transfer between the bulk-fluid and particle phases.
(7) The diffusional and mass transfer coefficients are constant and independent of the mixing effects of the components involved.

Based on the basic assumptions above, Eqs. (14.1) and (14.2) are formulated from the differential mass balances for each component in the bulk-fluid and particle phases, respectively. In Eq. (14.1), "$+v$" represents outward flow, and "$-v$" inward flow.

$$-\frac{1}{X}\frac{\partial}{\partial X}\left(D_{\mathrm{b}i}X\frac{\partial C_{\mathrm{b}i}}{\partial X}\right)\pm v\frac{\partial C_{\mathrm{b}i}}{\partial X}+\frac{\partial C_{\mathrm{b}i}}{\partial t}+\frac{3k_i(1-\varepsilon_{\mathrm{b}})}{\varepsilon_{\mathrm{b}}\mathrm{R_p}}\left(C_{\mathrm{b}i}-C_{\mathrm{p}i,R=\mathrm{R_p}}\right)=0 \tag{14.1}$$

$$\left(1-\varepsilon_{\mathrm{p}}\right)\frac{\partial C^{*}_{\mathrm{p}i}}{\partial t}+\varepsilon_{\mathrm{p}}\frac{\partial C_{\mathrm{p}i}}{\partial t}-\varepsilon_{\mathrm{p}}D_{\mathrm{p}i}\left[\frac{1}{R^2}\frac{\partial}{\partial R}\left(R^2\frac{\partial C_{\mathrm{p}i}}{\partial R}\right)\right]=0 \tag{14.2}$$

The initial conditions for the PDE system are

$$\text{At } t=0,\quad C_{\mathrm{b}i}=C_{\mathrm{b}i}(0,X) \tag{14.3}$$

$$C_{\mathrm{p}i}=C_{\mathrm{p}i}(0,R,X) \tag{14.4}$$

The boundary conditions are

$$\text{At the inlet } X \text{ position}\quad \partial C_{\mathrm{b}i}/\partial X=(v/D_{\mathrm{b}i})[C_{\mathrm{b}i}-C_{\mathrm{f}i}(t)] \tag{14.5}$$

$$\text{and at the outlet } X \text{ position}\quad \partial C_{\mathrm{b}i}/\partial X=0 \tag{14.6}$$

Eqs. (14.1) and (14.2) can be written in dimensionless forms as follows:

$$-\frac{\partial}{\partial V}\left(\frac{\alpha}{\mathrm{Pe}_i}\frac{\partial c_{\mathrm{b}i}}{\partial V}\right)\pm\frac{\partial c_{\mathrm{b}i}}{\partial V}+\frac{\partial c_{\mathrm{b}i}}{\partial \tau}+\xi_i\left(c_{\mathrm{b}i}-c_{\mathrm{p}i,r=1}\right)=0 \tag{14.7}$$

$$\frac{\partial}{\partial \tau}\left[\left(1-\varepsilon_{\mathrm{p}}\right)\ c^{*}_{\mathrm{p}i}+\varepsilon_p c_{\mathrm{p}i}\right]-\eta_i\left[\frac{1}{r^2}\frac{\partial}{\partial r}\left(r^2\frac{\partial c_{\mathrm{p}i}}{\partial r}\right)\right]=0 \tag{14.8}$$

In Eq. (14.7), the dimensionless variable, $V=\left(X^2-X_0^2\right)/\left(X_1^2-X_0^2\right)\in[0,1]$, is based on the local volume averaging method [13]. In Eq. (14.7), $\alpha=2(V+V_0)^{1/2}$

$\left[(1+V_0)^{1/2} - V_0^{1/2}\right]$ is a function of V. V_0 is a ratio of the RFC hollow center cylinder volume to bed volume (V_b) as shown in Fig. 14.2.

The initial conditions are

$$\text{at } \tau = 0 \quad c_{bi} = c_{bi}(0, V), \tag{14.9}$$

$$c_{pi} = c_{pi}(0, r, V) \tag{14.10}$$

The boundary conditions are

$$\partial c_{bi}/\partial V = \text{Pe}_i[c_{bi} - C_{fi}(\tau)/C_{0i}] \tag{14.11}$$

At the inlet V position

For frontal adsorption, $C_{fi}(\tau)/C_{0i} = 1$.

For elution

$$C_{fi}(\tau)/C_{0i} = \begin{cases} 1 & 0 \le \tau \le \tau_{\text{imp}} \\ 0 & \text{else} \end{cases} \tag{14.12}$$

After the introduction of a sample in the form of a rectangular pulse

$$\text{If component } i \text{ is displaced,} \quad C_{fi}(\tau)/C_{0i} = 0$$
$$\text{If component } i \text{ is a displacer,} \quad C_{fi}(\tau)/C_{0i} = 1$$
$$\text{At the outlet } V \text{ position,} \quad \partial c_{bi}/\partial V = 0$$

For the particle phase-governing equation, the boundary conditions are

$$\text{at } r = 0, \quad \partial c_{pi}/\partial r = 0; \tag{14.13}$$

$$\text{at } r = 1, \quad \partial c_{pi}/\partial r = \text{Bi}\left(c_{bi} - c_{pi,r=1}\right) \tag{14.14}$$

Note that all the dimensionless concentrations are based on C_{0i} that is the maximum of the feed profile $C_{fi}(\tau)$ for each component.

For RFC, the radial dispersion coefficient D_{bi} is a variable that depends on the linear velocity v. In liquid chromatography, it can be assumed that $D_{bi} \propto v$ [12, 14, 15]. Thus, $\text{Pe}_i = v(X_1 - X_0)/D_{bi}$ can be considered constant in liquid RFC. The variation of Bi_i values observes the following relationship:

$$\text{Bi}_i \propto k_i \propto v^{1/3} \propto (1/X)^{1/3} \propto (V + V_0)^{-1/6} \tag{14.15}$$

If $\text{Bi}_{i,V=1}$ values are known, Bi_i values anywhere else can be obtained from Eq. (14.16):

$$\mathrm{Bi}_{i,V} = [(1+V_0)/(V+V_0)]^{1/6}\mathrm{Bi}_{i,V=1} \tag{14.16}$$

ξ_i can be calculated from Bi_i using its definition $\xi_i = 3\mathrm{Bi}_i\eta_i(1-\varepsilon_\mathrm{b})/\varepsilon_\mathrm{b}$.

14.3 Numerical Solution

The strategy for the numerical solution to the model is identical to that used for the general rate model in Chap. 3. The PDE system of the governing equations is first discretized. The finite element and orthogonal collocation methods are used to discretize the bulk-fluid phase and the particle phase-governing equations, respectively. The resulting ordinary differential equation (ODE) system is then solved using VODE.

In the numerical procedure, $D_{\mathrm{b}i}$ and k_i values are treated as variables that are dependent on the variation of v along the radial coordinate V. Meanwhile, intraparticle diffusivities ($D_{\mathrm{p}i}$) are regarded as independent of the variations of v. Due to the special geometry of RFC, there are two space coordinate (V)-dependent variables, α and ξ_i. The finite element method can deal with this situation routinely without any extra trouble. The ability to deal with variable physical properties with ease is one of the advantages of the finite element method. Accuracy is another notable advantage of the method.

The accommodation of variable Bi_i in the particle phase is also easy. Since particle phase equations must be solved at each finite element node (with given nodal position, V) in the function subroutine of the Fortran 77 code, $\mathrm{Bi}_{i,V}$ values can be readily obtained from Eq. (14.16). The Fortran 77 code for the simulation of RFC is named "RATERFC.FOR." The code is similar to the Fortran 77 code RATE.FOR for AFC presented in Chap. 3.

A study of the effects of treating $D_{\mathrm{b}i}$ and k_i as variables compared to treating them as constants has been carried out by Gu et al. [14]. The comparison between RFC and AFC was also studied through computer simulation.

14.4 How to Use the Fortran 77 Code RATERFC.FOR

To demonstrate the usage of the computer code, the multicomponent Langmuir isotherm is used for simulation. Figure 14.3 shows simulated breakthrough curves for two components in inward flow RFC. The Fortran 77 code RATERFC.FOR requires a data file named "data" to provide simulation parameters upon the execution of the code. The heading generated by the code when it is executed for Fig. 14.3 is shown:

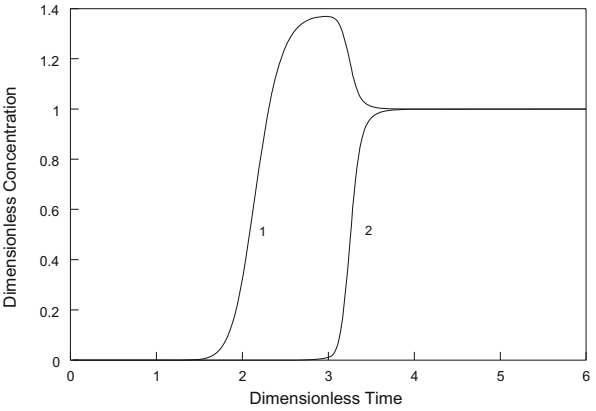

Fig. 14.3 Simulation of binary frontal adsorption in inward flow RFC

```
Radial Flow Chromatogr. Simulator by T. GU (Ohio U.)
=====================================================
in/outward (-1/1) V0     iave (1,2/0 for y,y/n)
    -1      0.04000    0
-------------------------------------------------------------
nsp nelemb nc index timp  tint tmax epsip epsib
 2  15   2  1   0.500 0.015 4.0 0.400 0.400
-------------------------------------------------------------
  PeL    eta    Bi   C0    consta  constb
 100.00  10.000  10.000 0.20000  1.000  2.000
  80.00  8.000  8.000 0.20000  10.000  20.000
======================================== End of data file.
Total ODE = 186  Data pts = 266
tol =  1.0000000000000D-05 <-- Double precision or not, see this.
-------------------------------------------------------------
index =1 Breakthru; =2, Elution with inert MP
index =3 Step-change disp. Last comp. is displacer
index =4 BT, switch to displacement at t = tshift
index =5 Same as index=4, but reverse flow
index =6 Elution, the last component is modifier
index =7 Same as =6, but sample is in inert...
index =10+ use separation factors
Input Bi value should be at its value at V=1.
If iave=0, then the code treats k, D as variables
If iave=1,2 an ave Bi is used by the code from Bi|V=1.
If iave=1, taking ave at (X1+X0)/2
If iave=2, taking ave at V=0.5
If spiral flow chromatography, in/outward (-10/10)
-------------------------------------------------------------
 Results (t, c1, c2,...) follow.  Please wait...
  0.01500  0.00000  0.00000
  (... more data points)
```

Stripping away the text lines in the heading above from the beginning to the "End of data file," the remaining numerical figures are what the file "data" contains. The first three inputs are the flag number for inward flow (input value $= -1$) or outward flow RFC (input value $= 1$), the value for V_0 ($V0$), and the flag number for how to treat D_{bi} and k_i (i_{ave}). If $i_{ave} = 0$, the code treats D_{bi} and k_i as variables. In order to study the effect of treating D_{bi} and k_i as variables compared to taking an averaged value [14], the code allows the user to take averaged D_{bi} and k_i values at $(X_1 + X_0)/2$, or at $V = 0.5$ for the calculation of Pe_i, Bi_i, and ξ_i by setting $i_{ave} = 1$ or 2, respectively. Other input data for the code are identical to those used for RATE. FOR. The user may consult Chap. 3 for details. $V_0 = 0.04$ for Fig. 14.3 means the RFC column's hollow center cylinder volume ($\pi X_0^2 h$) is 4 % of the bed volume. Figure 14.4 shows Chromulator 2.2 reproduction of Fig. 14.3 showing the GUI with input parameters.

Figure 14.5 shows a binary elution in inward flow RFC. The software can also simulate other operations such as step-change displacement, etc. More simulated chromatograms are given elsewhere by Gu et al. [14].

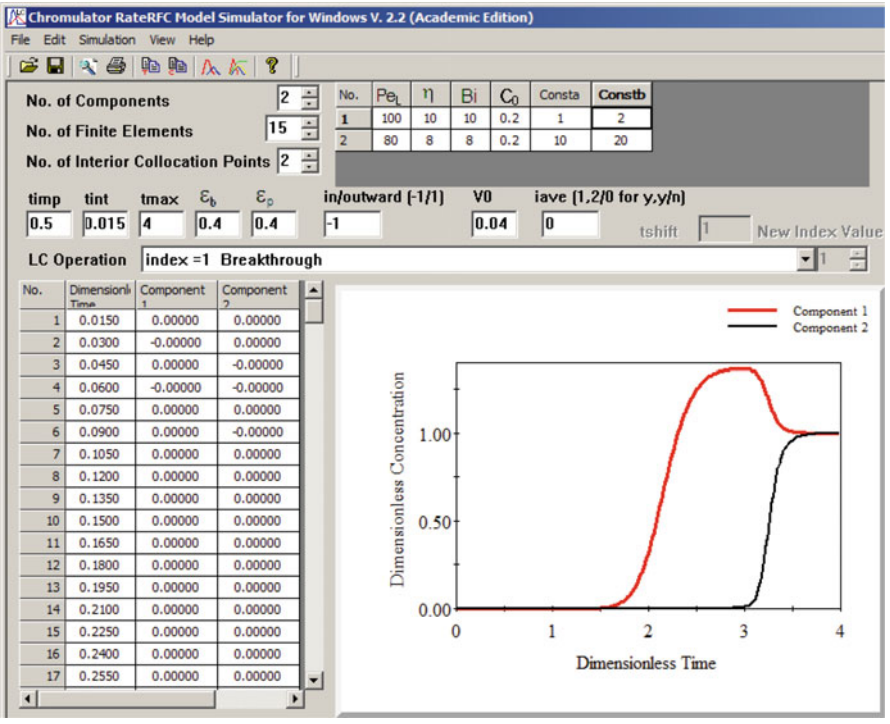

Fig. 14.4 Reproduction of Fig. 14.3 using chromulator 2.2 with GUI

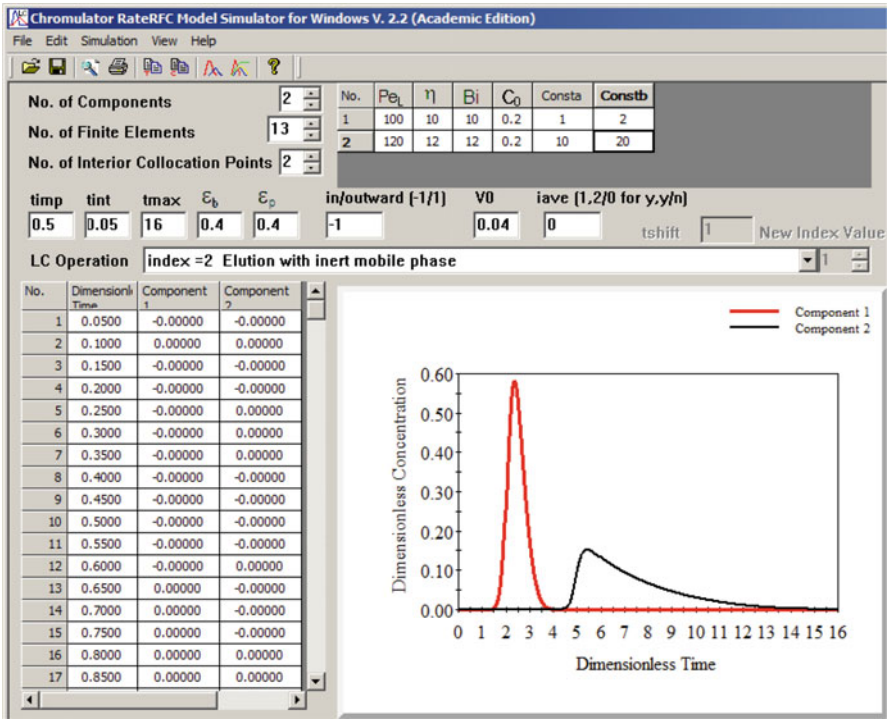

Fig. 14.5 Binary elution with an inert mobile phase in inward flow RFC

14.5 Theoretical Investigations Using the RFC Simulator

Using the RFC model presented in this chapter for a theoretical study, Gu et al. [14] found that inward flow RFC resulted in slightly sharper concentration profiles than outward flow RFC. This is supported by the experimental verification of Besselink et al. [16]. The simulation by Gu et al. also suggested that RFC's performance is similar or slightly better than that of a pancake-shaped AFC column with a radius equivalent to the RFC bed height and a column axial length equivalent to the RFC radial flow path length when nonideal flow is ignored [14]. This is consistent with the experimental finding by Kim and Lee [17]. It should be noted that some published experimental comparisons of RFC with AFC did not strictly follow this kind of dimensional equivalency and thus resulting in better performances for RFC [4, 18]. In practice, floor footage, ease of packing, and the ability to distribute flow better to prevent nonideal flow will determine which type of LC performs better. Column size availability from an established vendor will also be a major factor for column selection.

14.6 Extensions of the General Multicomponent Rate Model for RFC

Extensions to the basic general rate model for AFC in Chap. 3 have also been applied to the RFC model. These include second-order kinetics, size exclusion effect, and a reaction in the liquid phase for the modeling of biospecific elution using a soluble ligand as in affinity LC. The extensions have been carried out with ease. Details are omitted here since the necessary modifications for adding second-order kinetics involve only the particle phase-governing equation, in which the AFC and the RFC models do not differ, except that the k_i values in RFC are variables.

The addition of reaction terms for the interaction between a macromolecule and the soluble ligand involves the bulk-fluid phase, but it does not touch the characteristic terms of an RFC model. It has been implemented for a theoretical study of affinity RFC [19]. Figure 14.6 shows a simulated chromatogram of an affinity separation process with frontal adsorption, wash, and elution stages using RFC with inward flow and $V_0 = 0.04$. The Fortran 77 code used for the simulation is named "AFFIRFC.FOR." The parameters for simulation of Fig. 14.6 are the same as those for Fig. 11.14, except inward flow. $V_0 = 0.04$ and $i_{ave} = 0$ are used for Fig. 14.6. Compared with AFC for Fig. 10.14, Fig. 14.6 for RFC has almost no practical difference when the two figures are superimposed because comparable physical parameters as discussed earlier in this chapter are used in the two cases.

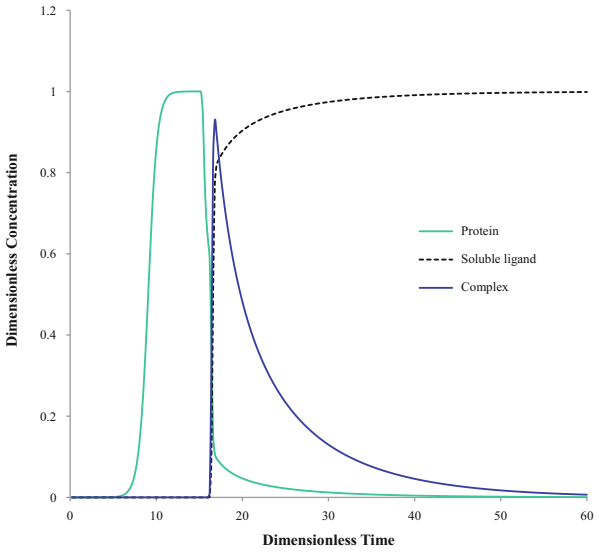

Fig. 14.6 Simulation of affinity RFC with inward flow

14.7 Summary

A general rate model for RFC has been presented. Radial dispersion and mass transfer coefficients are treated as variables in the model. The model is solved numerically by using the finite element and orthogonal collocation methods for the discretization of bulk-fluid and particle phase PDEs, respectively. Several chromatographic operations have been simulated. The fact that several earlier key theoretical findings regarding the performance comparison of RFC vs. AFC were later verified by experiments proves the value of the RFC model. The RATERFC simulator is part of the academic version of Chromulator 2.2, which is available free of charge for academic applications by contacting the author.

References

1. McCormick D (1988) Chromatography and affinity separations, 1988 report. Bio/technology (USA)
2. Ernst P (1987) Radial flow chromatography. Aust J Biotechnol 1:22–24
3. Saxena V, Weil AE, Kawahata RT, McGregor WC, Chandler M (1987) Applications of radial flow columns for fast affinity-chromatography. Am Lab 19:112
4. Saxena V, Weil AE (1987) Radial flow columns: a new approach to scaling-up biopurifications. BioChromatography 2:90–97
5. Lay MC, Fee CJ, Swan JE (2006) Continuous radial flow chromatography of proteins. Food Bioprod Process 84:78–83
6. Gu T (2013) Radial flow chromatography. In: Flickinger MC (ed) Downstream industrial biotechnology: recovery and purification. Wiley, New York, pp 1630–1641
7. Lapidus L, Amundson NR (1950) Mathematics of adsorption in beds. III. Radial flow. J Phys Colloid Chem 54:821
8. Rachinskii VV (1968) Basic principles of radial chromatography. J Chromatogr A 33:234–241. doi:10.1016/S0021-9673(00)98643-6
9. Inchin PA, Rachinskii VV (1977) Theory of radial-cylindrical sorption dynamics. V. Frontal equilibrium sorption dynamics with longitudinal diffusion. Russ J Phys Chem 47:1331–1333
10. Huang SH, Lee W-C, Tsao GT (1988) Mathematical models of radial chromatography. Chem Eng J 38:179–186
11. Kalinichev AI, Zolotarev PP (1970) The method of moments and the theory of radial—cylindrical frontal sorption dynamics for a single substance. Russ J Phys Chem 51:871–873
12. Lee W-C (1989) PhD thesis. Purdue University, West Lafayette, IN
13. Rhee H-K, Amundson NR (1982) Analysis of multicomponent separation by displacement development. AIChE J 28:423–433
14. Gu T, Tsai G-J, Tsao GT (1991) A theoretical study of multicomponent radial flow chromatography. Chem Eng Sci 46:1279–1288
15. Weber SG, Carr PW (1989) The theory of the dynamics of liquid chromatography. In: Brown PR, Hartwick RA (eds) High performance liquid chromatography. Wiley, New York
16. Besselink T, van der Padt A, Janssen AE, Boom RM (2013) Are axial and radial flow chromatography different? J Chromatogr A 1271:105–114
17. Kim Y-H, Lee EK (1996) Comparison of axial and radial flow chromatography on protein separation speed and resolution. Korean J Chem Eng 13:466–472
18. Cabanne C, Raedts M, Zavadzky E, Santarelli X (2007) Evaluation of radial chromatography versus axial chromatography, practical approach. J Chromatogr B 845:191–199
19. Gu T, Tsai GJ, Tsao GT (1992) Multicomponent affinity radial flow chromatography. Sep Technol 2:176–182

Index

© Springer International Publishing Switzerland 2015

T. Gu, *Mathematical Modeling and Scale-Up of Liquid Chromatography*,
DOI 10.1007/978-3-319-16145-7